Reactivity of Functionalised Surfaces with Atmospheric Radicals

Amy Wolstenholme-Hogg

PhD

University of York

Chemistry

April 2025

Abstract

Self-assembled monolayers (SAMs) are widely used in various technologies and as model systems for studying interfacial reactions [1]. However, their stability can be compromised by autoxidation, where molecular oxygen and organic molecules undergo a free-radical chain reaction, leading to monolayer degradation [2]. This project aims to understand the surface oxidation mechanisms following the radical initiation of organic chains. Upon radical initiation, the carbon-centred radical formed reacts with oxygen to generate a peroxyl radical. The propagation of these radical reactions via the peroxyl radical was investigated in monolayer systems with varying functionalities, including alkyl, branched alkyl, ether, and perfluorinated chains. The results indicate that H-abstraction of ether-containing chains by a peroxyl radical occurs more efficiently than alkyl chains, likely due to their lower C-H bond dissociation energies. The lack of H-abstraction by peroxyl radicals in alkyl chains suggests that peroxyl radicals undergo an alternative reaction pathway. A statistical model showed that the probability of two peroxyl radicals being close enough to react to form stable products is approximately 0.1%, due to the limited mobility of molecules in monolayer systems. Experiments with added NO, which readily reacts with peroxyl radicals to form more reactive alkoxyl radicals, indicated that NO contributes to reaction spreading but is not the dominant fate for peroxyl radicals. This suggests an unknown alternative reaction pathway for peroxyl radicals in the monolayer system, potentially involving reaction with the surface or atmospheric contaminants. This project provides insights into autoxidation mechanisms in monolayer systems, which can inform the stability of SAM-based technologies, such as chemical sensing, and enhance our understanding of oxidation processes on surfaces. Moreover, this project is part of a research programme funded by the European Commission, which aims to develop sensors based on Si junctionless nanowire transistor (Si JNT) devices for the real-time detection of short-lived atmospheric radicals (·OH and NOx). The interaction of ·OH radicals with functionalised planar silica substrates as a model system for Si JNT devices has shown that ether- or allylic-containing chains degrade faster than alkyl or perfluorinated chains. Initial atmospheric chamber tests demonstrated that functionalised sensor surfaces can detect ·OH radicals through a change in current.

Declaration

I declare that this thesis is a presentation of original work and I am the sole author. This work has not previously been presented for an award at this, or any other, university. All sources are acknowledged as references. Moreover, I declare that in the event the work of others has been used, this has been fully acknowledged in the text and as references.

Synthesis of precursors (Section 2.2.1) and development of the oxidative cleavage methodology (Section 2.3.3) was undertaken by Naeem Iqbal, a post-doc in the Victor Chechik research group. Atmospheric chamber testing of the sensor devices (Section 4.3.2) was conducted by Vaishali Vardhan and Subhajit Biswas at the University College Cork, Ireland.

Some of the research outlined in this thesis has been published in the following paper:

Iqbal N, Wolstenholme-Hogg A, Chechik V. Analytical Chemistry. 2025. Doi: 10.1021/acs.analchem.4c06937.

Acknowledgements

First and foremost, I would like to thank my supervisor Prof. Victor Chechik, who provided the highest guidance and support throughout my research and writing. His enthusiasm and scientific insight has further increased my motivation for science and for that I am grateful. I would also like to sincerely thank my IPM advisor, Prof. Neil Hunt, for his invaluable feedback, guidance, and encouragement. I am grateful for the comfortable and supportive environment he provided, which made it easy for me to reach out whenever needed.

A special thank you goes to the RADICAL team, who never failed to make me smile during our monthly meetings. Their unwavering support and encouragement were invaluable to my research. Many thanks to Tamela for her excellent organisation of the RADICAL project and the General Assemblies over the past three years.

Thank you to the academic support staff who provided training and guidance with performing experiments and measurements. A heartfelt thanks to Karl Heaton (GC-MS), who witnessed the challenges of this project and provided invaluable expertise with any GC-MS issues. His patience and kindness over the years will not be forgotten. A special thanks also for trusting me to use his valuable GC-MS instrument unsupervised. I'd also like to thank Scott Hicks (GC) for his assistance with GC during the initial stages of my PhD and for his support throughout my years at York. A very big thank you to Niall Donaldson (lab technician) who helped me to create some very interesting experimental set-ups and for being excellent company in the lab, especially during the final summer when the research group was small. I would like to thank Jim Hopkins and Katie Read for allowing use of their equipment at WACL and for their advice and support with my experiments.

A very special thank you needs to go to the members of the VC group. To Naeem, who deserves the biggest thanks: we battled through this project together, and I am eternally grateful to have had you by my side every step of the way. Your patience, kindness, and calm nature provided me with constant support throughout my PhD journey and I couldn't have asked for a better RADICAL partner. To Ivan, Mohammed, and Rajat — I will always be grateful for your friendship and encouragement throughout the years, and for lifting my spirits whenever it was needed. To Matt, who joined the group briefly, I thank you for your care and reassurance. To Andrew, Edward, Ben and Amber, who joined the group in my final months, I thank you for being such lovely company and for allowing my final few months in York to be truly enjoyable. To my good friend, Sanjana - I cannot thank you enough for your unwavering support and encouragement throughout my years in York. I will always be grateful for the day you arrived and our friendship began. To Alexandra (YPI) - thank you for your guidance at the Plasma Institute, for becoming a good friend and introducing me to the exciting world of rowing and

cycling adventures.

Finally, I would like to thank my family. To my dad — a heartfelt thank you for your unwavering support and invaluable advice throughout my PhD journey. I am forever grateful for our in-depth chemistry conversations and for having someone at home who truly understands and empathizes with the challenges of chemistry. To my mum - I cannot thank you enough for your constant support and strength that helped me through these past years. To my brother, Tom, who always inspires me to be my best - I thank you. To my partner, Joe — you made these past few years easier with your unfailing support and kindness and for that I am incredibly grateful.

Contents

List of Tables

List of Figures

Acronyms

·OH hydroxyl radicals. 1

AFM Atomic Force Microscopy. 10

AIBN 2,2'-azobisisobutyronitrile. 82

ATR Attenuated Total Reflectance. 7

BDE Bond Dissociation Energy. 24

BET Brunauer-Emmett-Teller. 51

CIMS Chemical Ionisation Mass Spectrometer. 36

FTIR Fourier-Transform Infrared Spectroscopy. 6

GC-MS Gas Chromatography-Mass Spectrometry. 41

NMR Nuclear Magnetic Resonance. 41

NOx nitrogen oxides, NO/NO_2. 1

O_3 ozone. 21

ODS Octadecylsiloxane. 6

OTS Octadecyltrichlorosilane. 5

QCM Quartz Crystal Microbalance. 21

R· carbon-centred radical. 24

ROO· peroxyl radical. 24

ROOH hydroperoxide. 24

SAMs Self-Assembled Monolayers. 1

Si JNT Silicon Junctionless Nanowire Transistor. 1

SiNW Silicon nanowire. 111

SOI Silicon-on-insulator. 123

TGA Thermal Gravimetric Analysis. 50

UV Ultraviolet. 21

VOC Volatile Organic Compounds. 29

XPS X-ray Photoelectron Spectroscopy. 17

Chapter 1

Introduction

Surface science focuses on the physical and chemical phenomena that occur at interfaces, such as solid-gas and solid-liquid [3]. For the application of nanotechnologies, surface properties can be tuned by the formation and chemical modification of Self-Assembled Monolayers (SAMs) [4]. SAMs can offer flexibility on the surface by introducing new chemical functionalities, while being relatively easy to prepare [5]. This makes SAMs a highly valuable tool in surface science, offering broad applicability across various fields and technologies, particularly in the design and development of sensors [6]. Moreover, their ability to incorporate a diverse range of functional groups into the monolayer structure makes them an invaluable tool for studying surface interactions and reaction mechanisms, providing fundamental insights into surface reactivity [1]. This project is part of a research programme called RADICAL which is funded by the European Commission. The overall project aims to develop sensors based on Silicon Junctionless Nanowire Transistor (Si JNT) devices for the real-time detection of short-lived atmospheric radicals, such as hydroxyl radicals ($\cdot$OH) and nitrogen oxides, NO/NO_2 (NOx). The role of this PhD project within the RADICAL project is to determine model organic compounds for the detection of oxidising radicals and to functionalise the model Si substrates with organic molecules for detecting $\cdot$OH radicals. In this chapter, current methods for the deposition and characterisation of SAMs will be discussed, followed by autoxidation pathways and gas-surface reactivity of SAMs.

1.1 Self-Assembled Monolayers

SAMs are ordered molecular assemblies formed by the spontaneous adsorption of a surfactant onto a solid surface, illustrated in Figure 1.1 [7].

SAMs can be prepared on a variety of different surfaces using a range of self-assembling molecules. The two most studied self-assembly systems are thiols on gold [8–10] and alkylsilanes on silicon [11, 12]. The self-assembly of alkylsilanes is particularly attractive because of its ability to form stable, covalently attached films on surfaces such as SiO_2 and Si [13]. Significant interest has been focused on the development of silanized glass surfaces for non-linear optical devices [14] and sensor applications [15].

There are three main components to self-assembling molecules: the reactive head group, the spacer (often alkyl chains), and the terminal functional group (Figure 1.1). The head group contains a functional group that exhibits a strong affinity

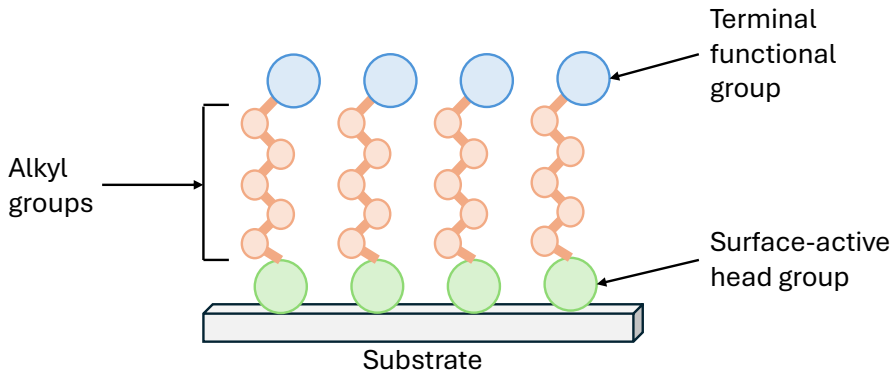

Figure 1.1: Construction of the self-assembled monolayer.

for a specific substrate [3]. If silicon oxide is used as the substrate, trichlorosilane (-$SiCl_3$), trimethoxysilane (-$Si(OCH_3)_3$, alkoxydimethyl (-$SiOH(OCH_3)_2$ or triethoxysilane (-$Si(OCH_2CH_3)_3$ have been used as reactive head groups [7]. Silicon oxide surfaces are typically hydrated, with silanol groups on the surface and a thin water layer covering the substrate [16]. Upon contact with the substrate, a hydrolysis reaction of the Si-X (X=Cl, OCH_3, OCH_2CH_3) bonds occur with the water present on the silicon oxide surface. The alkylsilane chains then bind through hydrogen bonds to the surface silanol groups and their close neighbours, followed by a condensation reaction which leads to covalent attachment to the substrate and cross-linking between adjacent molecules, shown in Figure 1.2. Monolayer formation appears to be driven by van der Waals interactions between hydrocarbon chains and Si-O linkages between adjacent silanols [17].

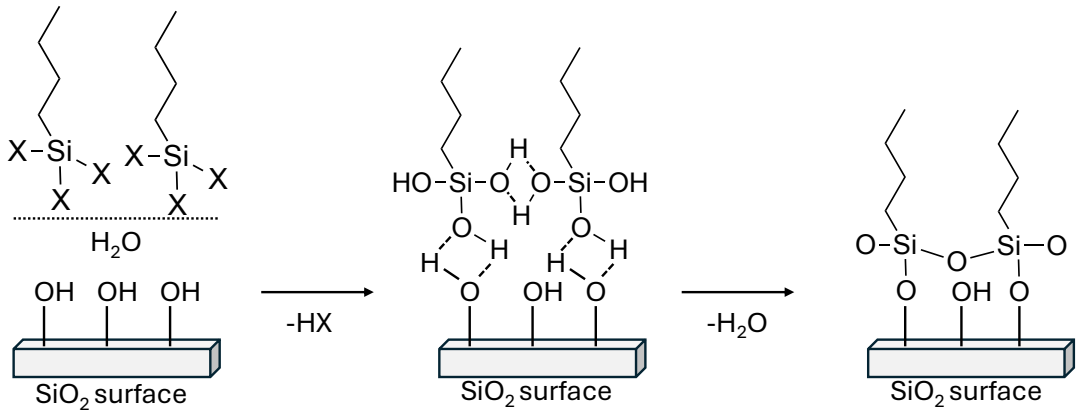

Figure 1.2: Schematic of the proposed mechanism of the silanisation reaction, where X= Cl, OCH_3 or OCH_2CH_3[16].

The spacer is generally an alkyl chain, as shown in Figure 1.1, however, it can also be an aromatic ring [18]. It is a key component of the self-assembling molecule, playing a vital role in the packing and organisation of molecules on the surface by providing interchain van der Waals and electrostatic forces [17]. The alkyl chain length can influence the packing density of SAMs. It has been reported that longer alkyl silane chains, with a minimum of 11 carbon atoms, can result in the formation of closely packed monolayers [19, 20].

The terminal group, shown in Figure 1.1, depicts the properties of the SAM surface. The chemical properties of the surface can be tailored by incorporating different functionalities into the SAMs, either by depositing self-assembled molecules with varying functionalities or by chemically modifying the SAM after its formation [21].

1.2 Deposition of SAMs

In this project, only trialkoxysilanes were used to functionalise silica surfaces. Thus, the next section will describe the functionalisation procedure for trialkoxysilanes on silica. The method most commonly used to functionalise silica surfaces is via silanisation; the self-assembly of alkyltrialkoxysilane or chlorosilane molecules [22]. This process initially involves thorough cleaning of the silica surface to remove any organic impurities using piranha solution (a 1:3 ratio of 30% H_2O_2 and concentrated H_2SO_4) or oxygen/water (O_2/H_2O) plasma treatment. This is to ensure the surface is activated with a high-density hydroxyl layer before being introduced into a solution of a silane derivative in an organic solvent [23]. SAMs can then be prepared by the immersion of this freshly cleaned substrate into a solution of the silane precursor, shown in Figure 1.3.

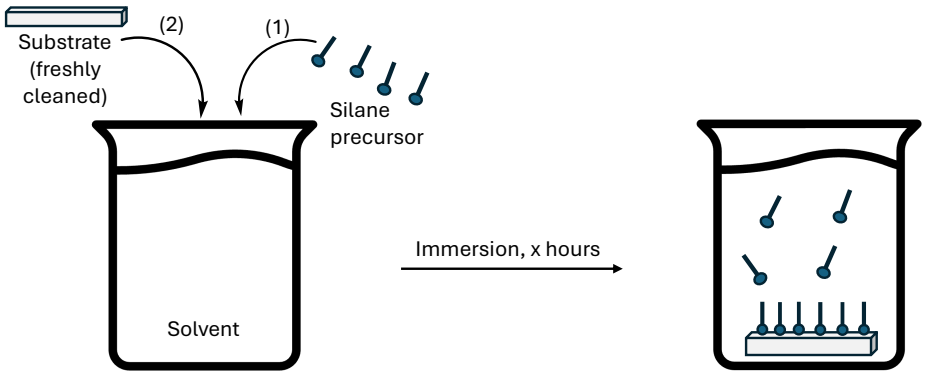

Figure 1.3: Deposition of SAMs in the liquid phase. Adapted from [3, 24].

The critical steps during silanisation are the hydrolysis of the trialkoxysilanes to silanetriols (equation 1.1)[25]:

$$R'Si(OR)_3 + H_2O \rightarrow R'Si(OH)_3 + 3ROH \tag{1.1}$$

and the condensation between the silanols and the solid substrate (equation 1.2):

$$R'Si(OH)_3 + surface{-}SiOH \rightarrow R'Si(OH)_2OSi{-}surface + H_2O. \tag{1.2}$$

Condensation of the silanols may also occur in the solution to form siloxanes (equation 1.3):

$$R'Si(OH)_3 + R'Si(OH)_3 \rightarrow R'Si(OH)_2OSi(OH)_2 - R' + H_2O \tag{1.3}$$

The hydrolysis reaction can occur in various solvent systems with rates influenced by the organofunctionality, the medium and a range of catalysts [25], which is

discussed further in Section 1.2.7. The hydrolysed trialkoxysilanes have the potential to react both with themselves and with the hydroxyl groups on the substrate surface [26]. Condensation of the silanols in solution versus on the surface determines whether a monolayer or multilayer forms. When condensation occurs in solution, the silane molecules undergo hydrolysis and condensation, becoming dispersed in the solution, which often results in the formation of oligomers or even multilayers. In contrast, when condensation occurs on a solid surface, the silane molecules typically self-assemble into a more ordered monolayer, as the surface provides a constrained environment that promotes the formation of a single layer with strong covalent bonding [26]. Three of the possible interactions are shown in Figure 1.4. The polysiloxane, which has formed a multilayer, is shown on the left. The next two structures involve linkage with the substrate. A structure with two surface Si-O linkages is less likely to form than the single surface Si-O linkage due to the spacing of reactive sites on the substrate [26]. The interfacial dynamics between the surface and the alkoxysilane molecules, as well as factors like solvent choice, temperature, and concentration, can significantly influence whether a monolayer or multilayer structure predominates.

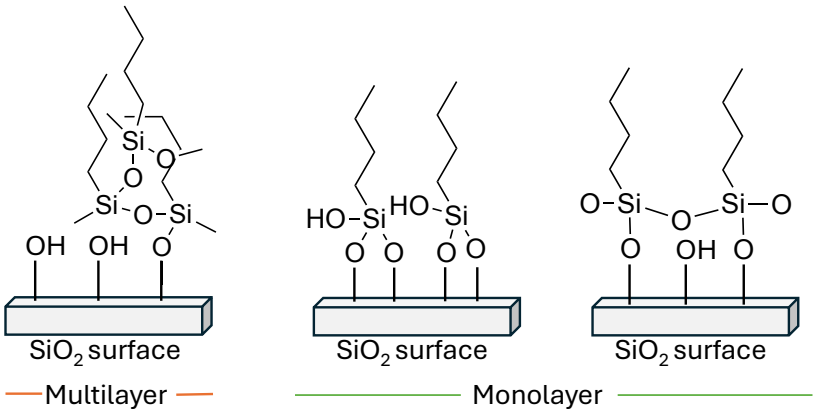

Figure 1.4: A diagram of the products of hydrolysis and condensation reactions of alkoxysilanes on silica, showing the formation of products with most to least extensive intermolecular reaction. Adapted from [26].

Although the experimental procedure of silanisation is relatively simple, producing a well-defined monolayer can be very difficult. Different laboratories and literature sources report widely varying results. SAMs have been reported to need reaction times ranging from a few minutes [27] to 24 hours [12, 28] to days [29]. The concern lies in the fact that the reaction is not limited to monolayers, as multilayers, which exhibit undefined morphology, can also form (Figure 1.4) [30]. Irreproducibility of SAMs can hinder their application to systems where well-defined and compact monolayers are essential [31]. One of the main reproducibility issues is the tendency for silanols to polymerise. The formation of polysiloxanes, which deposit onto the surface, can result in the development of macroscopic islands with poorly defined morphology [30]. There are several factors that influence the quality of the monolayer produced, these being: deposition time, concentration of surface OH groups, water content, solvent type, concentration of solution and type of surfactant [32],[16],[17]. These factors will be discussed in the following sections.

1.2.1 Deposition Time

The effect of deposition time on SAM formation has been studied, with results indicating that no changes in n-alkylsilane SAMs were observed for deposition times exceeding 6 hours, as monitored by contact angle analysis [33]. However, the deposition rate can be influenced by temperature. Studies have found that good quality Octadecyltrichlorosilane (OTS) monolayers formed at 18°C within 2 minutes, while satisfactory monolayers formed at 30°C within a deposition time of 24 hours [16]. Another study observed that the optimum deposition temperature for OTS monolayers on silicon oxide substrates was ∼28°C. Greater than this temperature and the film thickness gradually decreased, as shown in the ellipsometry measurements in Figure 1.5 [34]. The technique, ellipsometry, is described further in Section 1.4.2.1. In the literature, it has been discussed that grafting of organic silanes is preferred at lower temperatures, which seems paradoxical, as lower temperatures tend to slow chemical reactions. However, the decrease in temperature, reduces the solubility of either the water molecules or the silane molecules, which increases the kinetics of the physisorption step [16].

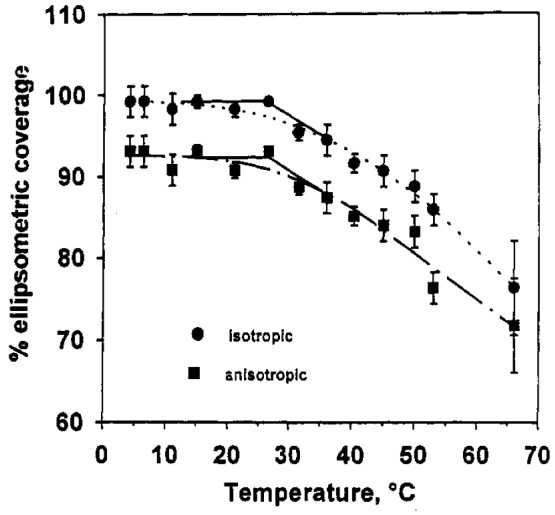

Figure 1.5: Preparation temperature dependence of film coverages of OTS monolayers on SiO_2/Si substrates. Figure reprinted from The Journal of Physical Chemistry, Vol. 98, No. 31, 1994 [34].

The effect of solution age on SAM formation has also been investigated, specifically the time between solution preparation and substrate immersion [35]. SAM films were tested after immediate immersion into a freshly made deposition solution or after immersion into a solution which had been stored for 2 hours after preparation. The results suggested that large polymer aggregates form on the surface if the solution is made in advance, i.e greater than 10 minutes, of substrate immersion [36, 37]. The polymer aggregates precipitate and are therefore, no longer available for chemisorption. The highest surface coverage was observed if the solution was left for a maximum of 10 mins [36].

1.2.2 Concentration of Surface OH Groups

Silanisation relies on water to hydrolyse the alkoxysilane groups into silanol groups. Water is needed on the surface of the substrate, as well as in the solution. On a native silicon surface, the density of OH groups is approximately 5 $\times 10^{14}$ OH groups per cm^2, meaning the area occupied by OH groups on silica surfaces is approximately 0.20 nm^2 [38]. This is similar to the packing density of alkoxysilane molecules as the cross-sectional area of trihydroxysilane headgroups has been modelled by Fontaine *et al.* to be 0.20 nm^2 [39]. Thus, this density of OH groups corresponds to a well packed monolayer. In the literature, it has been shown that OTS monolayers do not form on completely dry silica substrates [40]. Most reports agree that the OH concentration on the surface of the silica has a strong influence on the quality and formation of monolayer films [41]. Le Grange *et al.* compared monolayer formation on dehydrated, partially dehydrated and hydrated silica surfaces. Fourier-Transform Infrared Spectroscopy (FTIR) spectra of OTS monolayers on silica surfaces with different levels of hydration, shown in Figure 1.6, indicated that hydrated surfaces resulted in the formation of a dense monolayer [42].

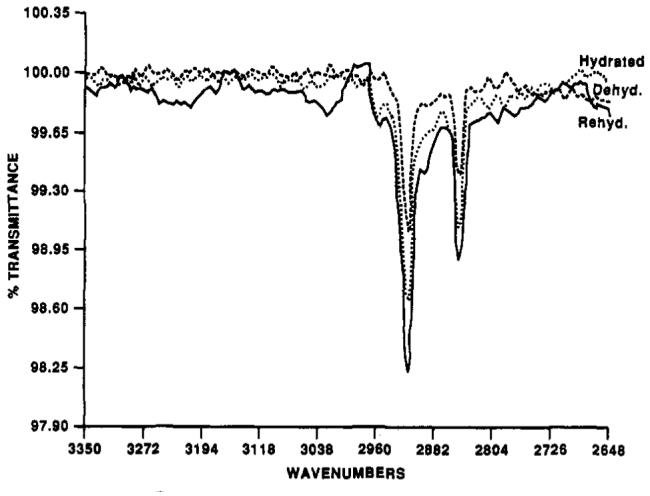

Figure 1.6: FTIR transmission spectra of OTS monolayers on silica surfaces, in the region of C-H stretching modes. The silica surfaces were fully hydrated (dotted line), rehydrated in room temperature water (solid line), and dehydrated (dashed line) before SAM deposition. Figure reprinted from Langmuir, Vol. 9, No. 7,1993 [42].

Using ellipsometry, Le Grange *et al.* estimated that only 1 out of 5 Octadecylsiloxane (ODS) molecules is directly bonded to the surface [42]. They concluded that the coverage of the surface depends on the number of OH groups on the surface, however, a completely hydrated surface is not necessary for complete monolayer coverage of the surface. The density and order of the monolayers are derived from the strong Si-O-Si bonds which form between silane chains [42]. Furthermore, Allara *et al.* used ellipsometry, IR spectroscopy, and contact angle measurements to report that ODS monolayers on silicon oxide showed the same properties as ODS monolayers on hydrated gold substrates without OH groups. This indicated that the monolayer films exhibit the same high conformational order [41]. Allara *et al.* concluded that few bonds form between the ODS molecules and the substrate, and

that the water film on the substrate is most likely responsible for film formation [41]. The discrepancies in previous literature suggest that there is no clear consensus on the role of surface water in monolayer formation.

1.2.3 Water Content

The water content in the surfactant solution needs to be carefully controlled to obtain high quality SAMs. An excess of water causes polymerisation of the alkylsilanes in solution which results in polysiloxane depositing on the surface rather than the alkyltrialkoxysilane securely bonding [7], [12]. However, incomplete monolayers are formed in the absence of water as water is needed to hydrolyse the alkyltrialkoxysilanes to form silanols which then form stable bonds with the silica [42]. Moreover, the monolayer formation is extremely slow in the absence of water [43]. The water content may be the source of discrepancies among different laboratories due to its difficulty to control. Initial reports claimed that traces of water in the deposition solution are essential for the formation of well-packed monolayers [42, 44]. Reports have also demonstrated that water increases the reaction rate [45, 46]. Vallant *et al.* used *in situ* Attenuated Total Reflectance (ATR) FTIR measurements (technique described further in Section 1.4.1.3) to study the absorption processes at the substrate/solution interface. They investigated the influence of water concentration in the deposition solution and found that higher water concentration promotes the formation of active silanol species through hydrolysis, which are kinetically controlled by the water concentration. These species favour the formation of pre-ordered silanol oligomers, which form more ordered submonolayer islands. The absorption rate was significantly increased with higher water content in solution: at a lower water concentration of 2.2 M the rate of absorption was 0.28 M^{-1} s^{-1}, and at the higher concentration of 6.4 M the rate of absorption was 0.67 M^{-1} s^{-1} [46]. As illustrated in Figure 1.2, the silane molecules initially physisorb onto the water film, undergo hydrolysis, and then crosslink with neighbouring silanols to form a 2D network. The molecules are stabilised by lateral bonding with the neighbouring molecules and hydrogen bonding to the surface. Thus, water plays a key role in the initial stages of SAM formation.

1.2.4 Silane Headgroup and Chain Length

The chain length and type of head groups of the surfactant can affect the quality of SAM formation. It has been reported that increasing the chain length of alkyltrimethoxysilanes positively impacts the smoothness of the monolayer, as demonstrated for chains with 6, 8, and 12 carbon atoms [47]. Moreover, the ordering behaviour of trichlorosilane films seems to depend on the length of the alkyl chain, with an optimum chain length of 18 carbon atoms. This chain length enables the alkyl chains to adopt a trans-conformation and orient perpendicularly to the surface [44]. Moreover, an increase in alkyl chain length can improve the film coverage due to increased van der Vaals interactions between neighbouring molecules [48]. Furthermore, a study by Fontaine *et al.* looked at the influence of headgroup cross-linking on the chain packing of alkyltrialkoxysilanes [39]. During hydrolysis of trimethoxysilanes, the molecules undergo a significant decrease in headgroup size. The cross-section of a trimethoxysilane group is 0.45 nm^2, according to their molecular models,

compared to 0.20 nm^2 for a trihydroxysilane headgroup [39]. Additionally, the area occupied by OH groups on silica surfaces is approximately 0.20 nm^2 [38]. Thus, in the initial formation of a monolayer, the headgroup of trialoxysilanes can limit the number of molecules per unit area on the substrate. This headgroup cross-sectional area is also larger than the cross-sectional area of octadecyltrialkoxysilane chains, which was modelled to be 0.20 nm^2. This means the molecules are too far away to experience strong van der Waals interactions between chains in a close packed state. After hydrolysis, however, the trihydroxysilane headgroup is now comparable with the cross-section of the aliphatic chain and the chains can exhibit an upright position in all trans-conformation [39].

Alkylsilanes can have head groups with one, two or three hydrolysable groups [30]). Monoalkoxysilanes can only form one covalent bond to the surface and can lead to highly disordered films due to the steric hindrance of the methyl groups at the interface and the lack of cross-linking between adjacent head groups, as shown in Figure 1.7 [49]. Dialkoxysilanes, as shown in Figure 1.7, typically form covalent bonds with the surface. However, the presence of a second hydrolysable group promotes vertical polymerisation, leading to multilayer formation [30]. Trialkoxysilanes can form densely packed monolayers due to their ability to cross-polymerise horizontally to the surface, as shown in Figure 1.7. Although, vertical polymerisation can still occur, therefore the deposition procedure needs to be carefully controlled [30].

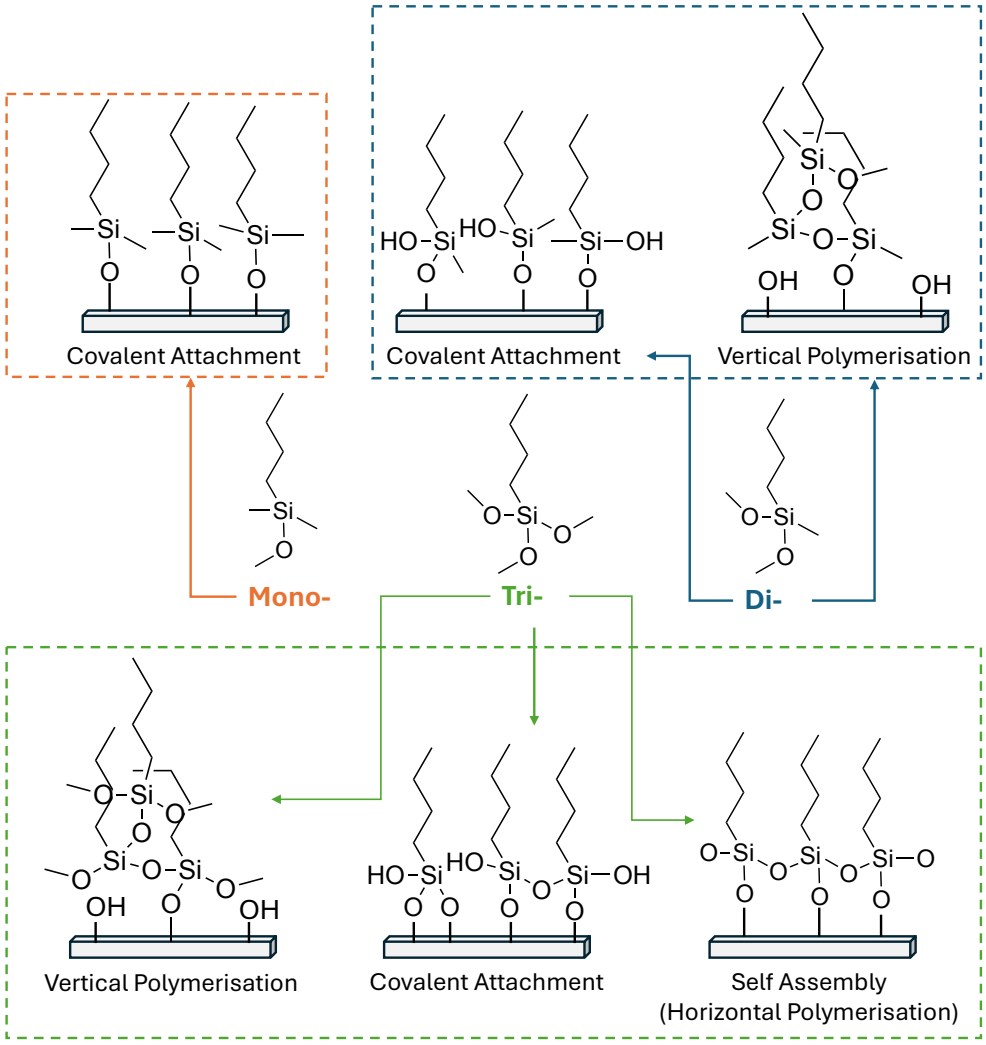

Figure 1.7: Possible products for the reaction of monomethoxysilane, dimethoxysilane and trimethoxysilanes with silicon dioxide surfaces. Adapted from [30].

1.2.5 Solvent Type

The effect of solvent polarity on SAM formation on silica has been previously studied [50]. It was observed that different solvent types affected water solubility and thus SAM formation; dodecane solutions resulted in multi-layered films whereas heptane solutions resulted in high-quality monolayer formation. Further studies showed toluene and hexadecane solutions to cause the formation of smooth monolayers [51]. Thus, there does not appear to be a clear consensus in the literature regarding the effect of solvent type on monolayer formation.

1.2.6 Concentration of Solution

The concentration of the deposition solution can highly influence the quality of SAM formation [52–54]. The silanisation of OTS has been tested at concentrations varying from 4×10^{-4} to 2.5×10^{-1} M [53]. It was observed that the rate of SAM formation increased with concentration. At the highest concentration (2.5×10^{-1} M), the SAM is almost complete after 2 seconds, shown in Figure 1.8(a). Whereas, it takes approximately 2 minutes to reach a similar SAM coverage at 10^{-2} M. However, at

the lower concentration (4×10^{-4} M), the silanisation led to isolated island formation with an incomplete monolayer, shown in Figure 1.8(c). Atomic Force Microscopy (AFM), used to form the images in Figure 1.8, is described in more detail in Section 1.4.2.2.

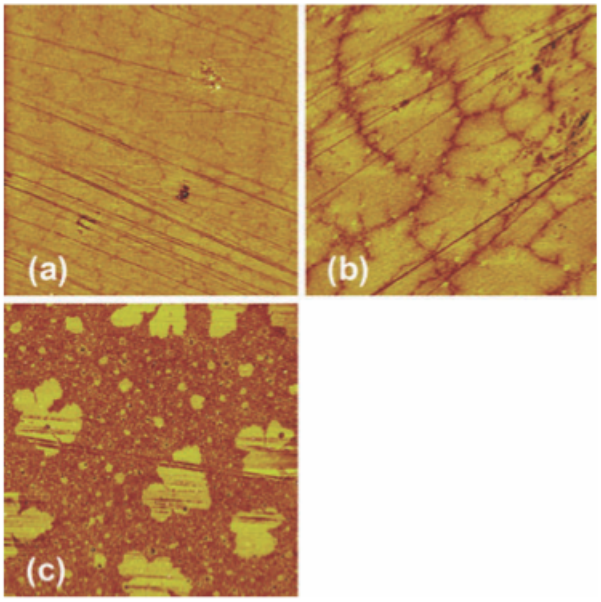

Figure 1.8: AFM images (10×10 μm^2) of interrupted OTS SAMs for different concentrations in solution: a) 2.5×10^{-1} M during 2 seconds, b) 10^{-1} M during 2 minutes, and c) 4×10^{-4} M during 30 minutes. AFM image reprinted from Phys. Chem. Chem. Phys., 2011, 13, 2870–2879 [53].

It was observed that by increasing the concentration even further to 2.5×10^{-1} M, the contact angle measurements of the surface reduced by $\sim 2^{\circ}$, indicating a lower packing density [53]. The results suggest that faster adsorption at higher concentrations prevents the formation of a densely packed, ordered monolayer and that irregular, rough films with lower density form instead. At high concentrations, the precursor molecules are present in excess in the solution. This leads to rapid adsorption onto the surface before the molecules have time to arrange themselves into an ordered structure, resulting in a disordered, incomplete monolayer. The rate of adsorption exceeds the time required for the molecules to organise and form a densely packed, well-ordered monolayer. The incomplete layers cannot be fully converted into monolayers even with prolonged exposure, further confirming that the surface sites are blocked due to irregular chemisorption of the adsorbate molecules during the initial phase of monolayer formation [54, 55].

1.2.7 Addition of a Catalyst

Catalysts can be used to increase the rate of hydrolysis and condensation of the silanols to a hydrolysed surface. In the case of acid catalysis, Brønsted acids can be utilised. It has been suggested that the mechanism undergoes a rapid equilibrium protonation of the substrate, followed by an S_N2 displacement of the leaving group by water, shown in Figure 1.9 [25]. Each decrease by 1 pH corresponds to a ten-

fold acceleration in the rate of hydrolysis and condensation of silanols. This has been shown to increase the amount of organic loading on silica surfaces and for the process to occur at a faster rate [56].

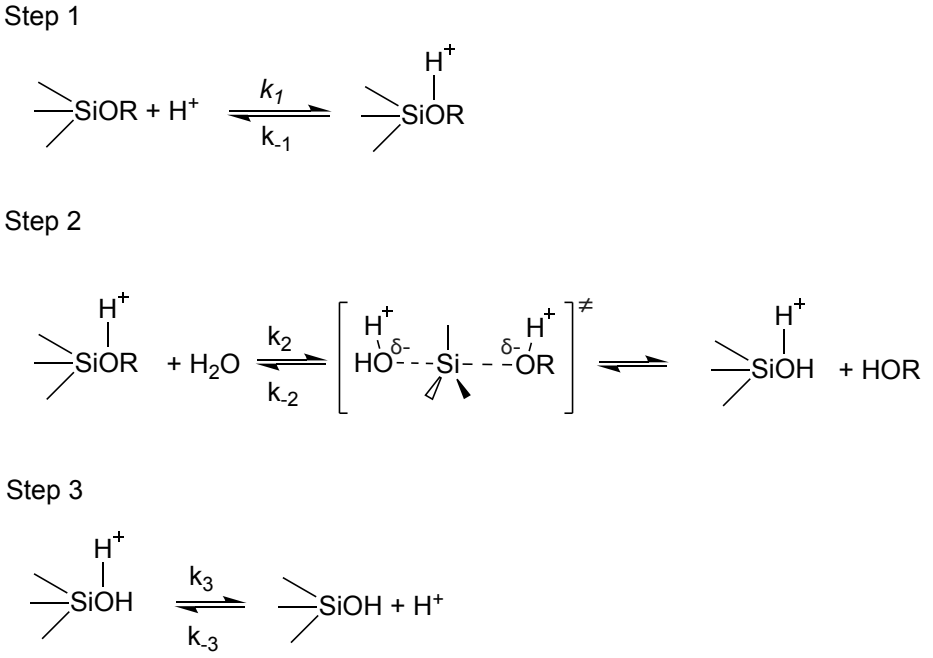

Figure 1.9: Proposed mechanism for an acid catalysed hydrolysis of alkylsilanes. Adapted from [25].

As well as for the formation of monolayer systems, alkoxysilane derivatives are often utilised for commercial applications such as basic framework polymers, and also as auxiliaries, such as adhesion promoters, coupling and crosslinking agents [57]. These compounds can react and couple with both organic and inorganic surfaces, forming strong chemical bonds between materials such as glass or metals and organic coatings like organic polymers [58, 59]. Thus, they can be used as sealants and adhesives. In the absence of a catalyst, the alkoxysilane crosslinking reaction is a slow process and catalysis of both the hydrolysis step and condensation step is essential [57]. The research of these applied systems provides useful information for monolayer systems as the chemistry is the same.

Apart from Brønsted acids, Lewis acids can also be used to catalyse the alkoxysilane crosslinking reactions. Organotin compounds are widely used as crosslinking catalysts, despite their harmful effects to human health [57]. Less harmful titanium-based catalysts have been studied, but their disadvantages are that they need to be added in stoichiometric amounts to have an effect [60, 61]. In recent years, boron-based catalysts have been developed. These compounds are more attractive than tin or titanium-based catalysts as they are a heavy metal free alternative. Lee at al. were the first to report a boron-based catalyst in 2005 [62]. In 2008, Nomura *et al.* proposed a modified mechanistic cycle of a boron triffluoride monoethylamine complex (BF_3–MEA), shown in Figure 1.10 [63, 64].

It is proposed that BF_3 initially coordinates to the alkoxysilane, to form species A in Figure 1.10. As soon as water is available, the rate of hydrolysis increases as formation of species A promotes alkoxy abstraction. The silanol that forms will

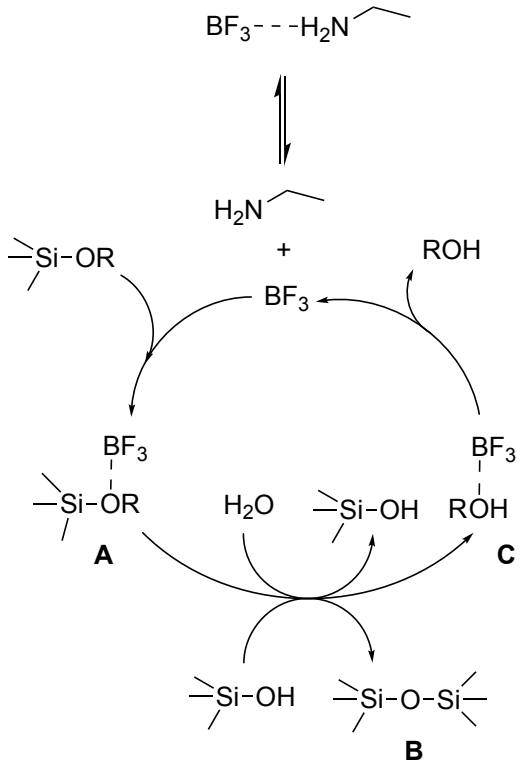

Figure 1.10: Proposed mechanism for a lewis acid (boron-based) catalysed hydrolysis of alkoxysilanes. Adapted from [57].

then react with alkoxysilanes which are also cooridinated to BF_3 to form siloxane crosslinks, species B in Figure 1.10. The boron trifluoride alcohol complexes produced in this cycle, species C in Figure 1.10, are proposed to dissociate and regenerate BF_3 as an active catalyst [57, 63, 64]. The use of Lewis acids for catalysing the hydrolysis and condensation steps for crosslinking agents, could thus be applied to the silanisation procedure for monolayer formation. This is discussed further in Section 2.2.3.3.

In the case of base catalysis, the proposed mechanism follows a bimolecular nucleophilic displacement reaction with a pentacoordinate intermediate [25]. The addition of base to the reaction results in a negative charge on the silicon atom within the transition state, as shown in Figure 1.11. This high negative charge density on the silicon and on the oxygen of the nucleophile produces a tight transition state structure. Thus, achieving a faster rate in hydrolysis [25].

Therefore, by introducing a catalyst into the deposition solution, a more robust system can be achieved. If the system is robust enough, it should be able to overcome any slight changes to water content, temperature, concentration etc., described above, that might occur naturally with each experiment. The control parameters will be further discussed in Chapter 2, including the effect of catalysis on improving the reproducibility of monolayer formation on silica surfaces.

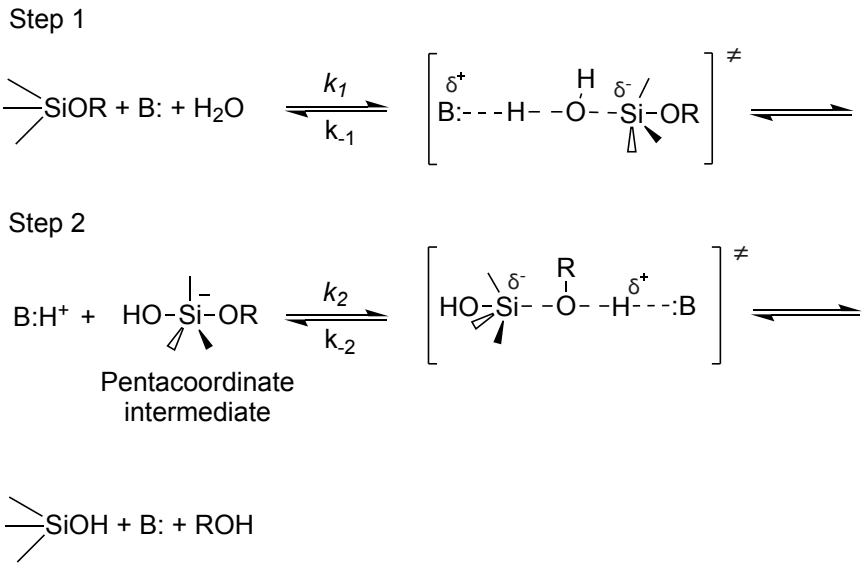

Figure 1.11: Proposed mechanism for a base catalysed hydrolysis of alkylsilanes. Adapted from [25].

1.3 Mixed Monolayers

It is possible to form mixed monolayers, consisting of two or more surfactants in the deposition solution, illustrated in Figure 1.12. Mixed monolayers give the opportunity to incorporate several functional groups into the monolayer. Mixed monolayers can serve as a valuable method for incorporating photoinitiators into the film to trigger the growth of surface-attached polymers [65]. Furthermore, a study demonstrated that mixed monolayers of azobenzene derivatives undergo cis-trans isomerization upon light irradiation. In well-packed monolayers, this process would be hindered by steric constraints; however, the more loosely packed structure of mixed monolayers allowed for efficient photoswitching [1, 66]. Thus, mixed monolayer systems are valuable tools which can be used in various applications. In this project, mixed monolayers containing a radical initiator chain are employed to investigate reactivity within SAMs.

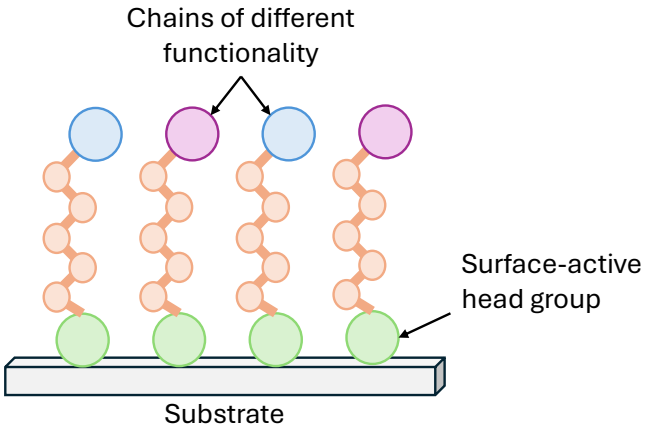

Figure 1.12: Illustration of mixed SAMs.

Mixed monolayers can either be homogeneously mixed or phase separated. Phase separation is favoured when interactions between the same chains are stronger than interactions between the different chains, or the chains and the solvent [67]. This can result in the formation of nanoislands, as illustrated in the AFM image in Figure 1.13.

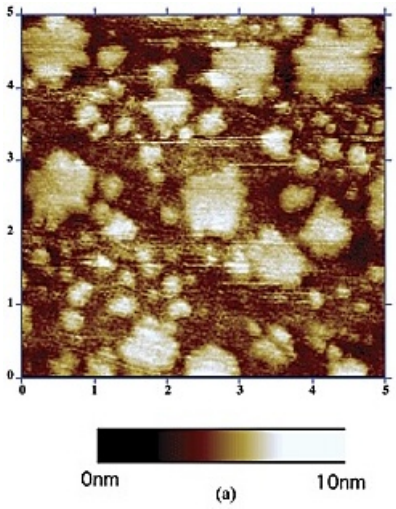

Figure 1.13: An example AFM image of a 1:1 ratio octadecyltrichlorosilan/ aminophenyltrimethoxysilane monolayer deposited from a carbon tetrachloride solution. AFM image reprinted from Langmuir 2003, 19, 8, 3254-3265 [67].

For the mixed monolayer to become phase separated, reversible adsorption is required. Thus, if silane monolayers are formed without a much faster physisorption step, such as if a catalyst is used to facilitate faster hydrolysis or if the silane is already partially hydrolysed and it can form covalent bonds with the surface more rapidly, then phase separation is less likely. Phase separation of mixed monolayers of thiols on gold surfaces has been observed experimentally by several studies [68, 69]. Mixed SAMs of alkyltrichlorosilanes on silica have also been studied, often these studies involve the determination of monolayer composition [70–72]. However, reports of phase separation in alkylsilane monolayers have shown that the surface morphology depends on the relative adsorbed amounts of the two surfactants [67]. The process of silane adsorption is irreversible due to the formation of siloxane bridges. Therefore, the relative adsorption amounts of each surfactant is determined by the rates of reaction. The rates can be determined by several factors: a) the ratio of each silane in the deposition solution; b) the relative affinity for the solvent used; c) the relative affinity for the silane head groups for the substrate surface; d) favourable interactions between the silanes of similar structures, such as van der Waals and hydrogen bonds; e) the interfacial free energy of the formed monolayer against the solvent system [67]. Phase separation is more likely to occur when the ratio of molecules in the monolayer compared to their ratio in the feed solution is different. If the same ratio is achieved, this suggests either lack of reversible physisorption, or similar interactions between the same and different chains [67]. Thus, the morphology can be controlled by the relative composition of the two silanes in the deposition solution and the type of solvent used.

1.4 Characterisation of SAMs

For the characterisation of functionalised surfaces, it is crucial to employ a range of analytical techniques to assess all aspects of the SAMs. Given the complexity and variability of SAM formation, the use of multiple methods allows a more thorough understanding of the thickness, packing density/order, homogeneity, structure and chemical composition of the monolayer. In this section, a detailed overview of the analytical techniques used in this project is provided, highlighting their role in characterising various aspects of the SAMs formed on silica surfaces.

1.4.1 Structure and Chemical Composition

1.4.1.1 Contact Angle Analysis

Contact angle analysis is a widely used technique to assess the hydrophobicity or hydrophilicity of a surface by measuring the angle formed at the three-phase interface between air, a liquid droplet, and a solid surface [7]. The contact angle, provides insight into the surface energy and wettability properties of the material. For the characterisation of SAMs, contact angle measurements are particularly useful as they can reveal key details about the surface functionalisation. The contact angle provides indirect information about the type of terminal functional group present within the monolayer, as different functional groups (e.g., -OH, -COOH, $-CH_3$) interact with water or solvent molecules in different ways, influencing the surface wettability [73]. Figure 1.14 illustrates the different levels of wettability of a surface [3].

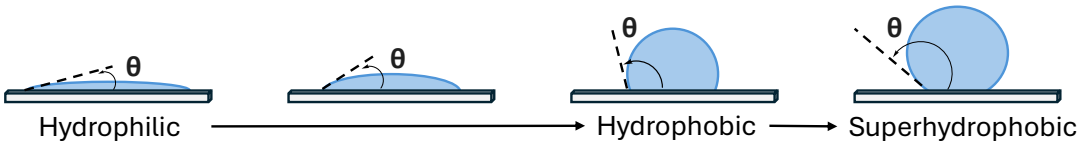

Figure 1.14: Diagram to show the different levels of wettability of a surface. Adapted from [3].

A hydrophilic surface is characterised by a contact angle smaller than 90°, indicating that water molecules are attracted to the surface, spreading out and forming a thin, wetting layer (Figure 1.14). This low contact angle suggests strong adhesive forces between the surface and the water molecules, often seen in surfaces with polar functional groups that can interact with the water through hydrogen bonding, such as hydroxylated surfaces [74]. On the other hand, a hydrophobic surface exhibits a contact angle greater than 90°, shown in Figure 1.14, where water molecules are repelled, forming a more rounded droplet [75]. This behaviour occurs due to weak interaction between the surface and water, typically observed in non-polar or low-energy surfaces, such as those coated with alkyl groups [76].

A superhydrophobic surface, however, is highly textured or rough, which significantly enhances its ability to repel water. The increased surface roughness traps air beneath the water droplet, creating a "Cassie-Baxter" state. A "Cassie-Baxter" state is a wetting state in which the droplet rests on top of the surface protrusions, trapping air in the grooves beneath it [77]. This leads to partial contact between

the liquid and the solid, with air pockets underneath the droplet, resulting in an extremely high contact angle, shown in Figure 1.14. This contact angle often exceeds 150°, indicating the surface is almost completely water repellent.

Contact angle hysteresis is an important physical characteristic [78]. It is most understood by imagining a water droplet on a surface as the surface is tilted. Gravity pulls on the droplet to move it down but contact angle hysteresis keeps the droplet in place. This leads to a droplet that is asymmetric: i.e one side of the droplet becomes thin with a low contact angle, while the other side becomes thicker with a higher contact angle [78]. The measurable quantities which characterise the surface are the advancing and receding contact angles, Θ_a and Θ_r, as shown in Figure 1.15.

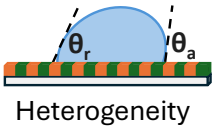

Figure 1.15: Diagram to show the effect of surface heterogeneity on the receding and advancing contact angles. Adapted from [79].

The difference between the two quantities is the contact angle hysteresis [79]:

$$\Delta\Theta = \Theta_a - \Theta_r. \tag{1.4}$$

In previous studies, the contact angle hysteresis has been reported to be highest for polar, heterogeneous or rough surfaces and lowest for smooth surfaces [80]. This is because on rough or heterogeneous surfaces, the contact line of a droplet can get trapped in different microstructures or regions with varying surface energies, leading to higher hysteresis (Figure 1.15). On smooth surfaces, the contact line moves more easily, resulting in lower hysteresis. Thus, it can be used to evaluate the smoothness of the monolayer, as well as the packing density of the monolayer. If the monolayer is uneven or poorly packed, it can cause increased hysteresis due to the surface having varying energy levels and roughness at different points. A well-packed, smooth monolayer would have a more consistent surface, resulting in lower hysteresis [80].

Moreover, advancing contact angle measurements can provide insight into the surface composition of bi-component mixed monolayers [81]. It has been reported that contact angle values can vary linearly with composition, as shown in Figure 1.16 [80]. In this study, contact angles were measured for mixed solutions of $HS(CH_2)_{10}CH_3$ and $HS(CH_2)_{10}CO_2H$, $HS(CH_2)_8CH_3$ and $HS(CH_2)_8CN$, $HS(CH_2)_{10}CH_3$ and $HS(CH_2)_{10}CH_2Br$, and $HS(CH_2)_{10}CH_3$ and $HS(CH_2)_{10}CH_2OH$ on gold surfaces.

For Br/Me surfaces, the plot of contact angle versus mole fraction of the polar-terminated species is linear, indicating ideal mixing behaviour [80]. However, for mixed monolayers containing alcohol, carboxylic acid, or nitrile groups, deviations from linearity are observed. These deviations are attributed to hydrogen bonding interactions between polar tail groups and are particularly evident at low mole fractions. This behaviour is thought to arise from two factors: (1) poor electrostatic solvation of the polar tail groups in the low dielectric medium provided by surrounding methyl groups, and (2) limited hydrogen bonding between dilute protic tail groups within the monolayer [80]. Overall, contact angle measurements offer

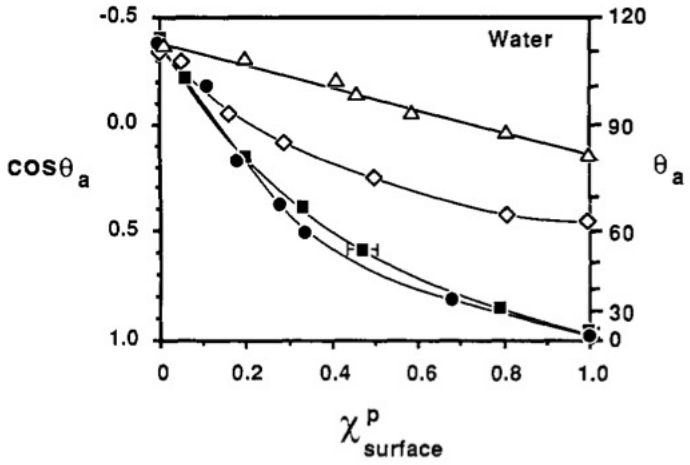

Figure 1.16: Advancing contact angles of water on monolayers adsorbed from ethanol onto gold slides: $HS(CH_2)_{10}CH_3$ and $HS(CH_2)_{10}CO_2H$ (circles), $HS(CH_2)_8CH_3$ and $HS(CH_2)_8CN$ (diamonds), $HS(CH_2)_{10}CH_3$ and $HS(CH_2)_{10}CH_2Br$ (triangles), and $HS(CH_2)_{10}CH_3$ and $HS(CH_2)_{10}CH_2OH$ (squares). X^p represents the mole fraction of the polar-terminated species on the surface. Figure reprinted from J. Am. Chem. Soc., Vol. III, No. 18, 1989 [80].

a simple yet sensitive method for probing the surface composition, intermolecular interactions, and miscibility of mixed-component monolayers.

1.4.1.2 X-ray Photoelectron Spectroscopy (XPS)

XPS is a sensitive surface analytical technique, involving the irradiation of a sample with monochromatic X-rays and the measurement of the kinetic energy of emitted core-level electrons, shown in Figure 1.17 [82, 83]. Its high sensitivity and ability to determine the chemical composition of materials makes XPS a powerful technique for surface characterisation [84].

The complete energy transfer of the incident X-ray radiation (hv) results in the emission of a core-level electron. This electron can be identified by its binding energy, which provides information of its parent element and atomic energy level. The binding energy can be calculated from the measured kinetic energy (E_k) and the energy of the incident X-ray radiation (hv), shown in equation 1.5 [3, 82].

$$hv = E_B + E_k \tag{1.5}$$

Each element has a characteristic set of peaks in an XPS spectrum, which are influenced by the oxidation state of the element and its chemical environment. Thus, elements can be distinguished in different oxidation states, such as CH_2 compared to C=O, with binding energies of 285.0 eV and 288.0 eV, respectively [85]. The intensity of the peaks corresponds to the concentration of that element within the sample [3]. The incident X-ray beam can penetrate deeply into a sample, however, the ejected electrons have a limited escape depth. This means any electrons ejected from depths greater than a few nm are likely to undergo energy loss via inelastic collisions before escaping the surface. Thus, these signals contribute to the background noise instead of a well-defined peak [82]. Therefore, XPS is primarily used as a surface analytical technique, rather than for bulk material analysis. In this

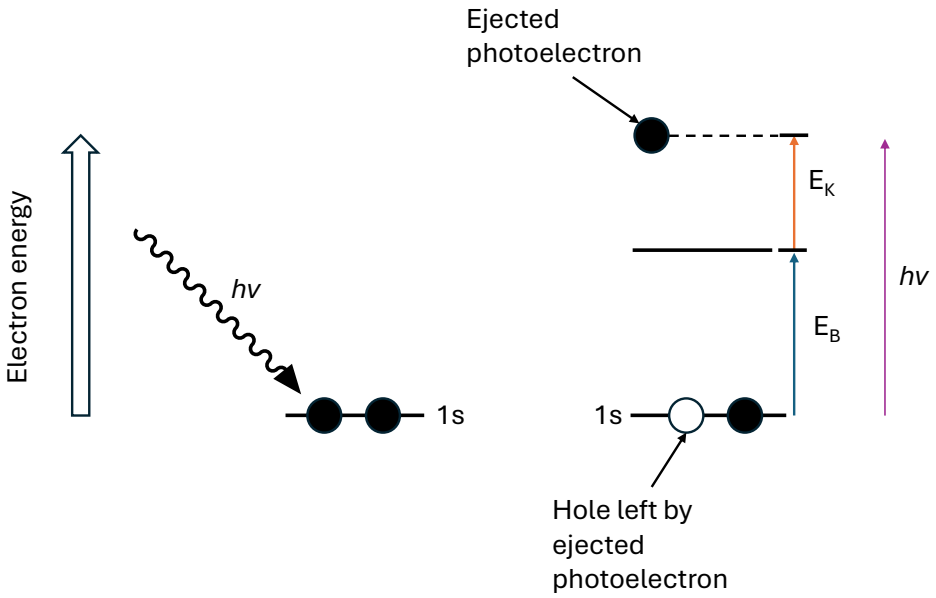

Figure 1.17: A diagram of a photoelectron emission process with a schematic illustration of the basic XPS equation. Adapted from [82, 84].

study, XPS has been used to evaluate the chemical composition of functionalised SiO_2 surfaces.

1.4.1.3 Fourier-Transform Infrared (FTIR) Spectroscopy

In addition to XPS and contact angle analysis, FTIR spectroscopy and Attenuated Total Reflectance (ATR) FTIR are commonly used to identify functional groups on the surface of monolayers [86, 87]. The vibration and rotation of molecules influenced by IR light at a particular wavelength is measured by FTIR [88]. ATR-FTIR provides a highly sensitive method for evaluating the surface composition of thin films and monolayers. It involves directing infrared light onto the surface of the sample through a high-refractive-index crystal, whereby the light undergoes total internal reflection within the crystal [89]. The generated evanescent wave penetrates the sample surface, interacting with the molecules. These interactions cause specific vibrational modes of the chemical bonds to absorb the infrared radiation [89]. Thus, producing a spectrum which reveals the functional groups present on the surface. The main challenge in the characterisation of functional groups within monolayer systems is the small amount of organic material, thus ATR can be used as it is sensitive to surface molecules only; however, sensitive detectors are still required for monolayer analysis. ATR-FTIR was used to characterise the surface functional groups on functionalised SiO_2 nanoparticles, which will be discussed further in Chapter 2.

1.4.2 Thickness and Packing Density

1.4.2.1 Ellipsometry

Ellipsometry is a sensitive, non-destructive characterisation technique used to determine the thickness of thin films[3]. It measures the polarisation change of an

elliptically polarized light beam upon interaction with a sample, as represented in Figure 1.18, and reports this as the phase shift (Δ) and the amplitude component (ψ) of the reflected light. The relationship between the reflection coefficients (r_p and r_s) and the measured quantities is given by:

$$\frac{r_p}{r_s} = \tan(\psi)\, e^{i\Delta} \tag{1.6}$$

where r_p and r_s are the reflection coefficients for p- and s-polarized light, and ψ and Δ are the amplitude and phase shift, respectively.

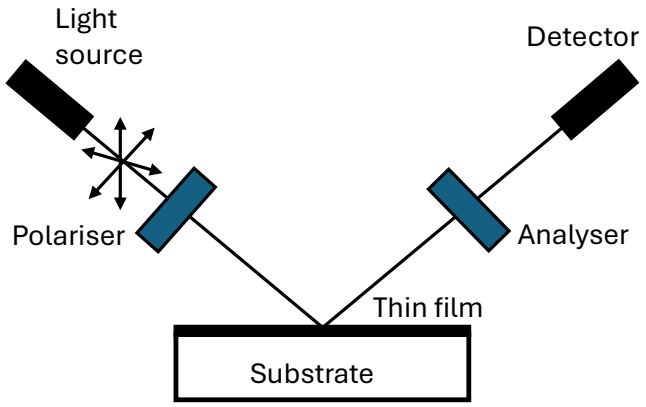

Figure 1.18: A diagram representing an ellipsometry experiment. Adapted from [3].

The parameters (ψ and Δ) of reflected light depend on the thickness and refractive index of thin film. Therefore, to obtain these optical constants and thickness, a model is constructed that represents the sample structure, including each individual layer with its corresponding complex refractive index ($\tilde{n} = n + ik$, where n is the refractive index of the sample and k is the extinction coefficient) and thickness. The thickness of each layer affects the optical path difference, which in turn modifies the Δ and ψ. By iteratively adjusting the layer parameters in the model and comparing the simulated Δ and ψ to the measured data, the best-fit thickness and optical constants of the sample can be extracted [3].

Ellipsometry is particularly useful for the characterisation of SAMs because it can measure thicknesses on the order of nanometres with high accuracy [12]. This high sensitivity makes it an ideal technique for confirming the successful formation of a monolayer and ensuring that no multilayer formation has occurred during the assembly process.

1.4.2.2 Atomic Force Microscopy (AFM)

AFM was developed in 1985 [90] and has since been a popular technique to characterise the surface topography of materials at the nanometre scale [91]. AFM measures the interaction forces between a sharp tip connected to a cantilever and the sample surface. The image contrast is obtained from the very short range repulsion experienced when the electron orbitals of the tip and sample overlap [92]. Further interactions between the tip and the sample can be used to investigate properties of the sample. These measurements are often given the term "force measurements" [92]. The tip material used in this study was made from antimony doped silicon.

The attractive and repulsive forces experienced between the sample surface and the sharp tip, deflects the cantilever. A laser beam is directed onto the top of the cantilever and with each deflection, it causes a change to the position of the reflected laser beam which is detected by a photodiode, as shown in Figure 1.19 [91]. The result of the force measurement, is the measurement of the cantilever deflection, Z_c, compared to the position of the piezo driver, Z_p, normal to the surface. The force, F, is calculated by multiplying the cantilever deflection with its spring constant, k_c [92]:

$$F = k_c Z_c \tag{1.7}$$

The distance between the tip and sample, D, is calculated by adding the deflection to the position [92]:

$$D = Z_p + Z_c \tag{1.8}$$

The controller electronics record the position of the laser beam on the photodiode via a feedback loop, which is then converted into an image. The image represents a map of interactions measured between the surface and the tip [3]. These images provide high-resolution surface topography, with lateral (xy) resolution typically ranging from 1-10 nm and vertical (z) resolution around 0.01 nm [93].

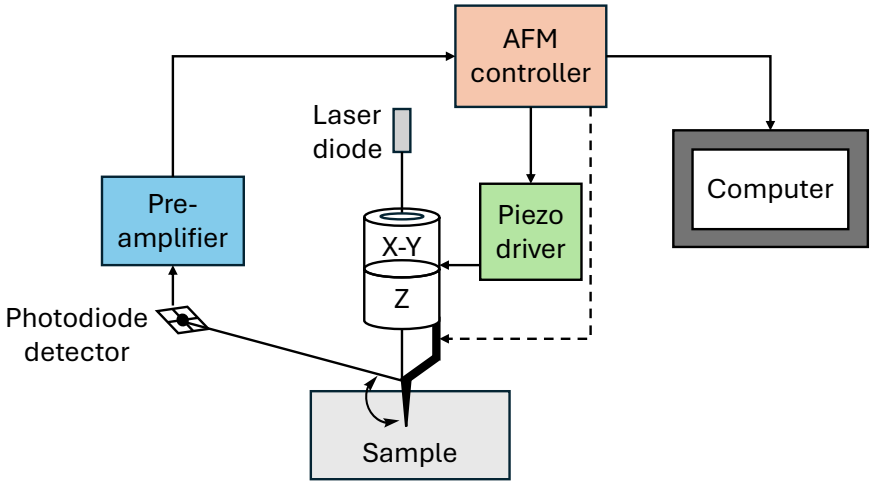

Figure 1.19: A diagram of the AFM system. Adapted from [94].

AFM can be conducted in a few different modes: the tapping mode, a non-contact mode and a contact mode [3]. In this study, the tapping mode was used. This mode allows the cantilever tip to oscillate and impact the sample for a minimal amount of time. Thus, lessening the damage done to the soft material, which is an important aspect for the analysis of SAMs [95].

AFM is particularly useful for the analysis of mixed SAMs, which consist of two or more different molecules attached to the surface. This is due to its ability to study the interfacial phenomena at molecular scale [96]. Thus, AFM can be used to determine whether phase separation has occurred within the mixed monolayer by showing distinct domains or irregularities on the surface [67]. In this study, AFM has been used to evaluate whether phase separation has occurred in the mixed monolayers.

1.4.2.3 Quartz Crystal Microbalance (QCM)

QCM is another common technique used to characterise the chemical interactions at surface interfaces. The quartz microbalance is a sensitive device, which is capable of measuring changes in mass that occur at an interface [97]. It works by measuring changes in the resonance frequency of a quartz crystal as a function of mass deposition on its surface. When molecules adsorb onto the surface of the crystal to form a SAM, the added mass causes a shift in the resonance frequency, which is monitored in real time [98]. Thus, it can be used to study the kinetics of SAM formation and the monolayer growth. It can also be used to study the chemical changes of a SAM upon interactions with the environment [99]. However, this technique was not accessible to use during this project.

1.5 Autoxidation

In the context of SAMs, the oxidation process is of particular interest as SAMs can be utilised in a variety of applications, including gas sensing and coatings, where the stability and chemical reactivity of the monolayer can significantly affect its performance in that role. For the application of gas sensing, oxidative degradation causes changes to chemical structure, surface properties and thus, the sensor responsivity [100]. This can also affect the sensor lifetime. Therefore, uncovering the underlying autoxidation pathways in SAMs is critical for improving their durability and efficiency, especially in environments prone to oxidative conditions.

Autoxidation refers to a chain reaction where one initiation can lead to the degradation of several groups. This process plays a crucial role in the degradation of various materials, from polymers and lipids to pollutants in the atmosphere [101, 102]. Autoxidation is a natural part of material ageing and interaction with the environment; therefore, understanding the specific pathways and mechanisms behind these reactions is essential for controlling material stability and functionality, especially in sensor technology.

This section will explore key autoxidation pathways of organic materials. It will discuss the similarities and differences between oxidation processes in the gas-phase, polymers, lipids and SAMs, which share common reactive intermediates and degradation mechanisms. These oxidation processes are particularly relevant to the RADICAL project, which aims to develop a low-cost atmospheric radical sensor. Autoxidation of the functionalised sensor surface could enhance sensitivity, as a single atmospheric radical may trigger rapid surface oxidation. However, this increased reactivity could also compromise the longevity of the sensor. Understanding these pathways not only aids the development of more stable SAM-based sensors but also provides insights into the broader field of materials degradation.

1.5.1 Reactive Species

Autoxidation can be initiated by heat, Ultraviolet (UV) light or reactive species [103]. The two key reactive species involved in the initiation of atmospheric autoxidation processes are the hydroxyl radical ($\cdot$OH) and ozone (O_3). The formation of these radical species will be addressed in the following sections.

1.5.1.1 Ozone (O_3)

Ozone is present in both the troposphere and the stratosphere. Tropospheric ozone is predominately formed via photochemical reactions involving precursors generated by natural processes and human influence [104]. Global background ozone concentrations at sea level typically show daily 1-hour maxima of ∼20–60 ppb. [105]. The reaction pathways for O_3 generation in the troposphere involves the conversion of NO to NO_2 at a sufficiently high rate in order to maintain a NO_2/NO ratio to sustain background levels of O_3 [104]. The formation of tropospheric ozone is demonstrated in the following steps:

1. The reaction between hydroperoxy radicals (HO_2) and nitric oxide (NO) leads to the formation of nitrogen dioxide (NO_2) and a hydroxyl radical (·OH):

$$HO_2 + NO \rightarrow HO + NO_2 \tag{1.9}$$

2. The photodissociation of NO_2 by UV light (with wavelengths less than 430 nm) produces NO and a ground state oxygen atom ($O(^3P)$):

$$NO_2 + hv(\lambda \leq 430\text{nm}) \rightarrow NO + O(^3P) \tag{1.10}$$

3. The atomic oxygen reacts with O_2 in the presence of a third body (M, usually nitrogen or oxygen under atmospheric conditions) to form ozone [106]:

$$O(^3P) + O_2 + M \rightarrow O_3 + M \tag{1.11}$$

At wavelengths shorter than 250 nm, ozone can also be generated via the photodissociation of molecular oxygen (O_2), which leads to the formation of two excited oxygen atoms (O^1D) (equation 1.12). Each of these excited oxygen atoms can then combine with an oxygen molecule to form ozone (equations 1.13 and 1.14).

$$O_2 + hv \rightarrow 2O(^1D) \tag{1.12}$$

$$O(^1D) + O_2 \rightarrow O(^3P) + O_2 \tag{1.13}$$

$$O(^3P) + O_2 + M \rightarrow O_3 + M \tag{1.14}$$

1.5.1.2 Hydroxyl Radical (·OH)

Hydroxyl radicals are commonly referred to as the atmosphere's 'detergent' due to their highly reactive nature. They serve as chain initiators in most oxidation processes involving organic compounds, driving the degradation of pollutants and effectively helping to cleanse the atmosphere [107]. Typical tropospheric ·OH concentrations are on the order of $\sim 10^6$ molecules cm^{-3} [108], including near the Earth's surface, though surface-level values can range from $\sim 10^5$-10^7 molecules cm^{-3} depending on environmental conditions [109]. In the upper troposphere, ·OH is produced by the photolysis of ozone and subsequent reactions between $O(^1D)$ and H_2O.

$$O_3 + h\nu(\lambda 240 - 340\text{nm}) \rightarrow O(^1D) + O_2 \tag{1.15}$$

$$O(^1D) + H_2O \rightarrow 2\,{\cdot}OH \tag{1.16}$$

Another significant pathway for the production of ·OH radicals is the ozonolysis of alkenes. Recent measurements have revealed that alkene ozonolysis provides an overlooked source of ·OH radicals, as they are a by-product of this reaction [110]. Alkenes, particularly terpenes and monoterpenes, are highly abundant in the atmosphere. The most emitted terpene is α-pinene which has been reported to have a daily average emission of $\sim$2.4 μg g^{-1} d.m.h^{-1} in the winter time and $\sim$15.7 μg g^{-1} d.m.h^{-1} in the summer time [111]. These compounds are emitted by plants and are also commonly used in flavourings and fragrances [112]. As a result, they are prevalent in both outdoor and indoor air, making them key attributes in atmospheric chemistry.

Ozone reacts with alkenes in a [3+2] cycloaddition to form a molozonide, which then breaks down into a zwitterionic carbonyl oxide, known as a Criegee zwitterion, and a carbonyl species, shown in Figure 1.20. This Criegee zwitterion is depicted by a resonance between two canonical structures, a zwitterionic carbonyl oxide and a biradical; together they are named Criegee intermediates. Vibrationally excited Criegee intermediates may either rearrange and decay into α-radical carbonyl species and an ·OH radical via a vinyl hydroperoxide intermediate, shown in Figure 1.20, or undergo collisional stabilisation to form stabilised Criegee zwitterions. In condensed phases, the reactivity differs due to the close proximity of the Criegee zwitterion and the aldehyde, which allows for recombination to form a more stabilized secondary ozonide. A key factor in this process is the rapid collision with surrounding molecules, which facilitates fast vibrational relaxation of the Criegee intermediate and thereby promotes secondary ozonide formation [113]. Hydroxyl radicals formed during this process can then further react with other species. In the presence of air, α-radical carbonyl species can react with O_2 to form relatively long-lived peroxyl radical species [114].

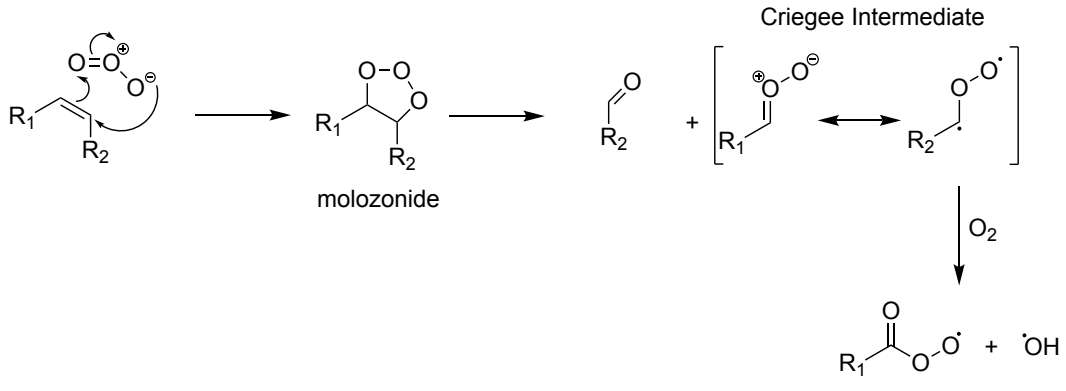

Figure 1.20: Ozonolysis of alkenes with ·OH as a by-product of the reaction.

1.5.2 Autoxidation Reaction Pathways

The oxidation of an organic compound typically begins with the attack of an ·OH, which often abstracts a hydrogen atom from a C-H bond to form a carbon-centred radical (or an O-H bond) to form an alkoxyl radical (equation 1.17) [115].

$$R{-}H + {\cdot}OH \rightarrow R{\cdot} + H_2O \tag{1.17}$$

The autoxidation cycle follows addition of oxygen to the carbon-centred radical (R·), which is an extremely rapid process and is essentially diffusion controlled at ambient O_2 concentrations at a rate of $\sim 10^9$ L mol^{-1} s^{-1} to form a peroxyl radical (ROO·), shown in equation 1.18 [116].

$$R{\cdot} + O_2 + M \rightarrow ROO{\cdot} + M \tag{1.18}$$

The peroxyl radical is highly resonance-stabilised, making it less reactive and more selective in its abstraction from hydrocarbons than the hydroxyl radical (·OH). It exhibits a strong preference for abstracting the weakest hydrogen atoms from hydrocarbons [117]. It has been well studied for gas-phase and in bulk liquid systems that the structure and functionality of the reactant can highly influence the rate of H-abstraction by a peroxyl radical [117, 118]. In many cases, the reaction of a peroxyl radical abstracting a hydrogen from another molecule is highly disfavoured due to the Bond Dissociation Energy (BDE) for R-H being larger than the corresponding ROO-H bond, shown in Table 1.1 [118].

R-H Bond	**BDE (kcal/mol)**	**Reference**
CH_2-H	104	[119]
CR_3-H	96	[120]
CH_2OCH_2-H	93	[121]
$CH_2{=}CHCH_2$-H	85	[119]
CF_3-F	121	[119]
ROO-H	90	[117]

Table 1.1: Bond Dissociation Energies (BDE) for various R-H bonds.

Typically the BDE for ROO-H is ∼90 kcal/mol [117], which is lower than typical alkyl CH_2-H BDE at 104 kcal/mol and perfluoro C-F BDE at 121 kcal/mol, implying that these reactions would be thermodynamically disfavoured. The BDE for ether-containing organic molecules and allylic compounds is comparable at 93 kcal/mol and ∼85 kcal/mol, respectively. Thus, the H-abstraction rate of these molecules should be higher. This means that in the presence of allylic compounds or ether-containing compounds, autoxidation can occur and the ROO· can abstract a hydrogen to form hydroperoxide (ROOH) and another carbon-centred radical (equation 1.19).

$$ROO{\cdot} + R{-}H \rightarrow ROOH + R{\cdot} \tag{1.19}$$

The rate of reaction, obtained experimentally in the literature, for different R-H groups, including alkyl C-H, tertiary alkyl C-H, allylic C-H and ether C-H, towards ROO· radical H-abstraction is shown in Table 1.2. Not included in Table 1.2 is

the C-F bond. An ROO· radical has a significantly low reactivity rate towards C-F bonds due to the high bond strength of the C-F bond, making it less susceptible to radical attack. As expected from the BDEs, the primary alkyl C-H has the slowest relative rate of reaction at 10^{-4} M^{-1} s^{-1}. The relative stability of a tertiary carbon centre to a primary/secondary carbon centre means the rate of H-abstraction is higher, by 10 orders of magnitude, for the tertiary carbon. The highest rate of reaction is seen for the allylic and ether-containing chains, which are 10^2 orders of magnitude greater than simple alkyl chains. This is due to the stabilisation of the radical centre. The presence of the double bond results in a resonance effect, whereby the unpaired electron after H-abstraction can delocalise over the conjugated π system, stabilising the radical and reducing the overall energy of the transition state. The oxygen atom in ether-containing molecules can stabilise the radical via the mesomeric effect, by donating electron density into the adjacent radical centre, thereby delocalising the unpaired electron and increasing the overall stability of the radical species. This suggests that straight alkyl chains do not undergo autoxidation, whereas ether-containing or allylic chains may be prone to it.

R-H Bond	**ROO· Radical H-Abstraction Rate (M^{-1} s^{-1})**	**References**
CH_2-H	5.50×10^{-4}	[122–124]
CR_3-H	2.50×10^{-3}	[122]
CH_2=$CHCH_2$-H	2.10×10^{-2}	[125]
CH_2OCH_2-H	1.60×10^{-2}	[123]

Table 1.2: ROO· Radical H-Abstraction Rates for Various R-H Bonds.

H-abstraction by a peroxyl radical leads to the formation of ROOH. Studies have indicated that the ROOH decomposition rate may vary depending on its stability, reactivity and environmental conditions (i.e. in the presence of heat or UV light) [126]. Some studies have shown that ROOH is stable in room temperature for as long as 24 hours [127, 128], whereas, ROOH formed in the troposphere in organic aerosols can undergo photolysis (λ = 300-400 nm) with decomposition rates ranging from 3×10^{-5} s^{-1} to 2×10^{-3} s^{-1} [129–131]. The decomposition of ROOH is thought to proceed via a unimolecular pathway, breaking the O-O bond to form RO· and ·OH at ambient temperature [126]. Results have shown that below 150°C unimolecular homolysis of saturated hydroperoxides does not occur rapidly enough to be a source of free radicals but hydroperoxides can be photolysed in the presence of UV light. Without the presence of UV light or high temperatures, faster routes to radical production, i.e. unimolecular decomposition reactions of hydroperoxides [132].

For compounds with stronger C-H bonds, the peroxyl radical follows alternative pathways. The behaviour of the peroxyl radical differs depending on the environment, such as in bulk liquids, the gas-phase, or more rigid systems like polymers, due to variations in factors like molecular mobility, intermolecular interactions, and the rigidity of the medium, which affect the radical reactivity and stability[101, 102, 117]. Understanding the behaviour of the peroxyl radical in these different contexts is crucial for studying monolayer systems as the fate of the peroxyl radical determines whether the material autoxidises or not. Monolayers are a single molecular layer at an interface, which can exhibit behaviour that is influenced by both bulk properties

(as seen in liquids and gases) and more constrained environments (similar to polymers/plastics). By reviewing the literature on liquids, gases, and polymers/plastics, insights into how peroxyl radicals behave under different conditions can be evaluated, which can help inform how they might interact in monolayers, where molecular mobility and reactivity are often more restricted. Additionally, the understanding of reaction pathways in different environments can provide useful models for predicting the reactivity and stability of radicals in monolayer systems. These environmental variations and corresponding reaction pathways will be discussed in the following sections.

1.5.2.1 Fate of ROO· in Solutions

In bulk liquids, the peroxyl radical can undergo several reactions, including H-atom abstraction, addition to double bonds, self-reactions and unimolecular decompositions [117].

H-abstraction. As discussed above, it is dependent on the strength of the R-H bond. However, even abstraction of an ROO· with an allylic C-H bond is a relatively slow process [133]. Other factors which determine the rate of H-abstraction from a ROO· include steric effects and polarity. Differences in rate constants have been observed both for the structural changes of the peroxyl radical and for structural changes of the oxidising substrate. In general, primary or secondary peroxyl radicals are three to five times more reactive than tertiary peroxyl radicals [117]. The substrate can be more reactive towards H-asbtraction if it contains electron donating groups. For example, 2,6-dimethylphenol is more reactive than phenol toward H-abstraction with a rate constant of $20{\times}10^3$ M^{-1} s^{-1} compared to $5{\times}10^3$ M^{-1} s^{-1}, respectively [117], shown in Figure 1.21.

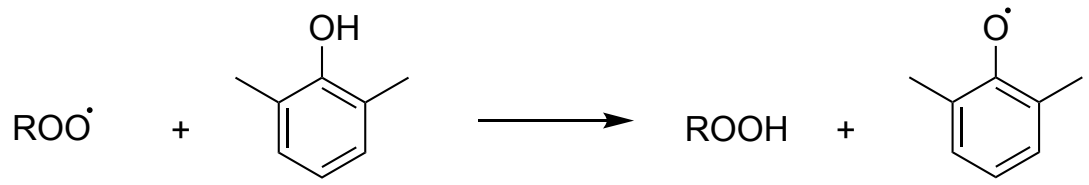

Figure 1.21: Scheme for the H-abstraction of 2,6-dimethylphenol by a peroxyl radical.

Addition. The peroxyl radical can add to a double bond to produce a more stable β-peroxy alkyl radical, shown in Figure 1.22. This β-peroxy alkyl radical will then react further with O_2 to form another peroxyl radical. If the oxidising substrate contains a double bond which is conjugated with an aromatic, carbonyl, nitrile or vinyl group, then this pathway is more favourable than abstraction of the allylic C-H [134]. Van Sickle *et al.* studied the addition versus abstraction rates of peroxyl radicals towards several cyclic alkenes [135]. It was reported that the pathway depended on the structure of the cyclic alkene. The rate for peroxyl radical addition to cyclopentene was 2.14×10^{-4} M^{-1} s^{-1} and the rate of abstraction was 3.67×10^{-4} M^{-1} s^{-1}, suggesting abstraction is favoured. However, for larger cyclic rings, such as cyclooctene, the rate of addition was ∼10 times faster than the corresponding abstraction reaction. It was discussed for cyclopentene that the strain

in the 5-membered ring makes abstraction (which does not induce further strain) more favourable than addition, whereas for cyclooctene, the larger, less strained ring makes addition, which forms a more stable intermediate much faster than abstraction. Thus, the rate of peroxyl radical addition increases significantly in larger cyclic alkenes due to reduced strain of the cyclic ring [135].

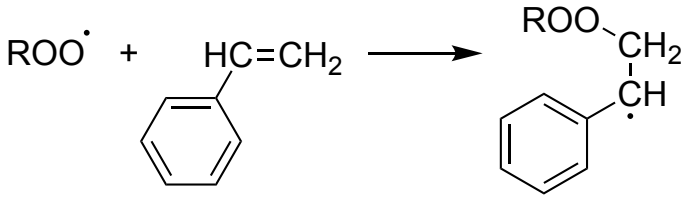

Figure 1.22: Peroxyl radical addition to a conjugated double bond to form a more stable β-peroxy alkyl radical.

Self-reactions. The self-reactions of a peroxyl radicals have been studied extensively [133, 134, 136–138]. The rate of reaction is highly dependent on the type of peroxyl radical involved, whether it is primary, secondary or tertiary. In general, the termination rate constants increase from tertiary peroxyl radicals < secondary peroxyl radicals < primary peroxyl radicals, as shown in Table 1.3 [117].

Peroxyl Radical Type	**Rate Constant (M^{-1} s^{-1})**
Primary peroxyl radical (RCH_2OO)	$2 - 4 \times 10^8$
Secondary peroxyl radical (RR'CHOO)	$1 - 10 \times 10^6$
Tertiary peroxyl radical (RR'R"COO)	$0.1 - 60 \times 10^4$

Table 1.3: Rate constants for the self-reaction of peroxyl radicals, depending on their structure [117, 134]

.

The relatively slow rate of the self-reaction between tertiary peroxyl radicals is due to the high activation energy barrier for the decomposition of the tetroxide intermediate to form alkoxyl radicals and oxygen [139, 140]. In fact, the differences in the rate constants for the peroxyl radical self-reactions is primarily due to the different activation energies required for the tetroxide decomposition [139]. For tertiary peroxyl radicals, the process can be represented by Figure 1.23.

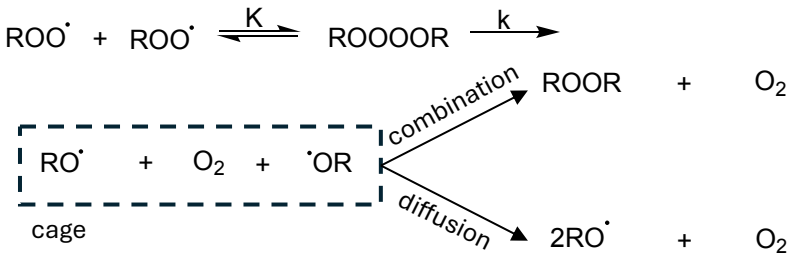

Figure 1.23: Self-reaction of tertiary peroxyl radicals. Adapted from [117].

Bartlett *et al.* have provided evidence of the formation of the tetroxide intermediate by monitoring electron spin resonance spectra (ESR) of *t*-butylperoxyl radical concentrations present in equilibrium with the tetroxide at low temperatures [140]. It was observed that at temperatures below -85°C, the peroxyl radical concentration did not change. However, it could be reversibly increased or decreased by raising and lowering the temperature [140]. The time available for the recombination of *t*-butoxyl radicals in the solvent cage is on the order of 10^{-9} s, which is much shorter than the spin-lattice relaxation time of approximately 10^{-6} s [139]. This significant difference in timescales means that cage recombination is unlikely. Since the time available for geminate pair recombination is so short, the radicals are more likely to escape the solvent cage via diffusion rather than recombine, as shown in Figure 1.23 [139].

In 1957, a mechanism was suggested by Russell [141] for the self-reaction of primary and secondary peroxyl radicals. This mechanism involved the decomposition of the tetroxide via a cyclic transition state, where one of the α-hydrogen atoms is transferred to produce a carbonyl, alcohol and oxygen [142]. The reaction scheme for the Russell mechanism is illustrated in Figure 1.24.

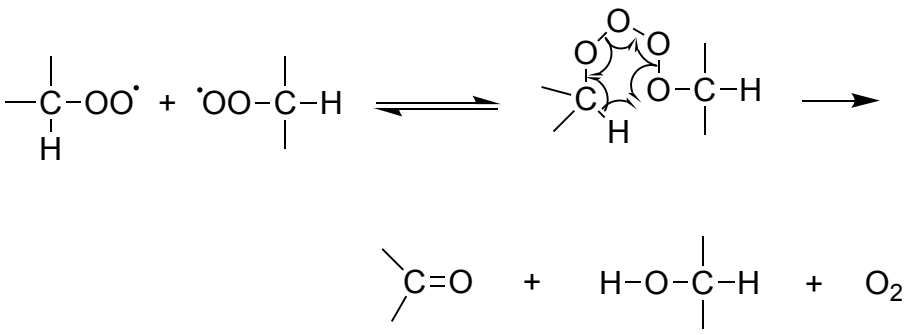

Figure 1.24: The Russell mechanism for primary and secondary peroxyl radicals [142]

This mechanism provides a clear explanation for the observed fast termination reactions of primary and secondary peroxyl radicals compared with tertiary peroxyl radicals. In bulk liquids, almost all interactions of secondary peroxyl radicals lead to chain terminations at 30°C [117, 132]. This mechanism also explains the termination of tertiary peroxyl radicals, which do not have α-hydrogens available to undergo this cyclic transition state. Thus, their termination can only lead to alkoxyl radicals [142].

Unimolecular reactions. Intramolecular H-abstractions by peroxyl radicals can also occur to yield dihydroperoxides, cyclic ethers, or carbonyl compounds and olefins [143]. The products of these intramolecular H-abstraction reactions depend on the experimental conditions. In the literature, it has been observed that the oxidation of 2,4-dimethylpentane in the liquid phase yields the corresponding dihydroperoxide with a high yield of 89% at 120°C, shown in Figure 1.25 [144].

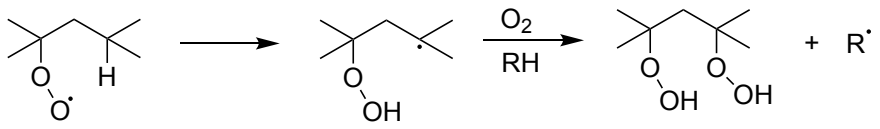

Figure 1.25: The formation of a dihydroperoxide in the liquid phase and elevated temperatures (120°C) for 2,4-dimethyl-pentane [144]

However, at increased temperatures (cool flame temperature range 250-300 ° C), the vapour phase oxidation of 2-methylpentane formed substantial yields of the corresponding O-heterocycles, shown in Figure 1.26 [145].

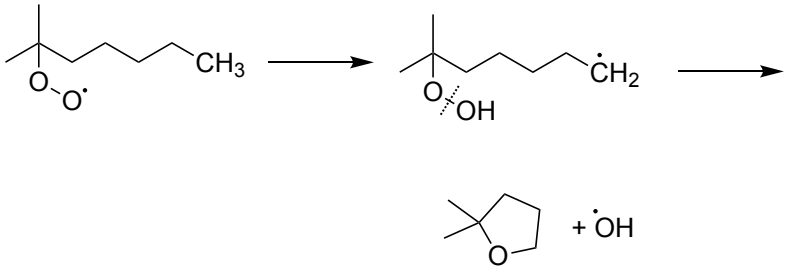

Figure 1.26: The formation of an O-heterocyle during the vapour phase oxidation of 2-methylpentane [145]

1.5.2.2 Fate of ROO· in the Gas-phase

Peroxyl radicals formed in the troposphere during the degradation of hydrocarbons and Volatile Organic Compounds (VOC)s, undergo several competing reactions [101]. The relative rates of these reactions are dependent on the ambient conditions and the structure of the RO_2 radical. These reactions include: bimolecular reactions with NO, NO_2, NO_3, OH and HO_2; the self-reaction with the other RO_2 radicals in the atmosphere; and the unimolecular isomerisation reactions such as H-atom shift or ring-closing reactions [101].

Bimolecular reactions. The reaction of RO_2 with NO provides a radical propagation pathway and plays a key role in tropospheric ozone formation, by oxidising NO to NO_2. This reaction often represents the major reaction for RO_2 radicals under relatively polluted conditions (equation 1.20) [101, 146].

$$ROO\cdot + NO \rightarrow ROONO \rightarrow RO\cdot + NO_2 \tag{1.20}$$

A typical rate constant for the reaction of alkyl peroxyl radicals such as those containing $\geq C_2$ atoms, cycloalkyls, hydroxyalkyls, hydroxyalkyl, with NO at 298 K is 9.0×10^{-12} cm^3 molecule^{-1} s^{-1} [101].

The reaction of an RO_2 radical with NO_2 has been reported to proceed via a reversible association reaction to form a peroxy nitrate ($ROONO_2$), shown in equation 1.21.

$$ROO\cdot + NO_2(+M) \rightleftharpoons ROONO_2(+M) \tag{1.21}$$

The thermal instability of the $ROONO_2$ products under lower tropospheric conditions (lifetime ∼0.2 s at 298 K) for alkyl peroxyl radicals, means this reaction does not play a significant role in the autoxidation of hydrocarbons [106]. However, for specific RO_2 radicals (where R is an acyl radical) and/or in colder parts of the atmosphere, the lifetime of the peroxynitrates can be longer, providing an additional sink for NOx and HOx species [106].

In the nighttime, when concentration of NO_3 are higher [147], the RO_2 radical can react with NO_3 to produce an alkoxyl radical, NO_2 and O_2, with a rate constant of 8.9 $\times 10^{-12}$ cm^3 molecule^{-1} s^{-1} at 298 K [101]:

$$ROO\cdot + NO_3 \rightarrow RO\cdot + NO_2 + O_2 \tag{1.22}$$

The reaction of RO_2 with ·OH radicals has been reported for alkyl peroxyl radicals containing 1-4 carbon atoms. Yan *et al.* used pulsed laser photolysis coupled to transient UV-vis absorption spectroscopy over a 292-526 K temperature range to study the reaction of methyl peroxyl radicals with ·OH radicals. This study provided a typical rate constant for this reaction at 298 K to be 3.7×10^{-11} cm^3 molecule^{-1} s^{-1} [148]. The reaction follows a few different channels and their branching ratios are strongly dependent on the size of R:

$$RO_2 + \cdot OH \rightarrow RO\cdot + HO_2 \tag{1.23}$$

$$RO_2 + \cdot OH \rightarrow ROH + O_2 \tag{1.24}$$

$$RO_2 + \cdot OH(+M) \rightarrow ROOOH(+M) \tag{1.25}$$

Self-reactions. In less polluted regions of the atmosphere where the reaction with NO does not dominate, reactions of RO_2 radicals with other RO_2 radicals or HO_2 radicals play a more significant role. These processes contribute to the radical removal or chain termination during oxidation reactions [106]. These reactions include:

1. The reaction of CH_3O_2 with HO_2 to produce a hydroperoxy radical and O_2, which has a rate constant of 5.2×10^{-12} cm^3 molecule^{-1} s^{-1} [101].

$$CH_3OO\cdot + HO_2 \rightarrow CH_3OOH + O_2 \tag{1.26}$$

2. The reaction of RO_2 with a methyl peroxyl radical to form two alkoxy radicals and O_2, which has a rate constant of 3.5×10^{-13} cm^3 molecule^{-1} s^{-1} [101]..

$$ROO\cdot + CH_3OO\cdot \rightarrow RO\cdot + CH_3O\cdot + O_2 \tag{1.27}$$

3. The reaction of RO_2 with a methyl peroxyl radical to form stable products: an alcohol, formaldehyde and O_2.

$$ROO\cdot + CH_3OO\cdot \rightarrow ROH + CH_2O + O_2 \tag{1.28}$$

4. The reaction of RO_2 with a methyl peroxyl radical to form stable products: a carbonyl, methanol and O_2.

$$ROO\cdot + CH_3OO\cdot \rightarrow R'C{=}O + CH_3OH + O_2 \tag{1.29}$$

In the liquid phase, the rate constant of two primary carbon-centred peroxyl radicals is 2-4 $\times 10^8$ M^{-1} s^{-1} [117, 134]. This rate is comparative to the gas-phase rate of 3.5×10^{-13} cm^3 $molecule^{-1}$ s^{-1} (2.1×10^8 dm^3 M^{-1} s^{-1}) [101]. However, in the liquid phase, there is a higher density of molecules. Thus, molecules are in closer proximity, which enables collisions to occur more frequently than in the gas-phase. This means that the self-reactions of peroxyl radicals are more likely in the liquid phase, compared to the gas-phase. In the gas-phase, the reactivity is influenced mainly by their intrinsic properties and the availability of other radicals or molecules for reaction.

In the atmosphere, the alkoxyl radicals produced during the RO_2 self-reaction can react with O_2 to form HO_2 radicals which can further react with RO_2 radicals:

$$RO\cdot + O_2 \rightarrow RC{=}O + HO_2 \tag{1.30}$$

$$RO\cdot + HO_2 \rightarrow ROOH + O_2 \tag{1.31}$$

Or RO· can abstract a hydrogen from another organic molecule, propagating the autoxidation cycle:

$$RO\cdot + R{-}H \rightarrow ROH + R\cdot \tag{1.32}$$

The H-abstraction by an RO· radical is faster than the H-abstraction by the corresponding ROO· radical by 10^6 orders of magnitude [149]. This means that formation of RO· radicals could facilitate faster propagation of the autoxidation cycle.

Unimolecular isomerisation reactions. RO_2 radicals can undergo unimolecular reactions such as ring closure or intramolecular H-abstraction, similar to the unimolecular reactions observed in bulk liquids [101]. However, the infrequency of collisions in the gas-phase enables these unimolecular isomerisation reactions to be a more dominant pathway compared to in liquid systems. In atmospheric chemistry, the classic unimolecular peroxyl radical rearrangement is the $RO_2 \rightarrow$QOOH reaction. This involves the H-atom transfer via a cyclic transition state which converts the peroxyl species into a carbon centred radical containing hydroperoxide species [106], demonstrated in the following equation:

$$CH_3CH_2OO\cdot \rightarrow \cdot CH_2CH_2OOH \tag{1.33}$$

These H-atom transfers typically occur via 5-, 6-, or 7- membered rings. The QOOH species can decompose to form HO_2 or OH species with a rate constant of 5.9×10^{-13} cm^3 $molecule^{-1}$ s^{-1} [150], such as

$$\cdot CH_2CH_2OOH \rightarrow CH_2{=}CH_2 + HO_2 \tag{1.34}$$

or can further react with O_2 to form a substituted peroxyl species (·OOQ(OOH)).

The atmospheric lifetime of RO_2 against bimolecular reactions, such as under typical NO concentrations, rarely exceeds a couple of minutes. Thus, the energy barriers for the RO_2 to QOOH isomerisation needs to be approximately 20 kcal/mol or less to have any significance to atmospheric chemistry [106]. The conditions where these reactions would be of significance are: a) if the lifetime of the peroxyl radical is long enough (i.e. in clean atmospheres where NOx concentrations are low); and b)

the molecules possess weak C-H bonds to facilitate the H-abstraction by the peroxyl radical (this is typical for ethers, such as dimethyl ether [151])[106].

As well as the RO_2 intramolecular H-abstraction reactions, another unimolecular isomerisation reaction involves ring-closure processes. This process requires the presence of a double bond in a molecule, which has a chain length long enough to facilitate cyclisation of the peroxyl radical via a 6-membered transition state, shown in Figure 1.27 [152].

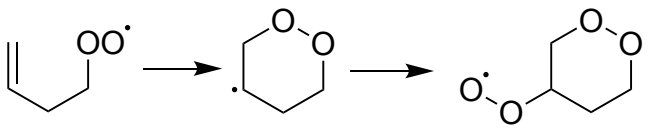

Figure 1.27: A basic ring-closure process of a peroxyl radical via a 6-membered ring transition state [152].

The transition state rate coefficient was predicted to be $k_{ringclose} \sim 0.2\ s^{-1}$ at 298 K. This is comparable with the rate of RO_2 and NO (1 ppbv in unpolluted areas). Moreover, the results from the literature suggest in pristine atmospheric conditions (i.e. above pristine forests), where the levels of NO, HO_2 and RO_2 are low, more than 90% of the peroxyl radicals will undergo ring-closure [152]. Thus, it is an important pathway in clean environments with low HOx and NOx concentrations.

1.5.2.3 Fate of ROO· on Surfaces

In more rigid systems, where the molecules have limited mobility, the autoxidation pathways can differ. Systems, such as polymers and plastics, have been extensively studied to understand their degradation mechanisms[103, 118]. This is crucial for improving their resistance to environmental factors [102]. Moreover, the air-drying process of a liquid paint layer as it converts to a durable film, is due to autoxidation [153]. Thus, the autoxidation of these compounds has been well studied to evaluate their solidification and hardening.

The basic autoxidation scheme for lipids and rubbers was proposed by Bolland and Gee [154–158]. Most materials degrade autocatalytically, which can lead to faster degradation than expected. It is proposed that this occurs due to chain transfer processes involving radicals, where one molecule transfers a hydrogen atom to another, turning into a non-radical while transferring its radical centre to the other molecule [102]. Figure 1.28(A) represents the basic autoxidation scheme proposed by Bolland and Gee, whereby H-abstraction of an organic chain (RH), leads to the formation of a carbon-centred radical (R·), which readily reacts with O_2 at a diffusion controlled rate. This ROO· radical then abstracts a H from a neighbouring chain to form another R· radical and ROOH. Thus, propagating the radical reactions. This means that one initiation event can potentially damage more than just the one chain before radical termination occurs.

The basic autoxidation scheme, investigated by Bolland and Gee, was formed for lipids and rubbers, which contain C=C bonds [154–158]. As discussed for H-abstraction by RO_2 radicals in Section 1.5.2.1, abstraction can take place for weaker allylic C-H bonds, where the bond strength (∼85 kcal/mol) is less than the corresponding ROO-H bond (∼90 kcal/mol) [117]. The product radical (-$\dot{C}$H-CH=CH-)

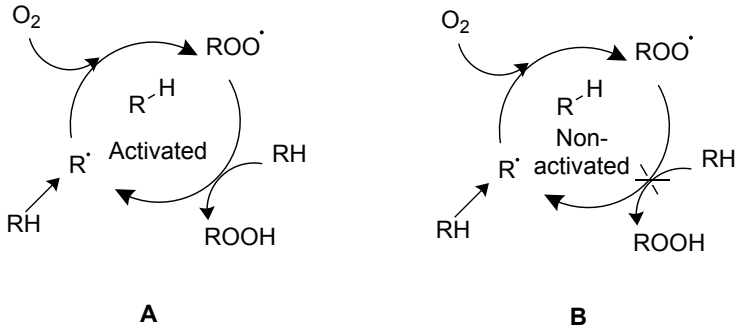

Figure 1.28: Autoxidation scheme proposed by Bolland and Gee [154].

is highly resonance stabilised, thus, the reaction is thermodynamically and kinetically favourable, shown in Figure 1.28(A) [102]. This scheme has been almost universally applied to all polymer systems [159]. However, most polymers do not contain C=C bonds, therefore, their carbon-centred radicals are less stable than the attacking RO_2 radical and so the reactions are strongly thermodynamically disfavoured [117], shown in Figure 1.28(B).

The chemical curing of oil-based paints also involves a complex free-radical process, which includes peroxidation, peroxide decomposition and cross-linking reactions [153]. The pathway of lipid peroxidation is initiated by abstraction of H from the activated C-H bond. This cleavage could be caused by heat, UV light or an initiator [160, 161]. Moreover, commercial air-drying paints always contain a certain quantity of hydroperoxides (ROOH), which appear upon synthesis. These ROOH can decompose effectively to initiate the autoxidation process, as shown in the following equations:

$$ROOH \rightarrow RO\cdot + \cdot OH \tag{1.35}$$

$$ROOH + M^{n+} \rightarrow RO\cdot + {}^{-}OH + M^{(n+1)+} \tag{1.36}$$

$$RO\cdot\,(\cdot OH) + RH \rightarrow ROH(H_2O) + R\cdot \tag{1.37}$$

The R· radical produced, reacts with oxygen to form an ROO· radical. The key step for radical propagation in this system, is also the H-abstraction of an activated C-H bond in the lipid tail by the ROO· radical. The rate of the peroxidation process is dependent on the pattern of the fatty acid. For example, the BDEs for the C-H bonds in methyl linolate differs depending on whether it is a bisallylic or allylic C-H bond, as shown in Figure 1.29. Thus, patterns containing more bisallylic C-H groups will have a faster rate in radical propagation. Although various products of autoxidation have been isolated, the reaction mechanisms of the autoxidation of conjugated fatty acids has yet to be fully clarified [153, 162].

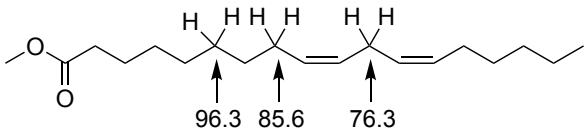

Figure 1.29: C-H Bond Dissociation Energies for Methyl Linoleate (in kcal/mol) obtained by theoretical calculations of dissociation energies. Adapted from [153, 163].

If the peroxyl radicals are unreactive towards H-abstraction of neighbouring chains, how do they react instead? Smith *et al.* proposed that peroxyl radical self-reaction could occur. This pathway has been discussed previously for peroxyl radicals in the gas-phase and bulk liquids [101, 117]. As discussed in Section 1.5.2.1 for bulk liquids, the structure of the RO_2 radical strongly influences the product formation of the RO_2 termination reaction [142]. For tertiary ROO· radicals, the products formed are highly reactive RO· radicals, which are capable of undergoing H-abstraction of neighbouring saturated chains (Figure 1.30(B)) [102]. Whereas, primary and secondary ROO· radicals form stable products (Figure 1.30(A)). Therefore, the structure of the carbon-centred radical highly influences whether the peroxyl termination leads to further radical propagation or chain breaking [102]. The study by Smith *et al.*, however, did not consider limited mobility in the solid polymers. Thus, the peroxyl radicals may not have the mobility necessary to be able to reach another peroxyl radical in order to react.

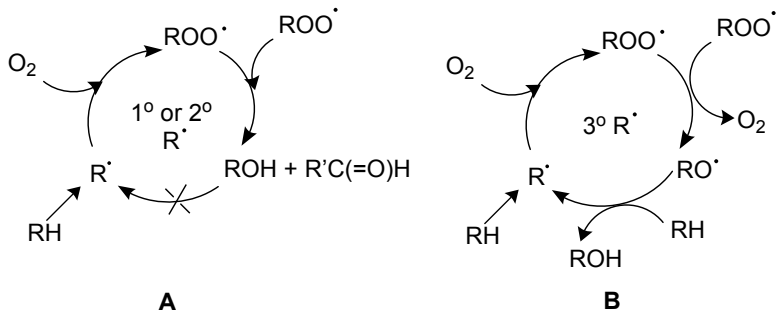

Figure 1.30: Reaction pathways for peroxyl radical termination in polymeric systems [102].

Other oxidants in our atmosphere can react with polymers to promote their degradation. These are reactive species such as ozone, HOx and NOx, which are present at low concentrations but nonetheless significant [108].

In the literature, ozone has been observed to accelerate the degradation of both saturated and unsaturated polymers [164–166]. Ozone has been reported to react with saturated hydrocarbons, aldehydes and ethers at low to ambient temperatures [167, 168]. Ozone is capable of initiating bond cleavage and generating RO· and HOO· radicals, which can further spread radical reactions [102], as shown in Figure 1.31.

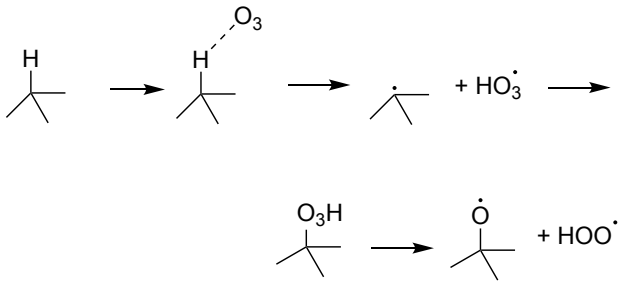

Figure 1.31: Initiation of polymer degradation by ozone. Adapted from [102].

HOO· radicals are also present in the atmosphere, along with ·OH radicals. Moreover, they can form when ozone reacts with polymer chains, as shown in Figure 1.31. It has been proposed in the literature that the propagation of RO_2 radicals could be explained by the H transfer between HOO· radicals and ROO·, to form ROOH which can break down to form RO· and ·OH radicals under elevated temperatures (> 150°C) or UV light (Figure 1.32) [132, 169]. Hydroxyl radicals generated in this process could then enhance degradation of the polymers through further initiation of chains [170, 171].

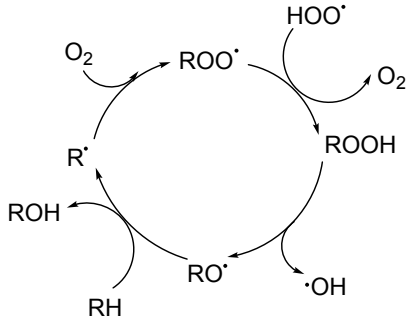

Figure 1.32: Initiation of polymer degradation by HOx. Adapted from [169].

The autoxidation of plastics in nature is slow and often results in incomplete degradation [103]. The slow autoxidation is primarily due to the chemical inertness of the polymer chains, thus, the concentration of polymeric radicals under mild conditions, such as room temperature, would be low. Moreover, the ROOH groups formed on the polymer chains, as shown in Figure 1.32, would need to be under harsh conditions, such as heat and UV light, to be able to undergo bond cleavage [103]. Therefore, the autoxidation rate increases under sunlight. Plastics which are exposed to sunlight and high concentration of O_2, corrode faster than plastics kept in environments with low solar irradiation and O_2 concentration [172]. Thus, the environment has a significant impact on the rate of polymer/plastic degradation.

The reactivity of RO_2 radicals has been shown to be strongly dependent on its environment and its molecular structure. This is clear for the reactivity of RO_2 radicals in bulk liquids, where structure of the molecules influenced either H-abstraction or addition by the peroxyl radical and their self-reaction product formation [117]. The dominant reaction for peroxyl radicals in the gas phase was the reaction with NO,

which plays a key role in polluted atmospheres. In more pristine atmospheric conditions, where the concentrations of NO are low, pathways such as the self-reaction of RO_2 or reacton with HO_2 become more significant, as well as unimolecular isomerisation reactions which can occur for longer chained species (i.e. the RO_2 radicals are able to form 5- or 6-membered rings) [106]. In cases where the RO_2 radicals have limited mobility, such as in polymer/plastic systems, the outcome of the termination of RO_2 radicals becomes important for exhibiting either radical propagation throughout the system or radical chain termination, which is strongly dependent on the structure of the molecules present [102]. This information can be utilised for the study of autoxidation within monolayer systems, which has generally been less explored by the literature. The following sections will outline previous reports on the reactivity of SAMs during their oxidation.

1.6 Reactivity of SAMs

SAMs have been used to study the chemical evolution of organic molecules bound to surfaces [173–175]. These studies are particularly relevant for understanding reactions on organic aerosol surfaces in the atmosphere, as well as for providing fundamental insights into the oxidation mechanisms within SAMs. The following sections will describe ·OH radical initiated oxidation of SAMs, photodegradation of SAMs and ozonolysis of unsaturated SAMs.

1.6.1 OH-initiated Oxidation

To study the chemical evolution of organic aerosols in the atmosphere, SAMs are often utilised as model organic surfaces [173, 176, 177]. Molina *et al.* studied the OH-initiated oxidation of octadecyltrichlorosilane (OTS) monolayers as models for alkane aerosols [173]. The surfaces were exposed to OH (0.1-100 $\times$ 10^8 molecules cm^{-3}) in the presence of NOx, O_2 and H_2O (3×10^{13}, 3×10^{12}, 6×10^{14} molecules cm^{-3}, respectively). The surface chemical changes were analysed by a series of analytical techniques such as FTIR, XPS, AFM and contact angle analysis. The gas phase products formed and the loss of ·OH during heterogeneous oxidation were monitored using a laminar flow reactor coupled to a Chemical Ionisation Mass Spectrometer (CIMS).

During this study, it was observed from the FTIR results that almost all of the CH_x groups were removed from the surface after 10 minutes of exposure to ·OH and O_2 and that the rate of CH_x loss was greater than the rate of ·OH loss (i.e. one OTS chain consisting of 18 carbons is removed as a result of the loss of 2-3 ·OH radicals). This insinuates that the ·OH radicals initiate a chain reaction within the monolayer chains [173]. The chain reaction mechanism proposed in this study is shown in Figure 1.33.

The proposed mechanism was based on the corresponding gas-phase mechanism, in which the rate limiting step is the reaction of ·OH with the surface organic chains. The surface alkyl radical then readily reacts with O_2 to form a surface alkylperoxyl radical (ROO·) in the presence of O_2 [178]. The long chain surface ROO· then undergo self-reaction. It was observed that the rate of carbon loss was not affected by the presence of NO, which suggests that the RO_2 self-reaction is very efficient on the surface. It was stated that at higher levels of NO, the surface peroxyl radicals

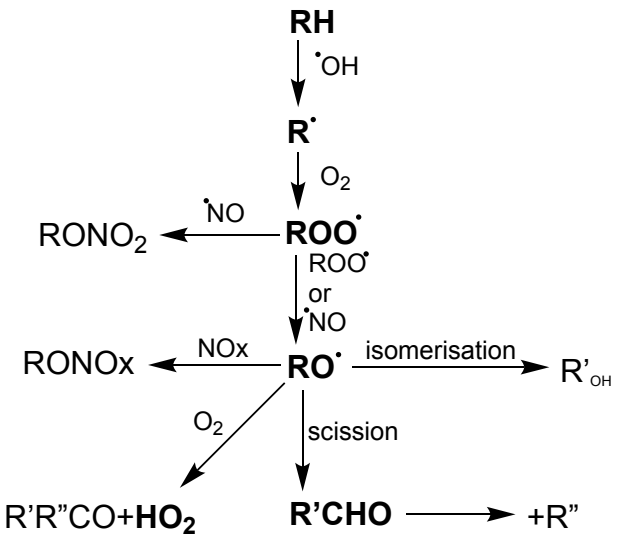

Figure 1.33: OH-initiation of the oxidation of SAMs in the presence of $NOx/O_2/H_2O$. Adapted from [173].

might react preferentially with NO, but in this study they did not observe loss of NO. This contradicts other literature on bulk chemistry, which suggest the reaction of NO with ROO· radicals is a dominant pathway [101]. The products of the RO_2 self-reaction was dominated by the formation of RO· radicals. As shown in Figure 1.33, there are several reaction pathways for the RO· radical. It was observed for longer chained RO· radicals that the C-C scission channel appeared to proceed at a faster rate than isomerisation (i.e. 1,5 H-shift) and the reaction with HO_2 [173]. It was therefore concluded that on an organic surface, the oxidation mechanisms lead predominantly to C-C bond scission via the self-reaction of RO_2 and the formation of RO· radicals. This is an unexpected conclusion, as it contradicts the theory that limited molecular mobility on these surfaces would prevent peroxyl radicals from coming into close proximity, thereby hindering their ability to self-react.

1.6.2 Photodegradation of SAMs

The stability of SAMs is an important attribute for their application in various technologies [175]. Alkanethiol SAMs have been observed to have lifetimes ranging from hours to months under ambient conditions [179] but lifetimes of minutes under UV irradiation [180]. For alkanethiol SAMs, this has been attributed to the thiolate headgroups, which are easily oxidised [180]. However, the alkyl chains themselves are also known to degrade under harsh photo irradiation [181, 182].

Understanding the photoreactivity of SAMs will not only aid in improving their stability but it can also serve as a fundamental understanding of photoreactivity in condensed phases, such as for organic aerosol chemistry [183]. The photoreactivity of SAMs has been explored by Ye *et al.* [175]. A low-pressure Hg/Ar lamp (254 nm) was used to irradiate octadecylsiloxane (ODS) SAMs. The UV light at 183 nm (3% of total intensity) was responsible for ozone generation [184], which was measured to have a steady-state of 100 ppm in the UV chamber. Their results suggested that UV degradation of octadecylsilane (ODS) SAMs required both UV and oxygen, and

that ozone alone did not degrade the alkylsiloxane SAMs. This suggested the role of UV-generated species, such as ·OH and atomic oxygen. Contact angle measurements provide further insights into the degradation mechanism, indicating that hydrophobic groups (CH_3 and CH_2) are converted to hydrophilic groups (such as CHO, OH, and COOH) as degradation progresses. However, after significant CH_2 loss, the contact angle does not drop to zero, suggesting that the surface is not fully covered with hydrophilic groups. The gradual increase in hydrophilic coverage could be due to oxygenated groups being buried within the monolayer, rough surface topography, or incomplete conversion of CH_2 groups, with some possibly leading to cross-linking instead of forming hydrophilic groups, as shown in Figure 1.34 [175]. These findings provide valuable insights into the degradation mechanisms of SAMs under UV irradiation, which could inform strategies for improving the stability of SAMs in various technological applications, including those in organic aerosol chemistry.

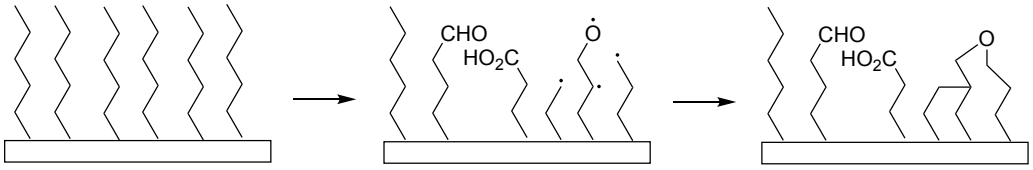

Figure 1.34: Proposed mechanism for the photoreactivity of SAMs. Adapted from [175].

1.6.3 Ozonolysis of Unsaturated SAMs

Unsaturated hydrocarbons are highly abundant in the troposphere [185]. The reaction between ozone and unsaturated hydrocarbons has been extensively studied in the gas-phase and in bulk liquids[185, 186]. In the troposphere, the unsaturated hydrocarbons can condense, either as pure liquids, such as in the bulk, aerosol particles or thin films, or they can adsorb onto a solid or liquid substrate [174, 187]. The use of SAMs as models for studying the reactions of organic molecules adsorbed onto solid substrates, such as dust particles in the atmosphere, has received attention [188]. A common conclusion of these studies is that surface-bound alkenes react with ozone faster than compared to the corresponding gas-phase reaction [187, 188]. The reaction of ozone on the surface follows a Langmuir-Hinshelwood mechanism, shown in Figure 1.35, which involves a rapid equilibrium between gas-phase ozone and adsorbed ozone, followed by a slower chemical reaction of ozone with the terminal alkene groups [174]. For surface-attached alkene molecules, the loss of ozone to the surface has shown to be faster than expected based on the gas-phase ozone-alkene reactions [183, 189, 190].

Dubowski *et al.* investigated the effect of ozone on the oxidation rate of OTS SAMs [174]. Molecular dynamic simulations were conducted to understand whether the enhancement in oxidation rate is due to increased reaction probability or longer residence time of ozone on the surface. The collision rates of ozone with the SAM surface and terminal alkenes were calculated and compared. The results showed that ozone collides with the terminal alkene much more frequently (at a collision rate of 20 $\times 10^{17}$ s^{-1} ppm^{-1} cm^{-2}) than with the surface itself (at a collision rate of 1.7 $\times 10^{17}$

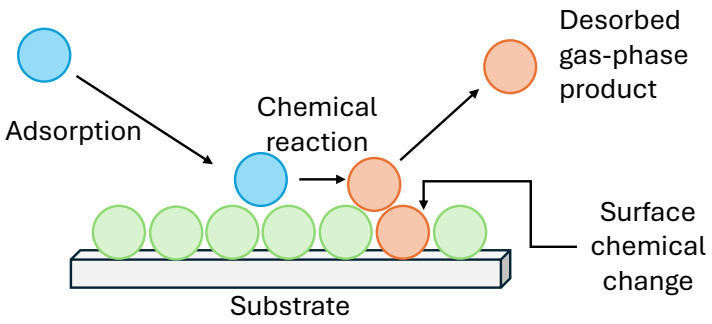

Figure 1.35: Langmuir-Hinshelwood mechanism.

s^{-1} ppm^{-1} cm^{-2}) [174]. This is due to inelastic collisions that cause ozone to interact multiple times with the alkenes after each surface collision. The residence time of ozone on the surface was found to be around 14-17 ps in the simulations, primarily due to van der Waals forces. However, the experimental data showed a much longer residence time (∼7 seconds), suggesting that the ozone is also chemisorbed, not just physically adsorbed, on the surface [174]. This implies that using a simple reaction probability that does not account for ozone concentration is not suitable for calculating ozone uptake or organic loss. Instead, a more complex approach, reflecting the molecular-level mechanism, should be used when incorporating such heterogeneous reactions into atmospheric models [174]. These insights highlight the importance of considering surface-specific reactions and chemisorption when studying ozone interactions with organic molecules in atmospheric chemistry.

1.7 Project Aims

SAMs are widely used in various technologies and as model systems for studying interfacial reactions due to their ability to incorporate diverse functional groups [1]. SAM stability can be affected by environmental interactions, particularly its oxidation by surrounding oxygen molecules. This spontaneous process, known as autoxidation, involves reactive species like ·OH radicals, which can lead to chain degradation through H-abstraction, forming carbon-centred radicals (R·) that react with oxygen to form peroxyl radicals (ROO·). While the reactivity of ROO· has been well studied in bulk liquids and the gas phase, less is known about these processes in more rigid systems, where limited chain mobility may influence reaction pathways.

The primary aim of this project is to investigate the reactivity of atmospheric radicals, specifically hydroxyl (·OH) and subsequent peroxy (ROO·) radicals, within monolayer surfaces. We will focus on the effect of ROO· radical propagation and assess its impact on the overall degradation rate of the monolayer. The propagation of these reactions is influenced by various factors, including packing density, chain functionality, and the composition of atmospheric constituents. Additionally, the inherent lack of mobility in SAMs could hinder the termination of ROO· radicals if the radicals are too far apart to react. As such, this project will also explore the alternative fate of the ROO· radical.

To conduct these studies, the first step is to produce high-quality and reproducible SAMs on a range of silica substrates. Chapter 2 will focus on the opti-

misation and development of the functionalisation procedure for generating these SAMs. Once the SAMs are prepared, a variety of characterisation techniques will be employed to confirm that the SAMs are well-packed and form a single, smooth molecular layer. These techniques will also examine the chemical changes that occur on the surface following reactions with atmospheric radicals.

Chapter 3 will describe autoxidation within SAMs, with the aim to assess the degree of radical propagation within SAMs. Comparisons between organic chains of varying functionalities, i.e. alkyl, ether-containing and perfluoro-containing chains, will be made to evaluate the effect of chain functionality on the propagation of radical reactions and hence, if autoxidation can occur in SAMs. Moreover, the fate of ROO· radicals in SAMs will be probed to further understand the surface oxidation mechanisms.

This project is part of a broader research programme funded by the European Commission, which aims to develop sensors based on Si junctionless nanowire transistor (Si JNT) devices for the real-time detection of short-lived atmospheric radicals, such as ·OH and NOx. A central focus of this project is the functionalisation of the sensor surfaces, specifically investigating a variety of organic molecules that can selectively react with these atmospheric radicals. Chapter 4 will investigate the exposure of model organic compounds, including alkanes, ethers, perfluorinated alkanes and arenes, to ·OH radicals, and analyse their reactivity using contact angle analysis.

Chapter 2

Functionalisation and Characterisation of Self-Assembled Monolayers on Silica Surfaces

2.1 Introduction

Silica substrates, including planar surfaces and porous or non-porous nanoparticles, can be functionalised with organic molecules of different functionalities to form self-assembled monolayers via a Si-C covalent linkage [191]. The most common method for monolayer formation on silica surfaces is through the use of trichloro- or trialkoxysilanes [192, 193]. As discussed in Chapter 1, these compounds have a tendency to self-condense and polymerise, which can be difficult to control. This can lead to problems with the reproducibility of monolayer formation. However, many reports in the literature have provided protocols for producing densely packed monolayers from trichloro-/trialkoxysilanes [7, 194].

SAMs on silica have grown in interest for their application towards a variety of fields, including: sensing, coatings, thin-film technology and microelectronics [7]. Structural and quantitative characterisation is essential for assessing the quality of monolayers, encompassing parameters such as thickness, packing density, chemical composition, and surface coverage uniformity. To thoroughly evaluate these aspects, a variety of characterisation techniques must be employed. While the development of applications for monolayer systems continues to advance, methods specifically designed for characterising the organic compounds attached to their surfaces have received less attention.

Monolayers on silica can be characterised *in situ* by techniques such as solid state NMR. This method can provide evidence of the Si-C bond linkage and other organic functional groups within the monolayer chains. However, the sensitivity of this technique is limited, thus only substrates with a sufficient amount of organic material attached can be analysed, i.e. silica nanoparticles. Other techniques such as XPS and FT-IR can be used to analyse organic functional groups quantitatively, however, these techniques also have sensitivity limitations. Alternatively, monolayers can be characterised by cleaving the molecules from the solid substrates [195]. The solution-phase products can then be characterised by more conventional techniques such as Gas Chromatography-Mass Spectrometry (GC-MS) and Nuclear Magnetic Resonance (NMR).

This chapter will introduce the functionalisation methodology developed to produce high quality and reproducible monolayers on silica surfaces. A range of organic alkoxysilane molecules will be used to form monolayers on various silica substrates. These functionalised silica surfaces serve as models for the radical sensor surfaces. Characterisation of these monolayers will be described, detailing a variety of techniques which have been utilised to provide sufficient information about the SAMs. Finally, an alternative methodology will be reported to chemically cleave the monolayers bound to the silica surface, providing both detailed qualitative and quantitative analysis of the attached organic molecules.

2.2 Functionalisation of Silica Surfaces

Glass slide surfaces and silicon dioxide (SiO_2) nanoparticles have been used as model substrates for this study. Glass slide surfaces (75 × 25 mm) were convenient and cost-effective surfaces to use as model planar silica sensor surfaces. However, after functionalisation, the amount of organic molecules attached to a glass slide is very small, approximately 0.4 mg for an eight-carbon alkane side chain per slide (assuming 0.2 nm^2 surface area per molecule in the monolayer) [38]. This amount is insufficient for full chemical structure characterisation by many standard analytical techniques. To increase the amount of organic functional groups, commercially available non-porous silicon dioxide nanoparticles (10-20 nm) were also used. The silica nanoparticles allowed more information about the monolayer surface and its reactivity with oxidising radicals to be obtained. For the sensor surfaces, silicon on insulator (SOI) and silicon junctionless nanowire transistor (Si-JNT) surfaces have been used for functionalisation. This section will introduce the optimised methods of functionalisation for each of the substrates.

2.2.1 Alkoxysilane Derivatives

For evaluating the suitability of a particular organic monolayer for the sensor surface, it was crucial to investigate organic molecules with various functionality and thus, reactivity towards oxidising radicals. The alkoxysilane molecules used for the formation of SAMs on various silica substrates in this study are shown in Figure 2.1. The commercially available alkoxysilane derivatives include:

a) C8AlkOEt: n-octyltriethoxysilane, C8AlkOMe: n-octyltrimethoxysilane
b) C8EneOMe: trimethoxy(7-oct-1-enyl)silane
d) C8PerfOMe: 1H,1H,2H,2H-perfluorooctyltrimethoxysilane
h) C6PhOEt: phenyltrimethoxysilane.

The remaining alkoxysilane derivatives were synthesised by a member of the research group. These include:

c) C6OneOEt: 6-(triethoxysilyl)hexan-2-one
e) C7DiEthOEt: 9,9-diethoxy-2,5,10-trioxa-9-siladodecane
f) C5EthOEt: triethoxy(3-ethoxypropyl)silane
g) C8BrAlkOEt: triethoxy(7-methyloctyl)silane.

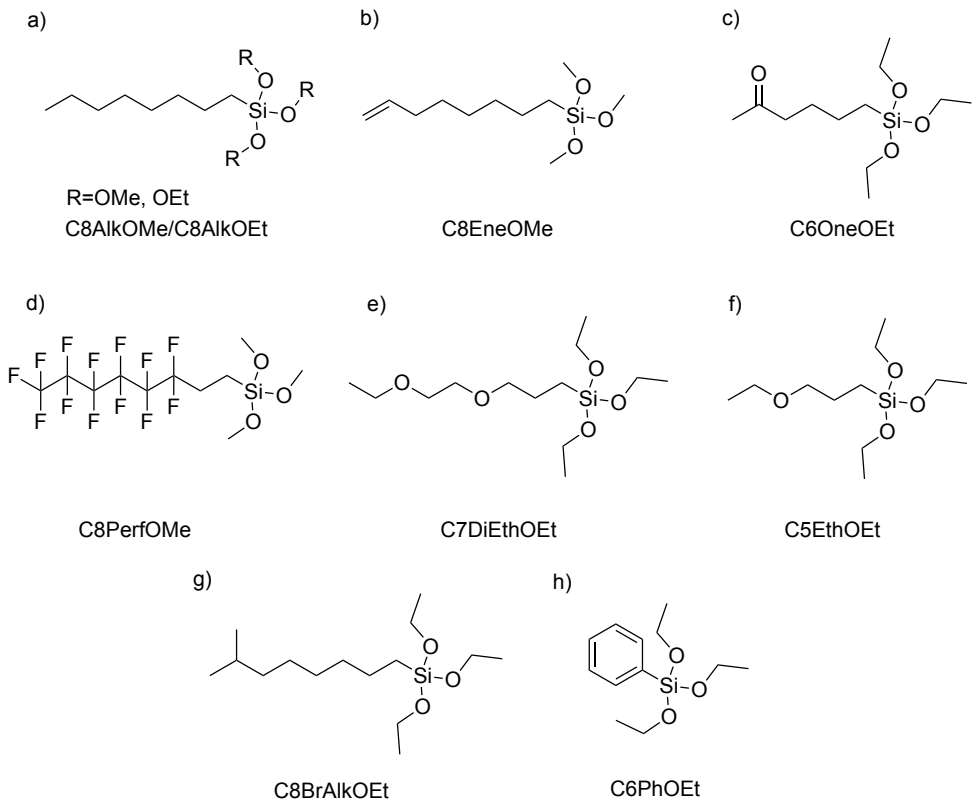

Figure 2.1: Alkoxysilane derivatives used for the functionalisation of silica surfaces.

2.2.2 Pre-treatment of Silica Surfaces

The deposition of a uniform and homogeneous monolayer is highly influenced by the condition of the silica surface; any contamination on the surface will cause defects and uneven formation of the monolayer. Therefore, to ensure high-quality and reproducible monolayers, it was crucial to use an appropriate cleaning procedure [196].

Prior to solution deposition, the silica surfaces should have a clean silicon oxide layer with a high density of hydroxyl groups. To achieve this, common cleaning procedures include two types of method: dry and wet. The dry methods consist of: oxygen-based plasma cleaning [197], UV irradiation in an O_2 atmosphere [198] and ozone cleaning [199]. These processes oxidise any organic impurities on the silica surfaces into gases or water-insoluble species which can then be removed by subsequent water washes [198]. Wet methods often involve heating the substrates in an acidic solution containing a 3:1 mixture of concentrated sulfuric acid (H_2SO_4) and 30% hydrogen peroxide (H_2O_2), called the "Piranha solution" [200]. The silica substrates are coated in this solution and heated to 80°C for approximately one hour to remove organic contaminants from the surface. The procedure is followed by several washes using water and then methanol, generating a clean silicon substrate with a high density hydroxyl layer [196].

Within this project, various types of silica surfaces were used: glass slide surfaces, silicon wafer surfaces and silicon dioxide nanoparticle surfaces (10-20 nm sized). Depending on the type of silica surface used for monolayer deposition, a wet or dry method of pre-treatment was used. For the pre-treatment of silica nanoparticles (10-

20 nm sized), Piranha solution cleaning was the only viable option. Typically, for the planar substrates (glass slides or silicon wafers), plasma cleaning was used. For this project, collaborations with the York Plasma Institute (YPI), allowed use of their atmospheric pressure plasma jet. A COST (Cooperation in Science and Technology) jet was used as the plasma source. It consists of a 30 mm x 1 mm x 1 mm (length x width x height) plasma channel connected to a housing which incorporates voltage and current probes in order to determine the power dissipated by the plasma. The power output for these experiments was typically set to 60 W, while the gas flow rates of each component—usually helium, oxygen, and water vapor admixtures—were adjusted according to the specific experimental requirements. The planar substrates were placed 3 mm below the plasma jet, which was attached to an XY translation stage. The translation stage was programmed to scan the planar substrate for 4 minutes and then the substrates were immediately placed into millipore water to avoid contamination. The quality of the cleaning procedure for planar substrates was monitored using contact angle analysis.

2.2.2.1 Pre-treated Planar Substrates: Contact Angle Analysis

Contact angle analysis is a measure of the wettability of a surface, with a smaller angle indicating higher wettability and thus a more hydrophilic surface. As shown in Table 2.1, the contact angles of a glass slide surface before cleaning treatments were between 15-20°. This suggests that some contamination was on the surface such as dust particles.

Cleaning Treatment	**Bare Glass Slide (°)**	**After Treatment (°)**
He/H_2O (0.2%) plasma	15.5	5.5
He/H_2O (0.5%) plasma	16.9	5.0
He/H_2O (0.5%)/O_2 (0.2%) plasma	18.4	4.4
Piranha solution, 80°C, 1 hr	21.2	5.0

Table 2.1: Contact angles for bare glass slides before and after cleaning treatments.

The plasma treatments were compared with Piranha solution treatment. Plasma treatments significantly reduced the contact angles to values $< 10°$, which is in good agreement with results from the literature [201]. This result indicated that the surface became more hydrophilic and the density of hydroxyl groups increased. The increase in oxygen content (added 0.2% O_2) tended to result in a slightly lower contact angle. This is likely due to increased concentrations of reactive species, such as ·OH, generated in the plasma jet (discussed further in Section 4.2.1.1). The Piranha solution treatment also substantially reduced the contact angle. The difference in the treatment with Piranha solution compared to the plasma treatment was minimal; however, the plasma treatment with added water and O_2 appeared to be the most effective for increasing the hydrophilicity of the glass slide surface. Therefore, this was the cleaning procedure chosen for planar silica substrates.

2.2.3 Functionalisation Procedure

The SAMs were prepared from alkoxysilane self-assembling molecules, outlined in Figure 2.1. Freshly cleaned silica surfaces (glass slide surfaces or silicon wafer sur-

faces) were dried thoroughly under a flow of N_2 air to remove any excess water. This was essential to prevent polymerisation of the alkoysilane derivatives. Once dried, the silica substrates were placed in a solution (8 mM) of the alkoxysilane precursor and (10 mM) n-butylamine in dry toluene. The primary amine, n-butylamine, was added to catalyse the silanisation reaction and increase the rate of hydrolysis. The silica substrates remained in solution for 20-24 hours at room temperature. This procedure is not the optimised procedure, however, it was performed in the initial stages of the project. The reaction scheme is outlined below in Figure 2.2. As shown, the contact angle results significantly increased to 103° from 4.4° after functionalisation, which agrees well with results from the literature for n-octyltrimethoxysilane monolayers [76]. This is due to the organic molecules increasing the hydrophobicity of the surface, confirming successful formation of a monolayer.

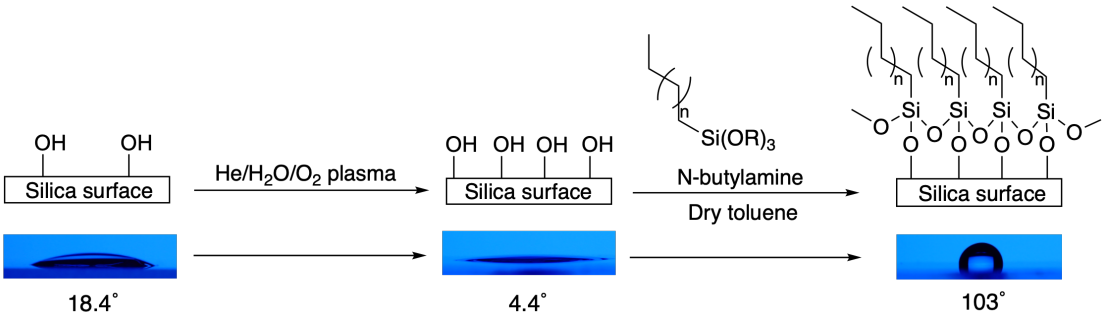

Figure 2.2: Functionalisation procedure of a silica surface using an alkoxysilane derivative. Contact angles are displayed below the scheme for each stage of the reaction.

Solution phase deposition is the most common method for the formation of SAMs on silica surfaces [202]. However, obtaining reproducible monolayers can be challenging as discussed in Chapter 1.2. It was observed during the winter months that the contact angles after solution phase deposition would fluctuate between 70-100° for n-octyltrimethoxysilane monolayers, suggesting uneven and/or incomplete monolayer formation. As discussed in Chapter 1.2, there are many factors that determine the level of definition of SAMs including water content, temperature, and catalysis. The water content in the surfactant solution needs to be carefully controlled to obtain high quality SAMs. An excess of water causes polymerisation of the alkoxysilanes in solution which results in polysiloxane depositing on the surface rather than the alkyltrialkoxysilane securely bonding [7], [12]. However, incomplete monolayers are formed in the absence of water as water is needed to hydrolyse the alkyltrialkoxysilanes to form silanols which then form stable bonds with the silica [42]. Moreover, the effect of preparation temperature has been studied in the range of 5-65°C and it was found that the optimum deposition temperature was 28°C [34]. Additionally, it was observed that the formation of SAMs can be initiated by different mechanisms at different temperatures, including island growth at low temperatures (<16°C) and homogeneous growth at high temperatures (>40°C) [203]. The reproducibility issues observed during the winter months suggested that the preparation temperature and humidity changes could be influencing the consistency of the results. In the next few sections, the effects of these factors on improving the reproducibility of alkoxysilane monolayers will be discussed.

2.2.3.1 Effect of Water Content

The water content of the solvent used in the deposition process, dry toluene, was investigated by Karl Fischer titrations. Results obtained immediately from the dry solvent column showed low water content of around 6-8 ppm which is within specifications for the purifying system of dry toluene [204]. This result led to a key question of whether our solutions needed slightly more water in order to form monolayers more effectively. Small water additions of 2, 4, 10 and 20 μL per 70 mL of dry toluene were tested, as shown in Table 2.2. The water was added to the dry toluene and sonicated to ensure homogeneous dispersion. The deposition procedure was then carried out in a sealed system to prevent more water being absorbed under ambient conditions by the solution. The addition of water showed to increase the hydrophobicity of the C8Alk functionalised glass slide surface after monolayer formation but there was no clear trend between the amount of water added and the measured contact angle. However, the addition of 20 μL of water to 70 mL of dry toluene was observed to increase the contact angle results the most with a relatively small error.

Water Content (μL)	**Average Contact Angle (°)**	**Error (± °)**
0	74.4	3.7
2	97.8	1.4
4	85.9	10.4
10	98.3	2.2
20	100.6	3.1

Table 2.2: Water content additions and corresponding average contact angle measurements of C8Alk functionalised glass slide surfaces with associated errors.

These results have implied the importance of small additions of water to the deposition solution, particularly 20 μL per 70 mL of dry toluene, which gave the most reproducibly high contact angles. This could be due to the water molecules hydrolysing alkoxysilane molecules to form silanols which can then form stable bonds with the silica [42]. The addition of water to the deposition solution was therefore used in future functionalisation procedures.

2.2.3.2 Effect of Temperature

The temperature of the deposition solution has been shown to affect the density of monolayer formation [34]. Therefore, temperature was investigated to assess whether this could be the factor causing fluctuations in the quality of SAMs produced. These experiments were performed by placing the vials containing the substrate and deposition solution into various temperature settings: the fridge freezer (-10°C), the fridge (5°C), the fumehood (room temperature, 21°C) and an oil bath (40°C). The results are displayed in Table 2.3. As can be seen in the results, -10°C gave the lowest contact angles and this is most likely due to the water in the solution freezing at this temperature, meaning hydrolysis of the silane precursor is reduced. The average contact angle for tests at 5°C, room temperature and 40°C do not vary significantly. However, the variation of contact angles for the room temperature tests was higher than when the temperature was controlled, with an error range of ±4.3°C. This

suggests uneven monolayer formation on the glass slide, which could be due to the temperature being inconsistent. By leaving it in the fumehood, the temperature could fluctuate due to the heating in the building being on throughout the day and off during the night. Thus, the temperature would reduce overnight. This could also support the repetition of reproducibility issues during the winter months as the temperature will decrease more significantly at night.

Temperature (°C)	**Average Contact Angle (°)**	**Error (± °)**
-10	56.2	5.2
5	90.6	1.0
21	90.5	4.3
40	83.8	1.0

Table 2.3: Average contact angles of C8Alk functionalised glass slide surfaces prepared from different temperatures of deposition solution with associated errors.

Nevertheless, the quality of these monolayers was lower than expected for alkoxysilane monolayers by approximately 10°, implying that temperature was not the significant factor for causing the discrepancies in the contact angle results. Thus, it was concluded to continue the preparation of SAM formation at room temperature.

2.2.3.3 Effect of Catalysis

To ensure that fluctuations in monolayer formation was reduced, it was crucial that a protocol was developed that could be robust enough to withstand any slight changes in humidity or temperature during the solution deposition process. Therefore, the effect of catalysis was investigated by testing various acids and bases to catalyse the silanisation reaction. The hypothesis was that these catalysts would increase the rate of hydrolysis, particularly the condensation of silanes binding to the glass surface, and each other, to form self-assembled monolayers, as discussed in Section 1.2.7.

The original protocol in this study for functionalisation of silica surfaces included n-butylamine to catalyse the silanisation reaction. Therefore, a range of primary amines with increasing numbers of free amino groups were screened, as shown in Table 2.4. The rationale behind this approach was that polyamines, with their multiple amino groups, could enhance the stability of transition states during the hydrolysis step by utilising the chelate effect.

The results showed low contact angles for all of the tested amines apart from 1,2-diaminoethane. No clear trend was seen for the number of amino groups and the effect on monolayer coverage. Therefore, acid catalysis was investigated.

Various Lewis acids were added to the deposition solution and the contact angle results are shown in Table 2.5. It was hypothesized that Lewis acids can activate the alkoxy groups of the trialkoxysilanes rendering the silicon centre electrophilic and causing it to be susceptible towards nucleophilic attack of hydroxyl groups present on the silica surface or water molecules present in the solution.

The results for the Lewis acid additives showed improved contact angles, particularly for the added titanium isopropoxide ($Ti(OiPr)_4$, boron trifluoride etherate ($BF_3 \cdot OEt_2$) and bismuth tris(trifluoromethanesulfonate) ($Bi(OTf)_3$). It was observed that the addition of water into the deposition solution improved the quality

Base (1 mM)	Average Contact Angle (°)	Error (± °)
n-butylamine	59.9	1.8
1,2-diaminoethane	101.8	6.4
Tris(2-aminoethylamine)	81.2	7.4
Diethylene triamine	89.0	1.4
Triethylene tetramine	92.6	1.8
Tetraethylene pentamine	80.5	15.5
Dimethylbenzyl amine	74.1	5.5
Triethylamine	81.8	2.3

Table 2.4: Average contact angles and associated errors for various 1 mM bases.

Lewis Acid (1 mM)	Variations	Average Contact Angle (°)	Error (± °)
$Ti(O\mathit{i}Pr)_4$	-	98.1	5.8
$Ti(O\mathit{i}Pr)_4$	No H_2O	95.2	0.8
$BF_3.OEt_2$	-	98.9	1.7
$BF_3.OEt_2$	No H_2O	94.8	0.6
$B(C_6F_5)_3$	(0.5 mM)	89.0	1.4
$Fe_2(SO_4)_3$	-	45.1	30.0
$Sc(OTf)_3$	-	54.9	4.4
$Bi(OTf)_3$	-	99.3	0.5

Table 2.5: Average contact angles and associated errors for various Lewis acids and their variations in water addition and concentration.

of the monolayers as can be seen in Table 2.5 for $Ti(OiPr)_4$ and $BF_3 \cdot OEt_2$. However, these contact angles were still lower than expected for n-octyltrimethoxysilane monolayers based on the literature and previous results [76].

Several Brønsted acids were added to the n-octyltrimethoxysilane deposition solution to investigate their effect on the reproducibility of monolayer formation. The results are outlined in Table 2.6. Hydrochloric acid (HCl) was tested due to reports suggesting its positive effect on the hydrolysis rate of alkoxysilanes [205]. However, the results obtained for added HCl suggested otherwise. The contact angles were substantially lower than other added catalysts, ranging between approximately 30 and 40°. The low contact angles indicate poor surface coverage, which may result from HCl inducing uncontrolled polymerization and the adhesion of aggregates to the silica surface, leading to the observed low contact angles.

A range of organic acids were employed to investigate their impact on surface functionalisation. These acids being: methanesulfonic acid (1 mM), acetic acid (1 mM), citric acid (1 mM), glutaric acid (1 mM), trifluoroacetic acid (1 mM) and ethylenediaminetetraacetic acid (EDTA) (1 mM). The results showed that the addition of these acids increased the contact angles from approximately 80°, achieved when using base catalysis, to contact angles above 100°. In particular, methanesulfonic acid gave consistently high contact angles of 107°. Further tests were performed to confirm the reproducibility of the monolayer formation using methane sulfonic acid as the catalyst and the contact angles were consistent. This optimisation study was carried out using purely n-octyltrimethoxysilane, therefore it was imperative

Acid (1 mM)	Variations	Average Contact Angle (°)	Error (± °)
HCl	5 µM	40.0	0.7
HCl	10 µM	39.0	0.1
HCl	Pre-hydrolysis	33.0	2.8
Acetic Acid	-	106.1	3.8
Glutaric Acid	-	101.1	0.2
Citric Acid	-	99.3	-
EDTA	-	50.2	-
Trifluoroacetic acid	-	102.6	1.7
Methansulfonic acid	-	107.0	0.4
Methansulfonic acid	n-octyltriethoxisilane	108.8	0.8

Table 2.6: Average contact angles and associated errors for various acids, with some including variations of concentration, methodology and silane precursor.

that different alkoxysilanes were tested with methane sulfonic acid as the catalyst. It has been reported that longer chain alkoxy groups tend to react slower with the surface hydroxyl groups, compared to shorter chain alkoxy groups [206]. Nevertheless, an experiment using n-octyltriethoxysilane gave a comparable contact angle to n-octyltrimethoxysilane monolayers in the presence of methanesulfonic acid, showing the generality of our optimised reaction conditions.

The addition of methanesulfonic acid to the deposition solution needed to be tested for the sensor surfaces to ensure no damage was caused to the sensor, particularly the Si-JNT surfaces which contain metal pads (Au and Ni). The concentration of acid used (0.1 mM) was unfortunately too high and did cause degradation of the metal pads. Therefore, the concentration of methanesulfonic acid was lowered, as shown in Table 2.7. It appeared that 0.05 mM of methanesulfonic acid in toluene was the maximum concentration which showed no effect on the metal pads. As a result, this was the concentration used for the functionalisation of sensor surfaces.

Precursor	Metal Pad	$MeSO_3H$ (X mM)	CA (°)	Metal Pad Status
Trimethoxy(7-octen-1-yl)silane	Ni/Au	1 mM	-	removed
Trimethoxy(7-octen-1-yl)silane	Ni/Au	1 mM	96	removed
Trimethoxy(7-octen-1-yl)silane	Ni/Au	0.1 mM	96	removed
Trimethoxy(7-octen-1-yl)silane	Ni/Au	0.05 mM	97	not removed
Trimethoxy(7-octen-1-yl)silane	Ni/Au	0.001 mM	94	not removed
n-octyltrimethoxysilane	Ni	0.05 mM	104.5	not removed
n-octyltrimethoxysilane	Au	0.05 mM	98.06	not removed

Table 2.7: Comparison of contact angle (CA) and metal pad status for different alkoxysilane precursors and concentrations of methanesulfonic acid.

The optimised protocol, using either the addition of water or the addition of methanesulfonic acid to the deposition solution, has been embedded into experiments involving monolayers (on glass slides or silicon wafers) and radical reactions to ensure reproducibility and reliability of results. However, it was observed for the functionalisation of SiO_2 nanoparticles, that the addition of water or methanesulfonic acid to improve the quality of the SAMs did not make a significant difference. Therefore, the deposition solution consisted of purely dry toluene for the functionalisation of SiO_2 nanoparticles.

2.2.4 Mixed Monolayers

Mixed SAMs have been used in this study to incorporate radical initiator chains alongside other organic chains on SiO_2 nanoparticles. Experiments involving mixed monolayers will be discussed further in Chapter 3.

Ketone and organic chain mixed SAMs were prepared by the solution deposition method by including a 1:1 ratio of the alkoxysilane derivatives. The preparation of mixed SAMs was therefore similar to the preparation of SAMs described in the previous section. A variation being the addition of a 1:1 molar solution of both alkoxysilane molecules to the vial containing the deposition solution and the silica surface, as shown in Figure 2.3.

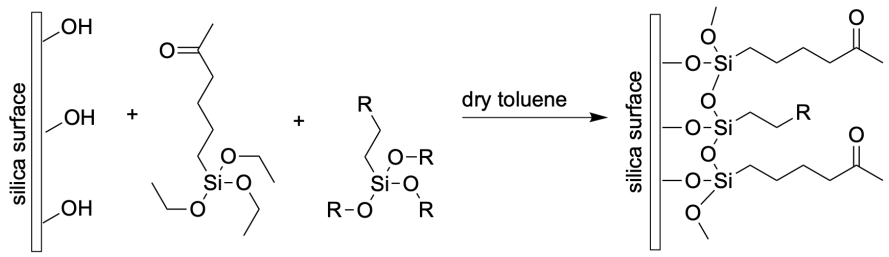

Figure 2.3: Reaction scheme for the functionalisation of mixed monolayers containing ketone chains and another organic chain.

2.3 Characterisation of SAMs

To thoroughly assess the quality of SAMs formed on functionalised silica surfaces (glass slides, silicon wafers and SiO_2 nanoparticles), it was essential to employ a variety of analytical techniques, ensuring comprehensive and reliable characterisation. Moreover, quantitative and qualitative analysis was crucial for studying the radical reactivity of the SAMs and thus, characterisation techniques needed to be evaluated for this role. These characterisation techniques include: contact angle analysis, XPS, ATR-FTIR, solid-state NMR, ellipsometry, Thermal Gravimetric Analysis (TGA), and AFM.

2.3.1 Thickness, Coverage and Surface Roughness

Physical properties of the SAMs such as thickness, density and surface roughness were essential for providing confirmation of the quality of monolayers formed. The characterisation techniques used in this study to analyse these properties include: ellipsometry (functionalised silicon wafers), TGA (functionalised SiO_2 nanoparticles) and AFM (functionalised glass slides).

2.3.1.1 Ellipsometry

Ellipsometry was conducted at Helmholtz-Zentrum Dresden-Rossendorf, Dresden, Germany. It was utilised to provide information for the thickness of the monolayer and to confirm no multilayer formation had occurred. Silicon wafer samples were functionalised with alkoxysilanes with 2 different chain lengths, C8AlkOMe and

C18AlkOMe. These molecules were used as comparisons to assess how the chain length affected the thickness of the monolayer and to evaluate the sensitivity of ellipsometry for the SAMs on silica surfaces. Table 2.8 shows the thickness of each monolayer. The thickness of a plasma cleaned silicon wafer surface was used as the base value for the functionalised silicon wafers, which was subtracted from each measurement.

Monolayer	**Monolayer Thickness (nm)**
C8Alk	0.48
C18Alk	1.11

Table 2.8: Monolayer thickness and associated errors for alkane SAMs and plasma-cleaned surfaces.

In the literature, ellipsometric thicknesses have been measured for a range of methyl terminated alkylsiloxane monolayers prepared by the adsorption of n-alklytrichlorosilanes, $CH_3(CH_2)_nSiCl_3$, onto SiO_2 substrates. The values obtained for an 8 carbon length chain and 18 carbon length chain was 1.26 nm and 2.57 nm, respectively [12]. These values are much higher than the values obtained in this study, which is likely due to our monolayer coverage being approximately 50% lower than the highest monolayer coverage in the literature (5 molecules/nm^2)[207]. However, the results shown in Table 2.8, suggested that multilayer formation had not occurred, since the value for C8Alk was below the typical 8-length carbon chain alkylsiloxane monolayers. Moreover, there was significant difference in thickness for the 18 length carbon chain monolayers, where the thickness was approximately double that of the 8 carbon length monolayer chains. Note that the ellipsometry instrument used in this study gave large errors and was not suitable for accurate thickness measurements of different monolayers. However, it was sufficient to check for multilayer formation.

This characterisation technique proved that the monolayers formed under the solution deposition process used in this study are not prone to multilayer formation. This validation was crucial for ensuring the accuracy of monolayer formation.

2.3.1.2 Thermal Gravimetric Analysis

The functionalisation of SiO_2 nanoparticles with SAMs gave the advantage of attaching enough organic material to the surface to facilitate effective analysis using techniques such as TGA. TGA was used to determine the loading of organic material attached to the silica surfaces. This was essential information to evaluate the degree of monolayer coverage and hence, the packing density of the chains. The specific surface area of the SiO_2 nanoparticles (10-20 nm) used in this study, was obtained by Brunauer-Emmett-Teller (BET) measurements to be 216 m^2/g, shown in Appendix A1. The surface coverage is dependent on the surface area of the nanoparticles, thus BET provided the most accurate measurement. Figure 2.4 shows the weight loss graphs of several functionalised SiO_2 nanoparticles, including: C8Alk, C6One, C5Eth, C7DiEth, C8BrAlk, C8Perf and the corresponding mixed monolayers with C6One chains. Depending on the mass of the alkoxysilane chain, varying degrees of weight loss were observed. In each case, the prominent weight loss is observed in the

temperature region of ∼200-600°C, corresponding to the degradation of the surface-bound organic species. In the literature, it has been reported that the degradation of silane monolayers occurs through the cleavage of C-C and Si-C bonds, which have bond dissociation energies (BDE) of 331 and 306 kJ/mol^{-1}, respectively, and decomposition temperatures >250°C [208]. Thus, the weight loss value was calculated in the temperature region of 200-600°C.

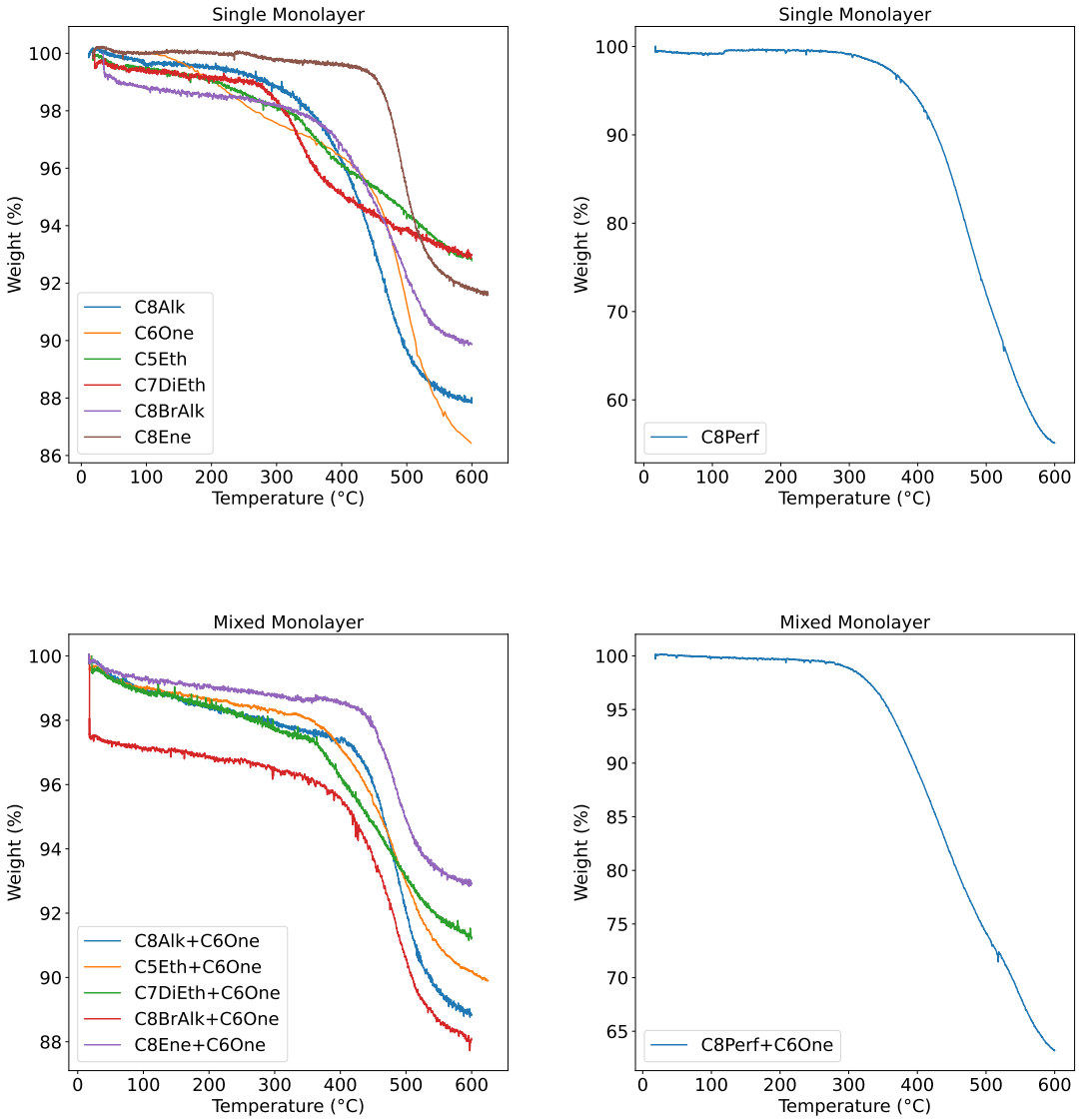

Figure 2.4: TGA plots for a selection of monolayers and mixed monolayers.

Table 2.9 shows the weight loss percentages for each of the functionalised SiO_2 nanoparticles with the corresponding monolayer coverage per nm^2. The monolayer coverage was calculated by equation 2.1

$$\text{Number of molecules per nm}^2 = \frac{W \cdot \rho_{SiO_2} \cdot V_{NP} \cdot N_A}{Mw \cdot (1 - W) \cdot SA_{NP}} \tag{2.1}$$

where W is the weight loss from TGA, ρ_{SiO_2} is the density of SiO_2 nanoparticles, V_{NP} is the volume of the SiO_2 nanoparticles, Mw is the molecular weight of attached

molecules, N_A is the Avogadro constant (6.022×10^{23}) and SA_{NP} is the surface area of the SiO_2 nanoparticles. The molecular weight for the mixed monolayer chains were taken as an average of the two alkoxysilanes present in the mixed monolayer. It should be noted that for the C8Perf and C6One mixed monolayers, the average molecular weight was calculated based on the ratio of C8Perf to C6One present on the surface. This will be discussed further in Section 2.3.3.

It has been reported that on a fully hydrated silica surface there are 5 OH groups per nm^2 [209]. The alkoxysilane molecules were deposited onto a fully hydrated surface, as detailed in Section 2.2.2. Therefore, the surface hydroxyl groups should bind to every alkoxysilane molecule. However, this can depend on several factors including alkyl chain length, shape and functionality of the alkoxysilane derivatives [207].

As shown in Table 2.9, the coverage of molecules on the silica nanoparticle surface varied with each alkoxysilane derivative. The alkoxysilane which produced the highest monolayer coverage was the C8Perf molecule. Perfluorinated alkoxysilanes are able to form more tightly packed monolayers due to the electronegative -C-F bonds, which form strong dipole-dipole interactions between adjacent chains, leading to more rigidity and a higher density of molecules to pack on the surface [210]. Typically, monolayer coverage on silica ranges between 2-4 molecules/nm^2 [38], which correlated well with the result for the alkane and ketone monolayers. However, lower surface coverage was seen for the ether-containing chains and the branched alkane. For the ether-containing alkoxysilanes, this could be due to the hydrophilicity of the ether group, increasing their interaction with water on the silica surface and preventing uniform monolayer formation. The branched molecule could have a lower coverage due to steric hindrance, inhibiting the packing efficiency.

Monolayer	**Weight Loss (%)**	**Coverage (molecules/nm^2)**
C8Alk	11.7	2.7
C6One	12.6	3.4
C5Eth	6.3	1.7
C7DiEth	6.2	1.2
C8BrAlk	8.6	1.7
C8Ene	8.4	1.7
C8Perf	44.4	5.4
C8Alk+C6One	9.6	2.1
C5Eth+C6One	8.7	2.4
C7DiEth+C6One	7.2	1.6
C8BrAlk+C6One	8.7	2.0
C8Ene+C6One	6.2	1.5
C8Perf+C6One	36.5	4.8

Table 2.9: Molecular coverage corresponding to the weight loss of various monolayers and mixed monolayers.

Overall, the coverage of the mixed monolayers was similar to the single monolayers, suggesting the intermolecular interactions between the different functional groups present in the molecules did not have a significant effect on the packing density of the monolayer.

TGA was an essential analytical technique for this study, providing information for the quality of SAMs formed on the silica surfaces. It was used as the control measure for each functionalised SiO_2 nanoparticle surface produced.

2.3.1.3 Atomic Force Microscopy

AFM was used to confirm whether phase separation occurred during the formation of mixed monolayers. Phase separation can occur in mixed monolayers, leading to the formation of nanoscale areas populated with different adsorbates [96]. This has been well documented for alkyl thiol monolayers; it can depend on the length of the alkyl chain, and the hydrogen bonding interactions of the terminal group [67]. Molecular dynamics simulations have shown phase separation for methyl-terminated thiols when the difference between the chain lengths is larger than approximately 7-10 methylene units [211]. However, kinetic studies have been reported for alkylsilanes on silica that the chain length does not affect the absorption efficiency and therefore, the monolayer was not expected to phase separate [96]. The silanes form siloxane bridges to the surface, reducing the mobility of the adsorbed silanes and making them less prone to phase separation [67]. For the application of mixed monolayers in this study, it was crucial that the mixed monolayers were forming a homogenous monolayer with the two alkoxysilanes distributed randomly. AFM has been used to determine the homogeneity of the functionalised silica surfaces. A selection of single monolayers and mixed monolayers have been tested by AFM. These monolayers were functionalised on silicon wafer samples rather than glass surfaces, as the roughness of glass substrates prevented accurate analysis of the monolayer.

The AFM image of a C8Alk monolayer functionalised silicon wafer is shown in Figure 2.5. The results obtained from the AFM analysis show the monolayer film is smooth and homogenous. The AFM results obtained for the mixed monolayers of C5Eth and C6One are shown in Figure 2.6. As it can be seen, there were no signs of island formation across the surface. The height of the mixed monolayer surface remained relatively constant.

Unfortunately, many silicon wafer samples used for the functionalisation of mixed monolayers for AFM analysis were damaged on the surface which caused defects to show on the AFM images, see Appendix A2. This damage was caused by repeated use of the same substrate, a common practice. Therefore, analysis of these images was more challenging.

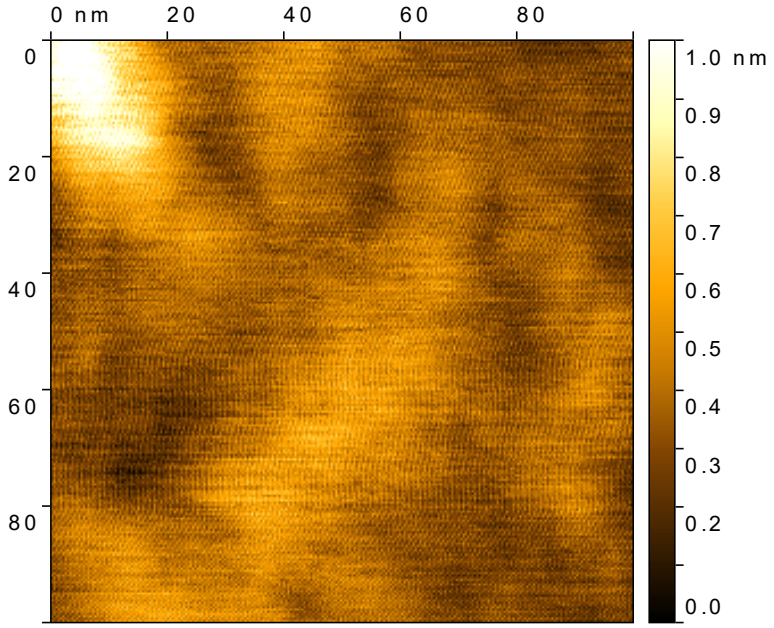

Figure 2.5: AFM image of a 100 x 100 nm area of a C8Alk monolayer functionalised silicon wafer.

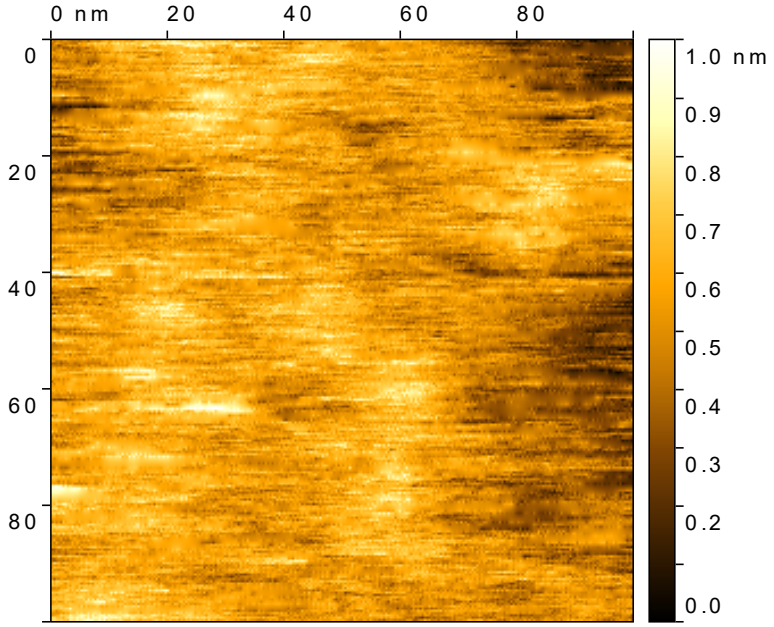

Figure 2.6: AFM image of a 100 x 100 nm area of a C5Eth and C6One mixed monolayer functionalised silicon wafer.

2.3.2 Structure and Functionality of Surface Molecules

Analysing the functionality of surface molecules was particularly important when using various alkoxysilane derivatives for silica surface functionalisation. Quantitative detection of functional groups, in the sense of confirming their measurable presence, enabled confirmation of successful functionalisation of a particular alkoxysilane derivative. Additionally, characterisation of surface functionality was imperative during experiments involving the exposure of organic molecules to oxidising radicals, which will be discussed further in Chapter 3 and 4. The characterisation techniques used in this study to analyse the functionality of the surface molecules include: contact angle analysis (functionalised glass slides), XPS (functionalised glass slides), ATR-FTIR (functionalised SiO_2 nanoparticles). Moreover, obtaining the molecular structure of the molecules attached to the silica surfaces was of great importance, particularly when conducting radical reactions within the monolayers. This section will introduce solid state ^{13}C NMR spectroscopy, which has been employed to determine the molecular structures of the molecules bound to the SiO_2 nanoparticle surfaces.

2.3.2.1 Contact Angle Analysis

Contact angle analysis has been used to analyse the hydrophobicity of the functionalised silica surfaces. Glass slide surfaces have been functionalised with a selection of organic molecules, their alkoxysilane derivatives are shown in Figure 2.1.

Depending on the functional groups present in the organic monolayer chains, varying degrees of hydrophobicity were observed. As shown in Table 2.10, increasing contact angles were measured for the more hydrophobic functionalised surfaces, such as the C8Perf monolayers. This is due to the water molecules being unable to interact with or hydrogen-bond to the fluorinated groups, resulting in the formation of spherical water droplets. The contact angle for perfluorinated monolayers often exceeds 110° [212]. The C8Alk and C8Ene monolayers gave contact angles > 90°, which agrees well with the literature [76, 213].

Molecule	Contact Angle (°)	Literature (°)	Reference
C8Alk	107 ± 2	106	[76]
C8Perf	117 ± 3	119	[212]
C6One	65 ± 2	-	-
C5Eth	70 ± 2	71	[214]
C8Ene	92 ± 2	95	[213]
C6Ph	75 ± 2	73	[215]

Table 2.10: Comparison of contact angles for different molecules with their corresponding literature values and references.

The C6One, C5Eth and C6Ph monolayer chains exhibit lower contact angles ranging from 65-75°. For the monolayers conatining C6Ph groups, the contact angle should be lower than respective C8Alk or C8Perf monolayers due to the hydrophilic nature of their phenyl ring [215]. The water molecules can have weak interactions through dipole-dipole interactions with the phenyl ring. The molecular packing in phenyl-containing monolayers may also be lower than straight alkyl chains which

could allow water to interact with the silica surface and lower the contact angle. The ketone and ether-containing monolayer chains are more hydrophilic, therefore able to interact and form hydrogen bonds with the water molecules, causing the contact angle to reduce [214].

The contact angles obtained for the various monolayers have all agreed well with the literature, as shown in Table 2.10. These results confirmed successful functionalisation of the different alkoxysilane derivatives. Contact angle analysis also proved to be effective for qualitative analysis of surface functional groups and could be used for further reactivity studies with SAMs on planar surfaces. This will be discussed further in Chapter 4.

2.3.2.2 X-ray Photoelectron Spectroscopy

XPS was conducted by HarwellXPS, a national EPSRC facility, University College London, London. Glass slides were functionalised with C8AlkOMe monolayers. One of the C8Alk functionalised samples was exposed to $He/H_2O/O_2$ plasma for 1 minute at a distance of 20 mm to partially oxidise the organic chains. A control sample of a freshly Piranha cleaned glass slide was also analysed. The XPS data of the samples prepared for analysis showed the presence of Si(2p), C(1s) and O(1s), as displayed in Table 2.11. There were no unexpected elements, meaning the surfaces were uncontaminated. Figure 2.7 displays the XPS spectrum of a C8Alk functionalised glass slide. The spectrum consists of sharp, narrow core-level photoelectron peaks (Si, C, O) and broad Auger peaks (C KLL and O KLL), confirming the presence of organic material on the glass slide surface.

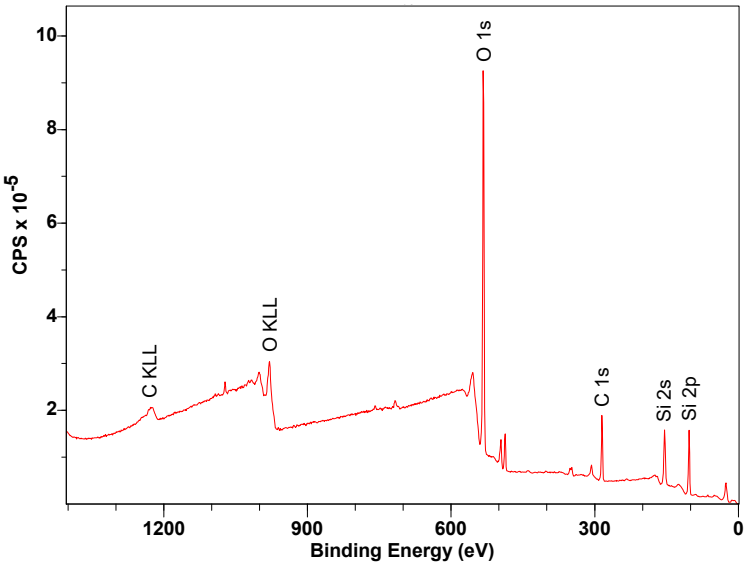

Figure 2.7: The XPS spectrum of a C8Alk functionalised glass slide.

A lower percentage of C(1s) at 8.9% was observed for the Piranha-cleaned glass slide, confirming the Piranha cleaning pre-treatment was effective for removing organic contaminants from the glass surfaces. The C(1s) detected on the Piranha-cleaned glass slide could be due to slight contamination during the transport to the HarwellXPS fascility. A similar C(1s), O(1s) and Si(2p) percentage was observed for the two C8Alk functionalised glass slides, despite one being exposed to plasma.

Sample	**C(1s) (%)**	**O(1s) (%)**	**Si(2p) (%)**
Piranha cleaned	8.9	59.2	32.0
C8Alk	21.0	50.0	29.0
C8Alk + plasma	20.4	50.9	28.7

Table 2.11: Surface chemical composition of different functionalised glass slide samples using XPS analysis.

The elemental composition of the C8Alk monolayers with and without plasma exposure, shown in Table 2.12, provided the functional groups present on the surfaces. The plasma exposed C8Alk monolayers had a slight increase in percentage of oxygenated functional groups: C-O (8.4%) and C=O (1.6%), compared to the unexposed C8Alk glass surface which had C-O (6.1%) and C=O (0%). This insinuates the oxidation of the monolayer upon oxidising radicals produced in the plasma. Moreover, the plasma exposed C8Alk monolayer had 3.8% less CC/CH constituents, suggesting the degradation of C-H bonds upon plasma exposure. Figure 2.8, displays the XPS spectra for the C8Alk chains with and without plasma exposure. The maximum peak at ∼285 eV in both spectra has been assigned to the CC/CH bonds in the alkyl chains. The peak at ∼287 eV was assigned to the C-O bonds, which have a slightly higher intensity in the plasma exposed C8Alk monolayer. The presence of C-O bonds in the non-exposed C8Alk monolayer could be due to contamination or oxidation of the samples during transportation to the facility. The peak at ∼288 eV was assigned to the C=O bonds, observed in the plasma exposed C8Alk monolayer.

Sample	**C-O (%)**	**C=O (%)**	**CC/CH (%)**
C8Alk	6.1	0	93.9
C8Alk + plasma	8.4	1.6	90.1

Table 2.12: Surface chemical composition of different functionalised glass slide samples using XPS analysis.

This technique provided additional evidence for the oxidation of the surface after Piranha cleaning and could be used as a qualitative and quantitative analytical technique for the monolayer surface. However, XPS was not an easily accessible technique. Thus, it could not be used regularly throughout the project.

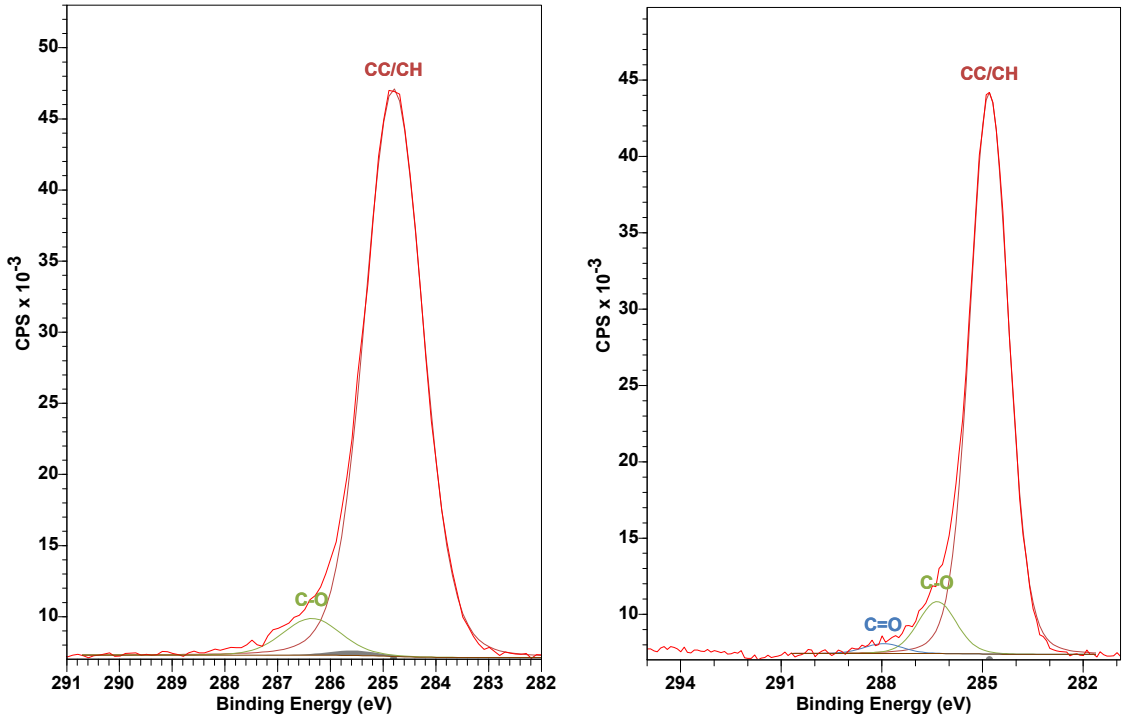

Figure 2.8: XPS spectra of C (1s) for a C8Alk functionalised glass slide (left) and a C8Alk functionalised glass slide which has been exposed to plasma for 1 minute (right).

2.3.2.3 ATR-FTIR

ATR-FTIR was used to further analyse the SAMs attached to the silica surfaces, providing qualitative information for the functional groups present within the monolayer chains. Due to the sensitivity limits of ATR-FTIR, functionalised SiO_2 nanoparticles were used instead of planar surfaces as the organic monolayer contributes a significant portion of the overall sample. SiO_2 nanoparticles were functionalised with a library of alkoxysilane molecules, including: C8AlkOMe, C8EneOEt, C6OneOEt, C5EthOEt, C8PerfOMe, and C8BrAlkOEt. Figure 2.9, displays the spectra for the functionalised SiO_2 nanoparticles. Several characteristic peaks are observed for the different SAMs. The 6 samples show absorption bands in the region between $\sim$ 2800-3000 cm^{-1}, corresponding to -C-H stretching. The most prominent -C-H stretching is observed for the C8Alk and C8BrAlk chains, where there is clear distinction between the $-CH_2-$ symmetric ($v_s(CH_2)$) and asymmetric ($v_{as}(CH_2)$) stretches at $\sim$ 2800 cm^{-1} and $\sim$ 2920 cm^{-1}, respectively, and the $-CH_3$ asymmetric ($v_{as}(CH_3)$) at $\sim$ 2960 cm^{-1}. The -C=O groups in the C6One monolayer gave rise to an additional absorption band at $\sim$ 1700 cm^{-1}, which agreed well with literature [216]. The C8Ene monolayer showed an absorption at $\sim$ 1640 cm^{-1}, corresponding to C=C stretching. This absorption wavenumber agreed well with the literature for 8-length carbon terminal alkene chains [174]. The lower intensity of the C=C band has been discussed in the literature to be indicative of a more highly ordered film. In well-ordered SAMs, the C=C stretch vibrations are mostly perpendicular to the substrate, an orientation to which ATR is not sensitive, therefore a reduced intensity is observed [174].

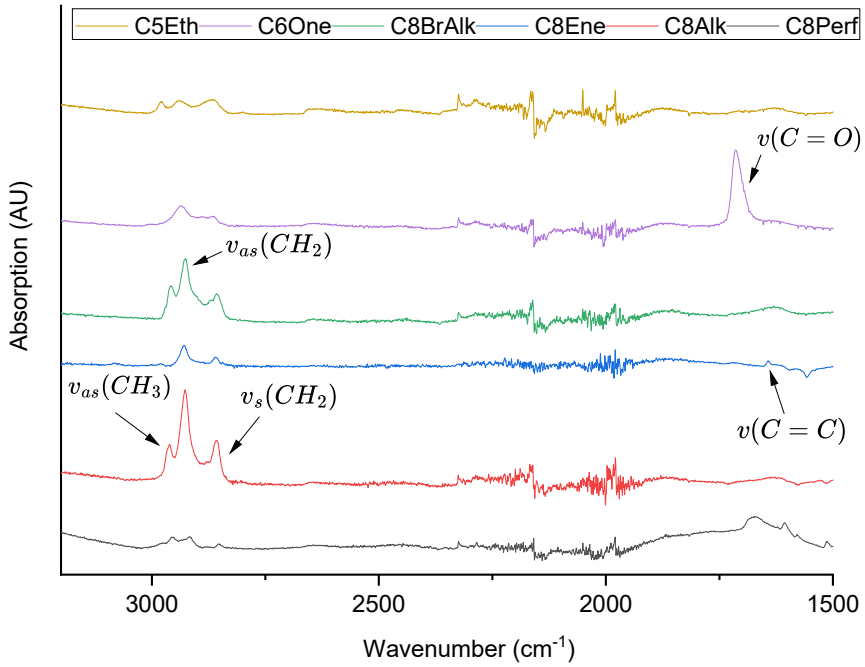

Figure 2.9: ATR-FTIR spectra of various functionalised SiO_2 nanoparticles.

Additionally, each of these individual alkoxysilane molecules were used to functionalise mixed monolayers with the C6One chains. The purpose of these mixed monolayers will be discussed further in Chapter 3. Figure 2.10 shows an ATR-FTIR spectra of three functionalised silica nanoparticles: pure C8Alk monolayer chains, pure C6One monolayer chains, and mixed monolayers of C8Alk and C6One chains. As shown, there are two prominent absorption bands in all three samples: at $\sim$ 1700 cm^{-1} and between $\sim$ 2800-3000 cm^{-1}. The absorption bands at $\sim$ 2800-3000 cm^{-1} are due to -C-H stretching. The -C=O groups in the C6One monolayers gave rise to an additional absorption band at $\sim$ 1700 cm^{-1}. This absorption band was specific to the C6One monolayers as no absorption was seen in this region for the pure alkane monolayers. Moreover, the intensity of these absorption bands correlated intuitively with the ratio of alkane to ketone chains within the monolayer. It was observed that the absorbance intensity of the -C=O groups in the pure ketone monolayer was greater than in the mixed monolayer. This trend was reflected in the -C-H stretching whereby the maximum intensity was seen for the full alkane monolayer compared to the mixed monolayer and the full ketone monolayer.

This charactisation technique proved to be useful for analysing mixed monolayers containing ketone functional groups, as it provided clear confirmation of successful mixed monolayer formation. However, the additional functional groups such as ether (-C-O-) and -C-F, present in C5Eth and C8Perf monolayers, could not be detected due to the absorption bands being in the fingerprint region, overlapping with the strong Si-O-Si absorption from the SiO_2 nanoparticle surfaces. This limited ATR-FTIR to the characterisation of only a few mixed monolayers. See Appendix A3 for more ATR-FTIR spectra of mixed monolayers.

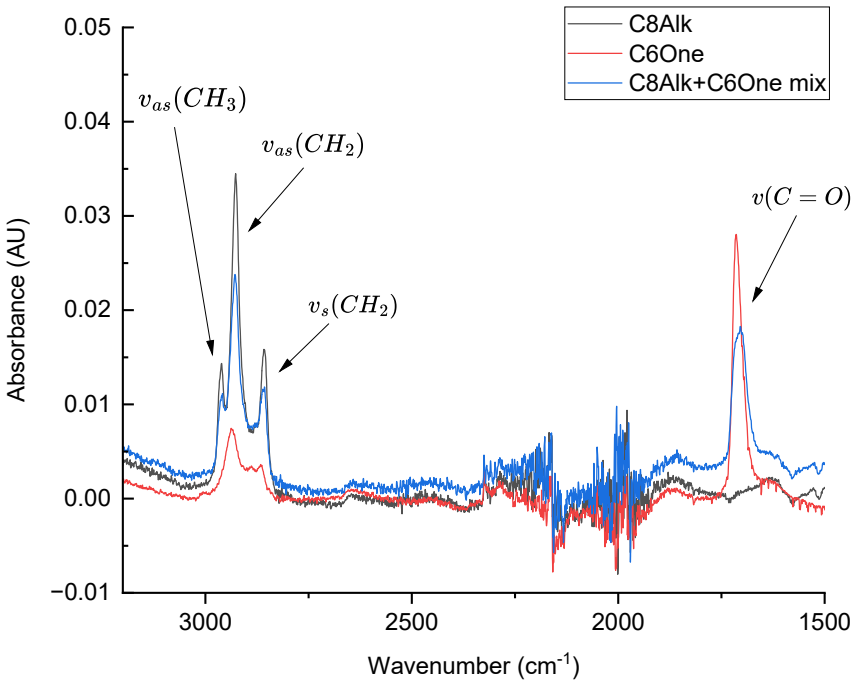

Figure 2.10: ATR-FTIR spectra of C8Alk, C6One and C8alk+C6One mixed monolayers on SiO_2 nanoparticles.

2.3.2.4 Solid State ^{13}C NMR Spectroscopy

Functionalised SiO_2 nanoparticles used in this study, including both full and mixed monolayers, were characterised with solid state ^{13}C NMR spectroscopy. The spectra in Figure 2.11 shows an array of full monolayers: C8Ene SAMs, C6One SAMs, C8Perf SAMs, C7DiEth SAMs, C5Eth SAMs, C8BrAlk SAMs and C8Alk SAMs. Each spectrum displays ^{13}C resonances typical of sp^3 CH_3 and CH_2 carbons in the range of 20-45 ppm, which are additionally displayed in Table 2.13. There is evidence of C-Si bonds in all presented spectra due to the resonance between 0-20 ppm, confirming the attachment of the alkoxysilane molecules to the silica surface. Carbon atoms which are chemically bonded to Si have increased shielding due to electron donation from the less electronegative Si atom. The differences between the spectra arose because a few of the molecules contained heteroatoms such as oxygen and fluorine. The C7DiEth and C5Eth SAMs (Figures 2.11(c) and 2.11(d)) form ^{13}C resonances between 60-75 ppm due to the carbon atoms adjacent to the oxygen in the ether bonds. This was also evident with the C6One SAMs (Figure 2.11(a)), whereby higher resonance was observed for the carbon atom adjacent to the carbonyl group with a chemical shift of 43.28 ppm. The C=O bond had too low of a signal intensity to be observed. This is due to the quaternary carbon lacking nearby ^1H atoms to enhance the signal through cross-polarisation. The sp^2 CH and CH_2 present in the C8Ene chains give rise to resonances in the range of 100-150 ppm, shown in Figure 2.11(a). Figure 2.11(c) shows resonances between 110-120 ppm for the C8Perf chains. Fluorine is more electronegative than oxygen, causing its de-shielding effect to be stronger. Thus, higher resonance is observed for the

C-F_2 and CF_3 carbon atoms.

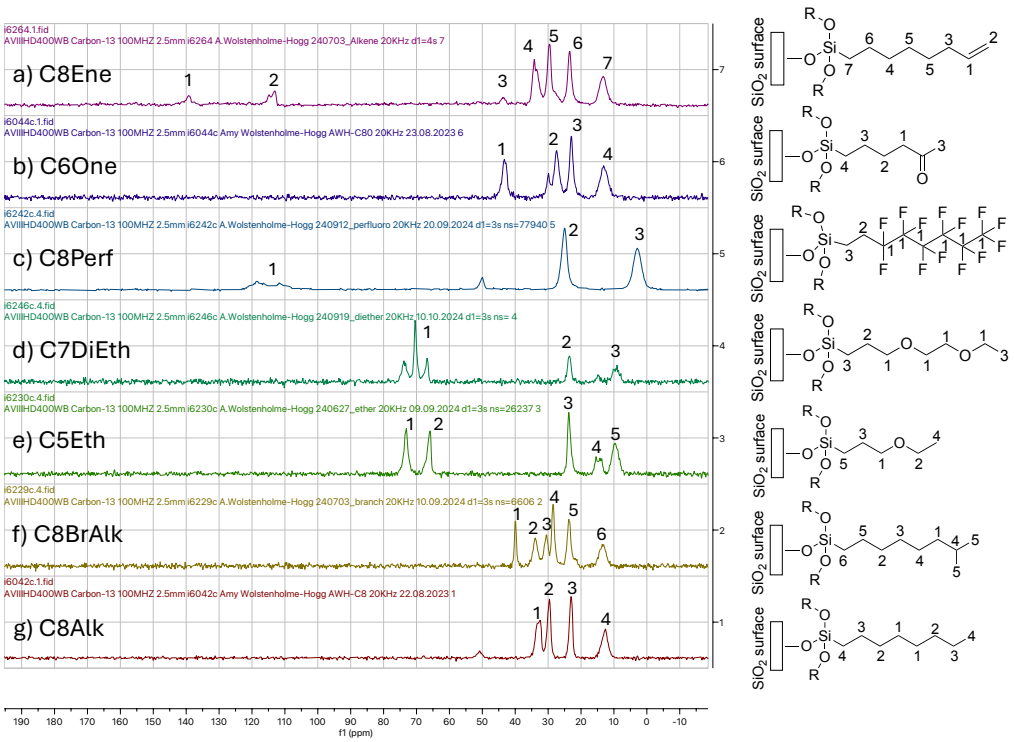

Figure 2.11: ^{13}C Solid State NMR spectra of a) C8Ene SAMs; b) C6One SAMs; c) C8Perf SAMs; d) C7DiEth SAMs; e) C5Eth SAMs; f) C8BrAlk SAMs; and g) C8Alk SAMs on SiO_2 nanoparticle surfaces.

Table 2.13: Chemical shift (δ) values (ppm) for different carbon sites shown in Figure 2.11.

Carbon Sites	**1**	**2**	**3**	**4**	**5**	**6**	**7**
a) C8Ene	139.10	112.81	43.71	34.04	29.35	23.34	13.20
b) C6One	43.28	27.41	22.96	13.05	–	–	–
c) C8Perf	117.7	25.06	2.9	–	–	–	–
d) C7DiEth	70.39	23.59	–	–	–	–	–
e) C5Eth	73.18	66.09	23.7	15.39	9.6	–	–
f) C8BrAlk	39.93	33.92	30.6	28.52	23.66	13.41	–
g) C8Alk	32.78	29.7	23.05	12.75	–	–	–

Solid state ^{13}C NMR could be used to characterise the mixed monolayers, as shown in Figure 2.12. The spectra displays mixed C8Alk and C6One SAMs compared to full C6One SAMs. It was evident from Figure 2.12(b) that C6One chains were present in the C8Alk and C6One mixed monolayers due to the resonance at $\sim$ 43 ppm. The ratio of C6One chains to C8Alk chains could be interpreted by the integrals of the peaks. It could be assumed that the Si-CH_2 peak in all compounds would give the same intensity. Thus, the ratio could be determined by comparing the peak at $\sim$ 43 ppm, characteristic to C6One chains only, with the Si-CH_2 peak

at ∼ 13 ppm, shown in Figure 2.12. The ratio of C6One chains to various other organic chains within mixed monolayers is displayed in Table 2.14. For each mixed monolayer, the ratio of C6One chains to total monolayer chains is approximately 1:1. The exception is the C8Perf and C6One mixed monolayers which exhibit a higher ratio of C6One chains to C8Perf chains. This could be due to the presence of fluorine in the C8Perf monolayer chains, causing weakening of signals and thus, a greater intensity was observed for the C6One Si-CH_2 groups. The main method for composition analysis was via dissociation of the molecules from the surface, which is discussed in Section 2.3.3.

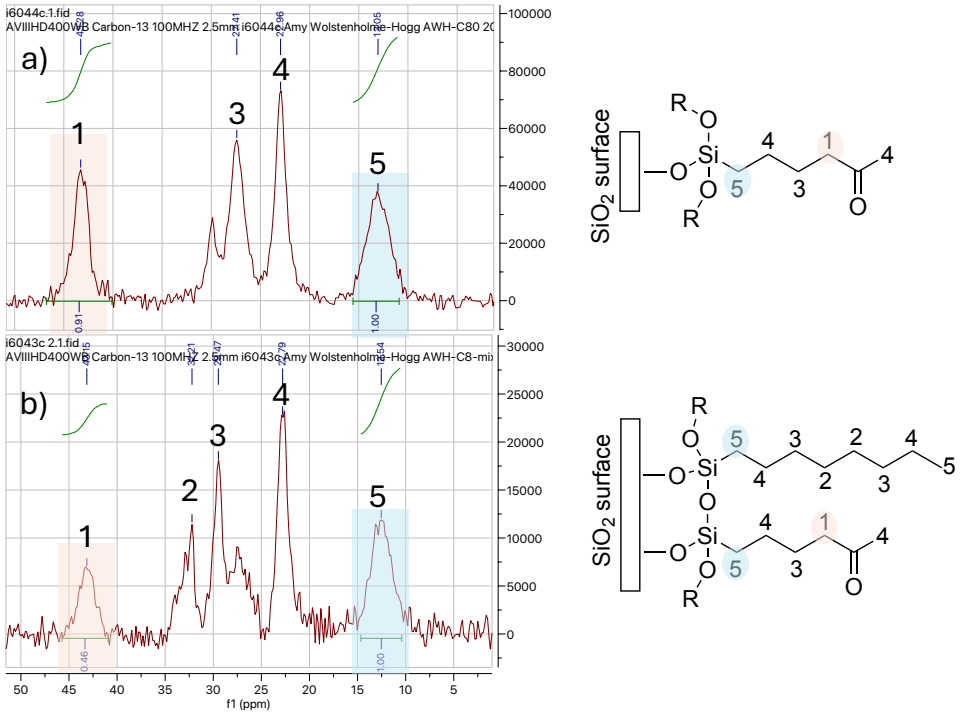

Figure 2.12: ^{13}C Solid State NMR spectra of a) C6One SAMs; and b) C8Alk mixed SAMs on SiO_2 nanoparticle surfaces.

Mixed Monolayer	C6One	Total Si-C
C8Alk mix	0.46	1.00
C8Ene mix	0.50	1.00
C8BrAlk mix	0.52	1.00
C5Eth mix	0.55	1.00
C8Perf mix	0.80	1.00

Table 2.14: Ratio of C6One chains to the other organic chain within the mixed monolayer on SiO_2 nanoparticle surfaces.

Solid state ^{13}C NMR can confirm the presence of functional groups and the structure of the surface-attached molecules. Moreover, it can provide evidence of the C-Si linkage and the ratio of two different organic molecules within a mixed monolayer. Unfortunately, this technique was not available to use frequently throughout the

study. Therefore, samples were prioritised purely for characterisation of the unreacted SAMs on SiO_2 nanoparticles. Additional solid state ^{13}C NMR spectra of mixed monolayers are available in the Appendix A4.

2.3.3 Oxidative Cleavage of Molecules Attached to Silica Surfaces

In the previous sections, characterisation of functionalised silica surfaces has been discussed using a variety of analytical techniques. A significant limitation of most of the characterisation techniques used in this study is that they primarily provide analysis of the functional groups, rather than offering detailed insights into the actual molecular structures. Methods such as solid state NMR, which could provide molecular structure analysis, were too expensive and slow to use frequently. Additionally, an analytical method was required to quantify the surface-bound molecules to enable in-depth characterisation of the SAMs after reactivity with radicals. This would provide a deeper understanding of the rates of radical reactions within the SAMs and therefore, the degree of spreading of radical reactions throughout the monolayers.

Alternatively, organic molecules can be characterised by dissociating the molecules from the solid substrates. The monolayer molecules are then in solution phase and can be studied using conventional analytical techniques. This approach has been used for organic Au-thiol monolayers, which can be readily dissociated from the Au surface as disulfides by treatment with an oxidising agent in the presence of a suitable ligand, such as O_2+CN^- or I_2+I_3^- [217]. However, dissociation of organosilane monolayers from SiO_2 surfaces is more challenging. The Si-C bonds are relatively resistant to oxidative cleavage, however, in 1982 Tamao *et al.* proposed a method for the oxidation of unactivated alkyl groups via the interaction of the oxidising agent with the Si center [195]. Fleming-Tamao oxidation is typically performed using hydrogen peroxide as the oxidant and a fluoride source (such as TBAF or KF) in methanol or THF at room temperature to 50°C, to convert organosilanes into alcohols. It was hypothesised that the C-Si bond in organosilane monolayers could be cleaved under the Fleming-Tamao oxidation conditions, which would remove the surface-attached molecule to give an alcohol as a dissociated product. This alcohol can then be isolated in pure form and characterised by ^1H NMR and GC-MS [195]. This methodology was initially optimised by Naeem Iqbal, another member of our research group, to provide a protocol which could operate at room temperature under mild conditions and be applicable to a broad range of substrates [218]. The protocol was further applied in this project for the analysis of mixed monolayer systems upon radical exposure and the quantification of organic molecules bound to planar surfaces. This approach of chemical cleavage of monolayer chains was a more attractive method than the alternative *in situ* characterisation techniques, as it could give more detailed and accurate structural information while being quantitative. Figure 2.13 shows the reaction scheme for the oxidative cleavage of the C-Si bond to yield an alcohol of the corresponding monolayer chain.

The product could be divided into two for each analytical technique, ^1H NMR and GC-MS. For the ^1H NMR sample preparation, the alcohol was concentrated under vacuum, added to a solution of dimethyl terepthalate (internal standard) in $CDCl_3$ and immediately processed.

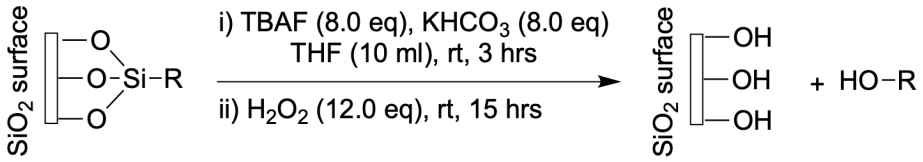

Figure 2.13: Reaction scheme for the oxidative cleavage of the C-Si bond to produce an alcohol.

The sample preparation for GC-MS involved further steps. To improve the chromatographic separation of the alcohol molecules from the other reaction components, it was essential to derivatise the -OH group via silylation, as shown in Figure 2.14. The reagent N,O-bis(trimethylsilyl)trifluoroacetamide (BSTFA) was used as a trimethylsilyl (TMS) donor, which was added to the alcohol product, along with pyridine base, and the reaction mixture was incubated at 100°C for 30 minutes. Silylation decreases the polarity of the alcohol and thus improves its volatility, leading to less tailing of the peaks and a lower limit of detection. It was important to remove water, fluorides and/or salts from the dissociation mixture prior to silylation as these species can readily react with the silylating agent, interfering with the derivatisation of the alcohol and reducing the product yield. Thus, a filtration step was required to remove these species from the dissociation mixture.

The dissociation mixture was filtered through a silica and cotton wool plug with a diethyl ether/ethyl acetate (3:1) mixture. The filtrate was collected and evaporated to dryness. Tests were performed to ensure no loss of the alcohol was seen during the filtration step and that the silylation procedure reacted to completion. These tests were conducted by taking a ^{1}H NMR sample and quantifying the amount of octanol after each step: initial mock dissociation solution, filtration, and silylation. The overall GC-MS preparation procedure has shown to be within 10% error each time for C8Alk dissociated monolayers and the chromatograms to be clean. Each GC-MS sample contained 1.0 mg/ml of the internal standard (dimethyl terepthalate) and was processed immediately after sample preparation.

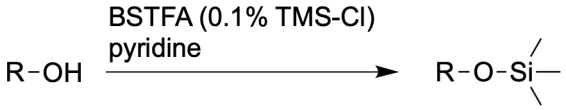

Figure 2.14: Reaction scheme for silylation of the alcohol product.

Quantification via ^{1}H NMR was achieved by the addition of an internal standard. The integrals of the key peaks were normalised to the integral of the internal standard. The quantity of internal standard was known (10 mg), therefore, the mass of each component could be obtained by comparison of their integral values. For GC-MS quantification, a calibration curve of derivatised authentic alcohols was produced to quantify the monolayer chain after dissociation (see Appendix A5). These alcohols included: octan-1-ol for the C8Alk chain, 3-ethoxy- propanol for the C5Eth chain, 1H,1H,2H,2H-perfluoro-1-octanol for the C8Perf chain, and oct-7-en-1-ol for the C8Ene chain. Some monolayer chains were not commercially available, such as triethoxy(7-methyloctyl)silane (C8BrAlk chain) and 9,9-diethoxy-2,5,10-trioxa-9-siladodecane (C7DiEth chain) as their alcohol equivalents; consequently, their quantification was determined exclusively through ^{1}H NMR rather than GC-MS.

The calibration was prepared using two batches of the derivatised alcohol, both of which were diluted from 0.1-1.0 mg/ml and to each sample the internal standard was added at 1.0 mg/ml concentration. Two batches were used to ensure any variation in the silylation procedure could be accounted for and the errors were therefore, reduced. To account for any instrumentation errors, the internal standard was added to each sample at the same concentration and the ratio of the derivatised alcohol to the internal standard was used to form the curve.

The yield of dissociated molecules from functionalised SiO_2 nanoparticles was determined based on the TGA weight loss data, seen in Section 2.3.1.2, which gave the amount of organic material bound to the silica surface. The yields of the mixed monolayers will be discussed further in Chapter 3, however, typical yields after the dissociation would range between 80-95% depending on the attached molecule. The error in the oxidative cleavage method was determined by repeat dissociations (5 times) of the same batch of C8Alk-C6One mixed monolayers. The error obtained for the yields was ±3.4% from the ^{1}H NMR analysis. The error obtained for the yield of C8Alk chains from the GC-MS analysis was ±2.8%. These errors were used for all reactivity studies to determine accurate yields after exposure to radicals.

The following sections will demonstrate examples of mixed monolayer dissociations from functionalised SiO_2 nanoparticles and the application of this method to planar surfaces.

2.3.3.1 C8Alk and C6One Mixed Monolayers

Figure 2.15, displays the ^{1}H NMR spectrum for the dissociation of mixed C8Alk and C6One monolayers. A distinct triplet peak can be observed at approximately 3.50 ppm, corresponding to the -CH_2 in the α-position to the alcohol group (H_{1a}, H_{1b}, H_{2a}, H_{2b}). The -CH_2 in the α-position to the carbonyl group on the C6One molecule could be used to distinguish the ratio of C6One to C8Alk in the mixed monolayer. As shown in the spectra in Figure 2.15, the C8Alk and C6One mixed monolayers have a 1:1 ratio of C6One to C8Alk molecules bound to the silica surface, indicated by the integral of the 3.50 ppm and 2.40 ppm shifts. The yields were calculated using an internal standard (dimethyl terepthalate) to be 85.9% for C8Alk chains and 87.5% for C6One chains.

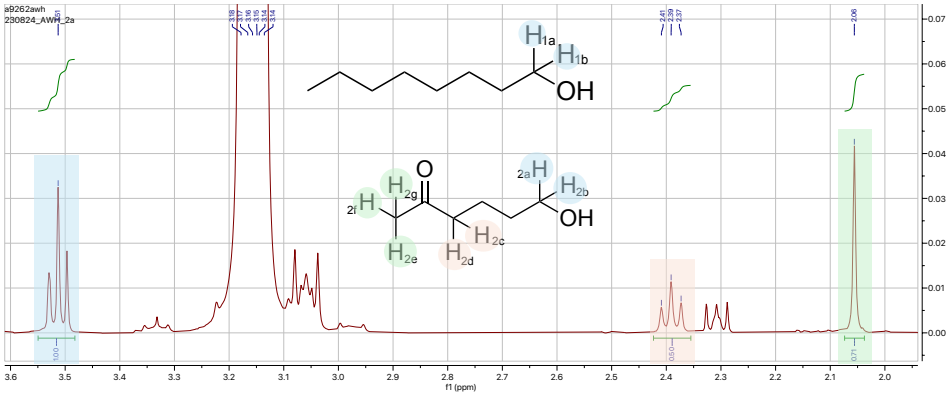

Figure 2.15: ^{1}H NMR spectrum of dissociated C8Alk and C6One mixed monolayers from functionalised SiO_2 nanoparticle surfaces.

As the -CH_2 adjacent to the alcohol group gives the peak at the same chemical

shift for both molecules, it was difficult to distinguish which of the two molecules had shown reactivity to the oxidising radicals, discussed in Chapter 3. For this reason, GC-MS was used to supplement ^{1}H NMR in these experiments.

Figure 2.16 shows the chromatogram for the dissociated mixed monolayer chains. The peak at 5.36 mins corresponds to the derivatised ketone-containing alcohol, the peak at 5.46 mins corresponds to the derivatised octanol (C8OTMS) and the peak at 7.30 mins corresponds to the internal standard, dimethyl terephthalate (IS). The peak at 5.54 mins is tributylamine, which is one of the main contaminants the filtering steps aid to reduce. The yield of C8Alk chains was calculated, using a calibration curve (see Appendix A5) to be 80.5%, which is within 10% error of the yield obtained by ^{1}H NMR.

The filtering step prior to the GC-MS sample preparation did cause variations with the dissociated C6One yield due to the higher polarity of this molecule and its affinity toward the silica gel. However, for the purpose of this study, the mass of C6One from the GC-MS was not essential. The main focus was on the quantity of the neighbouring chain after the radical reactions. Moreover, the ^{1}H NMR data for the C6One molecule provided sufficient quantification alone.

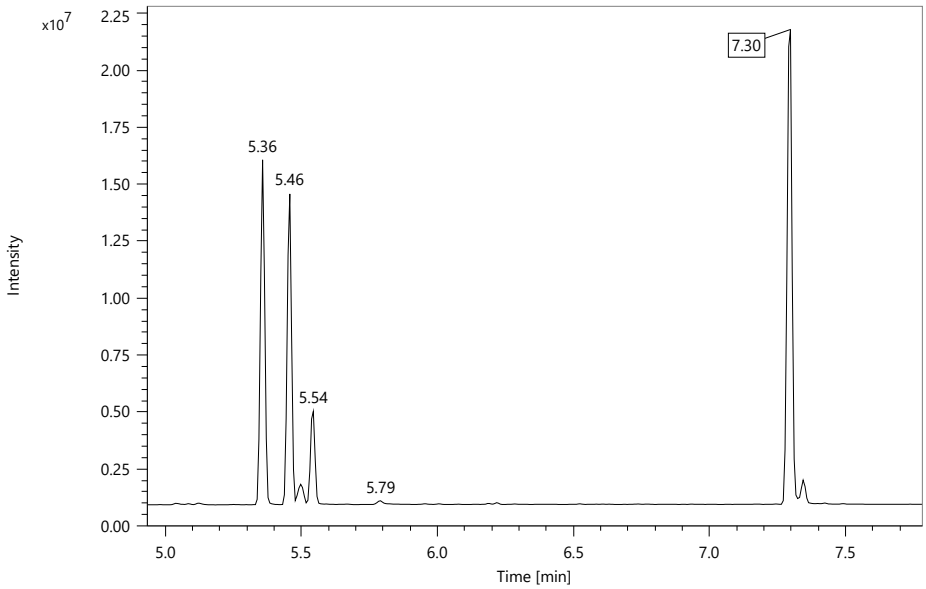

Figure 2.16: GC-MS chromatogram of dissociated C8Alk and C6One mixed monolayers from functionalised SiO_2 nanoparticle surfaces.

2.3.3.2 C5Eth and C6One Mixed Monolayers

For the C5Eth and C6One-based chains, the triplet peak at $\sim$ 3.50 ppm is also seen in the ^{1}H NMR spectrum, corresponding to the -CH_2 in the α-position to the alcohol group (H_{1a}, H_{1b}, H_{2a}, H_{2b}). The quartet peak at $\sim$ 3.40 ppm corresponds to the -CH_2 adjacent to the C5Eth group in the C5Eth molecule. This peak has an integral of 0.48 compared to the triplet peak at $\sim$ 3.50 ppm, confirming the ratio of C5Eth to C6One to be approximately 1:1. The yields obtained by ^{1}H NMR were 83.6% for C5Eth chains and 70.1% for C6One chains.

GC-MS analysis of C5Eth and C6One mixed monolayers was performed using the same protocol as for C8Alk and C6One mixed monolayers. Figure 2.18 shows

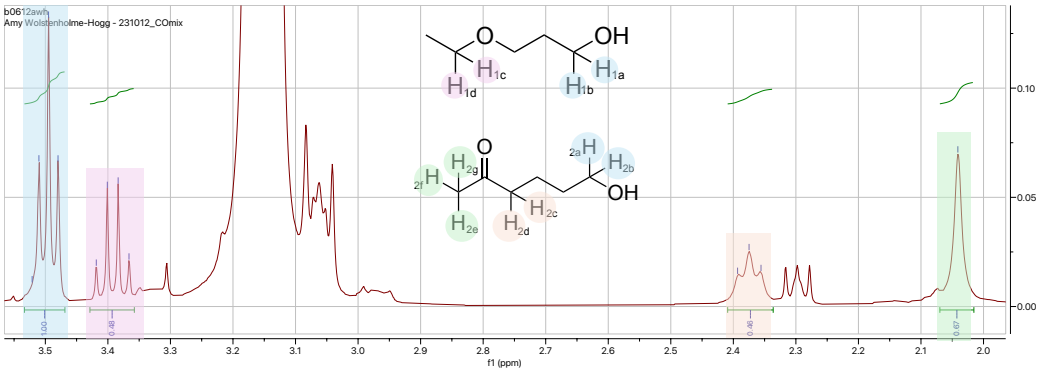

Figure 2.17: ^{1}H NMR spectrum of dissociated C5Eth and C6One mixed monolayers from SiO_2 nanoparticle surfaces.

the chromatogram for C5Eth and C6One dissociated chains after filtration and silylation. The peak at 3.90 mins corresponds to the derivatised C5Eth molecule, the peak at 5.38 mins corresponds to the derivatised C6One molecule and the peak at 7.32 mins corresponds to the internal standard, dimethyl terephthalate. The yield of C5Eth chains obtained by GC-MS was 81.8%, which was within 5% error of the yield obtained by ^{1}H NMR.

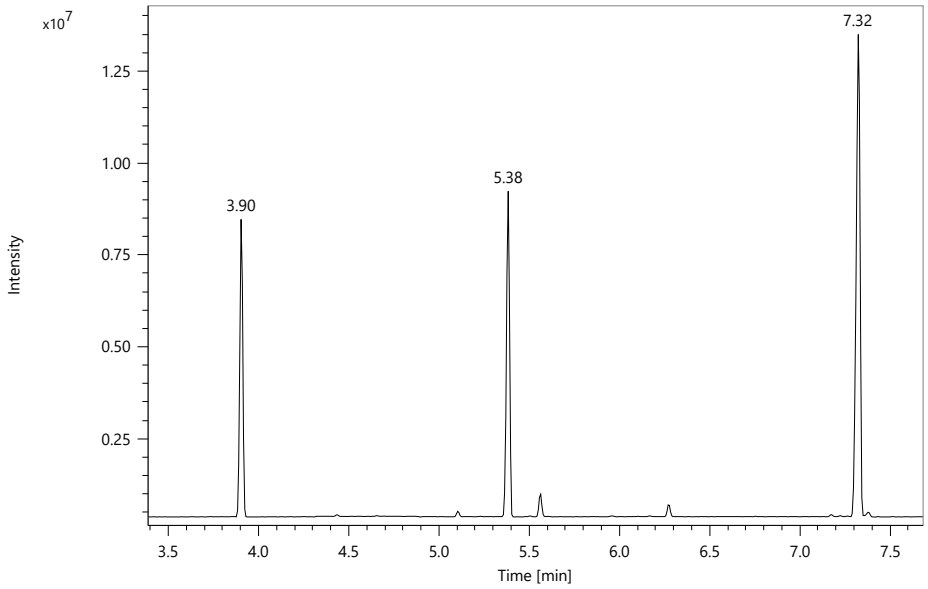

Figure 2.18: GC-MS chromatogram of dissociated C5Eth and C6One mixed monolayers from functionalised SiO_2 nanoparticle surfaces.

2.3.3.3 C8Perf and C6One Mixed Monolayers

Figure 2.19 displays the ^{1}H NMR spectrum for the dissociation of C6One and C8Perf monolayers. The ratio of the two molecules could be deducted from the peak at 3.75 ppm for the -CH_2 group next to the -CF_2 group on the C8Perf molecule and the peak at 3.44 ppm for the -CH_2 group in the α-position to the alcohol group on the C6One molecule. The ratio of C6One to C8Perf was much lower than previous mixed monolayer examples at approximately 3:8. This was likely due to the C8PerfOMe silane being more reactive than the C6OneOEt silane, dominating the

functionalisation of the silica surface. This ratio contradicted the measured ratio from the solid state ^{13}C NMR results in Table 2.14, however, this is likely due to the weakening of signals caused by the fluorine atoms in the solid state NMR.

The multiplet at $\sim$ 2.30 ppm is due to the -CH_2 groups (H_{1c} and H_{1d}) which are adjacent to the perfluorinated chain. The splitting of these signals arises due to the spin-spin coupling between the fluorine nuclei and the protons. This multiplet overlapped with the -CH_2 group adjacent to the carbonyl on the C6One molecule (H_{2c} and H_{2d}), hence the ratio of C6One to C8Perf was deducted from the peak at $\sim$ 3.50 ppm. The yields obtained from ^{1}H NMR were 91.4% for C8Perf chains and 97.8% for C6One chains.

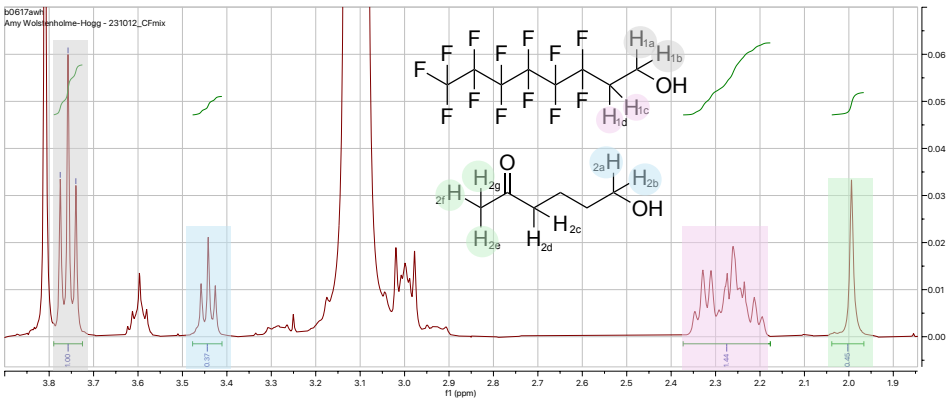

Figure 2.19: ^{1}H NMR spectrum of dissociated C8Perf and C6One mixed monolayers from functionalised SiO_2 nanoparticle surfaces.

The GC-MS chromatogram of dissociated C8Perf and C6One mixed monolayers is shown in Figure 2.20. The peak at 3.42 mins corresponds to the derivatised C8Perf molecule, the peak at 5.36 mins corresponds to the derivatised C6One molecule and the peak at 7.30 mins corresponds to the internal standard, dimethyl terephthalate. The yield of C8Perf chains obtained by GC-MS was calculated to be 94.8%, which is within 5% error of the yield obtained by ^{1}H NMR.

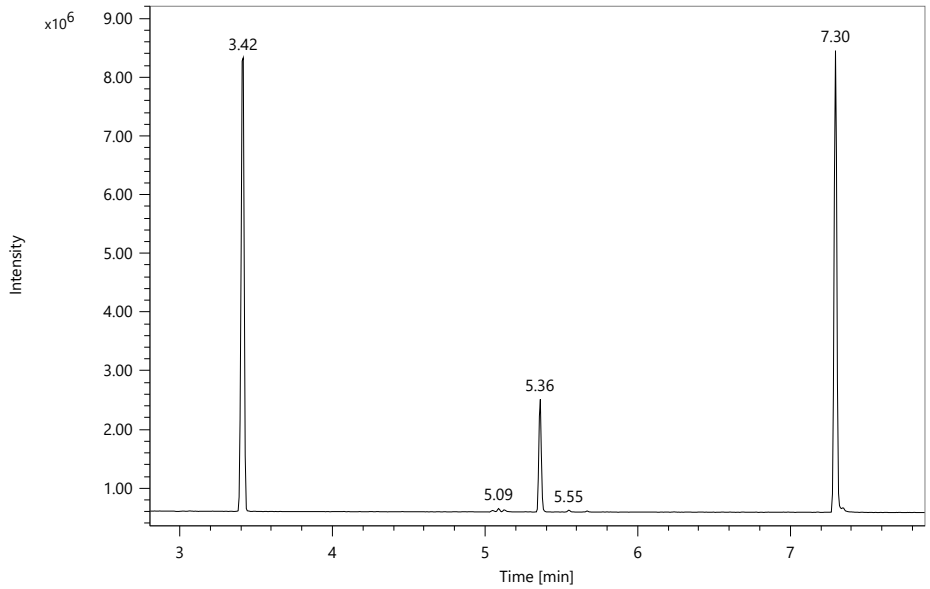

Figure 2.20: GC-MS chromatogram of dissociated C8Perf and C6One mixed monolayers from functionalised SiO_2 nanoparticle surfaces.

2.3.3.4 C8Ene and C6One Mixed Monolayers

Figure 2.21 shows the ^{1}H NMR spectrum for the dissociation of C6One and C8Ene mixed monolayers. There are a few characteristic peaks for the C8Ene molecule, including: the multiplet for the -CH adjacent to the C=C bond (H_{1c}) at ∼5.55 ppm; two doublets of doublets at ∼4.70 ppm for the terminal -CH_2 groups (H_{1d} and H_{1e}); and the triplet peak at ∼3.35 ppm for the -CH_2 adjacent to the OH group (H_{1a} and H_{1b}). The peaks for the C6One molecule are similar to previous spectra, whereby the triplet peak for the -CH_2 adjacent to the OH group appears at ∼3.35 ppm (H_{2a} and H_{2b}) and the triplet peak for the CH_2 adjacent to the carbonyl group appears at ∼2.25 ppm (H_{2c} and H_{2d}). The ratio of C8Ene to C6One in these mixed monolayers was approximately 1:1 due to the peak at ∼4.70 ppm and ∼2.25 ppm giving similar integral values. The yields obtained by ^{1}H NMR was 75.2% for C8Ene chains and 73.3% for C6One chains.

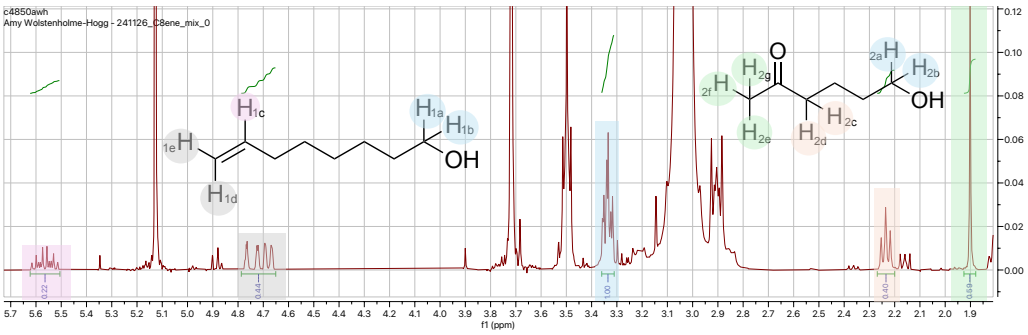

Figure 2.21: ^{1}H NMR spectrum of dissociated C8Ene and C6One mixed monolayers from functionalised SiO_2 nanoparticle surfaces.

Figure 2.22 displays the GC-MS chromatogram of the dissociated alkene and ketone mixed monolayers. The peak at 5.36 mins corresponds to the derivatised ketone molecule, the peak at 5.41 mins corresponds to the derivatised alkene molecule and

the peak at 7.29 mins corresponds to the internal standard. The yield obtained by GC-MS for C8Ene chains was 66.9%, which is within 10% error of the yield obtained by ^{1}H NMR.

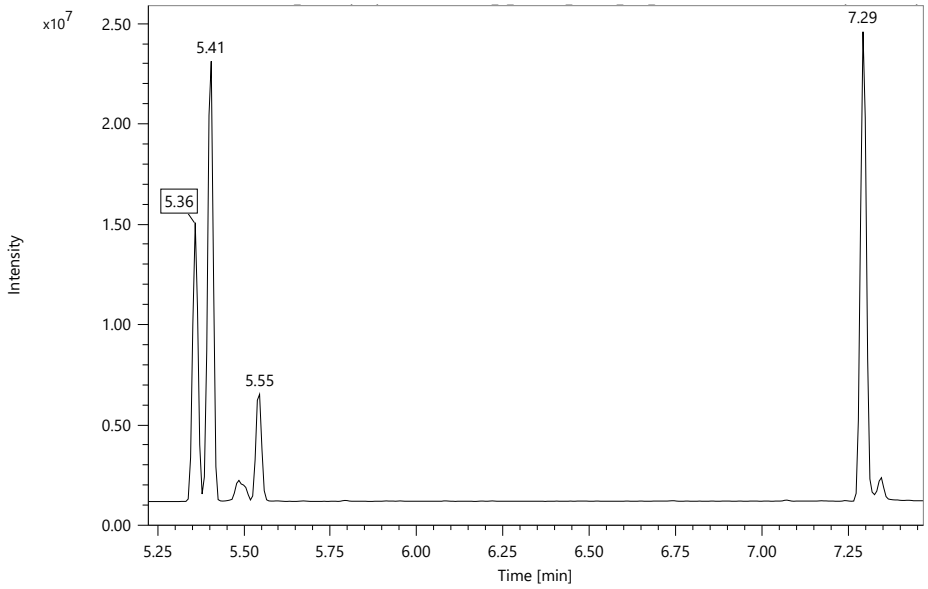

Figure 2.22: GC-MS chromatogram of dissociated alkene and ketone mixed monolayers from functionalised SiO_2 nanoparticle surfaces.

Additional ^{1}H NMR and GC-MS spectra of dissociated C8BrAlk-C6One mixed monolayers and C7DiEth-C6One mixed monolayers can be found in Appendix A6.

2.3.3.5 Application to Planar Substrates

A major application to surface functionalisation is in sensors [219, 220]. This often involves functionalisation of a planar substrate with an exceptionally small surface area, making both quantitative and qualitative analysis of these surfaces particularly challenging. In order to test the feasibility of detecting dissociated monolayers on a planar surface, a 9 cm diameter Petri dish was functionalised with C8AlkOMe. A glass Petri dish was used as it provided a larger surface area than typical microscopic glass slides and could be used as the container for the deposition solution and dissociation reaction mixture. The amount of organic material in a monolayer on a Petri dish is insufficient for NMR analysis, hence GC-MS was used for detection after monolayer dissociation. Figure 2.23, shows the extracted-ion chromatogram of the dissociated C8Alk chains from the surface of the functionalised petri dish. The peak at 5.50 mins corresponds to derivatised octan-1-ol. Quantification using a calibration curve built with derivatised authentic octan-1-ol (see Appendix A5) showed 10.4 μg of dissociated protected octan-1-ol which (assuming quantitative yield of dissociation) corresponds to surface coverage of 4 molecules/nm^2, close to the literature reports [38]. This method can thus be applied to qualitative and quantitative analysis of the monolayers on planar silica substrates. It can be estimated that this method with GC-MS analysis can be used to quantify a monolayer in a sample with ca. 60 cm^2 area (e.g., 1 mg of 500 nm nanoparticles with 12 m^2/g surface area or a 6×10 cm planar substrate).

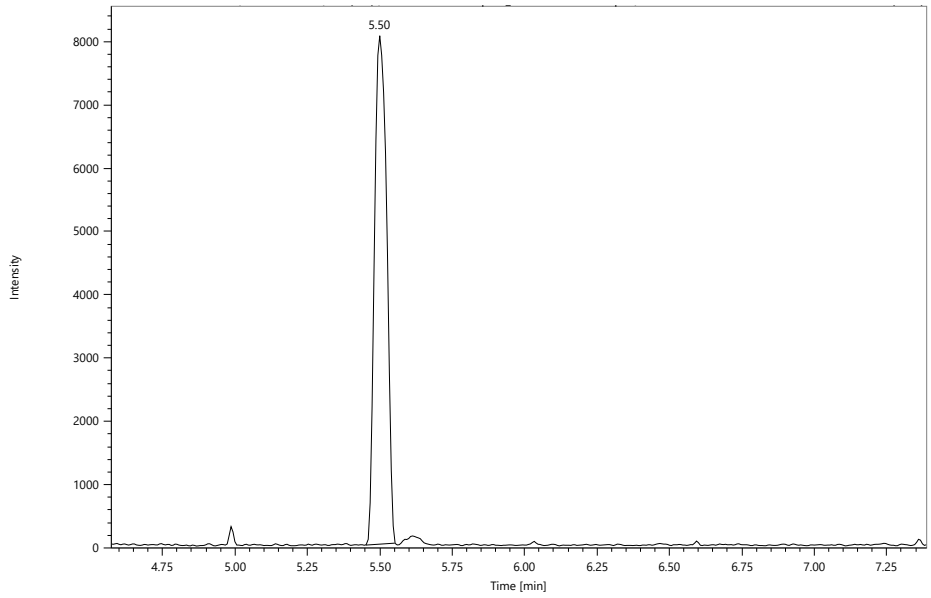

Figure 2.23: Extracted-ion chromatogram of dissociated C8Alk chains from the surface of glass (9 cm petri dish).

2.4 Conclusions

In conclusion, this study successfully established reliable methods for forming high-quality monolayers on silica surfaces, demonstrating good reproducibility. The combination of analytical techniques used provided comprehensive insights into the structural and functional properties of these monolayers. Contact angle measurements proved to be an effective and rapid technique for assessing monolayer quality on planar silica surfaces, while ATR-FTIR and solid-state ^{13}C NMR offered detailed information about the molecular composition and the presence of C-Si linkages. The quantitative analysis of TGA confirmed the binding of organic materials to silica, and AFM analysis provided key evidence of phase homogeneity, essential for future reactivity studies. Ellipsometry further confirmed the absence of multilayer formation, validating the optimised functionalisation process.

The development of an alternative oxidative cleavage method proved invaluable for both quantitative and qualitative analysis of the monolayer chains, particularly for mixed monolayers, providing a new tool for studying functionalised silica surfaces. This method has proved to be compatible with a range of silica substrates, including planar substrates, which is a valuable addition to the monolayer characterisation toolset applicable to a range of different applications.

Chapter 3

Autoxidation within Self-Assembled Monolayers

3.1 Introduction

Autoxidation is a complex process in which molecular oxygen and organic molecules react by a free-radical chain sequence, leading to the degradation of many organic systems [2]. This is a process that occurs in an abundance of systems in everyday life, be it the tropospheric degradation of hydrocarbons and other volatile organic compounds (VOCs), the combustion of fuels, the degradation of rubbers and polymers or the degradation of naturally occurring fats and oils [101, 102]. It has, thus, been well studied for a variety of contexts.

The key reaction pathways of autoxidation and ROO· radical chemistry were discussed in detail in Section 1.5.2, with a particular focus on gas-phase and bulk-phase processes. This chapter aims to focus on surface-bound systems, where the restricted mobility in monolayers may significantly alter the fate of reactive intermediates such as ROO· radicals.

The initial aim was to use computational methods to explore potential autoxidation pathways in monolayers and assess how molecular structure and radical mobility influence reaction outcomes. These insights were then used to guide the design of an experimental system, in which monolayers were subjected to radical initiation under controlled conditions to study degradation and propagation processes at the gas-surface interface.

Particular attention was given to how far radical reactivity can extend beyond the initially attacked molecule, and whether surface-bound ROO· radicals undergo termination, hydrogen abstraction, or alternative reactions. Figure 3.1 gives an overview of the basic autoxidation scheme and the influence which molecules containing activated C-H groups (i.e. ether or allylic chains) can have on the propagation of radical reactions [154]. Thus, a variety of organic molecule chains with different functionalities have been examined, specifically looking at the propagation of radical reactions to neighbouring chains. The rate of degradation following radical initiation was explored to assess how chain functionality within monolayer systems influences radical propagation.

The fate of the ROO· radical was studied by leveraging existing knowledge from gas-phase ROO· radical chemistry to determine whether similar mechanisms apply in monolayer systems. These findings will provide insight into the lifetime of radical

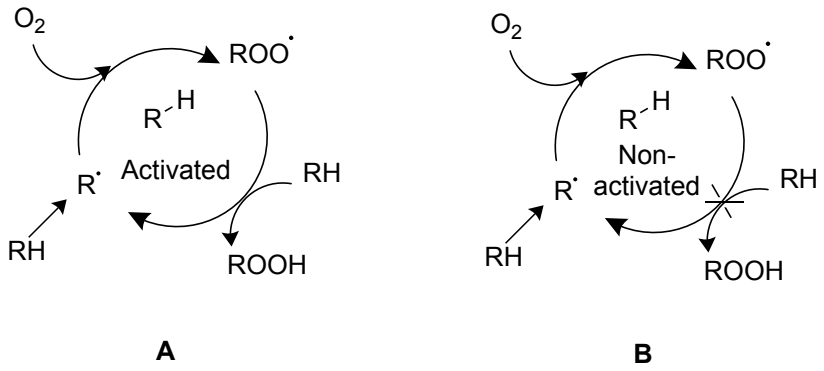

Figure 3.1: Basic autoxidation scheme for organic molecules with and without the presence of activated C-H bonds.

sensor surfaces, emphasizing how a single radical initiation can impact the molecules within the monolayer. Additionally, this study offers valuable insights into the autoxidation processes of various organic surface systems, with implications for the long-term stability of organic coatings, thin films, and sensor materials in ambient environments [7].

3.2 Computational Modelling of Autoxidation in SAMs

3.2.1 Kinetic Model

To gain a deeper understanding of the autoxidation processes in monolayer systems, a kinetic model was developed. This model was used to provide an illustrative and mechanistic understanding of the degradation of organic chains upon radical initiation. The kinetic model was designed using the Kintecus software [221]. Due to the lack of data for monolayer autoxidation, the rates of reactions used in this model have been taken from the literature on the autoxidation of alkane chains in bulk systems [123, 136, 137, 222]. The model is therefore 3-D and does not take into account the limited mobility of monolayer chains which are attached to a surface. The kinetic model could only be used to provide an approximation of the most dominant autoxidation reaction pathways which could take place within the alkyl chains but does not give an accurate representation of a monolayer system.

The kinetic model was used to simulate two different reaction sets: the first using dominant reactions for alkyl chains in bulk liquids (i.e. ROO· termination versus ROO· H-abstraction); and the second in the absence of molecular mobility, which includes dominant reactions in the gas-phase (i.e. ROO· + NO to form RO· + NO_2), as well as the exclusion of ROO· radical self-reaction. The reaction pathways for the first reaction set are displayed in Figure 3.2.

According to the research conducted for polymer systems, the outcome for primary or secondary centred ROO· radical bimolecular termination is the production of stable species, i.e. an alcohol and a carbonyl group [102]. A simple model was

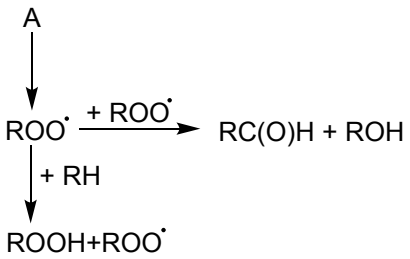

Figure 3.2: Radical reaction pathways for alkane chains in bulk systems.

generated using this information. The rate coefficients for these reactions are displayed in Table 3.1. The initiation rate of 5×10^{-5} s^{-1} was used to give a reasonable rate of degradation of the initial alkane chain (A), shown in Table 3.1. The initiation involved the generation of a carbon-centred radical on the alkyl chain via H-abstraction by a reactive species. Given that oxygen reacts with carbon-centred radicals at a significantly higher rate compared to other radical pathways, such as hydrogen abstraction, with a rate constant of $4 \times 10^9 M^{-1}s^{-1}$ [223], it can be assumed that any carbon-centred radical formed would almost immediately react with oxygen to form an ROO· radical. The fate of ROO· in the bulk is therefore to either abstract a hydrogen from a neighbouring alkane chain (RH) or react with another ROO· to form stable products (RC(O)H and ROH). The model simulation is shown in Figure 3.3 for autoxidation pathways in bulk systems.

Reaction	**Rate Coefficient**	**References**
A→ROO·	5.0×10^{-5} s^{-1}	-
ROO· + RH → ROOH + R·	5.5×10^{-4} M^{-1} s^{-1}	[122–124]
ROO· + ROO· → ROH + RC(O)H	4.0×10^{6} M^{-1} s^{-1}	[133, 136–138]
ROO· + NO → RO· + NO_2	4.0×10^{-1} s^{-1}	[101]
ROO· → X	4.0×10^{-1} s^{-1}	-
RO· + RH → ROH + R·	4.0×10^{2} M^{-1} s^{-1}	[149]

Table 3.1: Rates of reactions included in the kinetic model for peroxyl radical reactivity.

As shown in Table 3.1, the rate of ROO· radical termination is 10 orders of magnitude higher than the rate of H-abstraction of another unactivated alkane chain. The rate of hydrogen atom abstraction by a free radical depends on the activation energy of the reaction. Therefore, the reactions are only likely to be fast if the bond which is formed (ROO-H) is at least as strong as the bond which is broken (R-H). Peroxyl radicals are strongly resonance stabilised and have an estimated bond strength of 90 kcal/mol, however it is weaker than a typical alkyl C-H at $\sim$ 104 kcal/mol [117]. This means H-abstraction of an alkyl C-H bond by an ROO· radical is unfavourable and therefore, considerably slow. It is the Russel mechanism, shown in Section 1.5.2.1, that provides an explanation for the low activation energies and rapid termination of secondary or primary ROO· radicals to form stable products. Thus, the formation of stable species (RC(O)H and ROH) becomes the dominant pathway. This is reflected in Figure 3.3, where initial degradation of alkyl chain (A) is observed but no degradation of the neighbouring alkyl chains (RH) is observed or

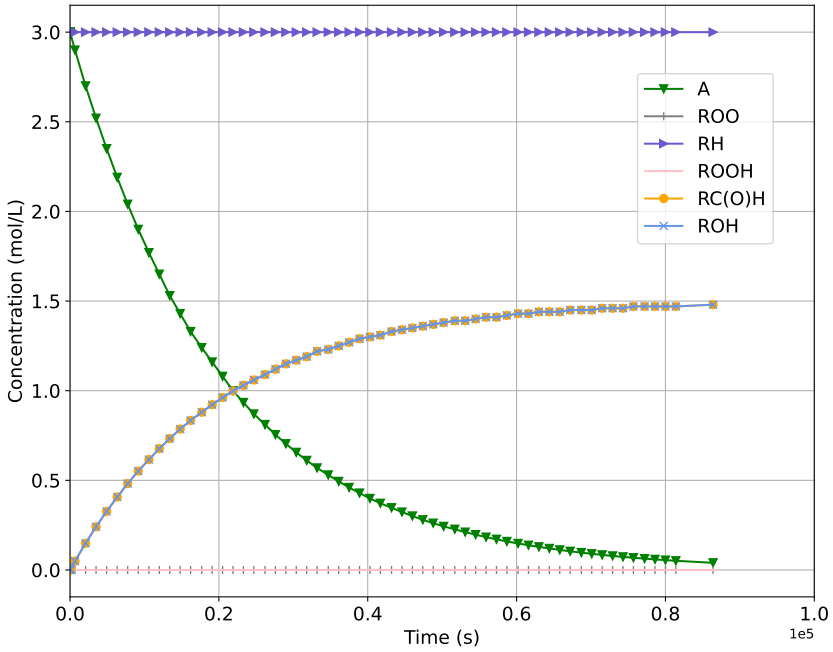

Figure 3.3: Degradation and formation of species during the autoxidation processes in bulk systems. No degradation of neighbouring alkyl chains (RH) is observed.

formation of the hydroperoxide (ROOH). However, formation of the stable species (RC(O)H and ROH) were observed as a result of ROO· termination.

The molecules in monolayer systems have limited mobility. Therefore, the chances of two peroxyl radicals being in close enough proximity to react to form stable products is likely very low, meaning the ROO·+ROO· is negligible. The probability of two ROO· radicals being in close enough proximity to react will be discussed further in Section 3.2.2. However, for this reason, a second reaction set was implemented into the kinetic model which excluded the ROO· self-reaction. Moreover, in a monolayer system, the alkyl chains are likely to interact with gas-phase species and undergo interfacial gas-surface reactions. The most dominant reaction for ROO· reactivity in the gas-phase is with NO to form a more reactive RO· radical and NO_2. This RO· radical can then abstract a hydrogen from a neighbouring chain (RH) at a faster rate than the corresponding ROO· radical, shown in Table 3.1 [149]. The rate constant for this reaction was obtained from the literature [101], and a concentration of NO of 40 ppb was used to calculate the reaction rate. This concentration was chosen because it was employed in experiments examining ROO· reactivity, which is discussed in more detail in Section 3.5.1. However, typical indoor NO concentrations are reported to be lower, in the range of 5-10 ppb [224]. Additionally, a termination pathway for ROO· radicals via an unspecified reaction was included in the model to account for potential interactions with the surface or atmospheric contaminants. The rate constant for this reaction was set equal to that of the ROO·+NO reaction (4.0×10^{-1} s^{-1})[101], reflecting the relatively high reactivity of ROO· radicals. This reaction rate ensures that the added termination pathway has an impact on the fate of ROO·, consistent with the fast reaction rates required to compete with known

gas-phase reactions. These reactions, shown in Figure 3.4 were added into the kinetic model to compare the degree of propagation of radical reactions with the bulk liquid system and the results are displayed in Figure 3.5.

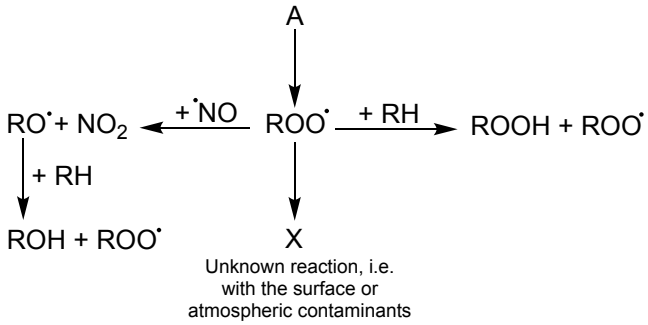

Figure 3.4: Proposed radical reaction pathways for alkane chains in monolayer systems.

The model simulation, shown in Figure 3.5, illustrates how the limited mobility of monolayer chains reduces the likelihood of ROO· radical termination, thereby enhancing their reactivity with gas-phase species. The reaction with NO occurs relatively quickly compared to the H-abstraction of a neighbouring chain by the ROO· radical. As a result, more reactive alkoxyl radicals (RO·) are produced. These RO· radicals can then propagate the reaction by abstracting hydrogen from neighbouring RH molecules, generating a carbon-centered radical that readily reacts with oxygen to form another ROO· radical. This leads to the degradation of neighbouring alkyl chains (RH), and the formation of ROH species confirms that the reaction pathway involves RO· with RH.

For a monolayer system, the ROO· radical reactivity could be very different, compared to bulk systems. Monolayers have limited mobility due to the chains being attached to the surface and so the chances of two ROO· radicals being in close enough proximity to terminate may be very low. However, ROO· H-abstraction could be significantly faster than in the bulk, due to short distances between the chains in the monolayer. Thus, the ROO· radicals may be forced to react with any nearby molecule instead, whether that be neighbouring chains or atmospheric molecules.

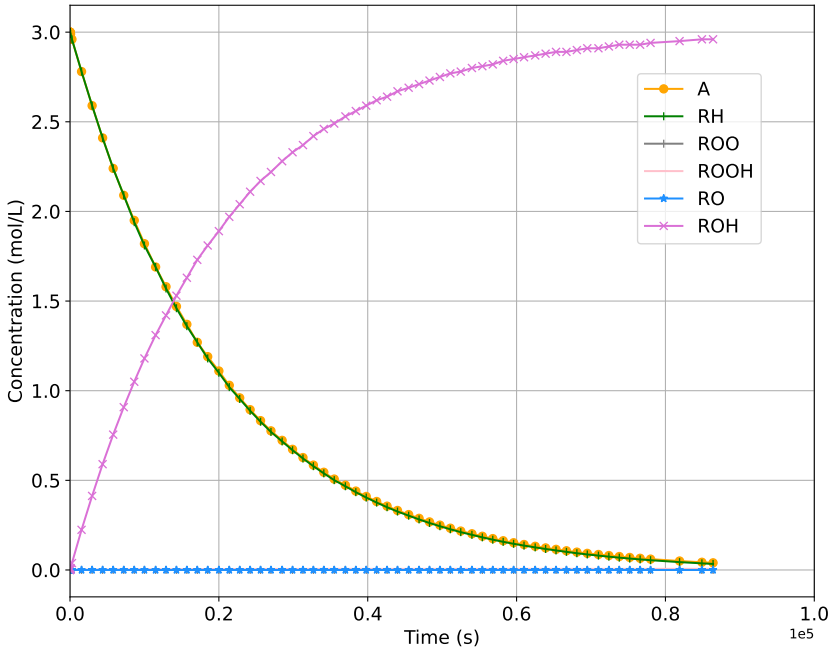

Figure 3.5: Degradation and formation of species during the radical reaction processes in bulk systems - including gas-phase processes. Degradation of neighbouring alkyl chains (RH) is observed, along with the formation of ROH as a result of the RO·+RH reaction.

3.2.2 Statistical Model

A statistical model was developed to investigate the probability of peroxyl radicals being in close enough proximity to react with each other in the monolayer. This model provided insights into the likelihood of peroxyl radical termination occurring within the monolayer chains, which was identified as one of the dominant pathways in the kinetic model.

The potential diffusion or mobility of surface-bound species should be considered in studies of thin films and SAMs. However, in the case of alkoxysilane monolayers covalently bound to silica, the surface attachment involves the formation of strong, irreversible Si-O-Si linkages between the alkoxysilane molecules and the silica surface [225]. Therefore, the lateral mobility of silane species on the surface is expected to be negligible. Studies have shown that depending on the packing density of the alkyl SAMs, the nature of the molecules can be described as solid-like or liquid-like [226]. The higher the packing and chain length, the more solid-like the alkane chains appear to be, whereas, a lower density allows for more fluid-like motion of the organic chains [227]. Nevertheless, a lower packing density would mean an increased distance between the chains, resulting in the inability to reach the neighbouring chains.

The monolayer coverage was calculated using the TGA weightloss data in Section 2.3.1.2, which suggested that there were approximately 2-4 molecules/nm^2 on the silica surface. This result correlated well with reports in the literature [38]. The distance between the molecules in a monolayer could, therefore, be calculated to be approximately 0.63 nm, using the value of 2.5 molecules/nm^2.

The aim of the statistical model was to calculate the proportion of ROO· radicals within reach of each other, as a function of their density. To construct the statistical model, a hexagonal grid was formed to represent the hexagonal structure of SAMs, shown in Figure 3.6 [228].

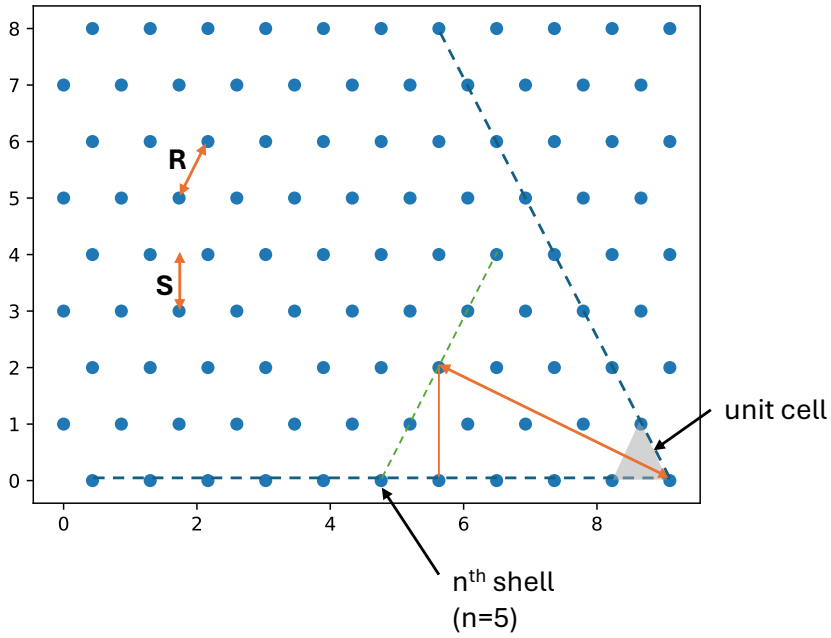

Figure 3.6: Representation of the hexagonal grid of points used in the statistical model.

The distance between points in the hexagonal grid is given the term R. The 6-fold symmetry of a hexagonal grid means that $1/6^{th}$ of all points surrounding the molecule could be considered and this could be named a sub-shell. The distance (S) between the lines is

$$S = R\frac{\sqrt{3}}{2}, \tag{3.1}$$

and the area (A) of the unit cell is

$$A = \frac{\sqrt{3}}{4}R^2. \tag{3.2}$$

The surface density (molecules/area) could be calculated from the estimated ROO· coverage, c, within the hexagonal grid:

$$\rho = \frac{2c}{\sqrt{3}R^2}. \tag{3.3}$$

For the n^{th} shell, there are n molecules in the subshell. A set with n shells will have

$$6\left[n + (n-1) + (n-2) + \cdots + 1\right] = 3(n^2 + n) \tag{3.4}$$

points, as shown in Figure 3.6. Therefore, the probability of finding a molecule in this shell is

$$p = 1 - (1 - c)^{3(n^2+n)} \tag{3.5}$$

The size of the box to find a particle with a probability of p and coverage c is then

$$n = \frac{-3\ln(1-c) - \sqrt{9\left[\ln(1-c)\right]^2 + 12\ln(1-c)\ln(1-p)}}{6\ln(1-c)}. \tag{3.6}$$

The distances between the points in the n-th shell and the given molecule are

$$d = R\sqrt{\left(\frac{n-i}{2}\right)^2 + (iS)^2} = R\sqrt{n^2 - ni + i^2} \tag{3.7}$$

where i=0,1,2,...n-1; these distances were repeated 6 times. For $n \leq 7$, the distances from the molecule to the points in the n^{th} shell are always shorter than the distances to the $(n+1)^{th}$ shell. Hence the distance to the nearest neighbour can be found by iterating through the shells with n=1,2,... until the neighbour is found. In order to find the shortest distance, the iterations started from the centre of the subshell moving in both directions until reaching the end of the subshell. This approach was used with a large set of randomly distributed molecules to determine the distribution of distances between the nearest neighbours. Albeit, it will only be correct for the first 7 shells, i.e. distances up to $7R$. However, this is sufficient, as the focus is on short distances where ROO· radicals can reach each other.

Figure 3.7 displays the result for a monolayer with R=0.63 nm (2.5 molecules/nm^2 density) and 1×10^{-5} coverage. A coverage of 1×10^{-5} was used as an estimate for the amount of active ROO· radicals in the monolayer at a given time. This value was an estimation based on the rate of ROO· radical consumption, calculated to be 0.4 s^{-1}, upon exposure to NO at a concentration of 40 ppb. This experimental result will be discussed further in Section 3.5.1. While this ROO· coverage value is an estimation, it allowed an initial approximation for the nearest neighbour distribution of ROO· radicals in a monolayer.

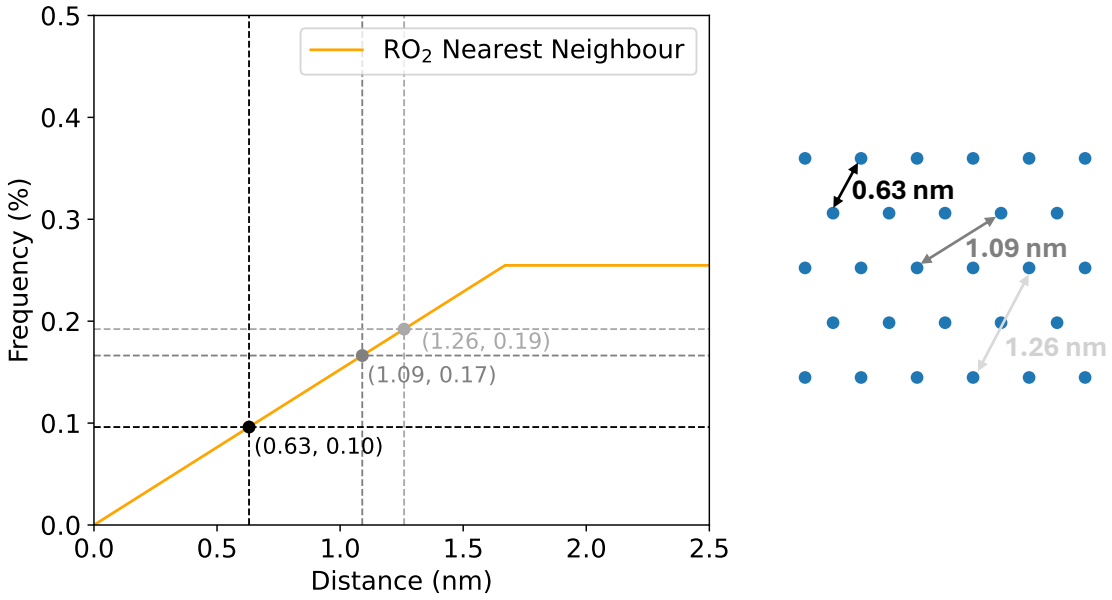

Figure 3.7: The distribution of the minimum distances between nearest neighbours of ROO· radicals in a hexagonal grid. The diagram on the right shows the hexagonal grid with various distances between molecules.

In Figure 3.7, a hexagonal grid has been illustrated to portray the various distances between the molecules. The closest distance being 0.63 nm, which is the distance between the chains if the surface coverage is 2.5 molecules/nm^2. The ellipsometry result discussed in Section 2.3.1.1, gave an indication to the thickness of 8 length carbon chains which was measured to be 0.48 nm. At this length, the ROO· radicals within the monolayer chains should be able to reach one another to react. The second closest distance is 1.09 nm, which depending on the fluidity of the molecules and length of the carbon chain, the ROO· radicals could potentially reach one another. However, this could be unlikely if the molecules are well-packed and more solid-like. Finally, a distance of 1.26 nm would be too great for ROO· radicals to reach each other if the length of the alkyl chains is around 0.48 nm. The length of a fully stretched 8-length alkane chain can be calculated to be 0.98 nm, using the following equation:

$$L = 0.126n + 0.1 \tag{3.8}$$

where L is the length (nm) of the alkyl chain, 0.126 represents the C-C bond length in the *trans* projection to the surface, and 0.1 includes the methyl terminal group [12]. At this length, the minimum distance that two peroxyl radicals cannot interact is 1.96 nm, which has a frequency of 0.25%. Thus, any distance greater than 1.96 nm can be assumed as too far for ROO· radical termination to occur.

As displayed in Figure 3.7, the frequency of ROO· radicals with a nearest neighbour at a distance of 0.63 nm, the distance the chains can definitely reach, is approximately 0.1%. This is a very low probability that ROO· radicals will be able to terminate with each other in the monolayer to form stable species, insinuating the possibility of alternative reaction pathways. Alternative pathways being H-

abstraction of neighbouring chains or reactivity with atmospheric molecules. This model has counteracted the kinetic model for bulk liquids and suggested that in monolayer systems, termination of ROO· radicals may not be the dominant pathway due to the limited mobility of the molecules attached to the surface. Moreover, this contradicts the report by Molina *et al.*, which stated the dominant pathway for ROO· radicals in monolayer systems is the self-reaction with a neighbouring ROO· radical [173].

While the statistical model used approximate values for the density of active ROO· radicals on the surface and estimates for the mobility and fluidity of the monolayer chains, these assumptions highlighted several uncertainties. Therefore, the aim of the experiments is to conduct further investigations to better understand the mechanism of surface oxidation, in particular the propagation of radical reactions within the monolayer and the fate of the ROO· radical.

3.3 Radical Initiation Within SAMs

Analysis of functionalised SiO_2 nanoparticles is considerably more informative than the analysis of glass slide surfaces, as the higher quantity of organic material on the nanoparticle surface enables the use of techniques such as TGA and oxidative cleavage for GC-MS and ^{1}H NMR analysis, described in Section 2.3.3. Thus, functionalised SiO_2 nanoparticles were the preferred substrates for reactivity studies. The next challenge was to initiate radical reactions within the monolayer chains attached to SiO_2 nanoparticles.

3.3.1 Thermal Radical Initiation

Azo compounds, such as 2,2'-azobisisobutyronitrile (AIBN), are widely used as radical initiators in polymer chemistry and organic synthesis due to their high decomposition ability and subsequent stability. Their covalent bonds can be cleaved at temperatures <150°C, shown in Figure 3.8, to form nitrogen gas and two carbon centred radicals [229].

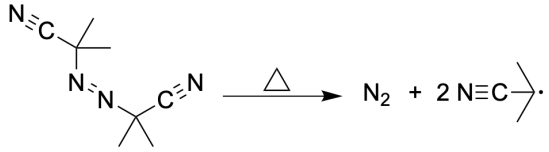

Figure 3.8: Decomposition of AIBN.

The primary aim of these experiments was to incorporate a surface-bound thermal initiator into the monolayer system, as illustrated in Figure 3.9. This approach would have been ideal for generating radicals directly within the monolayer, ensuring that radicals were confined to the monolayer chains. However, the synthesis of the azo-initiator silane molecule proved to be challenging, which led to the use of AIBN for the thermal-initiated experiments instead.

As an alternative method, AIBN was dissolved in a volatile solvent, such as DCM, and added to functionalised SiO_2 nanoparticles. The solvent was evaporated to leave AIBN coated nanoparticles. The quantity of AIBN used in these experiments was calculated based on the TGA weight loss results of the functionalised

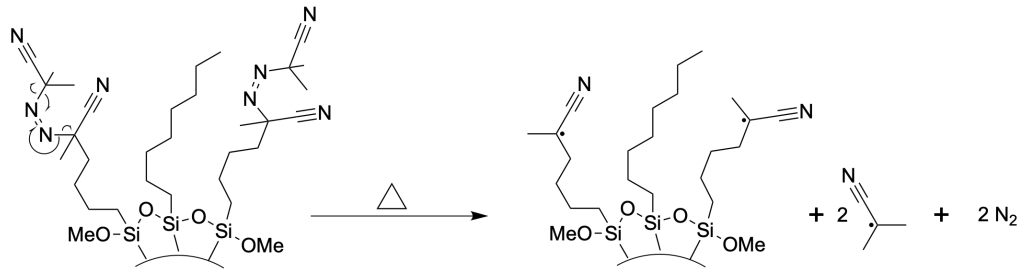

Figure 3.9: Scheme of a surface-bound azo initiator and its generation of radicals within a monolayer system.

SiO_2 nanoparticles, which provided the coverage of monolayer chains on the surface. The amount of AIBN added to the solution was equal to the number of monolayer chains attached to the SiO_2 nanoparticles, ensuring that two radicals could form per monolayer chain. A disadvantage of this methodology is that it does not guarantee a homogeneous distribution of radicals among the monolayer chains.

The first step was to find a suitable temperature and heating time for allowing at least 50% degradation of AIBN amongst the functionalised SiO_2 nanoparticles. This extent of AIBN degradation would indicate that the reaction has reached a point where the radical generation is efficient but controlled, providing more reproducible and reliable results. As well as temperature, the rate constant (k_d) of AIBN decomposition depends on the solvent/monomer system used. The best indicator of initiator activity is its half-life ($t_{1/2}$), which is the time required for the original initiator mass to reduce by half, at a given temperature. The half life is related to the rate constant as shown in equation 3.9.

$$t_{1/2} = \frac{ln2}{k_d} \tag{3.9}$$

AIBN has a half-life of approximately 10 hours at 65°C in solution (toluene)[230]. This was reproduced experimentally by heating a known concentration of AIBN in toluene for 10 hours at 65°C, followed by evaporation of the solvent and quantification by ^{1}H NMR. The results are shown in Figure 3.10. To reduce the reaction time, AIBN was heated at 75°C for 4 hours in toluene, which gave a similar extent of decomposition. For these experiments, AIBN needed to be in the solid phase to allow for gas-surface radical chemistry to be investigated. Therefore, solid AIBN (4 mg) was heated to 75°C, however, it was observed that the decomposition rate for solid phase AIBN compared to solution phase AIBN was considerably slower with <20% degradation seen after 20 hours of heating. This phenomenon can be explained by the crystallinity of solid AIBN, the rigidity and lack of mobility do not allow even the slightest movement necessary to break the R-N bond [231].

Raising the temperature to 85°C for heating AIBN in the solid phase resulted in a half-life of approximately 24 hours. To test the decomposition rate of AIBN amongst SiO_2 nanoparticles, a solution of AIBN in DCM (2 mg/mL, 2 mL) was added to SiO_2 nanoparticles (50 mg). The mixture was concentrated by vacuum and the AIBN coated nanoparticles were placed in a 85°C oil bath. Quantification of AIBN was achieved by ^{1}H NMR after several washes of the SiO_2 nanoparticles and the collection and evaporation of the supernatant. A control experiment involving the coating of AIBN solution onto SiO_2 nanoparticles, evaporation and subsequent washes to

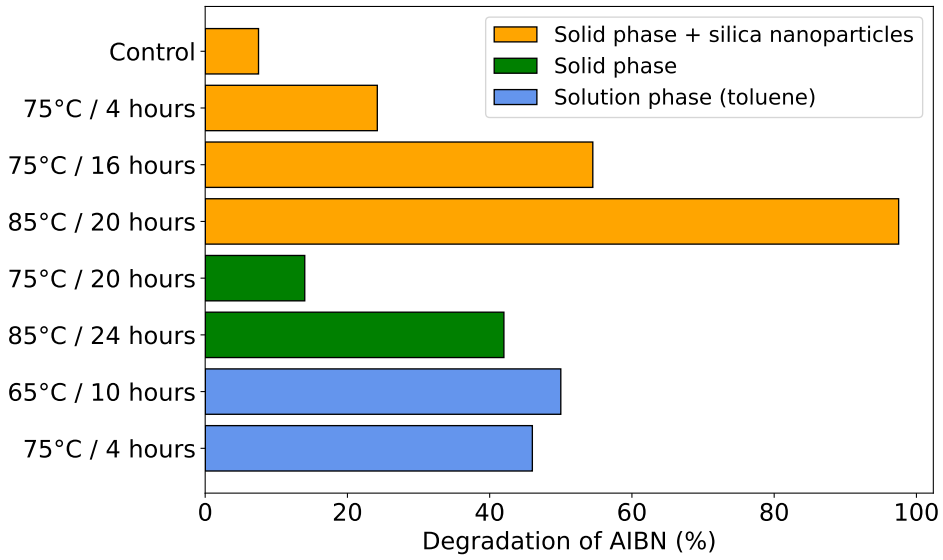

Figure 3.10: Degradation of AIBN in solution phase, solid phase and solid phase among SiO_2 nanoparticles with different temperatures and times. A control experiment is also shown which involved the same experimental procedure but without heating the SiO_2 nanoparticles.

remove AIBN from the SiO_2 nanoparticles, followed by ^1H NMR quantification is shown in Figure 3.10. The control experiment showed <5% of AIBN is lost in the process. Further differences in the decomposition rate of solid AIBN were observed when it was in the presence of unfunctionalized bare SiO_2 nanoparticles. It seemed as though AIBN followed a liquid-style decomposition when dispersed amongst the SiO_2 nanoparticles. At a temperature of 85°C, the AIBN completely decomposed after 24 hours. A half-life of approximately 16 hours could be achieved at 75°C, which was slower than in liquid-phase but faster than in solid-phase. The crystallinity must be sufficiently disrupted when AIBN is dispersed among the nanoparticles, allowing it to behave similarly to AIBN in solution. Moreover, this suggests that the distribution of AIBN in the monolayer is reasonably even, otherwise there would be crystallites. This makes it a suitable system for generating radicals among the monolayers as the radicals will be evenly dispersed.

Nevertheless, this methodology had limitations, as the radicals were not confined to the monolayer chains. To overcome this, an alternative approach was employed, using UV light to introduce a radical initiator attached to the silica surface via mixed monolayers.

3.3.2 Ketone Photolysis

Aliphatic ketones were chosen as reagents for this study due to their availability and well-defined photochemistry, particularly their ability to undergo photolysis and generate free radicals [232]. The photolysis of aliphatic ketones has been extensively studied in liquids and in the gas-phase [233, 234]. Aliphatic ketones exhibit a weak absorption band at $\sim$ 275 nm as a result of an $n \rightarrow \pi^*$ transition. Initially, the photoexcitation promotes the system to the first singlet state (S_1) of $n\pi^*$ character (equation 3.10) [233]. It has been well studied in the literature that intersystem

crossing (ISC) to the triplet state (T_1) occurs preferentially to reaction channels in the S_1 state (equation 3.11), due to the heights of the reaction barriers in the S_1 state being higher than in the T_1 state [234].

$$R_2C=O \xrightarrow{h\nu} R_2C=O^1 \tag{3.10}$$

$$R_2C=O^1 \xrightarrow{ISC} R_2C=O^3 \tag{3.11}$$

In the T_1 state, the photoexcited ketone can either undergo fragmentation into free radicals (Norrish type I, shown in Figure 3.11), or follow the Norrish type II pathway to yield a 1,4-biradical which eventually cleaves to form stable products (Figure 3.11) [234]. In the short time scale of 10 ps, Norrish type I is preferred over the $\gamma-H$ transfer during Norrish type II. However, in the gas-phase or condensed phase, collisions or interactions with the solvent provide the necessary energy and stabilisation for Norrish II to occur more frequently than Norrish I. Moreover, from an energetics point of view, it was shown that the Norrish type II reaction barrier is much smaller than the Norrish type I reaction [234]. Therefore, at longer timescales (up to 100 ps), it has been reported in the literature that the relative yield of Norrish Type I and Norrish Type II reactions is approximately 80% for the Norrish Type II reaction [235]. Consequently, it can be assumed that the majority of ketone photolysis pathways will proceed via the Norrish Type II reaction.

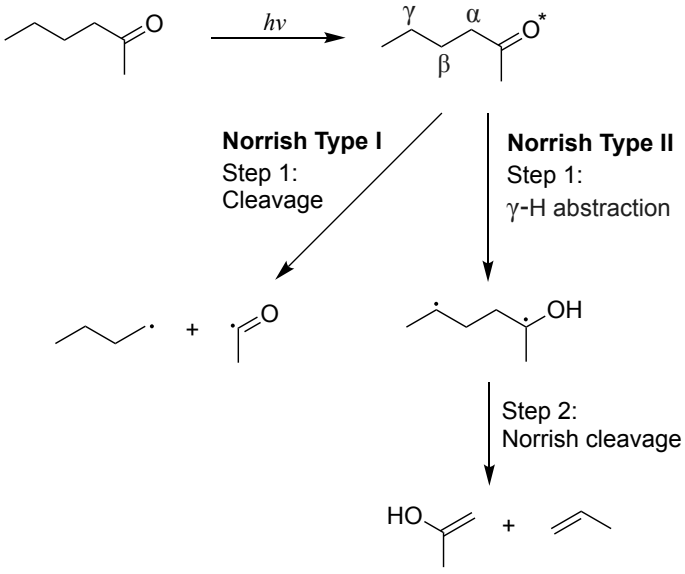

Figure 3.11: Schematic of hexan-2-one photolysis and possible reactions in the triplet state.

Using ketone photolysis, a methodology was developed to incorporate radical reactions into the monolayer. Mixed monolayers of a radical initiator, C6oneOEt, and another organic alkoxysilane were produced on SiO_2 nanoparticle surfaces. These mixed monolayers are homogenously mixed, as confirmed by the AFM results in Section 2.3.1.3. Figure 3.12 outlines a representation of the reaction pathways for the photoexcited ketone within the mixed monolayer. In the monolayer, where molecules are in closer proximity to each other and geometrical changes required for

Norrish II could be disfavoured, the ketone photolysis pathways could be different. Upon UV irradiation, the ketone-containing chain could either propagate radical reactions to the neighbouring organic chain, causing autoxidation to commence, or purely destroy itself via Norrish type II to form a surface-bound alkene and acetone, as shown in Figure3.12.

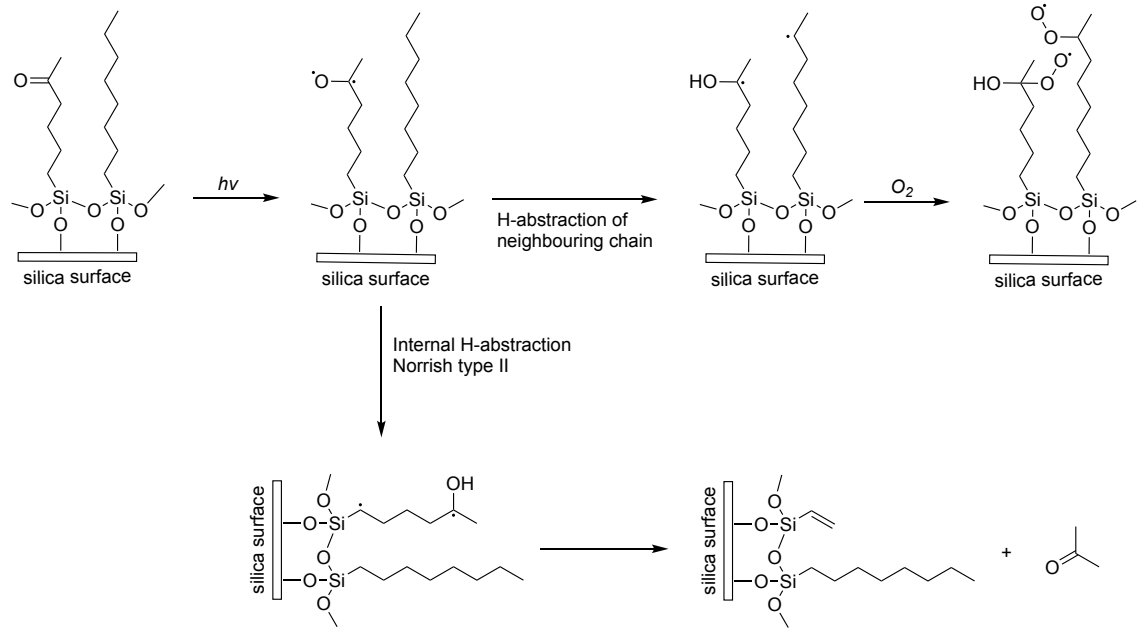

Figure 3.12: Reaction pathways for the photoexcited ketone within a C6One and C8Alk mixed monolayer.

The aim of this system is to utilise ketone photolysis to initiate radical reactions directly within the monolayer and study the radical propagation to neighbouring chains. The degree of autoxidation within the monolayers could be analysed by oxidative cleavage of the organic chains and quantification by ^{1}H NMR and GC-MS, discussed in Section 2.3.3. Comparison of the quantity of organic chains in the mixed monolayer without UV exposure allowed the degradation of the neighbouring organic chains to be evaluated.

To conduct these experiments, functionalised SiO_2 nanoparticles were placed on a glass dish 4 cm beneath a mercury UVG-11 lamp (254 nm, 230 V, 0.12 Amps, 27.6 W), contained in a black 24 L box. The power at 4 cm from the UV lamp was 4 mW/cm^2, measured with a power meter. The UV spectrum for this lamp showed the main wavelength below 300 nm to be 254 nm and no emission below 200 nm (see Appendix A7). This lamp was used because it provided a wavelength which is in the UV absorption range of aliphatic ketones [236], and sufficient power output to conduct experiments in a reasonable time frame.

The yield of C6One chains after exposure to UV light for 8, 16 and 24 hours was obtained via ^{1}H NMR and was normalised to the yield obtained for non-exposed C6One-C8Alk mixed monolayer functionalised SiO_2 nanoparticles, which would typically be close to 50% for 1:1 monolayers. A control experiment was conducted under zero air conditions (a 1:4 mixture of O_2 and N_2) to confirm that the degradation of C6One chains was due to ketone photolysis and not reactive species generated by the UV lamp. Zero air was supplied from a Pure Air Generator (PAG 003, ANNOX, UK), which was connected to a black 24 L box containing the functionalized

nanoparticles and the mercury lamp. The gas flow was set to 2 L/min, and the box was purged for over 30 minutes before the UV lamp was turned on, ensuring that only zero air (24 L) was present in the box during UV irradiation. Figure 3.13 illustrates the extent of C6One chain degradation under both ambient laboratory and zero air conditions.

It was observed that under both laboratory and zero-air conditions, the C6One chains degrade by approximately half of their initial yield, confirming photolysis of the C6One chains has occurred. The rate of degradation appears to be faster under the ambient laboratory conditions compared to the zero-air conditions. This variation is greater than the error in the dissociation yield obtained via ^{1}H NMR, which was calculated to be ±3.4% (Section 2.3.3). This could be due to additional reactivity between atmospheric molecules in the laboratory air with the C6One chains, providing additional radical initiation pathways and thus, quicker degradation of the C6One chains.

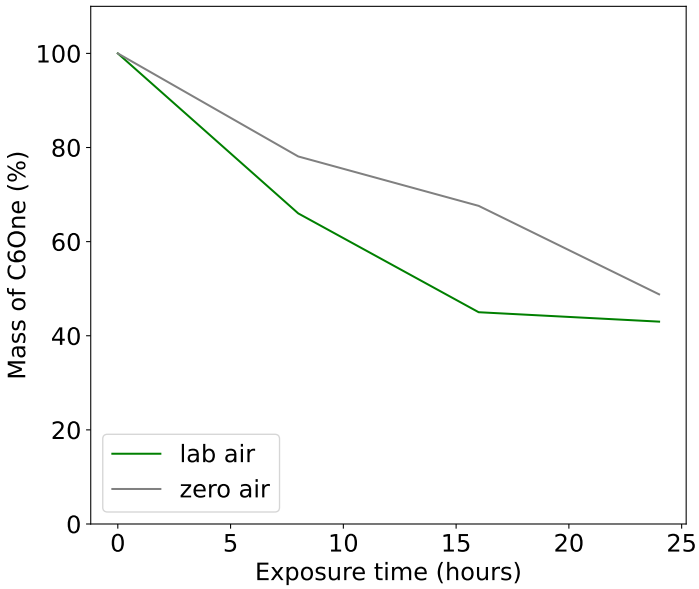

Figure 3.13: Degradation of C6One radical initator chains in the C6One-C8Alk mixed monolayer upon UV light exposure under ambient laboratory conditions and zero air conditions. Quantification performed by ^{1}H NMR.

3.3.2.1 Radical Initiator Ratio

To evaluate the impact of ketone photolysis on the degradation of neighbouring organic chains, the ratio of radical initiator chains to organic chains within the mixed monolayer system was varied. By adjusting this ratio, the influence of ketone photolysis on the rate of degradation of neighbouring chains was assessed, revealing how the initiation of radicals through photolysis affects the degradation of adjacent molecules. This was achieved by altering the molar ratio of C6OneOEt and C8AlkOEt in the functionalisation procedure of SiO_2 nanoparticles, Section 2.2.4. The molar ratios tested for this experiment included: C6OneOEt and C8AlkOEt

in a 3:1 ratio, 1:1 ratio and 1:3 ratio. The ratio of each mixed monolayer could be interpreted by ^{1}H NMR after dissociation of the molecules from the silica surface.

The C6One and C8Alk mixed monolayer functionalised SiO_2 nanoparticles were exposed to UV light for 8, 16 and 24 hours under laboratory conditions. The functionalised SiO_2 nanoparticles were then dissociated using the oxidative cleavage method and analysed by ^{1}H NMR and GC-MS. Both ^{1}H NMR and GC-MS were used to quantify the neighbouring C8Alk chains. ^{1}H NMR quantification is based solely on the -CH_2 peak adjacent to the alcohol group of the dissociated product (discussed in Section 2.3.3), which means any structural changes at the distal end of the C8Alk chain are not reflected in the yield. In contrast, GC-MS provides quantification based on the entire molecular structure, offering a more accurate measurement of the C8Alk yield. Each data point was normalised to the yields obtained for the corresponding non-exposed C6One and C8Alk mixed monolayers and plotted, shown in Figure 3.14. Unlike Figure 3.13, Figure 3.14 shows a plot of the C8Alk yields, not the C6One yields.

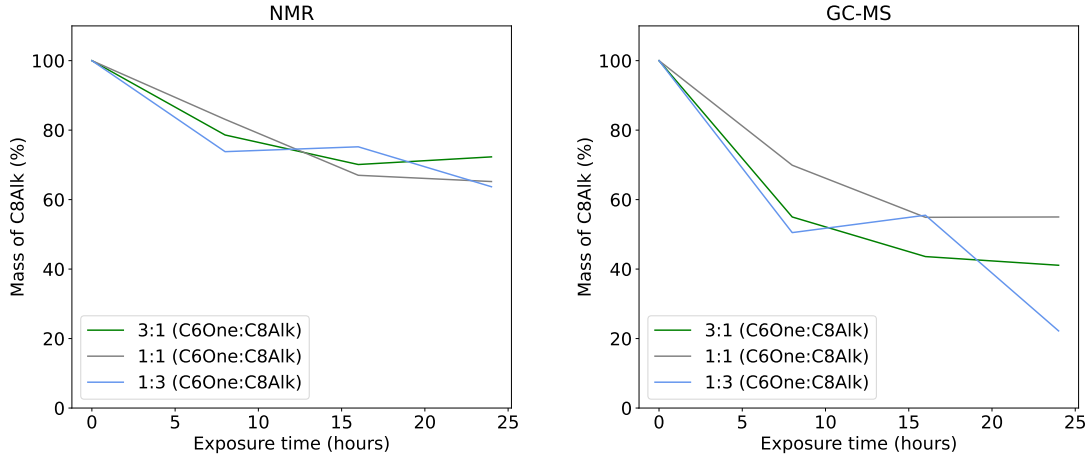

Figure 3.14: The degradation of neighbouring C8Alk chains in the C6One-C8Alk mixed monolayer after exposure to UV light at increasing times, demonstrating the effect of different ratios of C6One to C8Alk within the mixed monolayer. The plot on the left shows the normalised yields obtained via ^{1}H NMR and the plot on the right shows the normalised yields obtained via GC-MS.

Greater degradation of the C8Alk chains is observed in the GC-MS results (right side of Figure 3.14), likely due to structural changes along the chain that are not captured by ^{1}H NMR quantification. Nevertheless, both analytical techniques demonstrate that the C8Alk chains do degrade over 24 hours of UV exposure. The results indicate that the ratio of C6One chains to C8Alk chains has little impact on the degradation rate of the neighbouring C8Alk chains. This suggests that the photolysis of C6One does not significantly contribute to the degradation of adjacent C8Alk chains, implying that the primary degradation pathway for C6One occurs through internal H-abstraction via the Norrish type II mechanism. Consequently, this methodology did not proceed as expected, with limited radical initiation from ketone photolysis.

3.3.2.2 Effect of Atmospheric Molecules

The degradation of C8Alk chains, as observed in Figure 3.14, suggests the formation of radical species under UV light, potentially originating from atmospheric molecules present in the ambient air. Thus, to investigate the effect of ambient atmospheric molecules on the propagation of radical reactions within the monolayer, experiments were conducted under laboratory air conditions and zero air conditions (1:4 mixture O_2 and N_2). The yield of neighbouring C8Alk chains after exposure to UV light under zero air conditions was obtained via both ^{1}H NMR and GC-MS, as shown in Table 3.2. This is reflected in Figure 3.15, a plot of the data which has been normalised to the yield obtained for non-exposed functionalised SiO_2 nanoparticles (0 hour). Both the yields from ^{1}H NMR and GC-MS are comparable and thus, confirm the lack of degradation of the neighbouring C8Alk chains. These results show that upon radical initiation of the C6One chains, no propagation to the neighbouring alkane chains occurs.

Exposure Time (hours)	Yield (% ^{1}H NMR)	Yield (% GC-MS)
0	90.1	89.8
8	92.1	85.5
16	82.6	94.4
24	87.4	92.7

Table 3.2: Yield of C8Alk chains after exposure of mixed C8Alk-C6One monolayers to UV at different times under zero air conditions, quantified by ^{1}H NMR and GC-MS after dissociation from the silica surface.

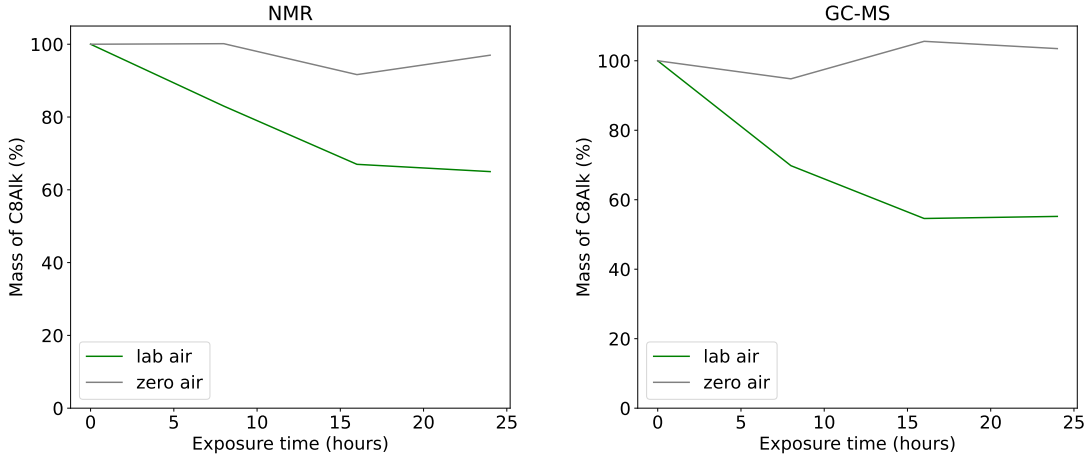

Figure 3.15: The degradation of neighbouring C8Alk chains after exposure of mixed C8Alk-C6One monolayers to UV light under laboratory air and zero air conditions. Quantification by ^{1}H NMR (left) and GC-MS (right).

In comparison, the yields obtained for the neighbouring C8Alk chains which had been exposed to UV light under ambient laboratory conditions, shown in Table 3.3, suggest degradation of the C8Alk chains has occurred. This is also reflected in

Figure 3.15, a plot of the data which has been normalised to the yield obtained for non-exposed functionalised SiO_2 nanoparticles (0 hour). The yields obtained by GC-MS for C8Alk chains after exposure to UV light are slightly lower than the results from ^{1}H NMR, however, the yield obtained for the non-exposed mixed monolayers were comparable. As demonstrated in Section 2.3.3, quantification of C8Alk chains is obtained by analysing a singular peak corresponding to the -CH_2 adjacent to the alcohol group. This means that any change in structure further up the alkyl chain will be unnoticed and accounted for in the overall yield of C8Alk chains. However, GC-MS quantification is based solely on the mass of derivatised C8AlkOH chains and therefore does not account for C8Alk chains that have undergone even slight structural changes, such as oxidation resulting from radical reactions. Thus, if the reaction only spread to adjacent chains far away from the surface, NMR yields would not drop at all. This suggests that there is significant degradation close to the surface, or that the molecules which have reacted once, are highly likely to react again, such as via internal abstraction by ROO· radicals. Nevertheless, both methods of quantification show a clear degradation trend of the C8Alk chains upon the UV light, which contradicts the result from the zero-air experiment.

Exposure Time (hours)	**Yield (% ^{1}H NMR)**	**Yield (% GC-MS)**
0	85.9	80.5
8	71.3	56.3
16	57.8	44.2
24	56.2	44.3

Table 3.3: Yield of C8Alk chains after exposure of mixed C8Alk-C6One monolayers to UV at different times under ambient laboratory conditions, quantified by ^{1}H NMR and GC-MS after dissociation from the silica surface.

These results suggest that atmospheric molecules play a crucial role in enhancing the propagation of radical reactions within alkyl monolayer chains. As explained further in Section 3.4.2.2, the dominant radical initiation mechanism, which led to the degradation of adjacent chains, was instead due to the presence of adventitious ozone in the ambient laboratory air.

3.3.3 Ozone Photodissociation

During experiments involving UV light and ketone photolysis, discussed further in Section 3.4.2.2, it was serendipitously discovered that the concentration of ozone in the ambient laboratory air was high enough to generate reactive species, such as ·OH, under UV exposure.

The concentration of ozone in the laboratory air was measured, using a dual-channel 2B Technologies Ozone monitor, to be 30 ppb. Ozone has a strong absorption at 254 nm [237]. At this wavelength, photodissociation occurs to form an oxygen molecule and atomic oxygen, represented in equation 3.12.

$$O_3 + h\nu(\lambda < 340nm) \rightarrow O_2 + O(^1D) \tag{3.12}$$

Most $O(^1D)$ atoms produced from ozone photolysis undergo collisional de-excitation to the ground-state oxygen atom, $O(^3P)$, by collisions with N_2 molecules which are

highly abundant in air. Although this quenching pathway is significant, the lifetime of $O(^1D)$ remains relatively long — approximately 148 seconds [237] — which allows a fraction of these excited-state oxygen atoms to undergo bimolecular reactions. Notably, $O(^1D)$ can react with water vapour to form highly reactive hydroxyl radicals (·OH), as shown in equation 3.13. These ·OH radicals can initiate the degradation of organic chains, or alternatively, atomic oxygen can react directly with monolayer chains.

$$O(^1D) + H_2O \rightarrow 2 \cdot OH \tag{3.13}$$

The results from experiments involving the use of ambient ozone concentration and UV light exposure will be further discussed in Section 3.4.2.

3.4 Propagation of Radical Reactions in SAMs

One of the main aims of this project is to investigate the degree of radical propagation within monolayer systems. This section will assess the effect of monolayer chain functionality on the propagation of radical reactions using a variety of radical initiator systems, discussed previously in Section 3.3.

After radical initiation, peroxyl radicals are likely to form within the monolayers. The peroxyl radicals could then abstract a hydrogen from another chain, shown in equation 3.14.

$$ROO \cdot + RH \rightarrow \dot{R} + ROOH \tag{3.14}$$

Consequently, various organic molecules were chosen due to their potentially different reactivity rates towards H-abstraction by a peroxyl radical, and thus their varying autoxidation rates. It is well established that the structure and reactivity of the reactant can significantly influence the rate of H-abstraction by a peroxyl radical, as observed in gas-phase and bulk liquid systems [117, 118]. In many instances, the reaction of a peroxyl radical abstracting a hydrogen atom from another molecule is highly unfavourable, since the BDEs for R-H are typically higher than those for the corresponding ROO-H bond, as discussed in Section 1.5.2 [118]. Various organic molecules were used to assess the reaction pathways involved in the autoxidation process within monolayers. These molecules, shown in Figure 3.16, include simple alkyl chains (C8Alk), branched alkyl chains (C8BrAlk), perfluoro-containing chains (C8Perf) and ether-containing chains (C5Eth and C7DiEth).

As discussed in Section 1.5.2, their differing reactivity rates toward ROO· radical H-abstraction could provide valuable insights into the behaviour of ROO· radicals and help determine whether H-abstraction from neighbouring chains was a predominant pathway in the autoxidation mechanism.

3.4.1 Thermal Initiation

SiO_2 nanoparticles were functionalised with homogeneous monolayers of C8AlkOMe and C5EthOEt using the standard functionalisation procedure, described in Section 2.2.3. These monolayers were chosen due to their varying C-H BDEs, described in Section 1.5.2. The monolayers were exposed to 75°C heat for 16 hours in a sealed round bottom flask over an oil bath with the presence of AIBN and ambient air,

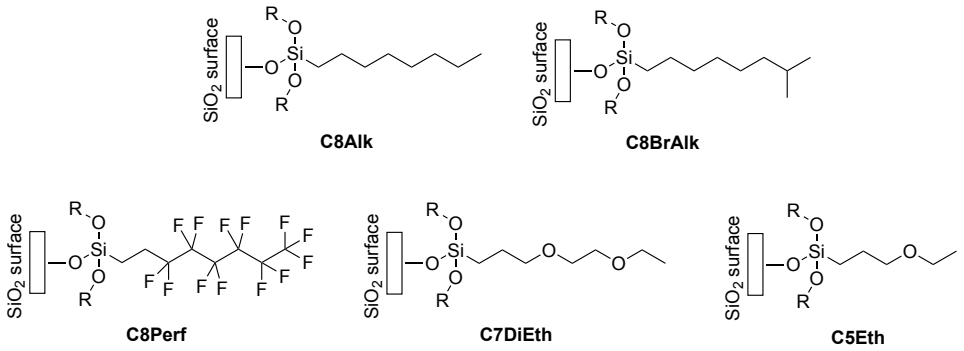

Figure 3.16: Various organic molecules used in the propagation of radical reactions study.

compressed air or N_2 before being dissociated from the silica surface and quantified by ^{1}H NMR. The results for the degradation of C8Alk and C5Eth chains under these conditions are displayed in Figure 3.17.

The control experiments, involving purely heating the functionalised nanoparticles at 75°C for 16 hours (C8Alk-Heat and C5Eth-Heat in Figure 3.17), showed that both monolayers degraded upon 75°C heat by approximately 18-25%, depending on the organic molecule. This was an unexpected result as monolayer degradation is not typically observed at these temperatures [238]. There have been studies on the thermal degradation of alkoxy monolayers on silica, which have stated observations of alkyl chain fragmentation upon 200-400°C heat [238]. However, no fragmentation was observed below 200°C heat in these studies. Thus, the reason for loss of monolayer chain mass could be due to the heating leading to stronger binding of some monolayer chains, inhibiting their removal from the silica surface during the dissociation procedure.

The slight increase in degradation seen for C5Eth chains, which degraded by 24.7%, after being heated for 16 hours compared to C8Alk chains, which degraded by 18.5% (Figure 3.17), suggests the degradation could be dependent on the functionality of the chains. Further controls were taken to evaluate the effect of air and heat on the degradation of the C8Alk chains. This was conducted by filling a balloon with compressed air or N_2 gas and connecting to the sealed round bottom flask. It was observed that slightly more degradation occurred under the compressed air environment than the N_2 environment (Figure 3.17). The increase in degradation observed for the C8Alk monolayers exposed to compressed air (24.8% degradation) compared to under a N_2 atmosphere (17.5% degradation), suggests that O_2 has an effect on the rate of degradation and thus, implies radical reactions may be occurring in the monolayer.

The functionalised SiO_2 nanoparticles were coated in a solution of AIBN in DCM. The solvent was evaporated under vacuum and the dry AIBN-coated nanoparticles were placed in a sealed round bottom flask under ambient air and heated at 75°C for 16 hours over an oil bath. After heating, the nanoparticles were washed several times with DCM to remove excess AIBN, dried under vacuum and the monolayer chains were dissociated for ^{1}H NMR quantification. The solution of excess AIBN was concentrated under vacuum and quantified via ^{1}H NMR to assess the degradation of AIBN during the experiment, shown in Table 3.4. Approximately, 50-60% of AIBN decomposed after 16 hours at 75°C, which corresponded well with control

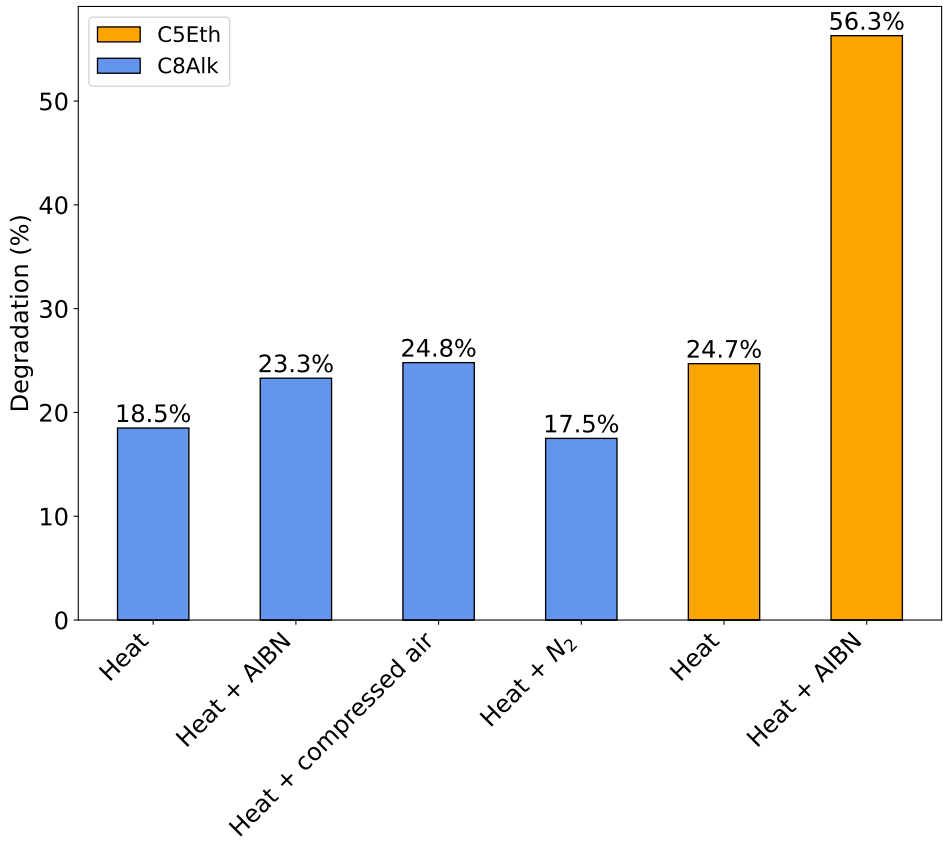

Figure 3.17: Degradation of two different homogeneous monolayers, C8Alk and C5Eth, under 75°C heat and ambient air for 16 hours with the addition of AIBN or alternative atmospheres, such as under compressed air or N_2. Quantification by ^{1}H NMR.

experiments in Figure 3.10 for AIBN amongst nanoparticles. This confirmed that radicals were generated amongst the functionalised SiO_2 nanoparticles and thus, could potentially initiate radical reactions within the monolayer chains.

Experiment	**AIBN Degradation (%)**
C8Alk monolayers	54.50
C5Eth monolayers	62.80

Table 3.4: Degradation of AIBN during heating of different monolayers for 16 hours at 75°C under ambient air. Quantification by ^{1}H NMR.

The results, shown in Figure 3.17, suggest that the addition of AIBN amongst the C8Alk monolayer chains did not cause a significant difference to the rate of their degradation. This suggests that the radical reactions initiated within the C8Alk chains did not propagate rapidly enough to produce a significant effect over the course of 16 hours. In comparison, the addition of AIBN to the system, caused a significant increase in degradation for the C5Eth chains. The mass of C5Eth chains after exposure to heat and AIBN decreased by >50% over 16 hours (Figure 3.17), insinuating that the propagation of radical reactions within the C5Eth chains was a faster process. This can be attributed to the greater lability of the C-H bonds in the

C5Eth chains, making them more susceptible to H-abstraction by nearby peroxyl radicals, which were generated from the initiation of AIBN radicals and subsequent reaction with O_2. These results suggest lack of autoxidation in straight alkanes but some autoxidation for ethers.

3.4.2 Ozone Photodissociation

3.4.2.1 Homogeneous Monolayers

As mentioned previously in Section 3.3, ambient ozone was serendipitously discovered to play a key role in radical initiation during experiments which involved UV irradiation of mixed monolayer functionalised nanoparticles. It was observed that the ketone photolysis within the mixed monolayers did not contribute significantly to radical initiation as an increase in the ratio of C6One to C8Alk chains in the mixed monolayer, had no effect on the rate of C8Alk degradation. However, degradation of the organic chains still occurred. This insinuated that reactive species, such as atomic O and ·OH radicals, generated under the UV lamp via ozone photodissociation could be initiating radical reactions within the monolayers.

Experiments were conducted for a variety of homogeneous monolayers, including C5Eth, C8Alk, C8BrAlk and C8Perf. Each of the full monolayer functionalised nanoparticles were exposed to UV light under different atmospheres for 16 hours, followed by dissociation of the monolayer chains from the silica surface via the oxidative cleavage method described in Section 2.3.3 and quantification using ^{1}H NMR. Figure 3.18 displays the yields of the C5Eth, C8Alk, C8BrAlk and C8Perf molecules under UV light with different ambient conditions.

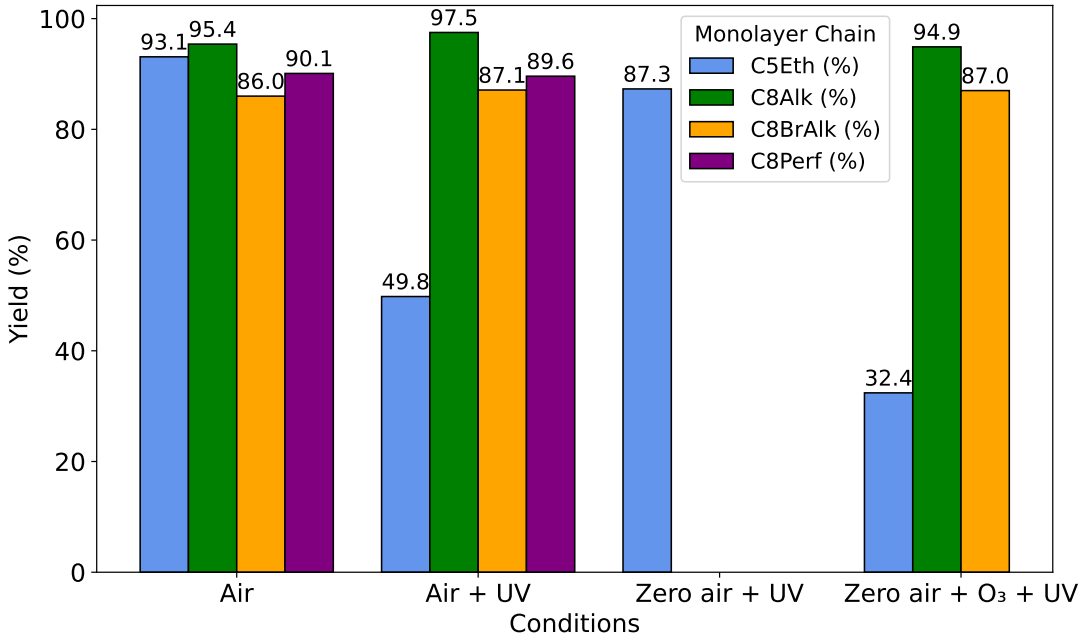

Figure 3.18: Yield of organic chains (%), which were dissociated from functionalised SiO_2 nanoparticles after UV exposure under different ambient conditions, including ambient air, zero air and zero air with ozone, for 16 hours. Quantification by ^{1}H NMR.

Initially, ambient laboratory conditions were tested to evaluate the effect of UV light and atmospheric molecules within the laboratory air on the degradation of the organic chains. As shown in Figure 3.18(Air + UV), C8Alk, C8BrAlk, and C8Perf did not show any degradation under the UV light; their yields were within experimental error (±3.4%, discussed in Section 2.3.3) of the baseline yields of dissociation after the monolayers were exposed in air in the absence of UV irradiation. This was expected as saturated hydrocarbons should have negligible absorption in the standard UV range (200-400 nm). Moreover, C-F bonds typically exhibit very weak absorption because of their strong bond strength; the high electronegativity of the fluorine atom results in fewer accessible excited states for UV absorption. However, the yield obtained for C5Eth chains after exposure to UV and air was almost half of the typical yield of dissociation for this molecule, suggesting degradation had occurred under the UV light. This was not foreseen as aliphatic ethers only begin to show pronounced absorption in the vacuum UV (100-200 nm) and have sufficiently low quantum yields of product formation above 200 nm [239]. Thus, this suggested that photodissociation of ozone had occurred under the UV lamp to produce atomic oxygen and subsequently ·OH radicals. These reactive species could then be initiating radical reactions within the monolayer chains.

This theory was further supported by conducting an experiment by exposing C5Eth monolayer chains to UV light under zero air conditions (1:4 mixture of O_2 and N_2). As shown in Figure 3.18, the yield obtained for the zero air experiment after dissociation of the chains from the silica surface was comparable with the yield without UV exposure. This implies that the UV irradiation itself had no effect on the C5Eth chains and that the degradation must be initiated by reactive species in the laboratory air generated under the UV light.

Ozone, at a concentration of 35 ppb, was added into the zero air flow during the UV exposure of functionalised nanoparticles. The results are displayed in Figure 3.18. A significant amount of degradation, ∼66%, was observed for the C5Eth chains upon UV light with added ozone. Moreover, the effect of ozone photolysis among the C8Alk and C8BrAlk chains was tested, shown in Figure 3.18. Here it was observed that no degradation occurred for the alkyl or tertiary alkyl chains. The BDE of C-H bonds in ether-containing chains is approximately 10 kcal/mol lower than in alkyl chains. This difference in bond strength makes the C5Eth chains more susceptible to radical attack and the subsequent propagation of radical reactions throughout the chains, compared to the C8Alk and C8BrAlk chains. As a result, a higher rate of degradation is observed for the C5Eth chains under UV light in the presence of ozone. Without autoxidation, the reaction of a monolayer with ·OH is negligible. Therefore, monolayers that do not undergo autoxidation show no degradation. In contrast, ether-containing monolayers experience degradation, primarily caused not by the direct reaction with ·OH, but by autoxidation following this reaction. This result is consistent with the results obtained via thermal initiation in Section 3.4.1.

3.4.2.2 Mixed Monolayers

As demonstrated previously, ozone could act as a radical initiator under the UV light, via photodegradation to form reactive atomic oxygen [237]. It was observed in the experiment of UV light exposure to C8Alk chains under zero air and ozone (35 ppb) conditions, that the C8Alk chains were unaffected by ozone under the UV light. This implied that the rate of radical propagation in C8Alk chains was

too low for significant degradation to be observed. However, degradation of the neighbouring C8Alk chains was observed after UV exposure of mixed monolayers containing C6One and C8Alk chains, as shown in Section 3.3.2. Thus, experiments were performed to evaluate whether ozone enhances the degradation of neighbouring C8Alk chains in the mixed monolayer containing C6One and C8Alk chains. This was to understand the cause of the degradation of C8AlK chains in the mixed monolayer upon UV light exposure.

Ozone was introduced into the zero air matrix to give a concentration of 35 ppb inside the box containing the mercury lamp and SiO_2 nanoparticles functionalised with a 1:1 mixed monolayer of C6One and C8Alk chains. Table 3.5 shows the yield of C8Alk chains after exposure to UV light for 8, 16 and 24 hours, and includes two control experiments: 16 hours of exposure to C8Alk mixed monolayers under zero air and ozone conditions without UV light and 16 hours of UV exposure to C8Alk chains in zero air and ozone conditions. It was observed that ozone without UV light did not affect the yield of C8Alk chains, both the ^{1}H NMR and GC-MS gave high yields of 88-97%. This was expected due to the unreactivity of ozone towards saturated hydrocarbons [240]. However, degradation was observed for the neighbouring C8Alk chains in the mixed monolayer upon UV light. This result suggested that the degradation of neighbouring C8Alk chains required the simultaneous presence of three factors: C6One chains, UV light and ozone.

Exposure Time (hours)	**Yield (% ^{1}H NMR)**	**Yield (% GC-MS)**
0	96.9	103.6
8	81.4	84.6
16	78.5	70.6
24	71.0	64.6
16 (ctrl, No UV)	97.4	88.9
16 (ctrl, C8Alk)	94.9	-

Table 3.5: Yield of C8Alk chains after exposure of the C6One-C8Alk mixed monolayer to UV at different times under zero air with added ozone (35 ppb), quantified by ^{1}H NMR and GC-MS. Control data after 16 hours in zero air and ozone environment with no UV exposure and after 16 hours UV exposure of homogeneous C8Alk chains in zero air and ozone environment is also included.

In order to understand the oxidation mechanism that required the presence of all three factors: C6One chains, UV light and ozone, a possible pathway has been hypothesised. During the photolysis of C6One chains, the predominant pathway is the Norrish type II pathway, as discussed in section 3.3, forming a surface-bound alkene group and acetone, as shown in Figure 3.20 [241]. The reactivity of ozone with surface-bound alkene-containing molecules is a fast process [174]. Thus, the alkene group formed during photolysis of C6One could readily react with ozone, via ozonolysis, to form an unstable primary ozonide which readily decomposes to form an aldehyde and a vibrationally excited Criegee intermediate. On the surface, these species are in close proximity to one another. Therefore, they are able to recombine to form a secondary ozonide, shown in Figure 3.20. The formation of a secondary ozonide is an established pathway for condensed phases [174]. However, in the gas phase, the aldehyde and Criegee intermediate can easily become separated, limiting

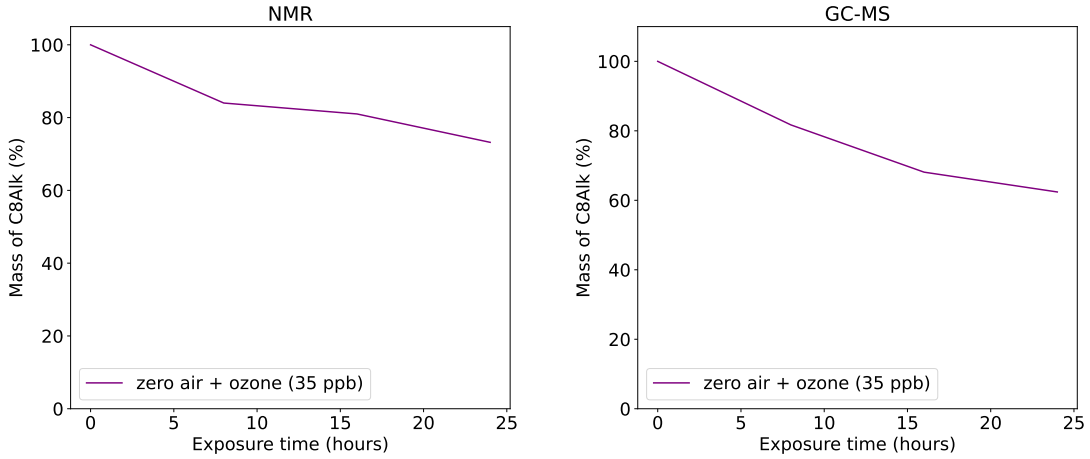

Figure 3.19: The degradation of neighbouring C8Alk chains after exposure of C6One-C8Alk mixed monolayer to UV light at increasing times under zero air with added ozone (35 ppb). Quantification by ^{1}H NMR (left) and GC-MS (right).

recombination [242]. Previous studies have shown that secondary ozonides are stable but can be easily photolysed [242]. There has been evidence for the photolysis of secondary ozonides to follow a radical mechanism, involving initial homolysis of the O-O bond to produce a biradical as shown in Figure 3.20 [242–244]. It is known from previous results that there is no autoxidation of the C8Alk chains under these conditions. Thus, this hypothesis could explain faster spreading of radical reactions within the monolayer as it provides an additional pathway for H-abstraction of the neighbouring C-H bonds.

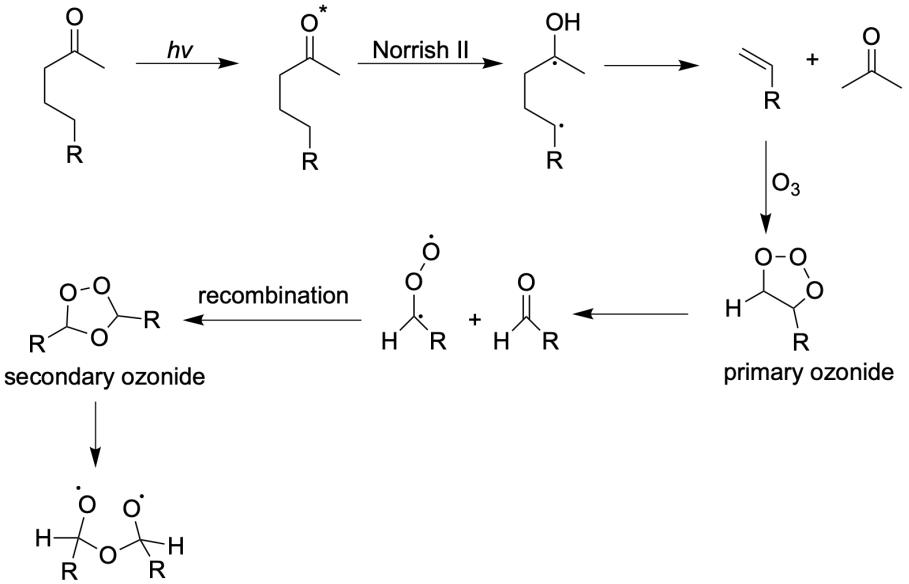

Figure 3.20: Photolysis of C6One chains, followed by reaction with ozone.

The rate of degradation of C6One chains in the mixed monolayer under zero air and ozone conditions was also greater than in zero air conditions, as shown in Figure 3.21. This suggests that the system may be primarily influenced by photodegrada-

tion products of ozone, such as atomic oxygen, which initiate radical reactions in the C6One chains. Consequently, facilitating a faster rate of degradation of the C6One chains and more radical pathways within the monolayer chains. The increase in rate of C8Alk degradation could also, therefore, be due to a larger quantity of radical reactions occurring within the monolayers from both the photolysis of C6One and the atomic oxygen reactivity as a result of ozone photodegradation.

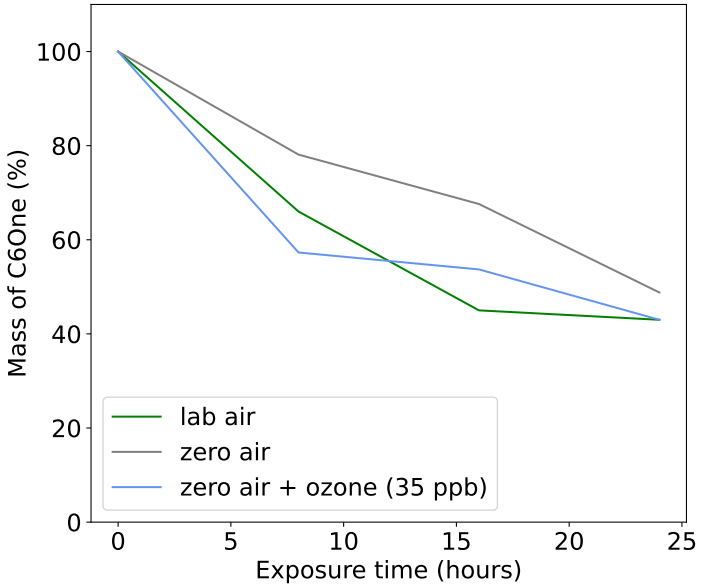

Figure 3.21: Degradation of C6One chains in the C6One-C8Alk mixed monolayer upon UV light under zero air and ozone (35 ppb) conditions, compared to zero air and laboratory air conditions. Quantification by ^{1}H NMR.

3.4.3 Effect of Functionality

Previous discussions have highlighted that ozone photodissociation is the dominant pathway for radical initiation under UV irradiation of mixed C6One and C8Alk monolayers in ambient air. This section aims to further investigate the propagation of radical reactions in ether-containing molecules compared to other organic molecules in monolayer systems. Unfortunately, these experiments were performed prior to establishing the role of ozone, therefore, they involve mixed monolayers of C6One chains with various other organic chains, rather than single component monolayers. Despite this, these experiments remain valuable, as the presence of C6One does not significantly perturb the overall results.

SiO_2 nanoparticles were functionalised with mixed monolayers of C6oneOEt and other organic alkoxyl silanes, including: C8AlkOEt, C8EneOEt, C8PerfOEt, C7Eth2OEt, and C8BrAlkOEt, displayed in Figure 3.22.

Mixed monolayers on SiO_2 nanoparticles have been exposed to UV light for 8-24 hours under laboratory conditions. These mixed monolayers include: C8Perf mix, C8BrAlk mix, C8Alk mix, C5Eth mix and C7DiEth, shown in Figure 3.22. After exposure to UV light, each batch of functionalised SiO_2 nanoparticles were

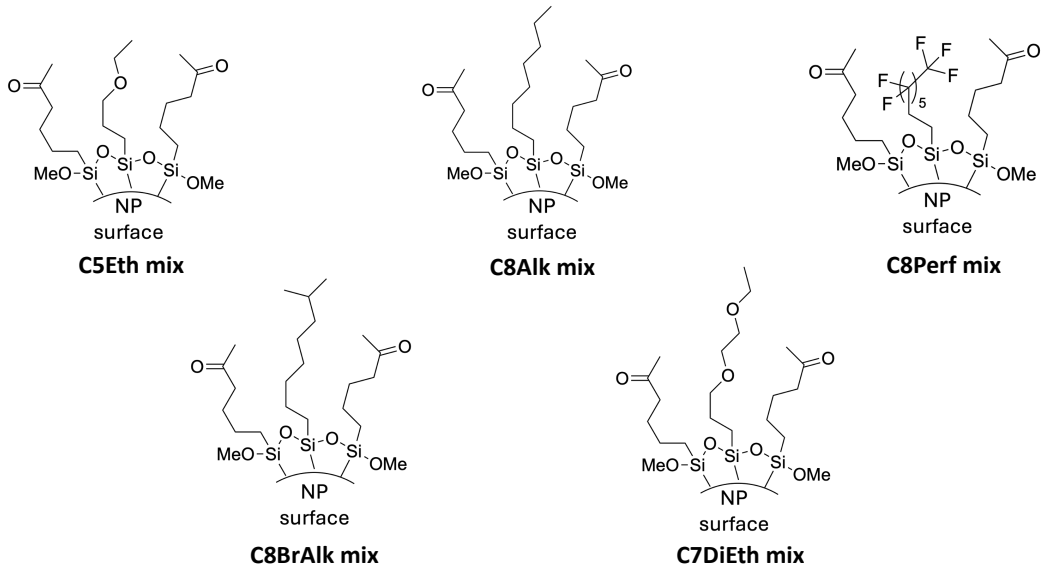

Figure 3.22: The mixed monolayers used in the reactivity study of autoxidation processes in monolayers.

dissociated, the organic chains cleaved from the silica surface and quantified by ^{1}H NMR and GC-MS.

The yields obtained for C8Perf mixed monolayers upon UV light exposure are shown in Table 3.6. The results indicate that no degradation is observed for the C8Perf chains upon radical initiation as all yields were within 10% of each other from both the ^{1}H NMR and GC-MS data. This was expected as a result of the relatively high C-F bond strength and consequently their unreactivity toward radical reactions [119]. Each yield for exposed mixed monolayers was normalised to the yield of their corresponding non-exposed mixed monolayers and the results are shown in Figure 3.23. Figure 3.23 (purple line) further illustrates the lack in degradation of the C8Perf molecules.

Exposure Time (hours)	**Yield C8Perf (% ^{1}H NMR)**	**Yield C8Perf (% GC-MS)**
0	91.4	94.8
8	89.0	88.8
16	80.8	96.5
24	84.2	98.2

Table 3.6: Yield of C8Perf chains after exposure of C8Perf-C6One mixed monolayers to UV at different times under laboratory air conditions. Quantification by ^{1}H NMR and GC-MS.

The yields obtained for the C8BrAlk and C8Alk, Table 3.7 and 3.8 respectively, suggest that the rate of degradation for the straight alkyl chain is faster than the rate for the branched/tertiary-containing alkyl chain. The C8Bralk chains could only be quantified via ^{1}H NMR due to this molecule not being commercially available to use as a GC-MS calibrant. Nevertheless, the trend in degradation was observed in the GC-MS chromatograms as the ratio of C8BrAlk to the internal standard decreased with increasing UV exposure, shown in Figure 3.23 (orange and green lines). This result was unexpected, as tertiary carbons are typically more reactive toward

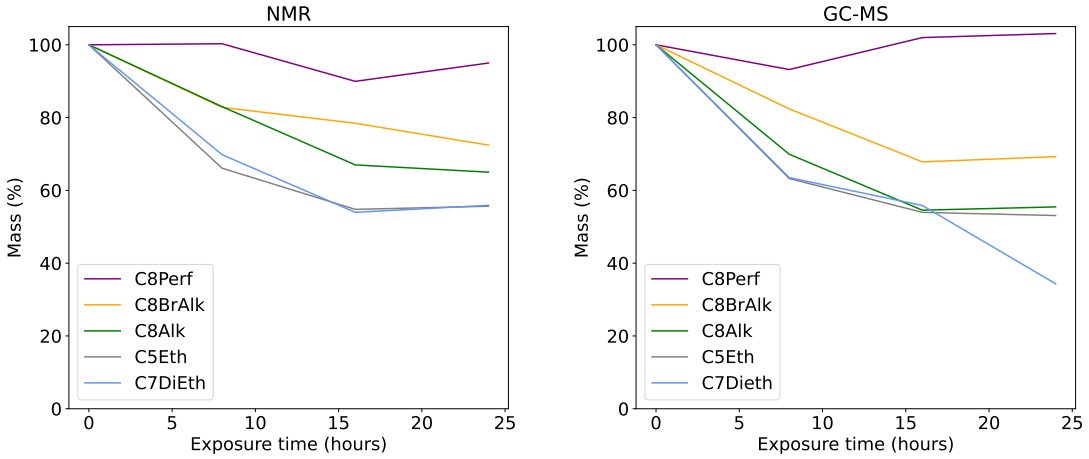

Figure 3.23: The degradation of various neighbouring organic chains in the mixed monolayer with C6One chains, including: C8Perf, C8BrAlk, C8Alk, C5Eth and C7DiEth, after exposure to UV light at increasing times. Experiment conducted under ambient laboratory conditions. Quantification by ^{1}H NMR (left) and GC-MS (right)

H-abstraction by peroxyl radicals, compared to secondary carbons, exhibiting reactivity up to 10 times higher due to their greater stability. [122]. In bulk liquids, an alkyl chain containing a branched moiety can exhibit two dominant pathways as two different radical types form. After the formation of peroxyl radicals by the reaction of a carbon centred radical with oxygen, primary/secondary centred carbons mainly terminate to form stable products, whereas, tertiary peroxyl radicals mainly propagate via formation of alkoxyl radicals which are highly reactive towards H-abstraction (see Figure 1.30) in Section 1.5.2.3) [149]. However, in a monolayer system the probability of two peroxyl radicals being in close enough proximity to terminate is very low, as discussed in Section 3.2.2. Therefore, the propagation of radical reactions amongst branched alkyl in a monolayer is slow. Moreover, the differences within a monolayer system compared to gas phase or in bulk liquids, could be due to steric hindrance or due to lack of mobility within monolayers and so the radicals generated within the monolayer are unable to reach the tertiary carbon. Nevertheless, this result is unexpected and remains inconclusive.

Exposure Time (hours)	**Yield C8BrAlk (% ^{1}H NMR)**
0	84.1
8	64.0
16	60.0
24	50.7

Table 3.7: Yield of C8BrAlk chains after exposure of C8BrAlk-C6One mixed monolayers to UV at different times under laboratory air conditions. Quantification by ^{1}H NMR.

A higher reactivity rate is seen for the C5Eth and C7DiEth chains, shown in

Exposure Time (hours)	Yield C8Alk (% ^{1}H NMR)	Yield C8Alk (% GC-MS)
0	85.9	80.5
8	71.3	56.3
16	57.8	44.2
24	56.2	44.3

Table 3.8: Yield of C8Alk chains in the C8Alk-C6One mixed monolayer after exposure to UV at different times under laboratory air conditions. Quantification by ^{1}H NMR and GC-MS.

Figure 3.23. The rate of a peroxyl radical abstracting a H from these molecules is 100 times faster than for a straight alkyl chain [121, 123]. This suggests that radical propagation within these chains will be a faster process, leading to faster rates in degradation. The C5Eth and C7DiEth showed very similar rates in degradation, Figure 3.23 (grey and blue lines), suggesting the extra ether group within the C7DiEth chains did not make a significant difference to the rate in degradation of those chains. The yields obtained for C5Eth and C7DiEth were also very similar at each UV exposure time point, shown in Table 3.9 and 3.10. As discussed in Section 3.4.2, ozone photolysis plays a key role in the degradation of ether chains. Under laboratory conditions, the concentration of ozone is approximately 30 ppb. Thus, the increased rate in degradation of the ether-containing molecules is likely due to reactivity from atomic oxygen, and subsequently ·OH radicals, generated via ozone photolysis. In bulk solution, the rate coefficient for the reaction of ·OH radicals with ethers has been compared depending on the number of ether-group functionality within the alkyl chains. It was reported that the rate coefficient for the reaction of an ·OH radical with diethyl ether (one ether group) versus diethoxymethane (2 ether groups) was comparable at 8.1×10^8 $M^{-1}s^{-1}$ and 9.2×10^8 $M^{-1}s^{-1}$, respectively. However, statistically the reaction should spread faster as there are more adjacent activated C-H groups. The similarity between the degradation rate of C5Eth and C7Dieth could, therefore, be due to a steric effect, such as reduced packing efficiency in the C7DiEth monolayer. Nevertheless, the lower BDE of the CH_2OCH_2-H bond ($\sim$ 93 kcal/mol) enables a faster rate in H-abstraction by newly formed peroxyl radicals within the monolayer chains [121]. As a result, radical propagation can occur more rapidly within these monolayer systems, allowing autoxidation to proceed—unlike in simple alkyl chains or perfluoro alkyl chains, where autoxidation is not observed. This result is consistent with the previous results from the thermal initiation experiments and ozone photolysis experiments of single component monolayers.

Exposure Time (hours)	Yield C5Eth (% ^{1}H NMR)	Yield C5Eth (% GC-MS)
0	83.6	81.8
8	55.8	53.6
16	46.4	45.9
24	48.3	47.7

Table 3.9: Yield of C5Eth chains in the C5Eth-C6One mixed monolaye after exposure to UV at different times under laboratory air conditions. Quantification by ^{1}H NMR and GC-MS.

Exposure Time (hours)	Yield C7DiEth (% ^{1}H NMR)
0	83.9
8	58.6
16	45.3
24	46.9

Table 3.10: Yield of C7DiEth chains in the C7DiEth-C6One mixed monolayer after exposure to UV at different times under laboratory air conditions. Quantification by ^{1}H NMR.

In summary, the functionality of organic chains within the monolayer system significantly influences the rate of autoxidation. The results from thermally initiated radical reactions align well with those from UV-initiated radical reactions, showing that ether-containing chains facilitate the propagation of autoxidation reactions, while other organic molecules, such as simple alkyl and perfluoro-containing chains, do not. This leads to the question: What happens to the ROO· radicals formed in alkyl chains upon radical initiation, if they cannot terminate due to limited mobility within the monolayer or abstract a hydrogen from a neighbouring chain? What is their fate? The next section will aim to address these questions.

3.5 Fate of Peroxyl Radicals

Autoxidation of alkyl chains can lead to the formation of ROO· radicals via initial H-abstraction by a reactive species, followed by reaction with O_2. The fate of these ROO· was discussed in Section 1.5.2 for bulk liquids, the gas-phase and polymer systems. Experimental results have shown that the ROO· radical is unlikely to propagate in an alkyl monolayer due to the slow reactivity of H-abstraction by an ROO· radical, despite the proximity of adjacent chains. A monolayer can experience interfacial reactions between gas-phase species and surface-attached species. Thus, the reactivity of ROO· radicals with atmospheric molecules needed to be explored. Discussions in Section 1.5.2 and results from the kinetic model in Section 3.2.1, suggested that a dominant pathway for ROO· in the gas-phase is through reaction with NO to form more reactive RO· radicals. Moreover, in areas of low NO concentration, another dominant pathway for ROO· radicals in the gas phase is via self-reaction with other ROO· radicals, which leads to either the formation of reactive RO· or the formation of stable species and no radical propagation, depending on the molecular structure [106]. This means ROO· radicals could react with some gas phase molecules to form more reactive species that can propagate the reaction in the monolayer.

In this section, the fate of the ROO· in monolayer systems will be explored by altering the surrounding atmospheric environment of the monolayers; zero air with added NO (40 ppb) and zero air with added VOCs (110 ppb). The radical initiation method used in these experiments was the ketone photolysis method, using mixed monolayers of C6One and C8Alk and UV irradiation. This method was employed as it provided radical initiation directly within the monolayer chains. Although it has shown to be not the most effective due to the Norrish II pathway, it involves radical initiation without the use of any other gas-phase species.

3.5.1 Nitric Oxide (NO)

ROO· radicals are highly reactive towards NO to form more reactive RO· radicals [101], shown in Figure 3.24. In typical indoor environments, the concentration of NO is approximately 5-10 ppb [224]. The pseudo-first-order rate coefficient for the reaction of an ROO· radical with NO to form an RO· radical and NO_2 is $\sim$0.1 s^{-1} at an NO concentration of 10 ppb, a relatively high rate coefficient for ROO· radical reactivity [245]. RO· radicals are approximately 10^6 times faster at H-abstraction of neighbouring alkyl chains than the corresponding ROO· radical [149]. This means formation of RO· radicals within the monolayer could accelerate the rate of autoxidation of the C8Alk chains, thus, increasing their degradation rate. This pathway represents one of the dominant pathways of ROO· radicals within alkyl monolayers, highlighting a key difference between autoxidation in bulk and monolayer systems.

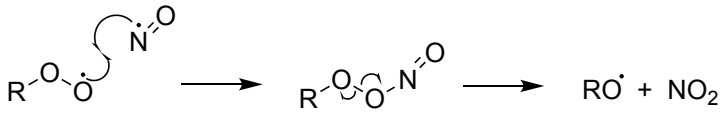

Figure 3.24: Mechanistic scheme of the reaction between ROO· radicals and NO to form RO· radicals.

Therefore, to evaluate the effect of NO on the degradation of the neighbouring C8Alk chains, NO gas at a concentration of 40 ppb was added to the zero air flow. A multigas blender was used to generate NO (40 ppb) in a zero air matrix to give a total flow rate of 2 L/min entering the box containing the mercury lamp and functionalised SiO_2 nanoparticles. A higher concentration of NO compared to typical indoor air allowed a potentially more significant effect on the rate of degradation to be observed. The NO concentration was measured downstream of the sample box using a T200 (Teledyne API Chemiluminescence T200, S/N 023828) to confirm the concentration of NO was 40 ppb in the experimental environment. The box was purged for $>$ 30 mins before turning on the UV lamp. C8Alk mixed monolayer functionalised SiO_2 nanoparticles were exposed to UV light for 8, 16 and 24 hours, before being dissociated from the silica surface and quantified by ^{1}H NMR and GC-MS.

The yield of C8Alk chains after UV light exposure is shown in Table 3.11. This table includes data from the control experiment of C8Alk mixed monolayers exposed to the NO and zero air gas mixture for 16 hours without UV light. This was to ensure degradation of the C8Alk chains was not caused by NO alone and was due to the reactivity with newly formed ROO· radicals after photolysis of C6One. As indicated by the C8Alk yield in the control experiment, no degradation was observed in the absence of UV light, confirming NO molecules alone do not affect the rate of degradation of C8Alk chains. Degradation of the C8Alk chains was observed after 24 hours. This is also represented in Figure 3.25, a plot of C8Alk mass (%) normalised to the yield of the non-exposed C8Alk mixed monolayer.

These results suggest that NO could be reacting with the newly formed ROO· radicals to form more reactive RO· radicals within the mixed monolayer. However, the extent of degradation is not as significant as observed under ambient laboratory

Exposure Time (hours)	Yield (% ^{1}H NMR)	Yield (% GC-MS)
0	83.9	84.2
8	81.8	81.3
16	80.7	80.6
24	66.3	73.2
16 (ctrl, No UV)	84.3	86.2

Table 3.11: Yield of C8Alk chains after exposure of C8Alk-C6One mixed monolayers to UV at different times under zero air with added NO (40 ppb), quantified by ^{1}H NMR and GC-MS. Control data after 16 hours in zero air and NO environment with no UV exposure is also included.

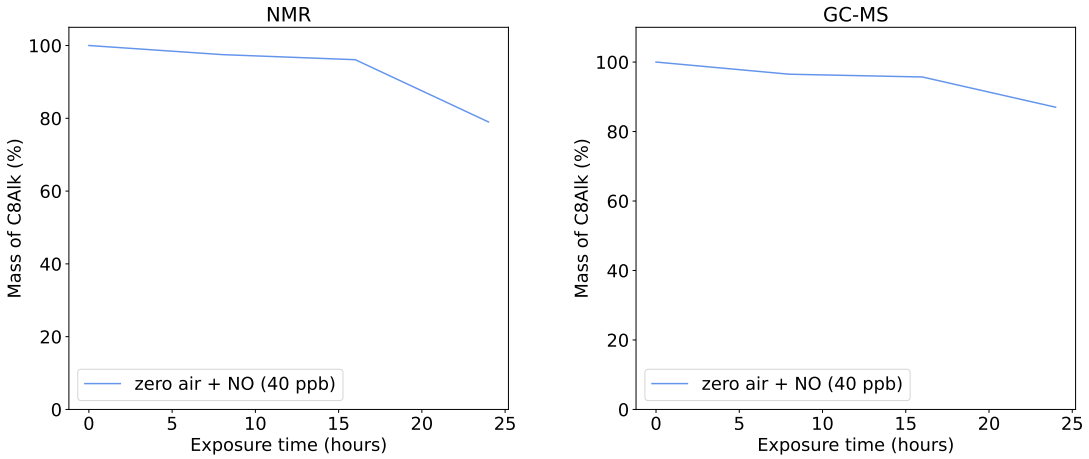

Figure 3.25: Yield of C8Alk chains after exposure of mixed C8Alk-C6One monolayers to UV light at increasing times under zero air with added NO (40 ppb). Quantification by ^{1}H NMR (left) and GC-MS (right).

conditions, suggesting that NO is not the only atmospheric molecule aiding in the increased rate of radical propagation within the monolayers. Nevertheless, this experiment enabled the lifetime of ROO· radicals to be estimated because under these conditions (zero air and NO (40 ppb)), the dominant reaction pathway would be for ROO· radicals to react with NO. The rate of formation of ROO· radicals could be estimated to be equal to the rate of C6One decay. The rate of ROO· formation is therefore:

$$\text{Rate of RO}_2\text{ formation} = k_1[A] \tag{3.15}$$

where k_1 is the rate constant and [A] is the concentration of C6One chains. The amount of C6One chains reacted across 24 hours (86400 s) was 43%, calculated from the dissociation ^{1}H NMR yield of C6One chains after the C6One-C8Alk mixed monolayer was exposed to UV for 24 hours. Hence,

$$[A]/[A]_0 = e^{-k_1 t} \tag{3.16}$$

$$k_1 = 6.5 \times 10^{-6}\ \mathrm{s}^{-1} \tag{3.17}$$

From the literature, ROO· radicals react with NO with the second order rate constant, k_3, at around 1×10^{-12} molecules^{-1} cm^3 s^{-1} [101]. At 40 ppb NO (4×10^{11} molecules cm^{-3}), the pseudo first order rate constant for ROO· radical degradation can be calculated to be

$$k_2 = k_3[NO] = 0.4\ \mathrm{s}^{-1}. \tag{3.18}$$

Furthermore, the proportion of active ROO· radicals on the monolayer surface could be estimated. Following a steady-state approximation, the concentration of ROO· radicals on the surface at a given time, can be expressed as

$$[ROO\cdot] = \frac{k_1[A]}{k_2}. \tag{3.19}$$

This gave the proportion of molecules on the surface which are ROO· radicals to be 1×10^{-3}%. This value was used in the statistical model in Section 3.2.2, to model the probability of ROO· radicals being in close enough proximity to be able to react with each other in the monolayer.

3.5.2 Carbonyl-containing VOCs

In the laboratory, there is a regular use of solvents including acetone, ethyl acetate, ethers and petroleum-based liquids, the majority of which are volatile. Thus, the concentration of VOCs in the laboratory air is likely to be high. A study has shown that the concentration of VOCs emitted from laboratory buildings can reach up to ∼100 ppm, which is at least 10 times greater than non-laboratory buildings [246].

In the troposphere, VOCs undergo chemical processes including photolysis, reaction with OH radicals during daylight hours, reaction with NO_3 during nighttime hours and reaction with O_3 [186]. The reaction mechanism after initial reaction with radicals depends on the VOC. In the laboratory environment, acetone is one of the most commonly used solvents. Gaseous acetone can undergo photolysis and react with OH radicals, however, no direct reaction with O_3 has been observed [247].

Under the mercury lamp (254 nm) photolysis of acetone can occur. In this process, the absorption of UV light causes decomposition of acetone to form a methyl and acetyl radical (equation 3.20)[248].

$$CH_3COCH_3 + hv \rightarrow CH_3CO\cdot + \cdot CH_3 \tag{3.20}$$

Due to the presence of O_2 in our system, the attack of O_2 toward the methyl and acetyl radical would be the next step (equations 3.21-3.23). The reaction of O_2 with acetyl radicals can result in the formation of formaldehyde, ·OH radicals and carbon monoxide, equation 3.21. The formation of ·OH radicals could therefore initiate radical reactions in the surface-bound molecules. Moreover, addition of O_2 to the acetyl radical can also occur, forming acetyl peroxyl radicals, equation 3.22. These peroxyl radicals could either abstract H from nearby organic molecules or self-react to form more reactive alkoxyl radicals.

$$CH_3CO\cdot + O_2 \rightarrow H_2CO + \cdot OH + CO \tag{3.21}$$

$$CH_3CO\cdot + O_2 \rightarrow CH_3CO(OO\cdot) \tag{3.22}$$

The methyl radical can react with O_2 to form methyl peroxy radicals, which again can follow competitive pathways for self-reaction or H-abstraction, shown in equations 3.23-3.25.

$$\cdot CH_3 + O_2 + M \rightarrow CH_3OO\cdot + M \tag{3.23}$$

$$2CH_3OO\cdot \rightarrow 2CH_3O\cdot + O_2 \tag{3.24}$$

$$CH_3OO\cdot + RH \rightarrow CH_3OOH + R\cdot \tag{3.25}$$

Consequently, all of these pathways generate radical species that can initiate radical reactions within the monolayer molecules. Additionally, any peroxyl radicals formed during photolysis of acetone may react with peroxyl radicals formed within the monolayers, thus generating reactive alkoxyl radicals. The key difference with acetone compared to C6One is that acetone cannot undergo Norrish II reaction as its chain length is too short for intramolecular H abstraction, hence it produces radicals instead. Therefore, it was crucial to investigate the effect of acetone (or any carbonyl-containing VOC) on the degradation of C8Alk chains in the mixed monolayer.

To make a constant concentration, acetone (20 μL) was injected into a 2 L evacuated gas cylinder before being pressurised up to 100 bar with oxygen-free nitrogen. The mixture was allowed to equilibrate before being analysed directly using a selected ion flow tube mass spectrometer (SIFT-MS) to determine its concentration (5.0 ppm). The gas cylinder was attached to the zero air flow to allow a concentration of 100 ppb to enter the experimental set-up. A concentration of 100 ppb acetone was sufficient to evaluate the effect on monolayer degradation.

Table 3.12 shows the yield of neighbouring C8Alk chains upon UV light exposure in a zero air and acetone (110 ppb) environment. A control experiment was conducted for full C8Alk monolayers under these conditions to investigate whether acetone affected the degradation of C8Alk chains without the presence of C6One chains. It was observed that no degradation of C8Alk chains occurs during exposure to UV and added acetone. Thus, it could be concluded that the radicals generated via acetone photolysis did not cause significant impact on the degradation rate of C8Alk chains alone. However, in a mixed monolayer of C8Alk and C6One chains, the C8Alk chains appeared to degrade by approximately 40% across 24 hours of UV exposure. This is also represented in Figure 3.26, a plot of the mass of C8Alk chains normalised to the mass of non-exposed monolayers.

These results suggest that the degradation of C8Alk chains depends on radical initiation through the photolysis of C6One chains, as well as the interaction with photodegradation products of acetone. This could be due to the ROO· radicals formed within the monolayers upon radical initiation from the excited C6One chains, reacting with methyl peroxyl radicals as a product of acetone photodegradation. Thus, the termination of ROO· radicals could either form more reactive alkoxyl radicals on the surface or form stable products such as a carbonyl and alcohol, which upon UV light the carbonyl would initiate further radical reactions. Consequently, causing the rate of degradation of neighbouring C8Alk chains to increase. Moreover,

Exposure Time (hours)	Yield (% ^{1}H NMR)	Yield (% GC-MS)
0	96.9	103.6
8	83.2	84.8
16	77.6	78.3
24	61.6	71.2
16 (ctrl, C8Alk)	99.1	97.1

Table 3.12: Yield of C8Alk chains after exposure of C8Alk-C6One mixed monolayers to UV at different times under zero air with added acetone (100 ppb), quantified by ^{1}H NMR and GC-MS. Control data after 16 hours UV exposure of C8Alk chains in zero air and acetone environment is also included.

a photodegradation pathway for acetone, equation 3.21, produces ·OH radicals. The reactivity of ·OH radicals with hydrocarbon chains and ketone-containing molecules via H-abstraction is relatively high and can initiate radical reactions within the monolayer [186]. The carbon-centred radical can react with O_2 to form more ROO· radicals which can react with other ROO· radicals, as discussed above, to form more reactive species. Thus, increasing the rate of autoxidation within the monolayer.

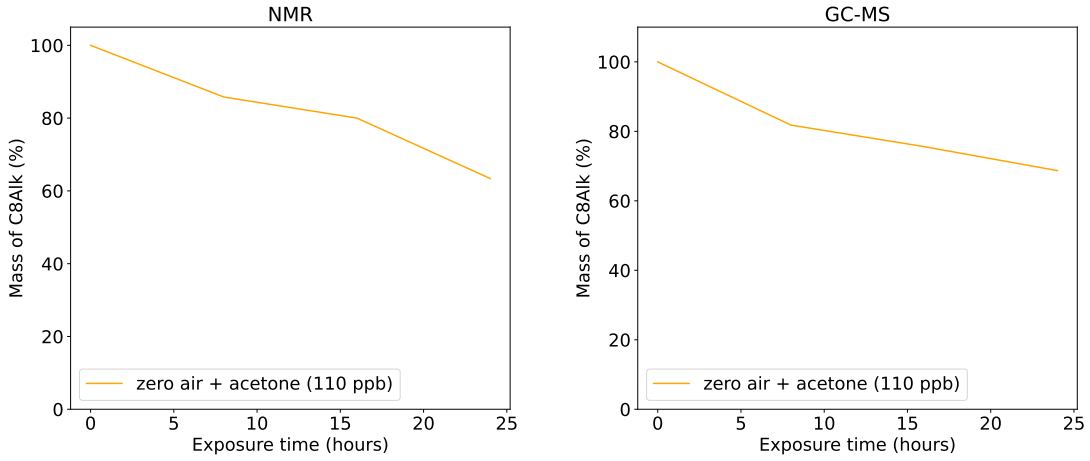

Figure 3.26: The degradation of neighbouring C8Alk chains after exposure of C8Alk-C6One mixed monolayers to UV light at increasing times under zero air with added acetone (100 ppb). Quantification by ^{1}H NMR (left) and GC-MS (right).

The addition of acetone gas to the zero air also affected the rate of degradation of the C6One chains, shown in Figure 3.27. The rate of degradation was similar to that in laboratory air, suggesting acetone in the laboratory air could be increasing the rate of C6One degradation. The increased rate is likely due to the generation of OH radicals upon acetone photolysis, initiating radical reactions in the C6One chains.

Acetone has demonstrated to have a positive impact on the degradation rate of mixed monolayer chains, increasing the quantity of reactive species within the monolayer and facilitating a higher degree of autoxidation throughout the monolayer chains.

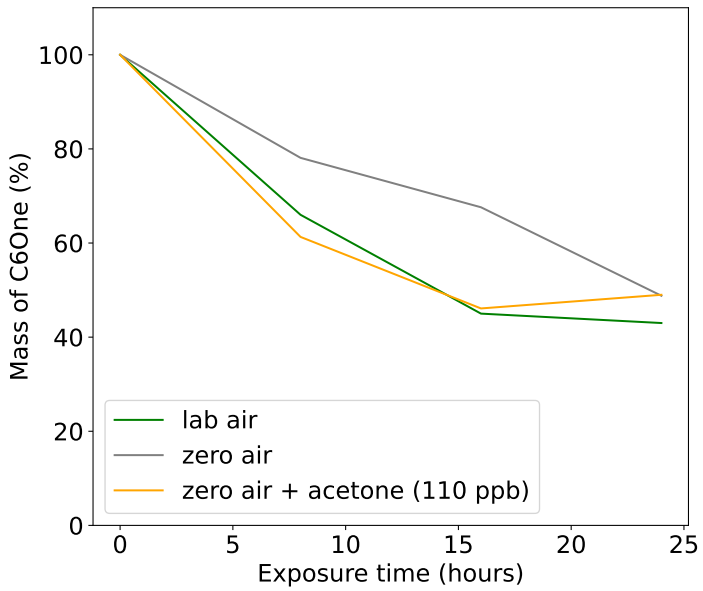

Figure 3.27: Degradation of C6One chains in the C8Alk-C6One mixed monolayer upon UV light exposure under zero air and acetone (110 ppb) conditions, compared to zero air and laboratory air conditions. Quantification by ^{1}H NMR.

In summary, these experiments have been crucial for understanding the mechanism of surface oxidation. Autoxidation within monolayer systems is initiated by H-abstraction by a radical species to produce a carbon-centred radical, which would immediately react with oxygen to form an ROO· radical, shown in Figure 3.28. Thus, ROO· radicals would be present within the monolayer chains. The fate of these ROO· radicals was investigated. Previous experimental results on the propagation of radical reactions in monolayer chains, Section 3.4, showed that the likelihood of a ROO· radical abstracting a H from a neighbouring chain is very low. Moreover, the chances of two ROO· radicals being in close enough proximity in the monolayer is too low for this to be a possible reaction pathway within the monolayer, demonstrated using the statistical model in Section 3.2.2. It was theorised, based on current literature and knowledge of ROO· radical chemistry in the gas-phase, that the dominant pathways for ROO· radical reactivity is through the reaction with NO or self-reaction with other ROO· radicals, shown in Figure 3.28. The fate of the ROO· radical was probed by adding either NO or other ROO· radicals (via photolysis of VOCs) into the experimental system. The addition of VOCs, particulary carbonyl-containing VOCs, had a significant impact on the rate of degradation of neighbouring chains, generating reactive species upon UV light which facilitated a faster rate of surface oxidation. The addition of NO showed slight increase in degradation of neighbouring chains, insinuating reactivity with ROO· radicals to form more reactive RO· radicals which would increase the rate of autoxidation. However, the extent of degradation was too low to suggest this was the dominant autoxidation pathway in ambient air. This suggests that stranded ROO· radicals likely undergo alternative unknown reactions, either with the surface or atmospheric contaminants, at reaction rates at least as fast as the reaction with NO, as illustrated in Figure 3.28.

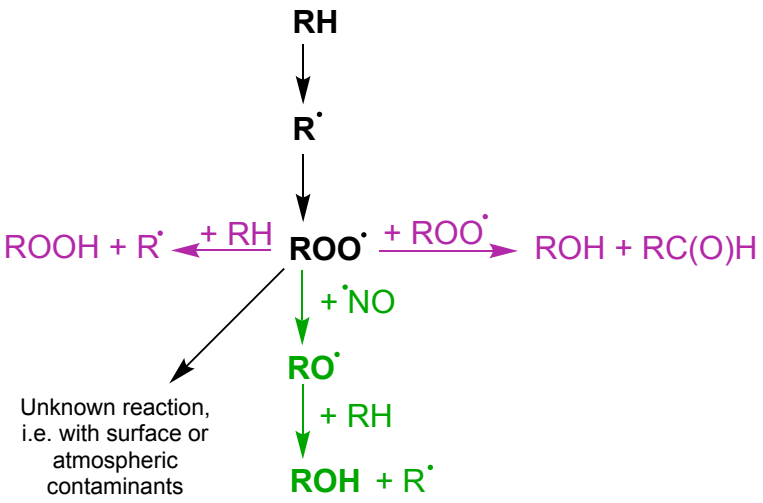

Figure 3.28: Proposed reaction scheme for the oxidation of a surface. The least likely reaction pathways shown in pink. The most dominant pathway shown in black.

3.6 Conclusions

Autoxidation of alkane surfaces has been investigated computationally and experimentally. The kinetic model for bulk solutions suggests that the dominant pathway in the autoxidation of straight alkyl chains is the termination of peroxyl radicals, leading to the formation of stable alcohol and carbonyl-containing compounds. However, the limited mobility of organic molecules attached to silica surfaces means that most newly formed peroxyl radicals are too far apart to interact, as demonstrated by the statistical model. Therefore, these peroxyl radicals must react with nearby molecules, such as atmospheric compounds or neighbouring organic chains, potentially initiating the propagation of radical reactions throughout the monolayer. Since bulk studies are not directly applicable to surface oxidation, the aim was to investigate the fate of peroxyl radicals and determine whether autoxidation on surfaces follows the same reactivity observed in bulk systems.

This was investigated experimentally using functionalised SiO_2 nanoparticles. Three different methods of radical initiation were utilised: thermal initiation using AIBN, ozone photolysis and ketone photolysis. The experiments using mixed monolayers of ketone-containing chains and organic chains under UV light, serendipitously led to the discovery that ozone photolysis was the major radical initiation under these conditions. Ketone photolysis alone did not contribute significantly to the radical initiation of organic chains within the monolayer due to the predominant Norrish II pathway. The experiments with thermal initiation, therefore, prevented the photolysis of ozone and could be used to compare the reactivity of organic chains after radical initiation.

These results highlighted the dependence of chain functionality on the propagation of radical reactions. All three radical initiation methods demonstrated that the reaction spreads with ether-containing chains but not with linear or branched alkane chains. This suggests that stranded ROO· radicals in alkane chains still do not initiate adjacent chains. Experiments with added NO, which readily reacts with peroxyl radicals to form more reactive alkoxyl radicals, indicated that NO con-

tributes to reaction spreading. However, this process does not appear to be the dominant pathway at realistic concentrations, although it likely contributes to some extent. Therefore, it is probable that isolated ROO· radicals, which cannot recombine due to being too far apart, undergo alternative reactions, possibly involving the surface or atmospheric contaminants. Given the very low concentration of ROO· radicals on the surface, even minimal atmospheric contamination could be sufficient to quench these radicals. As a result, the trends observed in bulk solutions appear to be applicable to monolayers, despite the limited mobility of ROO· radicals.

Chapter 4

Application to Sensing

4.1 Introduction

Air quality and climate are highly influenced by atmospheric radicals, particularly hydroxyl (·OH) and nitrogen oxides (NOx) [249, 250]. These species are the main drivers of chemical processes that determine atmospheric composition and thus their detection is critical for understanding our atmosphere. Currently, atmospheric radicals are measured using spectroscopic and mass spectrometric techniques, which are expensive and complex [249]. Therefore, there is a need for the development of new radical detection methods which are inexpensive and can be deployed more easily.

Silicon nanowire (SiNW)-based sensor devices were introduced in 2001 and have since received considerable interest as a general platform for the sensitive electrical detection of chemical and biological species [251]. A schematic representation of a SiNW)-based sensor device is shown in Figure 4.1. SiNWs are efficient sensor materials due to their high surface area-to-volume ratio, their ability to chemically interact with analytes on the surface and their ability to perform at ambient temperatures [252, 253]. When incorporated into transister-based devices, their sensing mechanism relies on the interaction between target analytes and the nanowire surface, where these molecules behave like a top gate, altering the electrical conductance of the nanowire, which forms the transister's channel [254]. This enables molecular interactions with the SiNW to be directly translated into easily detectable electrical signals. The adsorption of an oxidative species, such as NO_2, has been known to increase the concentration of free charge carriers (holes) and enhance the electrical conductivity in mesoporous Si layers [255].

A key advantage of SiNW-based sensors is that the nanowire surfaces can be modified to allow for the specific detection of analytes [22]. The application of SAMs to the surface modification of such sensors can offer considerable advantages, such as the ability to tune the chemical affinity on the surface. This can promote specific chemical interactions on the SAM-modified surface and thus, enhance the selectivity in gas-sensing applications [100]. Moreover, their small size with high surface area to volume ratio means a few gas molecules are sufficient to alter the electrical properties of the sensing elements, allowing the detection of a low concentration of gas within seconds [252].

There has been plenty of research dedicated to the detection of volatile organic compounds (VOCs) using SAM functionalised silicon nanowires (SiNWs) [256]. Functionalisation of SiNWs can help to improve the sensitivity and recognition to-

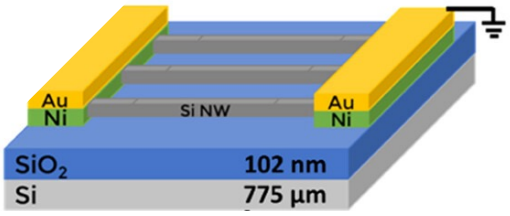

Figure 4.1: Schematic representation of a Si-JNT device. Adapted from [254].

wards specific analytes [257]. In the literature, oxide-coated SiNW field effect transistors (FETs) have been functionalised with amino silane molecules to form SAMs which provided relatively high sensitivity toward pH and a range of biological receptors to selectively detect biological species, such as DNA, proteins and viruses in solution [258]. Moreover, the detection of polar gas analytes, such as NO, NH_3, NO_2 and CO, have been reported using SiNW sensors [259]. SAM-modified SiNW-based sensors have also been used for the detection of VOCs [260].

Si JNTs modified with alkoxysilanes, such as OTS, have demonstrated detection of NOx, NH_3, and other VOCs at concentrations ranging from ppm to ppb levels, with response times on the order of seconds to minutes [257]. However, device stability remains a challenge: monolayer degradation via hydrolysis or environmental contamination can reduce sensitivity over time, with reported operational lifetimes ranging from several weeks to months under ambient conditions [257]. Compared to the requirements for detecting ·OH radicals, where ppt sensitivity, rapid response, and high stability in highly oxidative environments are essential, these devices highlight both the promise and current limitations of silane-functionalised Si-based sensors.

Wang *et al.* studied the effects of different functional groups within the SAMs attached to silicon nanowire-based field effect transistors (FET) for VOC detection [260]. The addition of a molecular layer to the SiNW surface induces a dipole moment due to the partial positive or negative charges of the functional groups within the layer. The electrostatic field of the molecular layer can, in turn, influence the charge carriers at the SiNW surface, affecting the sensor's electrical properties and response. Wang *et al.* found that the dipole moment of the molecular layer changed upon exposue to VOCs due to 3 main situations: 1) dipole-dipole interaction between the monolayer and the polar VOCs; 2) induced dipole-dipole interactions between the monolayer and the non-polar VOCs; 3) the tilt of the monolayer molecules upon diffusion of a VOC between the chains of the monolayer. The functional groups within the monolayer chains influenced the orientation of the adsorbed VOC molecules due to their electron-donating or electron-withdrawing properties, which in turn affect the sensing performance [260].

SAMs have emerged as a highly effective and versatile method for engineering sensor surfaces that exhibit high selectivity towards specific analytes. The unique properties of SAMs, including their ability to form well-ordered, robust coatings on a variety of surfaces, make them ideal for creating sensing surfaces with increased

sensitivity and specificity. This project is part of a research programme funded by the European commission and its central aim is to develop sensors, using Si junctionless nanowire transistor (Si JNT) devices, which electrically detect short-lived atmospheric radicals (·OH and NOx) in real time. In this collaboration, sensor samples were received from the collaborators in Dresden, these samples were then functionalised with an organic monolayer and characterised in York and then shipped to other collaborators in Ireland for atmospheric testing. This chapter explores the interaction of ·OH radicals with functionalised planar silica substrates as a model system for the Si JNT devices to evaluate the effect of ·OH radicals on the SAMs. Moreover, atmospheric chamber testing of the functionalised sensor surfaces will be discussed.

4.2 Reactivity of SAMs with ·OH radicals

To evaluate the lifetime of a functionalised radical sensor upon radical exposure, it was crucial to evaluate the rate of degradation of the organic SAM. The effect of functionality of the organic chains was investigated by screening a library of organic molecules attached to planar surfaces upon ·OH radical exposure. The autoxidation processes were investigated in Chapter 3 using non-porous SiO_2 nanoparticles surfaces, however, to model a sensor surface more accurately, glass slide surfaces were utilised. The next few sections will outline the methodology for ·OH radical generation and the results for the reactivity of SAMs upon radical exposure.

4.2.1 Generation of ·OH radicals using atmospheric pressure plasma

One method for the generation of ·OH radicals is using atmospheric pressure plasma and fortunately this was available at the University of York. Atmospheric pressure plasma is a source of reactive species, such as atomic oxygen, hydroxyl radicals, hydrogen peroxide and nitric oxide. These species are produced in the plasma via processes such as electron dissociation and recombination, discussed further in Section 4.2.1.1. The advantage of atmospheric pressure plasma is that it can operate at room temperature and atmospheric pressure, allowing easier treatment of thermally sensitive materials [261].

Collaboration with the York Plasma Institute (YPI) has allowed the use of their cold atmospheric pressure plasma jet to generate ·OH radicals which we can then use to test the reactivity of our monolayers upon radical exposure. A COST (Co-operation in Science and Technology) jet was used as the plasma source [262]. It consists of a 30 mm x 1 mm x 1 mm (length x width x height) plasma channel, illustrated in Figure 4.2, connected to a housing which incorporates voltage and current probes to determine the power dissipated by the plasma. The typical power output used in these experiments was set to 60 W, the device was operated at an excitation frequency of 13.56 MHz and the gas flow of each component was set based on the experimental requirements.

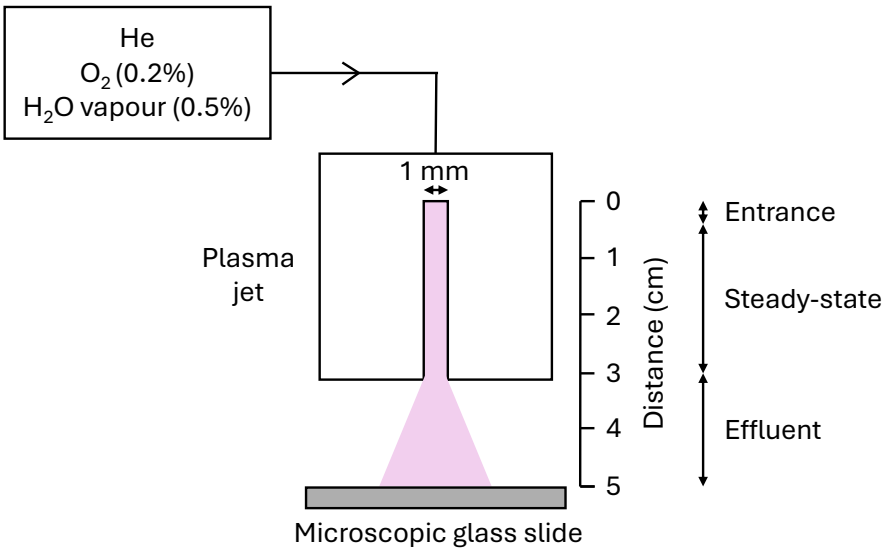

Figure 4.2: A diagram of an atmospheric plasma jet.

4.2.1.1 GlobalKin simulation

An advantage of using plasma as the source of ·OH radicals is that reasonable estimations can be made for the density of atomic O and ·OH radicals being produced. To acquire this information and further understand the reactive species and their dynamics in cold atmospheric pressure plasmas, zero-dimensional chemical kinetic models are often used [263]. The model, GlobalKin, is a 0-D plasma kinetics model which includes the power deposition in the plasma, options to alter the gas flow using a plug-flow approximation, diffusion to surfaces, surface kinetics using a surface site balance model and a liquid interactions module [264]. It consists of a reaction chemistry and transport module which is essentially the chemistry reaction set, a Boltzmann equation solver which provides the numerical solution of the Boltzmann equation for electrons in weakly ionised gases, and an ordinary differential equation solver for mass continuity equations, electron energy and temperature. The reaction mechanism includes 46 species and 578 reactions, the species listed below in Table 4.1.

GlobalKin has been reported in the literature to aid in the study of the formation of ·OH radicals in a cold atmospheric pressure plasma jet [263]. Experimental results obtained from UV broad-band absorption spectroscopy showed a rapid build-up of ·OH radicals in the entrance of the plasma channel, followed by a steady-state region throughout the plasma channel of around 10^{14} molecule cm^{-3} ·OH density and then a decay of ·OH radicals in the plasma effluent [263]. A similar trend was observed in the simulation, the absolute densities agreed within around 25% which is thought to be due to the combined uncertainties in the experimental data and the reaction rate values used in the model. A pathway analysis was performed to investigate the formation of ·OH in three different regions of the plasma jet: the entrance of the plasma channel, the steady state region, and the plasma effluent. At the entrance of the plasma channel, 0 - 0.2 cm in Figure 4.2, the main production mechanism of ·OH appeared to be through electron impact with water vapour as shown in equation 4.1.

$$e^- + H_2O \rightarrow \cdot OH + H + e^- \tag{4.1}$$

Species	Neutral	Positive	Negative
He	He $He(2^3S)$ $He_2{}^*$	He^+ He_2^+	
O	O $O(^1D)$ $O(^1S)$ O_2 $O_2(a^1\Delta)$ $O_2(b^1\Sigma)$ O_3	O^+ O_2^+ O_3^+ O_4^+	O^- O_2^- O_3^- O_4^-
H	H H_2		H^-
OH	OH HO_2 H_2O H_2O_2	OH^+ $H_2O^+(H_2O)_{n=0,1}$ $H^+(H_2O)_{n=1-9}$ $O_2^+(H_2O)$	OH^- $H_2O_2^-$ $OH^-(H_2O)_{n=1-3}$
Other			e

Table 4.1: Species and their positive and negative forms

This is due to the gas between 0 and 0.2 cm of the plasma jet mainly consisting of the initial feed gas and the rapidly formed species, such as ions and electrons. In the steady state region, 2 – 2.5 cm in Figure 4.2, the previous pathway still dominates, but now there are more species with slightly longer lifetimes which build up along the channel. Species such as the hydroperoxyl radical, HO_2, which add to the production of ·OH through equation 4.2.

$$H + HO_2 \rightarrow 2 \cdot OH \tag{4.2}$$

In the plasma effluent, 3 – 3.5 cm in Figure 4.2, there is a rapid decay of ·OH radicals which occurs in experiment and in simulation. This is due to the short-lived species recombining rapidly and leaving only the intermediate and long-lived species to dominate the plasma effluent. This means the main production pathway for ·OH in the effluent is through reactions between the hydroperoxyl radical and hydrogen, as shown in equation 4.2. However, the consumption reactions of ·OH occur at a higher rate in this region through the dominant reactions with H_2O_2 or He, as shown in equation 4.3 and 4.4.

$$\cdot OH + H_2O_2 \rightarrow HOO \cdot + H_2O \tag{4.3}$$

$$2 \cdot OH + He \rightarrow H_2O_2 + He \tag{4.4}$$

The chemistry of the afterglow of atmospheric pressure He/O_2 plasmas with humid air impurity has been reported in the literature [265]. A 0-D global plasma chemistry model was used to investigate the reactions and densities of reactive species occurring in the afterglow of an atmospheric pressure plasma jet with a feed gas of $He/O_2(0.5\%)$ and humid air impurities of less than 0.05%. The results from the model suggested that $O_2(^1D)$ and O_3 predominantly formed in the afterglow

with densities of 10^{15} molecule cm^{-3} and ·OH, H_2O_2, HNO_3 and NO_2/NO_3 with densities of 10^{13} molecule cm^{-3}. The production of HNO_3 and NO_2/NO_3 caused by reaction with N_2 in the air. The plasma afterglow mixes with ambient air, thus the reactions with N_2 cannot be ignored. After analysis of the dominant reaction pathways, it seemed that the reaction kinetics of atomic O, $O_2(^1D)$ and O_3 were significantly influenced by the formation of HO_2, H_2O_2 and HNO_3 even when the humid air fraction was set below 500 ppm [265].

In this project, the 0-D GlobalKin model was a valuable tool for estimating the density of ·OH radicals and other reactive species reaching the functionalised surfaces and interacting with the monolayer. The surface area and volume of the plasma jet we are using, 1.2 cm^2 and 0.03 cm^3 respectively, were implemented into the model input parameters. Initially, the model only simulated the densities and reaction pathways occurring within the plasma jet channel. Therefore, to simulate the processes occurring outside of the plasma jet – within the plasma effluent, the power needed to be specified as a function of distance. The length of the plasma was extended from 3 cm to 5 cm and the power between 3 – 5 cm was set to 0 W. This was a simple method to model the afterglow of the plasma, however air mixing was not taken into account. The gas admixture used for experiments consisted of helium gas with 0.5% water and 0.2% oxygen, thus these values were inputted into the model. Figure 4.3 displays the result from the GlobalKin simulation.

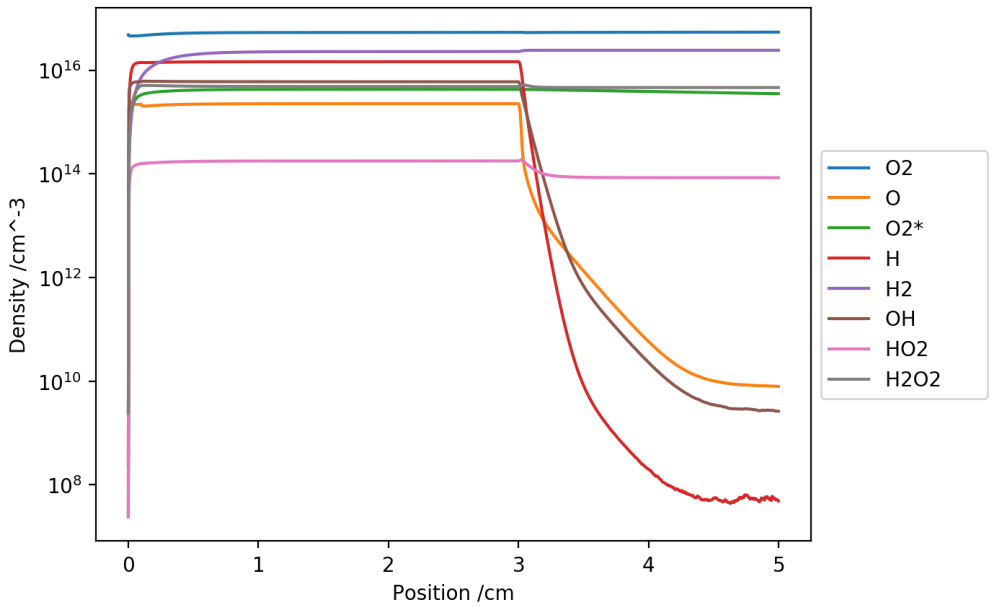

Figure 4.3: GlobalKin simulation result showing the concentration of reactive species of the plasma afterglow (3 - 5 cm) with an initial gas admixture of helium gas with 0.5% water vapour and 0.2% oxygen.

The results suggest that the density of ·OH radicals and atomic oxygen within the plasma afterglow (3 - 5 cm) could range from 10^{10} to 10^{15} cm^{-3}, depending on the distance from the plasma jet. This demonstrated the importance of the distance between the plasma jet and the functionalised surfaces for conducting reactivity studies using plasma. It seems in the afterglow, between 3 and 5 cm, there is a high density of O_2, H_2, H_2O_2 and $O_2(^1D)$ but these species would be relatively unreactive towards our surfaces. Moreover, there is a high concentration of HO_2

in the plasma afterglow, which can react with peroxyl radicals formed within the monolayer to form more reactive alkoxyl radicals, as shown in equation 4.5 [101]. Thus, the rate of autoxidation within the monolayer systems upon plasma exposure could be accelerated by HO_2. The species HO_2 can also add to the production of ·OH radicals via equation 4.5, increasing the density of radical initiators toward the monolayer.

$$ROO\cdot + HO_2 \rightarrow RO\cdot + \cdot OH + O_2 \tag{4.5}$$

4.2.2 Functionalised Glass Slide Surfaces

To evaluate the reactivity of different organic surfaces to ·OH radical exposure, a range of silane precursors with varying functionalities were used to functionalise the silica surfaces, shown in Figure 4.4.

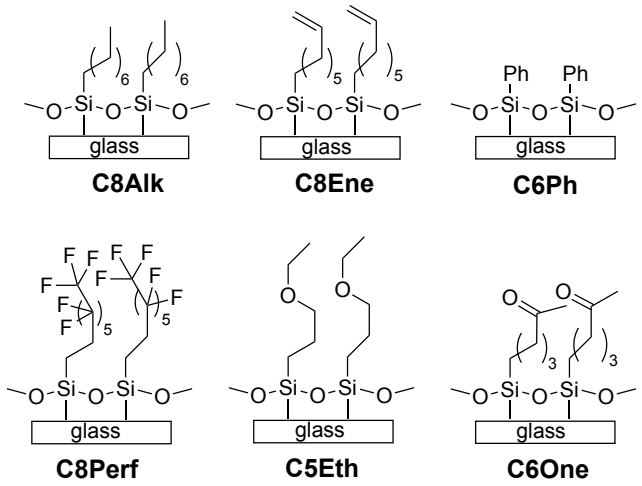

Figure 4.4: A selection of alkoxysilane SAMs used in the plasma reactivity study.

The reactivity of the organic molecules, as discussed in Chapter 3, is usually dominated by the feasibility of reaction spreading. Thus, organic molecules were chosen based on the reactivity of their C-H bonds toward H-abstraction. The selected molecules included C8AlkOMe, to represent a straight alkyl chain. The reaction rate constant for the H abstraction of C-H in an 8-length carbon chain at 298 K by an ·OH radical has been reported in the literature to be relatively fast at 8.1×10^{-12} cm^3 $molecule^{-1}$ s^{-1}, shown in Table 4.2. The addition of ether or ketone functionality increases the rate of H-abstraction by an ·OH radical to 21.7 and 9.0×10^{-12} cm^3 $molecule^{-1}$ s^{-1}, respectively. This is due to the lability of the C-H bonds adjacent to the ether/ketone functionality, hence C5Eth and C6One monolayers have been included in this study. The activated C-H bonds in ether compounds also facilitate faster spreading of radical reactions via H-abstraction from ROO· radicals as a result of the carbon-centred radicals reacting with O_2, as discussed in Chapter 3. This means that ether-containing chains could exhibit faster degradation upon exposure to ·OH radical exposure.

Additionally, C8PerfOMe was chosen for its relatively slower reactivity with ·OH radicals. DFT calculations were used to probe the reactions between an ·OH radical

Chain Functionality	Formula	Rate Constant k (10^{-12} cm^3 molecule^{-1} s^{-1})	Reference
Alkyl	C_8H_{18}	8.7	[266]
Ether	C_3H_7O-C_3H_7	21.7	[266]
Ketone	$CH_3C(O)$-C_4H_9	9.0	[266]
Alkene	C8H16	36.2	[267]

Table 4.2: Rate constants for various organic molecules at 298 K taken from the literature [266, 267]

and C8Perf, in terms of their energetics and kinetics. This was performed to further understand the rates in degradation of the monolayer chain. DFT calculations were performed by a member of the EU consortium; Leonidas Tseteris, Department of Physics, School of Applied Mathematical and Physical Sciences, National Technical University of Athens. The results were obtained using the NWChem code [268], the hybrid B3LYP [269, 270] exchange correlation (xc) functional and the DZVP DFT Orbital basis [271]. The minimum energy pathways and barriers of key reactions were calculated with the Nudged Elastic Band method and structures were rendered with VESTA [272].

Figure 4.5 shows the minimum energy pathway for the reaction between an ·OH radical and a C8Perf chain, which has a larger energy barrier. The minimum energy pathway follows the substitution of fluorine with oxygen to form a C-O bond and subsequently HF. This reaction would only be possible at elevated temperatures, such as during combustion, to overcome the high energy barrier. Thus, it is unlikely that this reaction would proceed under ambient laboratory conditions. The C8Perf molecules contain two CH_2 groups at the base of the monolayer chains. It is likely reaction with an ·OH reaction proceeds via H-abstraction of these C-H bonds rather than the stronger C-F bonds within the C8Perf chain. This information could be used for the interpretation of the plasma reactivity studies, discussed in Section 4.2.4.

The four molecules, discussed above, are expected to remain stable in the presence of other atmospheric constituents. C8EneOEt and PhOEt were also incorporated into the study, although these two molecules can react with ozone. Ozone is present in ambient air, as discussed in Chapter 3, however, it can also form further downstream the plasma jet at concentrations of 10^{15} molecules cm^{-3} [265]. Thus, its reactivity with unsaturated chains cannot be ignored. The rate of H-abstraction of the activated C-H groups by an ·OH radical in alkene-containing chains does, however, exhibit a relatively fast reaction rate of 36.2×10^{-12} cm^3 molecule^{-1} s^{-1}, shown in Table 4.2. This suggests that degradation of alkene-containing chains upon radical exposure could be a relatively fast process, compared to straight alkyl chains. The reaction of ·OH radicals with benzene has been studied in the literature [273]. The attack of an ·OH radical leads to the formation of mainly the OH/benzene radical adduct, shown in Figure 4.6. The OH/benzene radical adduct can then react further with O_2, followed by unimolecular reaction pathways [273]. The abstraction pathway to form H_2O and a phenyl radical accounts for only 5% of the overall reaction at 298 K, shown in Figure 4.6. The rate constants for k_1 has been reported as 1.1×10^{-12} cm^3 molecule^{-1} s^{-1} and k_2 as 4.7×10^{-14} cm^3 molecule^{-1} s^{-1}. Thus, the radical reaction spreading in C6Ph chains was explored.

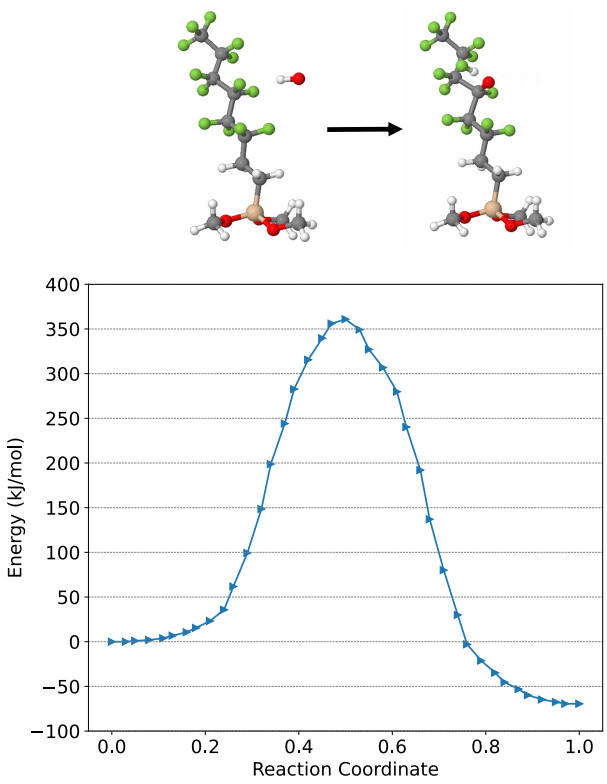

Figure 4.5: Minimum energy reaction pathway (MEP) for the replacement of a F atom by an O atom when ·OH reacts with C8Perf chains.

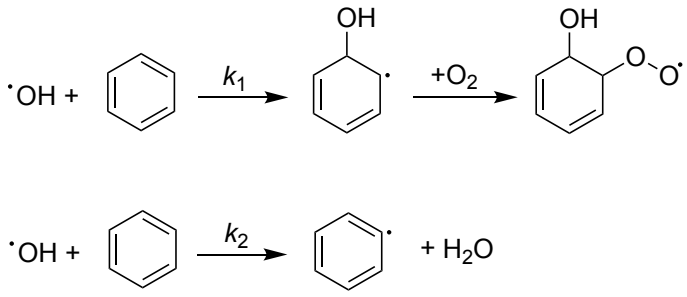

Figure 4.6: The reaction of ·OH with a phenyl ring. The two kinetic pathways with rate constants k_1 and k_2 are displayed.

4.2.3 Distance from the Plasma Jet

To develop a system for monitoring monolayer degradation by a reasonable stream of ·OH radicals and atomic oxygen, an experiment was conducted altering the distance between the glass slide surface and the plasma jet. For the gas admixture, helium gas mixed with 0.5% water vapour and 0.2% oxygen was used. This gas admixture was chosen because it was the most effective in increasing the hydrophilicity of the glass slide surface during initial testing results of silica surface cleaning, described in Section 2.2.2. The density of each gas in this gas admixture was included in the GlobalKin 0-D model in Section 4.2.1.1, showing the density of ·OH radicals reaching the functionalised glass surfaces would be approximately $10^{10} - 10^{15}$ molecules cm^{-3}, depending on the distance from the plasma jet. Glass slide surfaces were functionalised with the 6 different molecules, in Section 4.2.2 and then were exposed to plasma for one minute at distances varying from 2-24 mm. Each glass slide was divided into a grid of 12 (area of each square = 12.5 mm^2) and every other square was exposed to the plasma jet which had been programmed to move around the square using an XY translation stage, shown in Figure 4.7. Figure 4.8 shows the contact angle results for the functionalised glass slide surfaces upon exposure to plasma at increasing distances from the plasma jet.

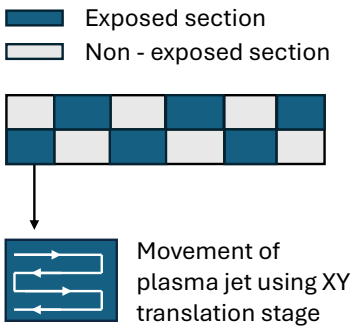

Figure 4.7: Schematic of the experimental protocol for the exposure of a functionalised glass slide to the plasma jet.

The results indicate that most organic monolayers completely degraded by the plasma when exposed for 1 minute at distances of less than 10 mm, with the exception of the C8Perf monolayer, which exhibited a reduction in contact angle to approximately 10°, as shown in the left plot in Figure 4.8. This suggests that the high density of ·OH and O radicals at a distance less than 10 mm from the plasma jet is sufficient for complete oxidation of the organic monolayer. The degradation of C8Perf monolayers must be initiated by the oxidation of the CH_2 groups at the base of the monolayer chains, as the reactivity of C-F bonds towards ·OH radicals is relatively slow. At these distances, the plasma can be used to clean and effectively hydrolyse silica surfaces. At distances greater than 10 mm, the surfaces appear less hydrophilic with contact angles between 20 and 80°, suggesting the density of radicals reaching the surface is lower. The reactivity studies of ·OH radicals with monolayer surfaces demonstrate that a distance of approximately 14 mm is sufficient to oxidize the monolayer, resulting in a 50% reduction in contact angle after 1 minute of exposure. The plot on the right of Figure 4.8 shows the results after normalisation to the starting contact angle of each monolayer. It can be observed

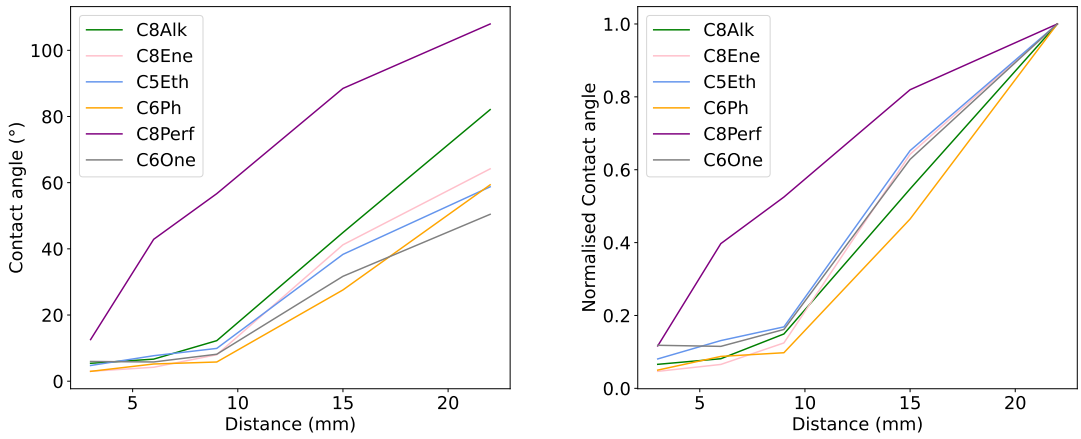

Figure 4.8: The effect of distance between the plasma jet and the functionalised glass slide surface on the contact angle for 6 different alkoxysilane monolayers.

that most of the molecules follow a similar trend in degradation rate as distance is increased, except C8Perf which is less reactive at all distances.

4.2.4 Plasma Exposure

To evaluate the degradation rate of various monolayers upon exposure to ·OH radicals, the plasma exposure time was varied. The results from Figure 4.8 indicated that distances greater than 10 mm would be appropriate for testing the reactivity of monolayers with ·OH radicals. Consequently, the distance between the plasma jet and the functionalised glass slide surface was set to 22 mm, allowing for longer exposure times while ensuring only partial degradation of the monolayer chains. A gas admixture of He/H_2O (0.5%)/O_2 (0.2%) was used. The glass slides had been previously functionalised with the seven different molecules, described in Section 4.2.2. Each functionalised glass slide was divided into a grid of 12 and every other square was exposed to the plasma jet which had been programmed to move around the square using an XY translation stage, shown in Figure 4.7. The total scanning time of each square area of the glass slide was increased from 0 to 420 seconds, 15 second intervals to 60 seconds and then 180 second intervals to 420 seconds. The contact angle measurements were normalised to the initial contact angle at 0 second exposure for each functionalised glass slide. The results are shown in Figure 4.9.

Significantly less degradation was observed for the C8Perf chains, which was expected due to the relative unreactivity of C-F bonds toward ·OH radicals. Nevertheless, after 7 minutes of plasma exposure, the C8Perf chains had ∼40% reduction in contact angle, insinuating the monolayer had become more hydrophilic. DFT studies in Section 4.2.2 suggested that the energy barrier for the reaction between an ·OH radical and a C-F bond is nearly 365 kJ mol^{-1}, indicating that elevated temperatures would be required to overcome this barrier. Therefore, oxidation is likely to result from the reaction of ·OH radicals with the CH_2 groups at the base of the C8Perf monolayer chains. This reaction would form oxygenated species, introducing more hydrophilic groups into the monolayer.

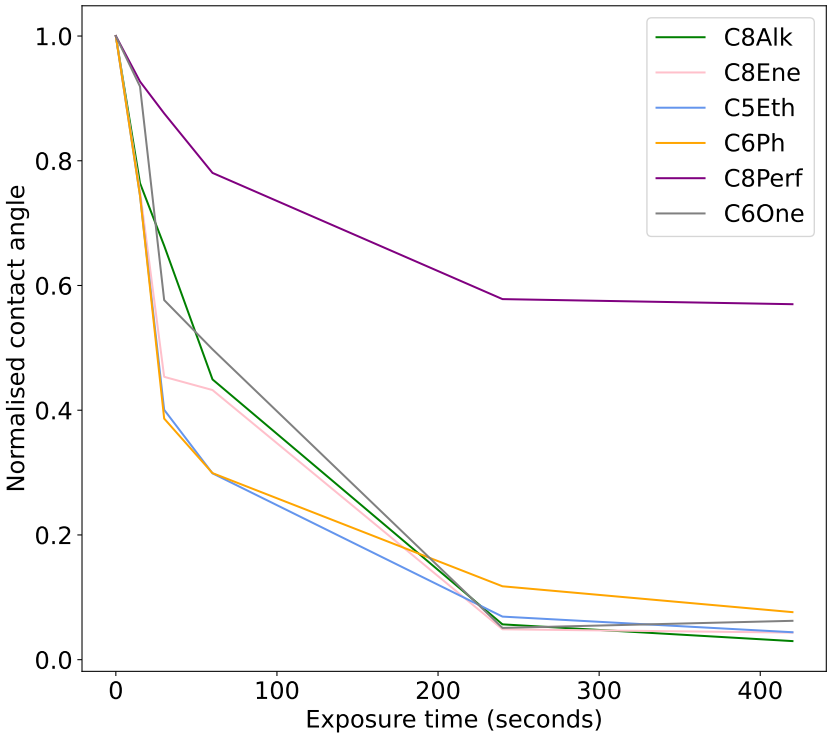

Figure 4.9: Contact angle measurements with increasing plasma exposure time (distance from plasma jet 22 mm) for various functionalised glass slides.

The fastest rate of degradation was observed for the C5Eth, C8Ene and C6Ph chains. This supports the results presented in the autoxidation study within monolayer systems, discussed in Section 3.4.3, whereby the presence of ether or conjugated double bond functionality accelerates the propagation of radical reactions. The ·OH radicals are likely to abstract a H from the monolayer chains, forming a carbon centred radical which will readily react with O_2 upon air, leading to the formation of peroxyl radicals. The peroxyl radicals can then react with other species, such as the highly abundant HO_2 from the plasma (discussed in Section 4.2.1.1), forming more reactive alkoxyl radicals, which can abstract H from neighbouring chains. Due to the lability of C-H bonds in ether and double bond-containing chains, the monolayers can exhibit a faster rate in autoxidation. The monolayer chains with less labile C-H bonds, undergo a slightly slower rate in degradation. This was observed for the C8Alk and C6One chains. However, it is surprising that the rate in degradation of the ether-containing and alkene-containing chains is only marginally faster than the straight alkyl chains. This could be due to the higher density of reactive species generated in the plasma jet, such as HO_2, which could be reacting with surface bound alkoxyl radicals before they are able to react with adjacent chains. Hence, the rate in degradation is dependent on the initial attack by the ·OH radicals rather than the propagation to neighbouring chains within the monolayer.

These results have provided an insight into the various reactivity rates of organic molecules upon ·OH radical exposure, confirming that molecules containing activated C-H bonds, such as ether and alkene groups, will degrade faster than a

simple alkyl chain or perfluoro-containing chain. The methodology for generating ·OH radicals and monitoring the reactions using a simple yet effective analytical technique enables rapid testing of any future modifications to the prototype radical sensor, such as adjusting its surface reactivity toward ·OH radicals. If the sensor sensitivity is sufficient, simple alkanes can be used as a coating as only one molecule will react with an ·OH radical, and so the sensor will have a long lifetime. However, if higher sensitivity is needed, ethers can be used as the spread of reaction will mean that more than one molecule reacts with one ·OH radical. Although, due to the irreversibility of the radical reactions with the functionalised sensor surface, the sensor lifetime will be reduced.

4.3 ·OH Detection by Functionalised Sensors

This project involved the collaboration of several research groups, including Helmholtz-Zentrum Dresden-Rossendorf (Dresden, Germany) and University College Cork (Cork, Ireland). The team based in Dresden led the fabrication of the sensor devices, while the team at Cork led the atmospheric chamber testing of the functionalised sensor devices.

Silicon-on-insulator (SOI) devices were fabricated in Dresden using a commercially sourced ultra-thin SOI substrate with a 775 μm (lightly p-doped) bulk Si carrier, a 102 nm SiO_2 buried oxide layer, and a 20 nm intrinsic top Si layer with a carrier concentration of 1.12×10^{16} cm^{-3}. Nickel pads (100 nm) were deposited using UV lithography, HF dip, and sputtering. These SOI devices were then shipped to the University of York to be functionalised. Figure 4.10 illustrates the functionalised sensor device. SOI devices were used initially as an alternative to Si-JNT devices as they were simpler and cost-effective device configurations.

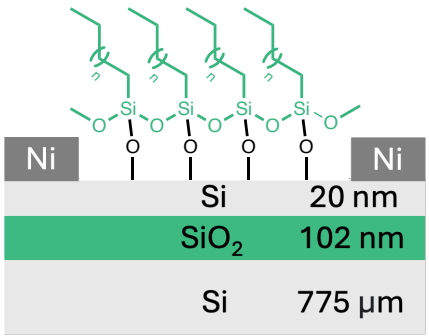

Figure 4.10: A diagram representing the functionalised SOI sensor surface for ·OH radical detection.

4.3.1 Functionalisation of SOI devices

The SOI devices were functionalised with C8AlkOMe and C8EneOEt monolayers for ·OH detection, as both molecules undergo reactions with ·OH radicals. Alkene-terminated chains react with ·OH radicals via different mechanisms, in comparison to straight-alkyl chains, due to their structural differences. The reaction of an ·OH radical with alkene-terminated chains is initiated by electrophilic addition, forming

β-hydroxy-alkoxyl radicals and subsequently peroxyl radicals in the presence of O_2 [274]:

$$RCH{=}CH_2 + {\cdot}OH + M \rightarrow R{-}CH(OH){-}CH_2 + M \tag{4.6}$$

$$R{-}CH(OH){-}CH_2 + O_2 + M \rightarrow R{-}CH(OH){-}CH_2O_2 + M \tag{4.7}$$

Straight-alkyl chains and ·OH radicals react via H-abstraction, generating peroxyl radicals upon reaction with O_2 [275]. The ·OH radicals exhibit faster reactions with the electron-rich double bonds within the C8Ene chains, compared to the C8Alk chains by 10 times [276, 277]. The peroxyl radicals can then react with NO, HO_2 to form alkoxyl radicals, which can then propagate the radical reactions to neighbouring chains [115]. The increase in oxidation across the sensor surface is expected to alter the surface dipole moment, influencing the electrical characteristics of the SOI device.

Functionalisation of the SOI surface was confirmed through contact angle analysis, which revealed an increase from 4.4° to 92° for the C8Ene monolayers and 5.2° to 101.9° for the C8Alk monolayers, indicating a significant enhancement in surface hydrophobicity. These samples were flushed under a stream of N_2 gas and tightly sealed in a container for immediate shipment to Cork, Ireland.

4.3.2 ·OH Sensor Tests with Functionalised SOI Device

Functionalised SOI sensors were tested by the team in Cork and compared across various mixing ratios of ·OH in a semi-customised gas-tight micro probe station with a volume of 100 cm^3 (Nextron). The C8Ene-functionalised sensors were tested first due to their slightly faster reactivity with ·OH radicals. The functionalised sensors were placed inside the probe station and exposed to dry N_2 with varying ·OH mixing ratios ranging from 1 ppbv to 18 ppbv. To introduce HOx (·OH + HO_2), the pen-ray lamp was turned on 20 minutes prior to the experiment to ensure stable radical generation. Before exposure, the C8Ene-functionalised SOI device was kept under vacuum for approximately 30 minutes to remove residual moisture. Synthetic air (N_2) was then passed through a flow tube containing Milli-Q water at a constant flow rate of 5 slpm to generate ·OH radicals. The concentration of HOx was controlled by adjusting the exposure of the lamp (e.g. uncovering it by 0.3 cm resulted in a HOx concentration of 1 ppb) with different concentrations achieved by varying the uncovered distance accordingly. The electrical measurements were performed using electrical Keithley source metres.

The electrical response of the C8Ene-functionalised SOI Schottky device to ·OH detection was investigated by exposing the sensor to 1 ppb and 18 ppb of ·OH for 30 minutes, while continuously monitoring the current. A flow-through set-up with N_2 as the carrier gas was used to prevent interference from ozone formation, which was confirmed by Teledyne ozone measurements showing zero ozone concentration.

Upon exposure to 1 ppb ·OH, the sensor exhibited a notable current reduction from 3.63×10^{-9} A to 2.34×10^{-9} A, shown in the shaded reigion of Figure 4.11(a). At a higher ·OH concentration of 18 ppb, the current decreased from 4.56×10^{-9} A to 1.26×10^{-9} A over the same duration, shown in the shaded region of Figure 4.11(b). The calculated responsivity was 35.6% and 72.4% for 1 ppb and 18 ppb

OH, respectively. Unlike the C8Ene functionalised SOI, the current for the bare SOI, shown in Figure 4.11(c), does not decrease.

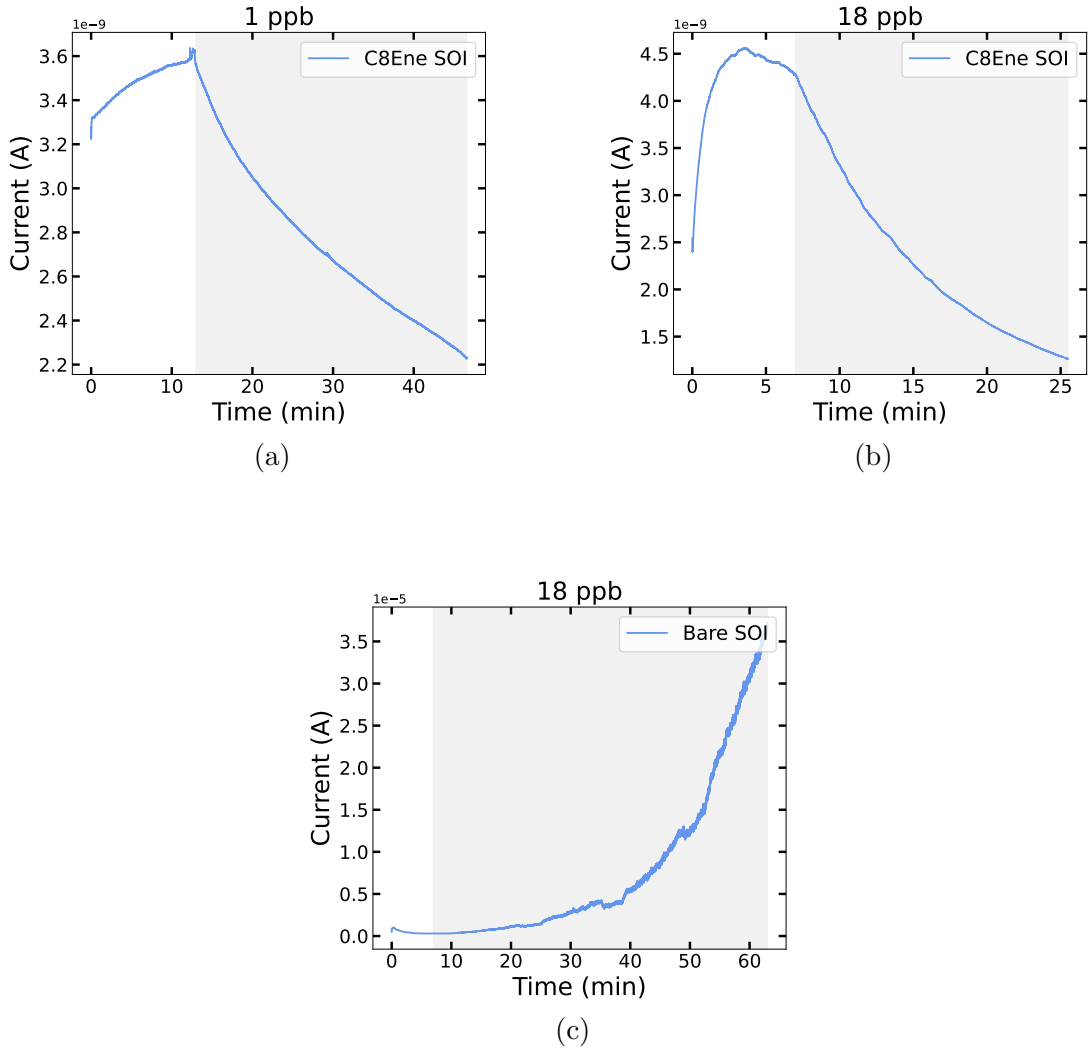

Figure 4.11: Change in current observed in C8Ene functionalised SOI devices upon exposure to (a) 1 ppb and (b) 18 ppb ·OH. A multi-fold increase in the current signal is observed for both OH concentrations. (c) The time-dependent current plot for 18 ppbv ·OH exposure on the bare SOI. Unlike the C8Ene functionalised SOI, the current here does not decrease.

This change in current is likely attributed to surface modifications induced by ·OH interaction with the organic chains on the SOI surface. The oxidation of the organic chains, initiated by the ·OH radicals, leads to dipole change across the sensor surface and an electrostatic field that affects charge conduction in the SOI channel. The challenges involved with this functionalised sensor is the slow response time. A noticeable change in current was observed over the course of 30 minutes. If we assume the coverage of organic molecules on the sensor surface is 4 molecules/nm^2, as shown in the oxidative cleavage experimental results for functionalised planar surfaces in Section 2.3.3. This means there are 4×10^{14} molecules/nm^2 per sensor surface (1 cm^2). If the rate of reaction for ·OH radicals with alkene-terminated chains is 36.2×10^{-12} cm^3 molecule^{-1} s^{-1} and the density of ·OH radicals is approximately

10^{10} cm^3 molecule^{-1}, this gives a rate of 1.5 molecules s^{-1}. At this rate of reaction, all organic chains will have reacted with ·OH radicals within 3 seconds. Given the rapid reaction rate and the limited number of available reactive molecules, the sensor would likely stop functioning after a very short period, as all of the surface molecules would be consumed by the ·OH radicals in just a few seconds. After this initial reaction, it would be expected that the sensor would no longer detect significant changes in current, as there would be no more reactive molecules left on the surface to interact with ·OH radicals. However, that is not what is observed in Figure 4.11. The sensor continued to respond for 40 minutes. This means either the ·OH radical concentration in the probe station is lower than expected, the reaction rate is incorrect, or the reaction mechanism is incorrect and each molecule on the sensor may react with many ·OH radicals, or the sensing mechanism does not involve the reaction between ·OH with alkene-terminated chains. The latter is unlikely, as without the monolayer, as seen in Figure 4.11(c), there is no sensitivity, which insinuates that the monolayer does play a role in the sensing mechanism.

However, this concentration of ·OH is higher than the typical atmospheric concentrations ($\sim 1\times10^6$ molecules cm^{-3}), so the time it would take for all organic chains to react would be longer at 7.5 hours. As a result, this functionalised sensor is not well-suited for practical ·OH radical detection over long periods of time, such as days or weeks. But could provide information for a few hours. If the sensor was required to be stable for longer periods of time, the organic monolayer would need to include less reactive organic molecules, such as perfluorinated chains, to slow the rate of degradation. Future work will involve more in-depth analysis of the sensor surface transformations upon exposure to ·OH radicals.

4.4 Conclusions

Glass slides have been used as model sensor substrates and were functionalised with a variety of organic molecules. Their reactivity towards oxidising radicals, formed in a nonthermal plasma, was monitored by contact angle analysis. The GlobalKin model was used to give an estimate of the density of radicals reaching our surfaces under the conditions set for our experiments and implied that the reactive radical species reaching the functionalised surfaces mainly consisted of ·OH, O and HO_2. Results indicate that organic molecules with activated C-H groups, such as C5Eth, C8Ene, and C6Ph, exhibit slightly faster reactivity compared to simple alkyl chains like C8Alk. This is attributed to the enhanced rate of radical propagation within these molecules. The presence of activated C-H bonds facilitates a more efficient H-abstraction by neighbouring ROO· radicals, which are generated through the reaction of O_2 with the carbon-centred radical formed during the attack of ·OH radicals. The C8Perf chains showed to degrade relatively slower due to the unreactivity of C-F bonds toward ·OH radicals. This study established the methodology for functionalising surfaces with different organic molecules, exposing the surfaces to ·OH radicals and monitoring the reactions by a simple but effective analytical technique. In the future, this methodology can be used for quickly altering the design of the organic molecules in case they need to be more or less reactive to ·OH radicals for the prototype sensors.

Functionalisation of an SOI sensor device with C8EneOEt was performed and monolayer formation was confirmed by contact angle analysis. Initial tests of the

functionalised sensor indicated that the current did change upon exposure to ·OH radicals. Moreover, the change in current was dependent on the concentration of ·OH radicals in the probe station. This suggested that the current is likely due to dipole changes across the functionalised sensor surface as a result of oxidation upon ·OH exposure. Calculations have shown that the time for all organic chains on the sensor to react with ·OH radicals under typical atmospheric ·OH concentration, 1×10^6 molecules cm^{-3}, to be around 7.5 hours. This time period is long enough to detect ·OH radicals for a few hours but is not practical for detection periods longer than a day. To improve the longevity of the sensor surface, less reactive molecules, such as perlfuorinated chains, should be incorporated into the monolayer (either as mixed monolayers or homogeneous monolayers). Future work will involve more in-depth analysis of the sensor surface transformations upon exposure to ·OH radicals.

Chapter 5

Conclusions

This thesis has systematically explored both the formation and stability of alkoxysilane monolayers on silica surfaces, the chemical reactivity of these surfaces under radical-initiated oxidative conditions, and the practical application of these functionalised surfaces in sensor devices.

The initial chapters established robust and reproducible protocols for preparing well-defined monolayers, verified by multiple characterisation techniques, including contact angle measurements, ATR-FTIR, XPS, solid-state ^{13}C NMR, TGA, AFM, and ellipsometry. The development of an oxidative cleavage protocol enhanced the analytical method for detailed monolayer composition analysis, especially for mixed monolayers across various silica substrates.

Subsequent experimental and computational studies on autoxidation highlighted that, unlike bulk solutions where peroxyl radical termination dominates, limited mobility on surfaces restricts recombination. Peroxyl radicals instead interact with atmospheric species or adjacent chains, with propagation dependent on chain functionality. Ether-containing chains facilitated reaction spreading, whereas linear and branched alkane chains did not. Additionally, nitric oxide (NO) was found to aid radical propagation but only to a limited extent under realistic conditions.

Extending these insights to sensor applications, glass slides functionalised with a variety of organic molecules were exposed to ·OH radicals, atomic oxygen, and hydroperoxyl (HO_2) radicals generated in non-thermal plasma. Contact angle analysis demonstrated that molecules with activated C-H bonds exhibited enhanced reactivity compared to simple alkyl chains, due to more efficient radical propagation via hydrogen abstraction. Conversely, perfluorinated chains showed slower degradation, reflecting the inertness of C-F bonds toward ·OH radicals.

Functionalisation of silicon-on-insulator (SOI) sensor devices with reactive chains was confirmed by contact angle measurements. Preliminary electrical tests showed sensor current changes proportional to ·OH radical concentrations, suggesting dipole changes at the surface due to oxidation. However, the estimated sensor surface lifetime under typical atmospheric ·OH levels ($\sim$7.5 hours) limits long-term detection. Incorporating less reactive molecules, such as perfluorinated chains, into monolayers is proposed to enhance sensor longevity.

5.1 Future Work

While this thesis has advanced understanding of alkoxysilane monolayers on silica surfaces and their radical-induced reactivity, several avenues remain to be explored to further enhance sensor design, surface stability, and fundamental insight into surface oxidation chemistry.

1. Enhancing Sensor Longevity and Stability

The limited lifetime of reactive monolayers, especially under typical atmospheric ·OH radical concentrations, limits continuous sensor operation. Future work should investigate the incorporation of mixed monolayers containing both reactive and inert (e.g., perfluorinated) chains to balance sensitivity with longevity. Optimising the ratio of these components could provide surfaces that maintain responsiveness to ·OH radicals while minimising degradation.

2. In-depth Mechanistic Studies of Radical Propagation

The current work highlighted how chain functionality influences radical propagation, but the detailed molecular pathways on surfaces remain incompletely understood. Future studies should include systematic variation of reactive radical species concentrations combined with kinetic monitoring of surface reactions, such as changes in contact angle or sensor response, to derive reaction orders and rate laws. This approach would provide valuable insight into the rate-determining steps and interaction dynamics of radicals on the surface. Additionally, advanced spectroscopic and microscopic techniques, such as in situ electron paramagnetic resonance (EPR) or time-resolved spectroscopy, could be employed to directly observe radical intermediates and clarify reaction kinetics on the surface. Computational modelling incorporating surface confinement effects would complement experimental data.

3. Exploration of Alternative Radical Sources and Environmental Conditions

Further investigation into radical initiation under different environmental conditions, such as varying humidity, temperature, or presence of other atmospheric gases, will help simulate real-world sensor operating environments. Exploring other ·OH radical sources or photochemical radical generation methods could identify more controlled or efficient radical production routes.

Experimental

6.1 General Reagent Information

All commercially available reagents were purchased from Sigma-Aldrich, Alfa Aesar, fluorochem or TCI companies and were used without further purification. A full list of chemicals used is available in Section 6.3. Silica NPs (10-20 nm) were purchased from Sigma Aldrich. Glass Microscopic Slides (25 × 75 nm) were purchased from Fisher Scientific.

6.2 General Analytical Information

Brunauer–Emmett–Teller (BET). The specific surface area (SSA) of the samples were estimated from Brunauer-Emmett-Teller (BET) theory using nitrogen adsorption–desorption isotherm data obtained at -196°C (77 K) on a constant-volume adsorption apparatus with The Micromeritics TriStar II Plus. The samples were degassed at 200°C for 12 hours (3 hours for Al_2O_3) before BET analysis.

Thermal Gravimetric Analysis (TGA). The functionalised SiO_2 nanoparticles (10-20 nm) were characterised by Thermogravimetric analysis (TGA). TGA was performed on the PL Thermal Sciences STA 625 (Simultaneous Thermal Analyser) at the University of York, under a flow of nitrogen with a temperature gradient of 10°C per minute from room temperature to 600°C.

Atomic Force Microscopy (AFM). AFM measurements were conducted using a Bruker BioScope Resolve BioAFM at the York JEOL Nanocentre. The AFM tip was fabricated from Antimony (n)-doped silicon with a resistivity of 0.01-0.025 Ω-cm. The cantilever used had the following dimensions: thickness (T) = 3.4 μm, length (L) = 125 μm, and width (W) = 40 μm.

Contact Angle Analysis. Contact angle measurements were performed with a Theta Lite Optical Tensiometer. Deionised water was used as the liquid for analysis using the sessile drop method. Drop profiles were fitted through the Young-Laplace method, and contact angles between fitted function and baseline were calculated.

Fourier Transform Infrared Spectroscopy – Attenuated Total Reflectance (FTIR-ATR). FTIR spectra were recorded using a Bruker Vertex 70v spectrometer equipped with an attenuated total reflectance (ATR) module, which featured a diamond crystal surface. A total of 128 scan averages were collected at a resolution of 1 cm^{-1}, with measurements referenced to a nitrogen (N_2) background of the same averaging.

^{13}C Solid State NMR. The functionalized silica NPs (10-20 nm) were characterised by ^{13}C Solid State NMR. This was performed on an AVIIIHD console using a PH MAS 400WB VL2.5 N-P/F-H probe, with Topspin version of 3.6.5 and a 400MHz Widebore Ascend Magnet.

^{1}H NMR Spectroscopy. The dissociated alcohols were characterized by 1H NMR. Spectra were recorded on a Varian 400 MHz instrument (400 MHz for ^{1}H NMR). ^{1}H NMR experiments were reported in units, parts per million (ppm), and were measured relative to residual chloroform (7.26 ppm) in the deuterated solvent. Coupling constants were reported in Hz.

Gas Chromatography - Mass Spectroscopy (GC-MS). GC-MS was performed using a Waters GCT Premier Time of Flight mass spectrometer coupled to an Agilent 7890A GC system. The column (Phenomenex ZB-5MSplus) dimensions were 30.0 m x 250 µm x 0.25 µm (length x internal diameter x thickness) and the carrier gas was helium. For the GC method: the initial temperature was 60°C and this was ramped to 260°C for 25°C/minutes, hold time 2 minutes, then ramped at 50°C/minutes to 320°C. Total time 15 minutes.

6.3 Chemicals

All chemicals in this list were used without further purification. n-octyltrimethoxysilane (97%, Fluorochem), n-octyltriethoxysilane (97%, Sigma-Aldrich), trimethoxy(7-oct-1-enyl)silane (>90%, Tokyo Chemical Industry), 1H,1H,2H,2H-perfluorooctyltrimethoxysilane (98%, Fluorochem), phenyltrimethoxysilane (97%, Fluorochem), octan-1-ol (>99%, Sigma-Aldrich), 1H,1H,2H,2H-tridecafluorooctan-1-ol (>97%, Apollo Scientific), 7-octen-1-ol (>96%, Tokyo Chemical Industry), 3-ethoxy-1-propanol (ChemCruz), methanesulfonic acid (>99%, Sigma-Aldrich), azobisisobutyronitrile (98%, Sigma-Aldrich), tetra-n-butylammonium fluoride (1M soln. in THF, ThermoFisher Scientific), potassium bicarbonate (99.7%, Sigma-Aldrich), N,O-bis(trimethylsilyl)trifluoroacetamide (with 1 % trimethylchlorosilane, 98%, ThermoFisher Scientific), pyridine (99.8%, Sigma-Aldrich).

The following compounds were synthesised by Naeem Iqbal, a member of the Victor Chechik research group: 6-(triethoxysilyl)hexan-2-one, 9,9-diethoxy-2,5,10-trioxa-9-siladodecane, triethoxy(3-ethoxypropyl)silane, triethoxy(7-methyloctyl)silane.

6.4 Experimental Protocols

6.4.1 Functionalisation Procedure

6.4.1.1 Pre-treatment of Silica Surfaces - Piranha Cleaning

The substrates were placed in piranha solution (a 1:3 ratio of 30% H_2O_2 and concentrated H_2SO_4) for one hour, then rinsed several times with deionised water and methanol and dried under a stream of nitrogen gas. The substrates were then used

immediately for monolayer preparation or placed in deionised water to avoid contamination.

6.4.1.2 Pre-treatment of Silica Surfaces - Plasma Cleaning

The substrates were exposed to Helium/ H_2O (0.5%)/O_2 (0.2%) plasma (RF power = 60 W; humid He gas flow = 208 sccm; dry He gas flow = 790 sccm; O_2 gas flow = 1.98 sccm) at a distance of 3 mm. Using an XY translation stage, the plasma jet was scanned the substrate for 4 minutes on each side. The substrates were then immediately placed in deionised water to avoid contamination. The substrates were washed with methanol and dried under a stream of nitrogen gas prior to monolayer preparation.

6.4.1.3 Glass Slides - SAM Preparation

Freshly cleaned substrates were placed in a solution of silane precursor (8 mM), methanesulfonic acid (0.05 mM) and dry toluene (70 mL) and left sealed overnight at room temperature under a nitrogen atmosphere. The substrates were then rinsed with methanol several times and dried using a stream of nitrogen prior to contact angle analysis.

6.4.1.4 Silica Wafer/SOI - SAM Preparation

Freshly cleaned substrates were placed in a solution of silane precursor (8 mM), methanesulfonic acid (0.05 mM) and dry toluene (5 mL) and left sealed overnight at room temperature under a nitrogen atmosphere. The substrates were then rinsed with methanol several times and dried using a stream of nitrogen prior to contact angle analysis.

6.4.1.5 Glass Petri Dish - SAM Preparation

A solution of silane precursor (8 mM), methanesulfonic acid (0.05 mM) and dry toluene (15 mL) was added to a freshly cleaned Petri dish (9 cm diameter) and left sealed overnight at room temperature under a nitrogen atmosphere. The substrates were then rinsed with methanol several times and dried using a stream of nitrogen.

6.4.1.6 SiO_2 Nanoparticles - SAM Preparation

10-20 nm sized SiO_2 nanoparticles were cleaned with piranha solution (a 1:3 ratio of 30% H_2O_2 and concentrated H_2SO_4) for 1 hour over an 80°C water bath. The particles were then rinsed thoroughly with Millipore water and centrifuged 3 times, then rinsed with methanol and centrifuged 3 times, before being dried under reduced pressure at 40°C for 2 hours. The particles (1 g) were then added to a solution of dry toluene (25 mL) and the silane precursor (2.7 equivalent per mole to the surface hydroxyl groups) and stirred at room temperature under a nitrogen atmosphere overnight. The particles were then rinsed with methanol, centrifuged 3 times and dried on a rotary evaporator under reduced pressure at 40°C.

6.4.1.7 SiO_2 Nanoparticles - SAM Preparation of Mixed Monolayers

An equimolar solution of the respective trialkoxysilane (1.35 eq.) and 6-(triethoxysilyl)hexan-2-one (1.35 eq.) in dry toluene (5 mL) was added to a suspension of dry, piranha-cleaned silica nanoparticles (10-20 nm, 1 g) and dry toluene (20 mL) and stirred at room temperature under a nitrogen atmosphere overnight. The particles were rinsed with methanol and centrifuged 3 times, then dried under reduced pressure at 40°C.

6.4.2 Atmospheric Conditions

A multigas blender (Environics S6100, S/N 3601) was used to generate ozone, O_3 (range 0-100 ppbV) and Nitric oxide, NO (range 0-40 ppbV) in a zero-air matrix to give a total flow rate of 2000 mL/min overflowing the sample box. The zero air was supplied from a Pure Air Generator (PAG 003, ANNOX, UK), the NO from a cylinder (certified 25.3ppmV S/N 246220SG, BOC Gases), and the ozone from an ozone generator within the Multigas blender.

NO and ozone were measured downstream of the sample box using a T200 (Teledyne API Chemiluminescence T200, S/N 023828) and 2b ozone instrument (S/N 1752DB) respectively.

This work was carried out in the COZI-Lab, Wolfson Atmospheric Chemistry Laboratories (WACL) at the University of York. It is funded through the Atmospheric Measurement and Observation Facility (AMOF), National Centre for Atmospheric Science (NCAS), managed by Dr Katie Read.

6.4.2.1 Zero Air with Acetone

Conditioning and Cleaning of the Cylinder. A 2-litre gas cylinder was conditioned to remove any of its previous contents that may have interfered with the experiment. The conditioning procedure was as follows: (1) initial evacuation to a pressure of 3×10^{-3} mbar using a BOC Edwards scroll pump (XDS10); (2) filled to 2 bar (gauge pressure) with VOC-free humidified air; (3) left to equilibrate for 30 minutes; (4) the contents of the cylinder were then vented to the atmosphere. This procedure was repeated 15 times to ensure the cylinder was VOC free prior to preparation of the acetone gas mixture. Finally, the cylinder was evacuated to 3×10^{-3} mbar ready for use.

Preparation and Analysis of the Cylinder Concentration. 20 μl of acetone was injected into the evacuated cylinder before being pressurised up to 100 bar with oxygen-free nitrogen (OFN) from BOC. The mixture was then left to equilibrate for several hours before being analysed directly using a selected ion flow tube mass spectrometer (SIFT-MS), model: VOICE 200 Ultra, provided by Syft Technologies, to determine its concentration (4.85 ppm).

6.4.3 Radical Generation

6.4.3.1 Thermal Initiation

A solution of azobisisobutyronitrile (AIBN) in DCM (2 mg/mL) was made in a volumetric flask. The AIBN solution (2 mL) was added to functionalised nanoparticles

(100 mg) in a round bottom flask and sealed. The round bottom flask was placed in an oil bath at 75°C for 16 hours. The functionalised nanoparticles were washed with DCM (5 mL) 3 times and the solution was collected. The solution was rotary evaporated to dryness and analysed by ^{1}H NMR. The remaining functionalised nanoparticles were dried under reduced pressure and immediately transferred to a round bottom flask for the oxidative dissociation reaction.

6.4.3.2 UV Initiation

A mercury TLC lamp (UVG-11, 254 nm, 230 V, 0.12 Amps, 27.6 W) was used for all experiments involving UV light exposure. The power at 4 cm from the UV lamp was 4 mW/cm^2.

6.4.3.3 Ketone Photolysis

Mixed monolayer functionalised SiO_2 nanoparticles containing 6-(triethoxysilyl)hexan-2-one chains (100 mg) were placed on a glass plate, 4 cm beneath a Mercury Lamp inside a 24 L black box, which was placed in a laboratory fumehood. The functionalised nanoparticles were exposed for 8-24 hours, depending on experimental requirements. After exposure, the functionalised nanoparticles were immediately transferred to a round bottom flask for the oxidative dissociation reaction.

6.4.3.4 UV Exposure of Functionalised SiO_2 Nanoparticles in Ambient Laboratory Air

Functionalised SiO_2 nanoparticles (100 mg) were placed on a glass plate, 4 cm beneath a Mercury Lamp inside a 24 L black box, which was placed in a laboratory fumehood. The functionalised nanoparticles were exposed for 8-24 hours, depending on experimental requirements. After exposure, the functionalised nanoparticles were immediately transferred to a round bottom flask for the oxidative dissociation reaction.

6.4.3.5 UV Exposure of Functionalised SiO_2 Nanoparticles in Zero Air

Zero air (1:4 mixture of O_2 and N_2) was supplied from a Pure Air Generator (PAG 003, ANNOX, UK) which was connected to the 24 L black box. The flow rate was set to 2 L/min. Functionalised SiO_2 nanoparticles (100 mg) were placed on a glass plate, 4 cm beneath a Mercury Lamp inside the black box. The box was then purged for 30 minutes before turning the UV lamp on. The functionalised nanoparticles were exposed for 8-24 hours, depending on experimental requirements. After exposure, the functionalised nanoparticles were immediately transferred to a round bottom flask for the oxidative dissociation reaction.

6.4.3.6 UV Exposure of Functionalised SiO_2 Nanoparticles in Zero Air with Ozone

A multigas blender (Environics S6100, S/N 3601) was used to generate ozone in a zero-air matrix to give a concentration of 35 ppb and a total flow rate of 2 L/min. Functionalised SiO_2 nanoparticles (100 mg) were placed on a glass plate, 4 cm

beneath a Mercury Lamp inside the black box. The box was then purged for 30 minutes before turning the UV lamp on. The functionalised nanoparticles were exposed for 8-24 hours, depending on experimental requirements. After exposure, the functionalised nanoparticles were immediately transferred to a round bottom flask for the oxidative dissociation reaction.

6.4.3.7 UV Exposure of Functionalised SiO_2 Nanoparticles in Zero Air with NO

A multigas blender (Environics S6100, S/N 3601) was used to generate NO in a zero-air matrix to give a concentration of 40 ppb and a total flow rate of 2 L/min. Functionalised SiO_2 nanoparticles (100 mg) were placed on a glass plate, 4 cm beneath a Mercury Lamp inside the black box. The box was then purged for 30 minutes before turning the UV lamp on. The functionalised nanoparticles were exposed for 8-24 hours, depending on experimental requirements. After exposure, the functionalised nanoparticles were immediately transferred to a round bottom flask for the oxidative dissociation reaction.

6.4.3.8 UV Exposure of Functionalised SiO_2 Nanoparticles in Zero Air with Acetone

A gas cylinder containing acetone at 4.85 ppm was added to the zero-air matrix to give a concentration of 110 ppb and a total flow rate of 2 L/min. Functionalised SiO_2 nanoparticles (100 mg) were placed on a glass plate, 4 cm beneath a Mercury Lamp inside the black box. The box was then purged for 30 minutes before turning the UV lamp on. The functionalised nanoparticles were exposed for 8-24 hours, depending on experimental requirements. After exposure, the functionalised nanoparticles were immediately transferred to a round bottom flask for the oxidative dissociation reaction.

6.4.4 Atmospheric Pressure Plasma

A COST (Cooperation in Science and Technology) jet was used as the plasma source. It consists of a 30 mm x 1 mm x 1 mm (length x width x height) plasma channel, connected to a housing which incorporates voltage and current probes to determine the power dissipated by the plasma. The typical power output used in these experiments was set to 60 W and the gas flow of each component was set based on the experimental requirements.

6.4.4.1 Exposure of Functionalised Glass Slide Surfaces to Atmospheric Pressure Plasma

Functionalised glass slide surfaces were divided into a grid of 12. Every other square of the grid was exposed to Helium/ H_2O (0.5%)/O_2 (0.2%) plasma (RF power = 60 W; humid He gas flow = 208 sccm; dry He gas flow = 790 sccm; O_2 gas flow = 1.98 sccm) for one minute at distances varying from 2-24 mm. The plasma jet was attached to an XY translation stage which was programmed to move around the square.

6.5 Analytical Protocols

6.5.1 Dissociation of Organic Molecules from Functionalised Surfaces

6.5.1.1 Dissociation from a Petri Dish

A solution of THF (HPLC grade, 6 mL), $KHCO_3$ (14 mg) and Bu_4NF (128 µl) was stirred in a piranha cleaned round bottom flask for 15 minutes. The solution was transferred to a functionalised petri dish using a syringe and the petri dish was covered and sealed for 3 hours. H_2O_2 (15 µl) was added to the petri dish and then covered and sealed for overnight. The solution was concentrated on a rotary evaporator for approximately 20 mins (190 mbar, 30 °C) until complete dryness.

6.5.1.2 Dissociation from SiO_2 Nanoparticles (10-20 nm)

Functionalised 10-20 nm sized silica nanoparticles (100 mg) were added to a solution of THF (dry, 10 mL), $KHCO_3$ (8 eq., 62.4 mg), Bu_4NF (8 eq., 624 μl) and stirred for 3 hours under N_2 atmosphere, before adding H_2O_2 (12 eq., 106 μl) and leaving to stir for 20-24 hours. The particles were then centrifuged, and the solution collected. The particles were washed with DCM and centrifuged 3 times and the solutions were collected in a round bottom flask. The solution was concentrated on a rotary evaporator for approximately 20 mins (190 mbar, 30 °C) until complete dryness. For NMR analysis, dimethyl terephalate was added as an internal standard (10 mg) and the compounds were dissolved in $CDCl_3$. For GC-MS analysis, diethyl ether (1 mL) was added and the solution was filtered through a glass pipette containing a cotton/silica plug (height of silica plug approx. 2 cm). The cotton plug was washed 6 times with diethyl ether (0.5 mL) and then 4 times with diethyl/ethylacetate mixture (3:1) and the solution collected. The solution was concentrated to dryness on a rotary evaporator prior to the silylation procedure.

6.5.1.3 Silylation of Alcohol Derivatives for GC-MS Analysis

Silylation was performed by addition of N,O-bis(trimethylsilyl)trifluoroacetamide (BSTFA) containing 1 % trimethylchlorosilane (TMCS; 100 μL) and pyridine (20 μL). The solution was heated at 100°C for 30 mins.

Appendix A

A1 BET measurements

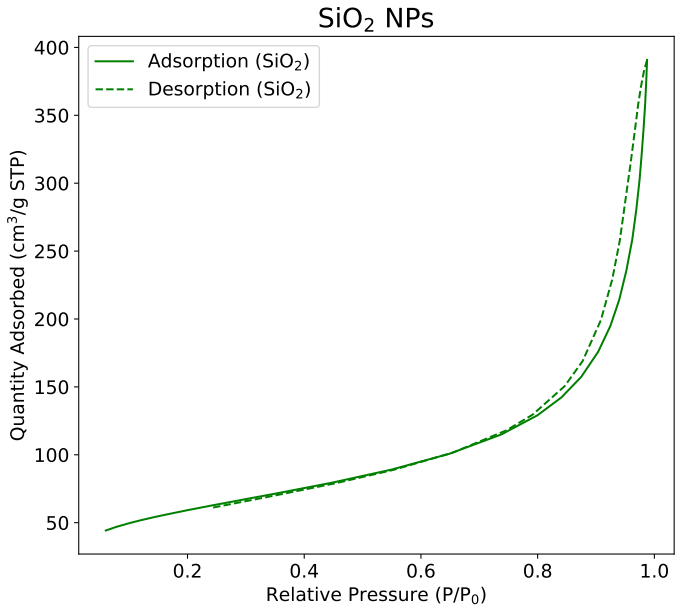

Figure A.1: BET surface area analysis of SiO_2 nanoparticles (10-20 nm sized).

A2 AFM images

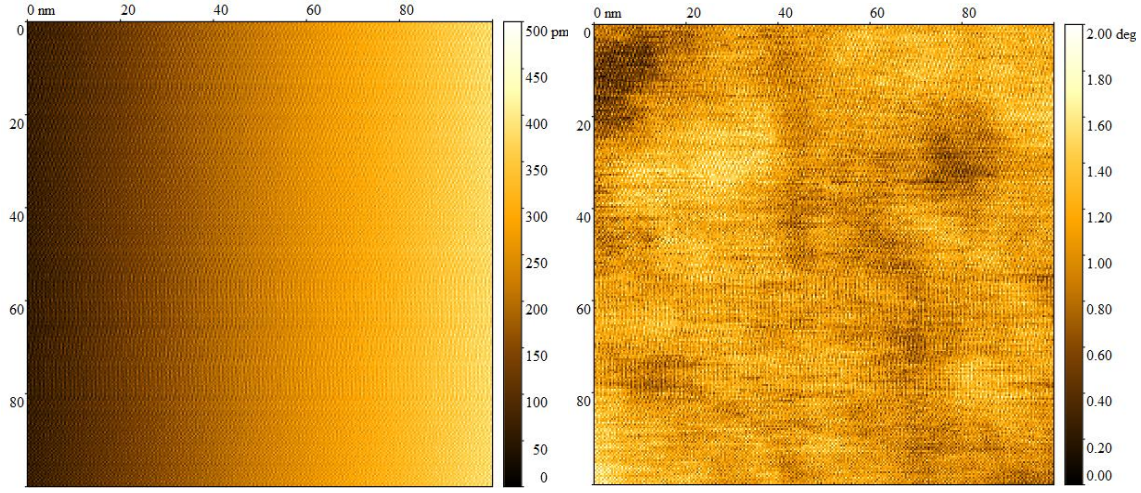

Figure A.2: AFM image of a 100 x 100 nm area of a C8Alk functionalised Si wafer surface. The left image showing the amplitude and the right image showing the phase.

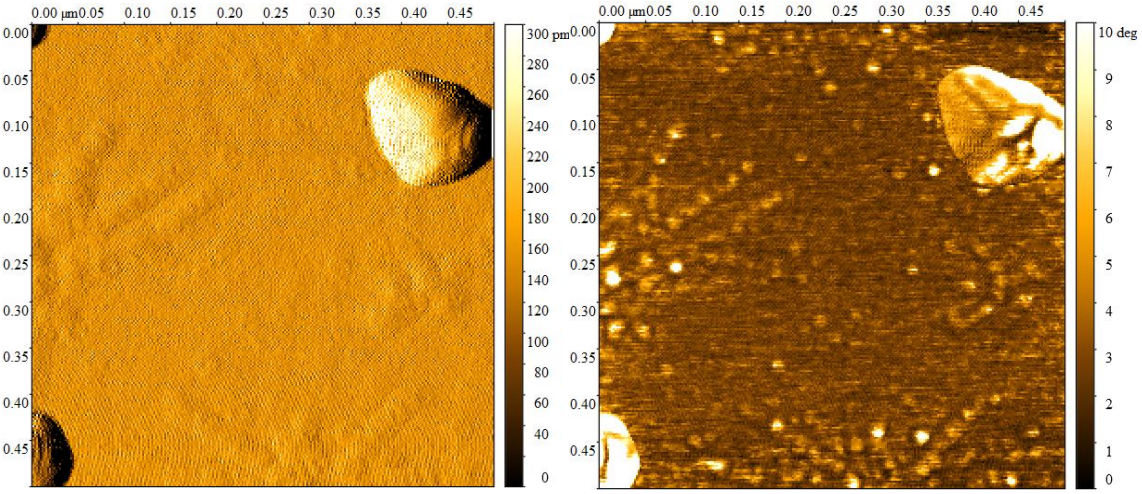

Figure A.3: AFM image of a 500 x 500 nm area of a C5Eth functionalised Si wafer surface. The left image showing the amplitude and the right image showing the phase.

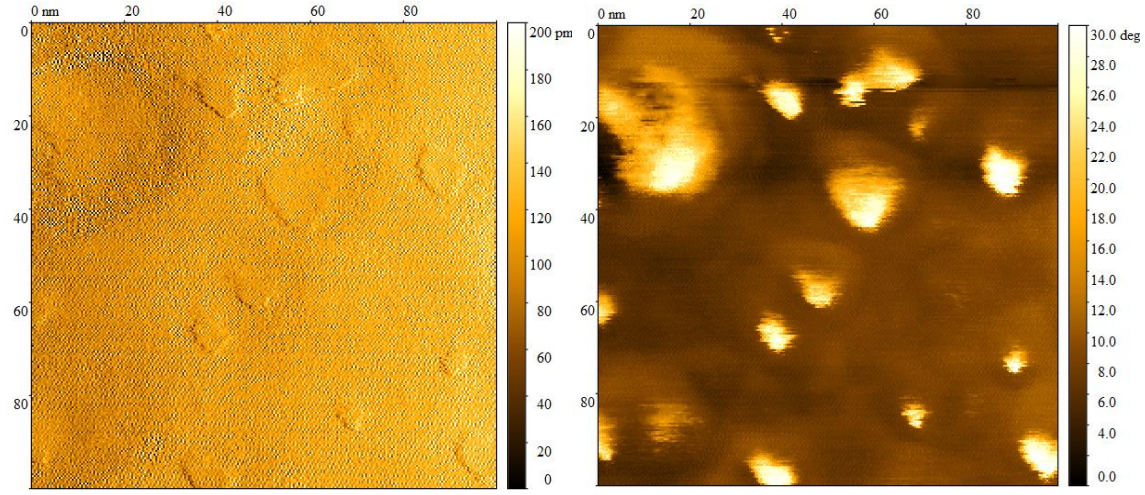

Figure A.4: AFM image of a 500 x 500 nm area of a C6One functionalised Si wafer surface. The left image showing the amplitude and the right image showing the phase.

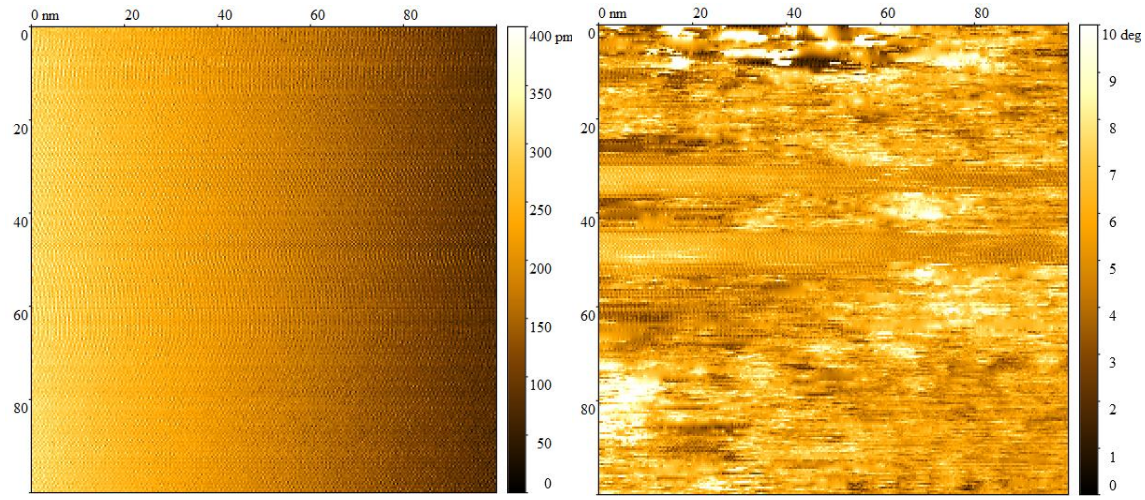

Figure A.5: AFM image of a 100 x 100 nm area of a C8Perf functionalised Si wafer surface. The left image showing the amplitude and the right image showing the phase.

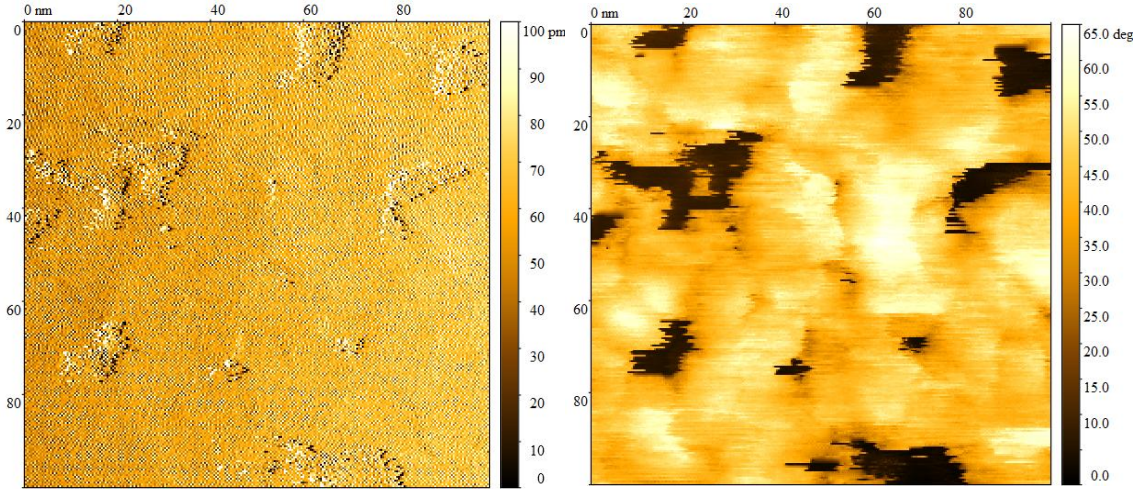

Figure A.6: AFM image of a 100 x 100 nm area of a C8Alk-C6One mixed monolayer functionalised Si wafer surface. The left image showing the amplitude and the right image showing the phase.

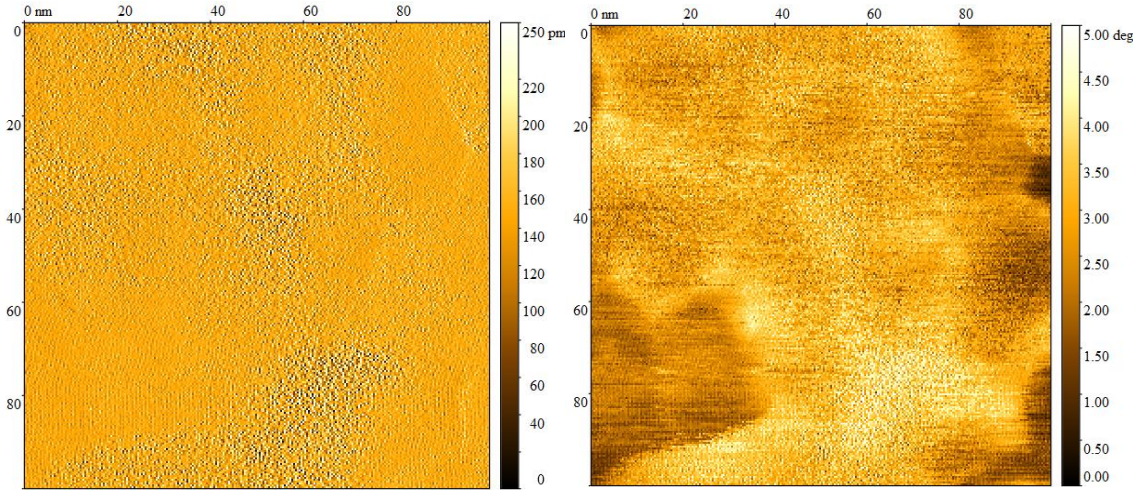

Figure A.7: AFM image of a 100 x 100 nm area of a C8Perf-C6One mixed monolayer functionalised Si wafer surface. The left image showing the amplitude and the right image showing the phase.

A3 ATR-FTIR

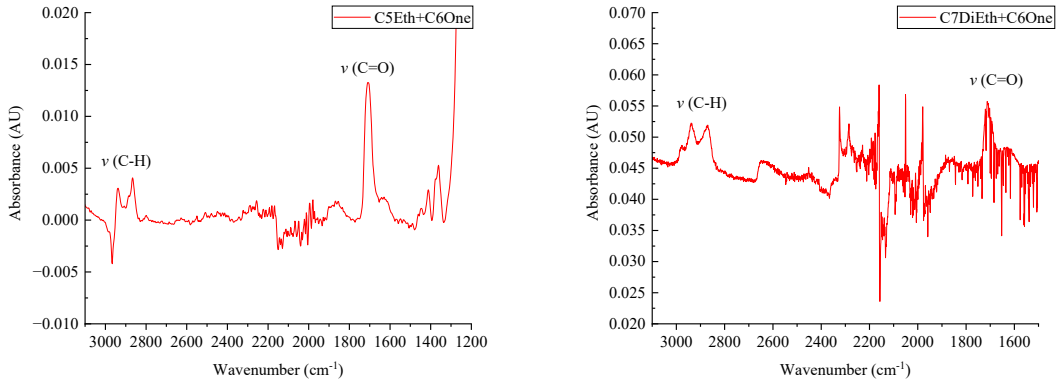

Figure A.8: ATR-FTIR spectra of C5Eth-C6One (left) and C7DiEth-C6One (right) mixed monolayer functionalised SiO_2 nanoparticles.

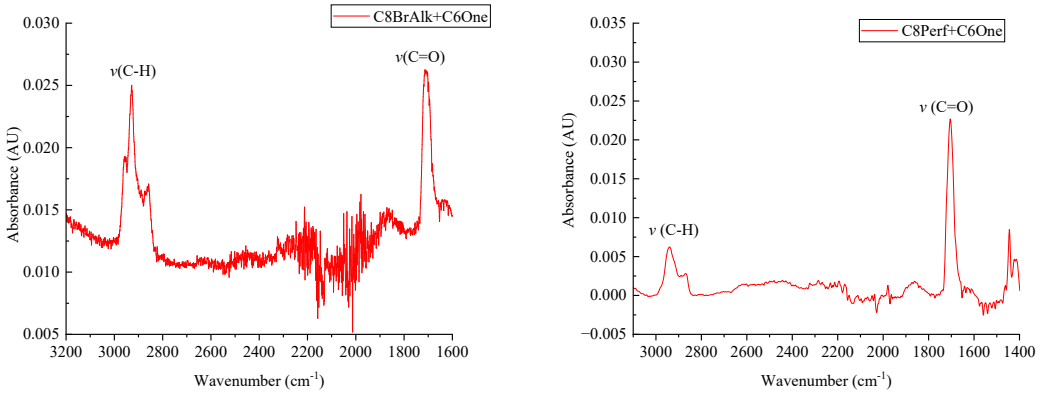

Figure A.9: ATR-FTIR spectra of C8BrAlk-C6One (left) and C8Perf-C6One (right) mixed monolayer functionalised SiO_2 nanoparticles.

A4 ^{13}C Solid State NMR

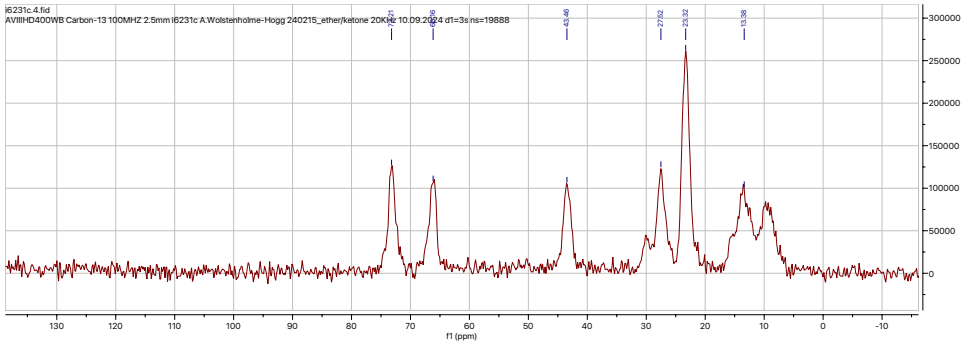

Figure A.10: ^{13}C Solid State NMR spectrum of C5Eth-C6One mixed monolayer functionalised SiO_2 nanoparticles.

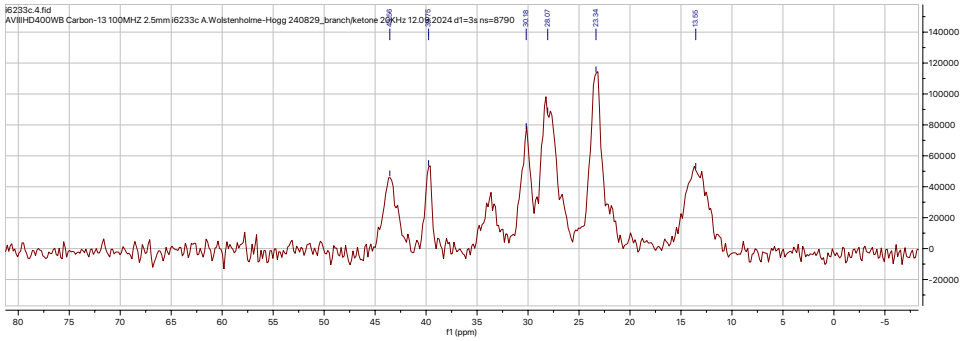

Figure A.11: ^{13}C Solid State NMR spectrum of C8BrAlk-C6One mixed monolayer functionalised SiO_2 nanoparticles.

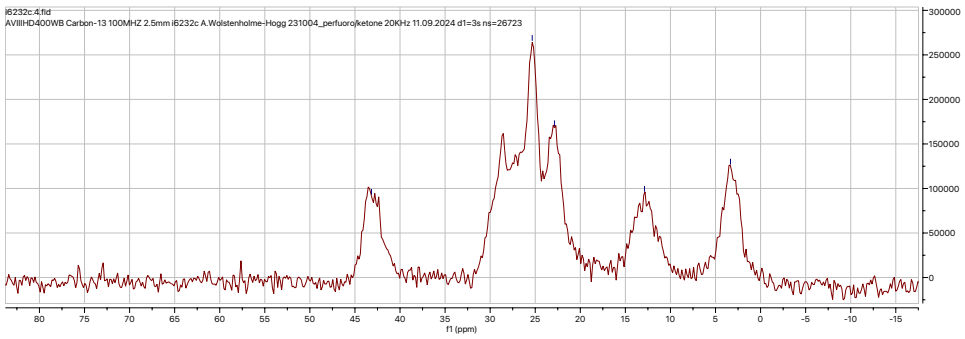

Figure A.12: ^{13}C Solid State NMR spectrum of C8Perf-C6One mixed monolayer functionalised SiO_2 nanoparticles.

A5 GC-MS Calibration Curves

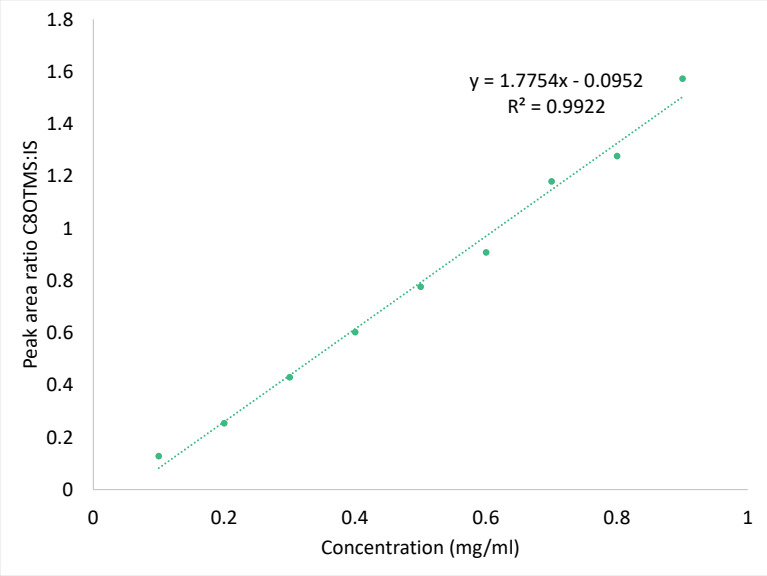

Figure A.13: Calibration curve of derivatised octan-1-ol ($C_8H_{17}OTMS$) as a ratio to the internal standard (dimethyl terepthalate) at 1 mg/ml.

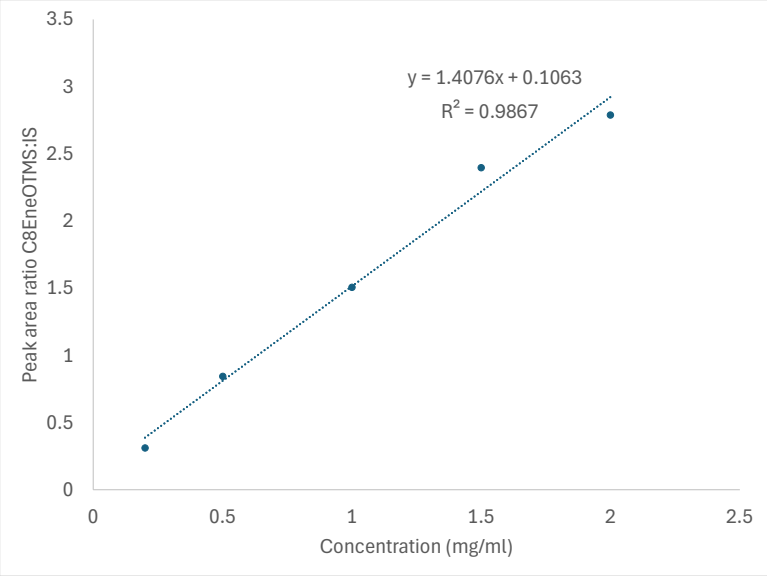

Figure A.14: Calibration curve of derivatised oct-7-en-1-ol ($C_8H_{16}OTMS$) as a ratio to the internal standard (dimethyl terepthalate) at 1 mg/ml.

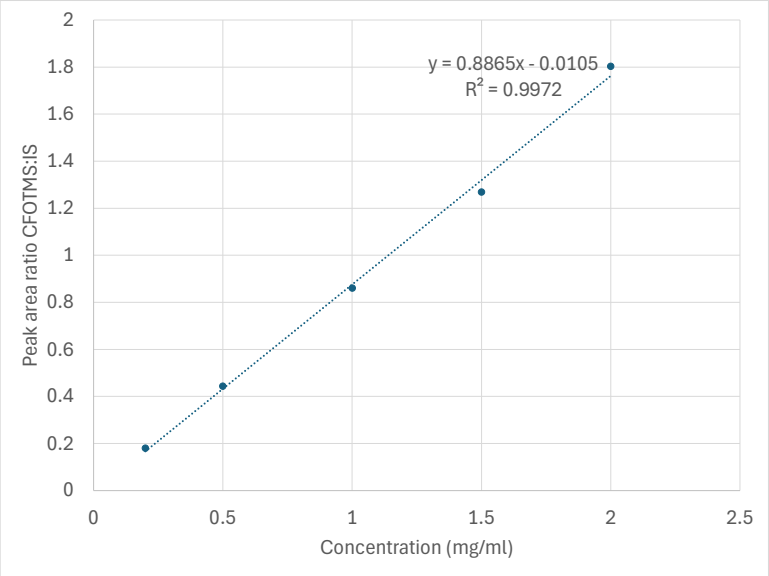

Figure A.15: Calibration curve of derivatised 1H,1H,2H,2H-perfluoro-1-octanol ($C_8H_2F_6OTMS$) as a ratio to the internal standard (dimethyl terepthalate) at 1 mg/ml.

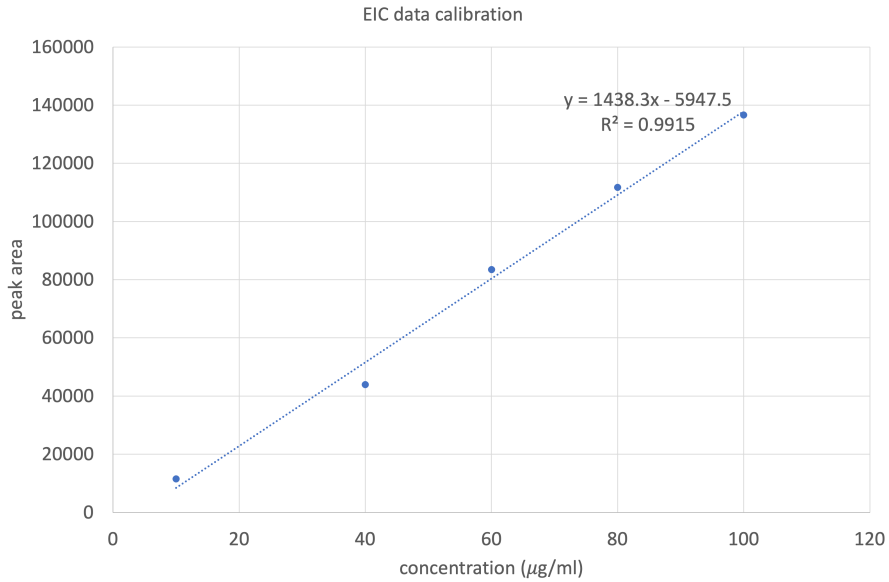

Figure A.16: Calibration curve of derivatised octan-1-ol ($C_8H_{17}OTMS$) using the peak area of the extracted ion chromatogram (m/z=187).

A6 Oxidative Dissociation of Molecules from Functionalised Surfaces

A6.1 C8BrAlk

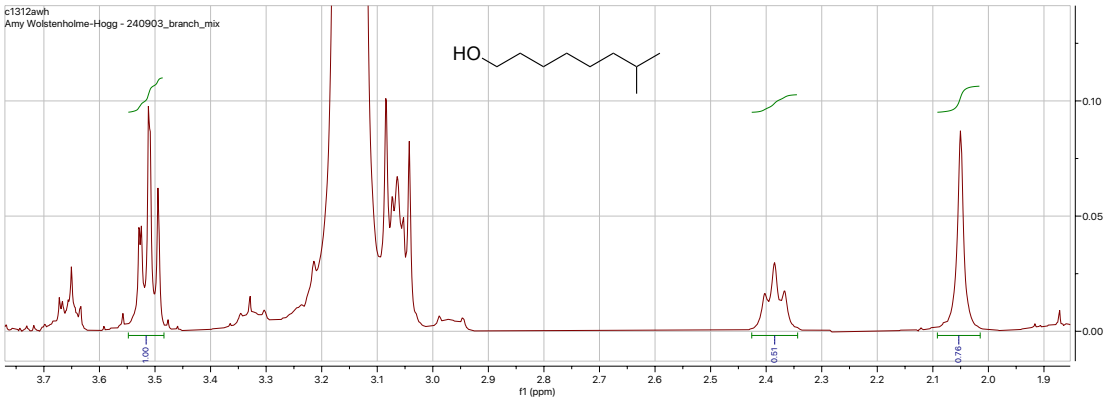

Figure A.17: ^{1}H NMR spectrum of the oxidative dissociation of C8BrAlk-C6One mixed monolayer functionalised SiO_2 nanoparticles.

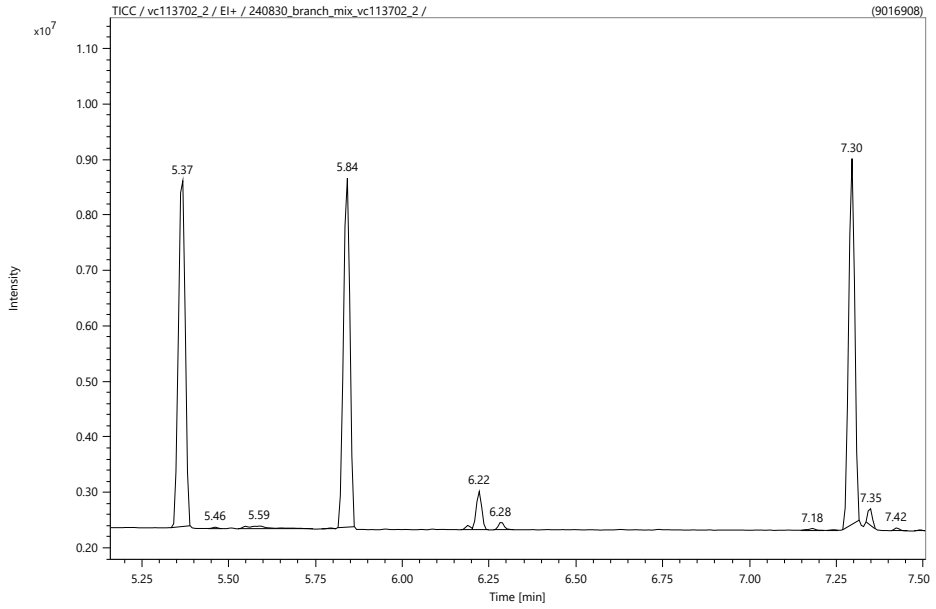

Figure A.18: GC-MS chromatogram of the oxidative dissociation of C8BrAlk-C6One mixed monolayer functionalised SiO_2 nanoparticles.

A6.2 C7DiEth

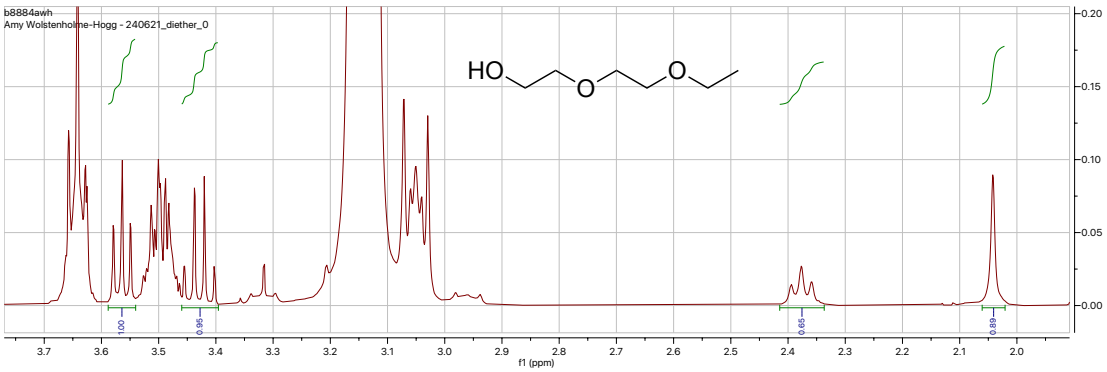

Figure A.19: ^{1}H NMR spectrum of the oxidative dissociation of C7DiEth-C6One mixed monolayer functionalised SiO_2 nanoparticles.

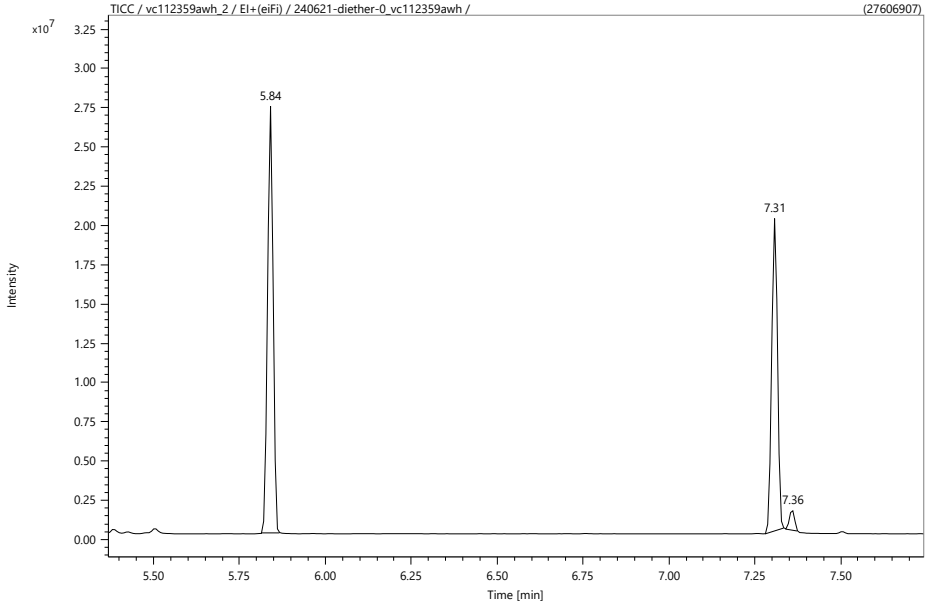

Figure A.20: GC-MS chromatogram of the oxidative dissociation of C7DiEth-C6One mixed monolayer functionalised SiO_2 nanoparticles.

A7 Mercury Lamp UV emission

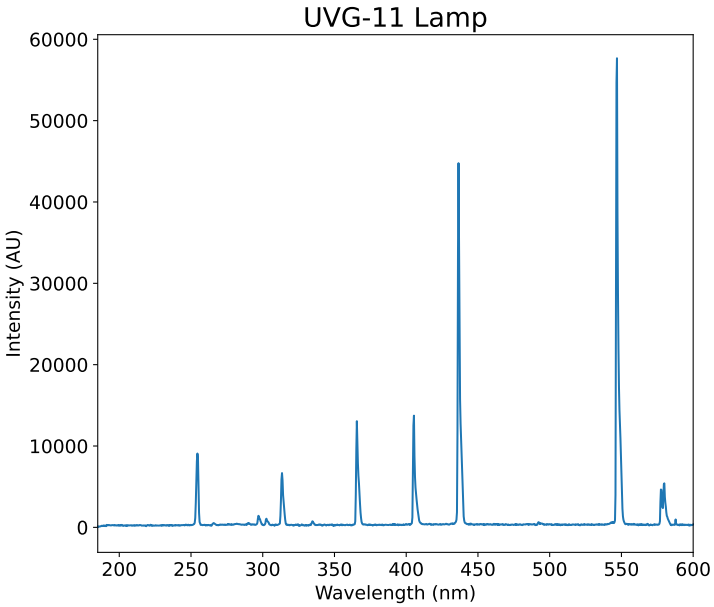

Figure A.21: Emission wavelengths of the UVG-11 lamp used in the experiments involving UV light exposure.

Bibliography

(1) Chechik, V.; Crooks, R. M.; Stirling, C. J. *Advanced Materials* **2000**, *12*, 1161–1171.

(2) Porter, N. A. *Accounts of Chemical Research* **1986**, *19*, 262–268.

(3) Adamkiewicz, M. Self-assembled monolayers on silicon: deposition and surface chemistry, Ph.D. Thesis, University of St Andrews, 2013.

(4) Van Hove, M. *Catalysis Today* **2006**, *113*, 133–140.

(5) Herzer, N.; Hoeppener, S.; Schubert, U. S. *Chemical Communications* **2010**, *46*, 5634–5652.

(6) Chaki, N. K.; Vijayamohanan, K. *Biosensors and Bioelectronics* **2002**, *17*, 1–12.

(7) Ulman, A. *Chemical Reviews* **1996**, *96*, 1533–1554.

(8) Nuzzo, R. G.; Allara, D. L. *Journal of the American Chemical Society* **1983**, *105*, 4481–4483.

(9) Porter, M. D.; Bright, T. B.; Allara, D. L.; Chidsey, C. E. *Journal of the American Chemical Society* **1987**, *109*, 3559–3568.

(10) Creager, S. E.; Rowe, G. K. *Analytica Chimica Acta* **1991**, *246*, 233–239.

(11) Netzer, L.; Sagiv, J. *Journal of the American Chemical Society* **1983**, *105*, 674–676.

(12) Wasserman, S. R.; Tao, Y. T.; Whitesides, G. M. *Langmuir* **1989**, *5*, 1074–1087.

(13) Maoz, R.; Sagiv, J. *Journal of Colloid and Interface Science* **1984**, *100*, 465–496.

(14) Roscoe, S. B.; Kakkar, A. K.; Marks, T. J.; Malik, A.; Durbin, M. K.; Lin, W.; Wong, G. K.; Dutta, P. *Langmuir* **1996**, *12*, 4218–4223.

(15) Lee, G. U.; Chrisey, L. A.; Colton, R. J. *Science* **1994**, *266*, 771–773.

(16) Silberzan, P.; Leger, L.; Ausserre, D.; Benattar, J. *Langmuir* **1991**, *7*, 1647–1651.

(17) Gooding, J. J.; Ciampi, S. *Chemical Society Reviews* **2011**, *40*, 2704–2718.

(18) Combellas, C.; Kanoufi, F.; Pinson, J.; Podvorica, F. I. *Journal of the American Chemical Society* **2008**, *130*, 8576–8577.

(19) Barness, Y.; Gershevitz, O.; Sekar, M.; Sukenik, C. N. *Langmuir* **2000**, *16*, 247–251.

(20) Jin, Z.; Vezenov, D.; Lee, Y.; Zull, J.; Sukenik, C.; Savinell, R. *Langmuir* **1994**, *10*, 2662–2671.

(21) Herzer, N.; Haensch, C.; Hoeppener, S.; Schubert, U. S. *Langmuir* **2010**, *26*, 8358–8365.

(22) De Smet, L.; Ullien, D.; Mescher, M.; Sudhölter, E. J. *Nanowires-Implementations and Applications* **2011**, 267–288.

(23) Aswal, D.; Lenfant, S.; Guérin, D.; Yakhmi, J.; Vuillaume, D. *Analytica Chimica Acta* **2006**, *568*, 84–108.

(24) Tjong, S.-C., *Nanocrystalline Materials: their Synthesis-Structure-Property Relationships and Applications*; Newnes: 2013.

(25) Osterholtz, F.; Pohl, E. *Journal of Adhesion Science and Technology* **1992**, *6*, 127–149.

(26) Miller, J. D.; Ishida, H. *Langmuir* **1986**, *2*, 127–131.

(27) Schwartz, D.; Steinberg, S.; Israelachvili, J.; Zasadzinski, J. *Physical Review Letters* **1992**, *69*, 3354.

(28) Lambert, A. G.; Neivandt, D. J.; McAloney, R. A.; Davies, P. B. *Langmuir* **2000**, *16*, 8377–8382.

(29) Fadeev, A. Y.; McCarthy, T. J. *Langmuir* **1999**, *15*, 3759–3766.

(30) Fadeev, A. Y.; McCarthy, T. J. *Langmuir* **2000**, *16*, 7268–7274.

(31) Jun, Y.; Zhu, X. *Journal of Adhesion Science and Technology* **2003**, *17*, 593–601.

(32) Tian, R.; Seitz, O.; Li, M.; Hu, W.; Chabal, Y. J.; Gao, J. *Langmuir* **2010**, *26*, 4563–4566.

(33) Liu, Y.; Wolf, L. K.; Messmer, M. C. *Langmuir* **2001**, *17*, 4329–4335.

(34) Parikh, A. N.; Allara, D. L.; Azouz, I. B.; Rondelez, F. *The Journal of Physical Chemistry* **1994**, *98*, 7577–7590.

(35) Vallant, T.; Brunner, H.; Mayer, U.; Hoffmann, H.; Leitner, T.; Resch, R.; Friedbacher, G. *The Journal of Physical Chemistry B* **1998**, *102*, 7190–7197.

(36) Leitner, T.; Friedbacher, G.; Vallant, T.; Brunner, H.; Mayer, U.; Hoffmann, H. *Microchimica Acta* **2000**, *133*, 331–336.

(37) Reiniger, M.; Basnar, B.; Friedbacher, G.; Schleberger, M. *Surface and Interface Analysis* **2002**, *33*, 85–88.

(38) Feichtenschlager, B.; Lomoschitz, C. J.; Kickelbick, G. *Journal of Colloid and Interface Science* **2011**, *360*, 15–25.

(39) Fontaine, P.; Goldmann, M.; Rondelez, F. *Langmuir* **1999**, *15*, 1348–1352.

(40) Britt, D. W.; Hlady, V. *Journal of Colloid and Interface Science* **1996**, *178*, 775–784.

(41) Allara, D. L.; Parikh, A. N.; Rondelez, F. *Langmuir* **1995**, *11*, 2357–2360.

(42) Le Grange, J.; Markham, J.; Kurkjian, C. *Langmuir* **1993**, *9*, 1749–1753.

(43) Imhof, R.; Xie, X.; Calzaferri, G. *Spectrochimica Acta Part A: Molecular and Biomolecular Spectroscopy* **1997**, *53*, 981–989.

(44) Bierbaum, K.; Kinzler, M.; Wöll, C.; Grunze, M.; Hähner, G.; Heid, S.; Effenberger, F. *Langmuir* **1995**, *11*, 512–518.

(45) Flinn, D.; Guzonas, D.; Yoon, R.-H. *Colloids and Surfaces A: Physicochemical and Engineering Aspects* **1994**, *87*, 163–176.

(46) Vallant, T.; Kattner, J.; Brunner, H.; Mayer, U.; Hoffmann, H. *Langmuir* **1999**, *15*, 5339–5346.

(47) Huo, L.; Du, P.; Zhou, H.; Zhang, K.; Liu, P. *Applied Surface Science* **2017**, *396*, 865–869.

(48) Ito, Y.; Virkar, A. A.; Mannsfeld, S.; Oh, J. H.; Toney, M.; Locklin, J.; Bao, Z. *Journal of the American Chemical Society* **2009**, *131*, 9396–9404.

(49) Angst, D. L.; Simmons, G. W. *Langmuir* **1991**, *7*, 2236–2242.

(50) Rozlosnik, N.; Gerstenberg, M. C.; Larsen, N. B. *Langmuir* **2003**, *19*, 1182–1188.

(51) Cheng, Y.-a.; Zheng, B.; Chuang, P.-h.; Hsieh, S. *Langmuir* **2010**, *26*, 8256–8261.

(52) Yu, C.-J.; Richter, A.; Kmetko, J.; Dugan, S.; Datta, A.; Dutta, P. *Physical Review E* **2001**, *63*, 021205.

(53) Desbief, S.; Patrone, L.; Goguenheim, D.; Guérin, D.; Vuillaume, D. *Physical Chemistry Chemical Physics* **2011**, *13*, 2870–2879.

(54) Foisner, J.; Glaser, A.; Kattner, J.; Hoffmann, H.; Friedbacher, G. *Langmuir* **2003**, *19*, 3741–3746.

(55) Woodward, J.; Schwartz, D. *Journal of the American Chemical Society* **1996**, *118*, 10944–10944.

(56) García, N.; Benito, E.; Guzmán, J.; Tiemblo, P.; Morales, V.; García, R. A. *Microporous and Mesoporous Materials* **2007**, *106*, 129–139.

(57) Huber, M. P.; Kelch, S.; Berke, H. *International Journal of Adhesion and Adhesives* **2016**, *64*, 153–162.

(58) Pantoja, M.; Díaz-Benito, B.; Velasco, F.; Abenojar, J.; Del Real, J. *Applied Surface Science* **2009**, *255*, 6386–6390.

(59) Pantoja, M.; Encinas, N.; Abenojar, J.; Martínez, M. *Applied Surface Science* **2013**, *280*, 850–857.

(60) Zhou, X.; Hu, S.; Shephard, N. E.; Ahn, D. *ACS Publications* **2003**.

(61) Delattre, L.; Babonneau, F. *Chemistry of Materials* **1997**, *9*, 2385–2394.

(62) Lee, T.-M.; Ma, C.-C. M.; Hsu, C.-W.; Wu, H.-L. *Polymer* **2005**, *46*, 8286–8296.

(63) Nomura, Y.; Sato, S.; Mori, H.; Endo, T. *Journal of Applied Polymer Science* **2007**, *106*, 3165–3170.

(64) Nomura, Y.; Sato, S.; Mori, H.; Endo, T. *Journal of Applied Polymer Science* **2008**, *109*, 608–616.

(65) Higashi, N.; Mori, T.; Niwa, M. *Journal of the Chemical Society, Chemical Communications* **1990**, 225–226.

(66) Evans, S.; Johnson, S.; Ringsdorf, H.; Williams, L.; Wolf, H. *Langmuir* **1998**, *14*, 6436–6440.

(67) Fan, F.; Maldarelli, C.; Couzis, A. *Langmuir* **2003**, *19*, 3254–3265.

(68) Stranick, S.; Parikh, A.; Tao, Y.-T.; Allara, D.; Weiss, P. *The Journal of Physical Chemistry* **1994**, *98*, 7636–7646.

(69) Tamada, K.; Hara, M.; Sasabe, H.; Knoll, W. *Langmuir* **1997**, *13*, 1558–1566.

(70) Erard, J. F.; Kovats, E. S. *Analytical Chemistry* **1982**, *54*, 193–202.

(71) Wirth, M. J.; Fatunmbi, H. O. *Analytical Chemistry* **1992**, *64*, 2783–2786.

(72) Fatunmbi, H. O.; Bruch, M. D.; Wirth, M. J. *Analytical Chemistry* **1993**, *65*, 2048–2054.

(73) Faucheux, N.; Schweiss, R.; Lützow, K.; Werner, C.; Groth, T. *Biomaterials* **2004**, *25*, 2721–2730.

(74) Gentleman, M.; Ruud, J. *Langmuir* **2010**, *26*, 1408–1411.

(75) Wang, S.; Song, Y.; Jiang, L. *Journal of Photochemistry and Photobiology C: Photochemistry Reviews* **2007**, *8*, 18–29.

(76) Niehoff, P.; Ebbinghaus, P.; Keil, P.; Erbe, A. *Applied Surface Science* **2012**, *258*, 3191–3196.

(77) Murakami, D.; Jinnai, H.; Takahara, A. *Langmuir* **2014**, *30*, 2061–2067.

(78) Eral, H. B.; 't Mannetje, D.; Oh, J. M. *Colloid and Polymer Science* **2013**, *291*, 247–260.

(79) Butt, H.-J.; Liu, J.; Koynov, K.; Straub, B.; Hinduja, C.; Roismann, I.; Berger, R.; Li, X.; Vollmer, D.; Steffen, W., et al. *Current Opinion in Colloid & Interface Science* **2022**, *59*, 101574.

(80) Bain, C. D.; Troughton, E. B.; Tao, Y. T.; Evall, J.; Whitesides, G. M.; Nuzzo, R. G. *Journal of the American Chemical Society* **1989**, *111*, 321–335.

(81) Horr, T. J.; Ralston, J.; Smart, R. S. C. *Colloids and Surfaces A: Physicochemical and Engineering Aspects* **1995**, *97*, 183–196.

(82) Stevie, F. A.; Donley, C. L. *Journal of Vacuum Science & Technology A* **2020**, *38*.

(83) Morgan, D. J. *Cardiff Catalysis Institute, School of Chemistry, Cardiff University, Cardiff* **2014**.

(84) Aziz, M.; Ismail, A., *X-ray photoelectron spectroscopy (XPS)*; Elsevier: 2017, pp 81–93.

(85) Artemenko, A.; Shchukarev, A.; Štenclová, P.; Wågberg, T.; Segervald, J.; Jia, X.; Kromka, A. In *IOP Conference Series: Materials Science and Engineering*, 2021; Vol. 1050, p 012001.

(86) Matijašević, J.; Hassler, N.; Reiter, G.; Fringeli, U. P. *Langmuir* **2008**, *24*, 2588–2596.

(87) Liu, Y.-J.; Navasero, N. M.; Yu, H.-Z. *Langmuir* **2004**, *20*, 4039–4050.

(88) Eid, M. M. In *Handbook of Consumer Nanoproducts*; Springer: 2022, pp 1–30.

(89) Kazarian, S. G.; Chan, K. A. *Analyst* **2013**, *138*, 1940–1951.

(90) Binnig, G.; Quate, C. F.; Gerber, C. *Physical Review Letters* **1986**, *56*, 930.

(91) Maurice, P. A. *Colloids and Surfaces A: Physicochemical and Engineering Aspects* **1996**, *107*, 57–75.

(92) Butt, H.-J.; Cappella, B.; Kappl, M. *Surface Science Reports* **2005**, *59*, 1–152.

(93) Hoh, J. H.; Hansma, P. K. *Trends in Cell Biology* **1992**, *2*, 208–213.

(94) Trache, A.; Meininger, G. A. *Current Protocols in Microbiology* **2008**, *8*, 2C–2.

(95) Mourougou-Candoni, N. *Atomic Force Microscopy Investigations into Biology–From Cell to Protein* **2012**, 55–84.

(96) Zhang, Q.; Archer, L. A. *The Journal of Physical Chemistry B* **2003**, *107*, 13123–13132.

(97) Roush, J. A.; Thacker, D. L.; Anderson, M. R. *Langmuir* **1994**, *10*, 1642–1646.

(98) Chen, Q.; Xu, S.; Liu, Q.; Masliyah, J.; Xu, Z. *Advances in Colloid and Interface Science* **2016**, *233*, 94–114.

(99) Marx, K. A. *Biomacromolecules* **2003**, *4*, 1099–1120.

(100) Park, H.; Kim, J.-H. *ACS Sensors* **2024**.

(101) Jenkin, M. E.; Valorso, R.; Aumont, B.; Rickard, A. R. *Atmospheric Chemistry and Physics* **2019**, *19*, 7691–7717.

(102) Smith, L. M.; Aitken, H. M.; Coote, M. L. *Accounts of Chemical Research* **2018**, *51*, 2006–2013.

(103) Oh, S.; Stache, E. E. *Chemical Society Reviews* **2024**.

(104) Krupa, S. V.; Manning, W. J. *Environmental Pollution* **1988**, *50*, 101–137.

(105) Singh, H. B.; Ludwig, F. L.; Johnson, W. B. *Atmospheric Environment (1967)* **1978**, *12*, 2185–2196.

(106) Orlando, J. J.; Tyndall, G. S. *Chemical Society Reviews* **2012**, *41*, 6294–6317.

(107) Gligorovski, S.; Strekowski, R.; Barbati, S.; Vione, D. *Chemical Reviews* **2015**, *115*, 13051–13092.

(108) Stone, D.; Whalley, L. K.; Heard, D. E. *Chemical Society Reviews* **2012**, *41*, 6348–6404.

(109) Cooper, D. J. *Journal of Atmospheric Chemistry* **1996**, *25*, 97–113.

(110) Zhang, D.; Zhang, R. *The Journal of Chemical Physics* **2005**, *122*.

(111) Llusia, J.; Peñuelas, J.; Seco, R.; Filella, I. *Journal of Atmospheric Chemistry* **2012**, *69*, 215–230.

(112) Gkatzelis, G. I.; Coggon, M. M.; McDonald, B. C.; Peischl, J.; Gilman, J. B.; Aikin, K. C.; Robinson, M. A.; Canonaco, F.; Prevot, A. S.; Trainer, M., et al. *Environmental Science & Technology* **2021**, *55*, 4332–4343.

(113) Zhou, Z.; Zhou, S.; Abbatt, J. P. *Environmental Science & Technology* **2019**, *53*, 12467–12475.

(114) Hammes, J.; Lutz, A.; Mentel, T.; Faxon, C.; Hallquist, M. *Atmospheric Chemistry and Physics* **2019**, *19*, 13037–13052.

(115) Jenkin, M. E.; Valorso, R.; Aumont, B.; Rickard, A. R.; Wallington, T. J. *Atmospheric Chemistry and Physics* **2018**, *18*, 9297–9328.

(116) Jenkin, M. E.; Valorso, R.; Aumont, B.; Rickard, A. R.; Wallington, T. J. *Atmospheric Chemistry and Physics* **2018**, *18b*, 9329–9349.

(117) Ingold, K. U. *Accounts of Chemical Research* **1969**, *2*, 1–9.

(118) Gryn'ova, G.; Hodgson, J. L.; Coote, M. L. *Organic & Biomolecular Chemistry* **2011**, *9*, 480–490.

(119) DS-NES, N. *Soft Matter* **1970**, *31*, 6–48.

(120) Hudzik, J. M.; Bozzelli, J. W.; Simmie, J. M. *The Journal of Physical Chemistry A* **2014**, *118*, 9364–9379.

(121) Auzmendi-Murua, I.; Charaya, S.; Bozzelli, J. W. *The Journal of Physical Chemistry A* **2013**, *117*, 378–392.

(122) Chenier, J.; Tong, S.; Howard, J. *Canadian Journal of Chemistry* **1978**, *56*, 3047–3053.

(123) Howard, J.; Chenier, J.; Holden, D. *Canadian Journal of Chemistry* **1978**, *56*, 170–175.

(124) Garrett, G. E.; Pratt, D. A.; Parent, J. S. *Macromolecules* **2020**, *53*, 2793–2800.

(125) Korcek, S.; Chenier, J.; Howard, J.; Ingold, K. *Canadian Journal of Chemistry* **1972**, *50*, 2285–2297.

(126) Zhang, W.; Zhao, Z.; Shen, C.; Zhang, H. *Environmental Science & Technology* **2023**, *57*, 6965–6974.

(127) Zhao, Z.; Yang, X.; Lee, J.; Tolentino, R.; Mayorga, R.; Zhang, W.; Zhang, H. *ACS Earth and Space Chemistry* **2019**, *4*, 283–296.

(128) Virtanen, A.; Joutsensaari, J.; Koop, T.; Kannosto, J.; Yli-Pirilä, P.; Leskinen, J.; Mäkelä, J. M.; Holopainen, J. K.; Pöschl, U.; Kulmala, M., et al. *Nature* **2010**, *467*, 824–827.

(129) Krapf, M.; El Haddad, I.; Bruns, E. A.; Molteni, U.; Daellenbach, K. R.; Prévôt, A. S.; Baltensperger, U.; Dommen, J. *Chem* **2016**, *1*, 603–616.

(130) Pospisilova, V.; Lopez-Hilfiker, F. D.; Bell, D. M.; El Haddad, I.; Mohr, C.; Huang, W.; Heikkinen, L.; Xiao, M.; Dommen, J.; Prevot, A., et al. *Science Advances* **2020**, *6*, eaax8922.

(131) Mertes, P.; Pfaffenberger, L.; Dommen, J.; Kalberer, M.; Baltensperger, U. *Atmospheric Measurement Techniques* **2012**, *5*, 2339–2348.

(132) Hiatt, R. R.; Mill, T.; Mayo, F. R. *The Journal of Organic Chemistry* **1968**, *33*, 1416–1420.

(133) Howard, J.; Ingold, K. *Journal of the American Chemical Society* **1968**, *90*, 1058–1059.

(134) Ingold, K. *Pure and Applied Chemistry* **1967**, *15*, 49–68.

(135) Van Sickle, D. E.; Mayo, F. R.; Arluck, R. M. *Journal of the American Chemical Society* **1965**, *87*, 4824–4832.

(136) Nangia, P. S.; Benson, S. W. *International Journal of Chemical Kinetics* **1980**, *12*, 43–53.

(137) Thomas, J.; Ingold, K. *The Journal of Physical Chemistry A* **1968**.

(138) Lee, R.; Gryn'Ova, G.; Ingold, K.; Coote, M. L. *Physical Chemistry Chemical Physics* **2016**, *18*, 23673–23679.

(139) Thomas, J. *Journal of the American Chemical Society* **1965**, *87*, 3935–3940.

(140) Bartlett, P. D.; Guaraldi, G. *Journal of the American Chemical Society* **1967**, *89*, 4799–4801.

(141) Russell, G. A. *Journal of the American Chemical Society* **1957**, *79*, 3871–3877.

(142) Russell, G. A. *Journal of Chemical Education* **1959**, *36*, 111.

(143) Fish, A. *Quarterly Reviews, Chemical Society* **1964**, *18*, 243–269.

(144) Rust, F. F. *Journal of the American Chemical Society* **1957**, *79*, 4000–4003.

(145) Fish, A. *Proceedings of the Royal Society of London. Series A. Mathematical and Physical Sciences* **1967**, *298*, 204–237.

(146) Orlando, J. J.; Tyndall, G. S.; Wallington, T. J. *Chemical Reviews* **2003**, *103*, 4657–4690.

(147) Vaughan, S.; Canosa-Mas, C. E.; Pfrang, C.; Shallcross, D. E.; Watson, L.; Wayne, R. P. *Physical Chemistry Chemical Physics* **2006**, *8*, 3749–3760.

(148) Yan, C.; Kocevska, S.; Krasnoperov, L. N. *The Journal of Physical Chemistry A* **2016**, *120*, 6111–6121.

(149) De Keer, L.; Van Steenberge, P.; Reyniers, M.-F.; Gryn'Ova, G.; Aitken, H. M.; Coote, M. L. *Polymer Chemistry* **2022**, *13*, 3304–3314.

(150) Whelan, C. A.; Blitz, M. A.; Shannon, R.; Onel, L.; Lockhart, J. P.; Seakins, P. W.; Stone, D. *The Journal of Physical Chemistry A* **2019**, *123*, 10254–10262.

(151) Sehested, J.; Møgelberg, T.; Wallington, T.; Kaiser, E.; Nielsen, O. *The Journal of Physical Chemistry* **1996**, *100*, 17218–17225.

(152) Vereecken, L.; Peeters, J. *The Journal of Physical Chemistry A* **2004**, *108*, 5197–5204.

(153) Honzicek, J. *Industrial & Engineering Chemistry Research* **2019**, *58*, 12485–12505.

(154) Bolland, J. *Proceedings of the Royal Society of London. Series A. Mathematical and Physical Sciences* **1946**, *186*, 218–236.

(155) Bolland, J.; Gee, G. *Transactions of the Faraday Society* **1946**, *42*, 236–243.

(156) Bolland, J.; Gee, G. *Transactions of the Faraday Society* **1946**, *42*, 244–252.

(157) Bolland, J.; Ten Have, P. *Transactions of the Faraday Society* **1947**, *43*, 201–210.

(158) Bolland, J. *Transactions of the Faraday Society* **1948**, *44*, 669–677.

(159) Audouin, L.; Achimsky, L.; Verdu, J. In *Handbook of Polymer Degradation*; CRC Press: 2000, pp 753–764.

(160) Ye, G.; Courtecuisse, F.; Allonas, X.; Ley, C.; Croutxe-Barghorn, C.; Raja, P.; Taylor, P.; Bescond, G. *Progress in Organic Coatings* **2012**, *73*, 366–373.

(161) Brash, A. R. *Journal of Biological Chemistry* **1999**, *274*, 23679–23682.

(162) Yurawecz, M. P.; Hood, J. K.; Mossoba, M. M.; Roach, J. A.; Ku, Y. *Lipids* **1995**, *30*, 595–598.

(163) Wilson, Z. R.; Siebert, M. R. *Energy & Fuels* **2018**, *32*, 1779–1787.

(164) Popov, A.; Blinov, N.; Krisyuk, B.; Karpova, S.; Peverov, A.; Zaikov, G. Y. *Polymer Science USSR* **1981**, *23*, 1666–1674.

(165) Razumovsky, S.; Podmasteriyev, V.; Zaikov, G. *Polymer Degradation and Stability* **1986**, *16*, 317–324.

(166) Cataldo, F.; Ricci, G.; Crescenzi, V. *Polymer Degradation and Stability* **2000**, *67*, 421–426.

(167) Lee, R.; Coote, M. L. *Physical Chemistry Chemical Physics* **2016**, *18*, 24663–24671.

(168) Schubert, C. C.; Schubert, S.; Pease, R. N. *Journal of the American Chemical Society* **1956**, *78*, 2044–2048.

(169) Chen, L.; Yamane, S.; Sago, T.; Hagihara, H.; Kutsuna, S.; Uchimaru, T.; Suda, H.; Sato, H.; Mizukado, J. *Chemical Physics Letters* **2016**, *657*, 83–89.

(170) Ali, S.; Zhong, S.-P.; Doherty, P.; Williams, D. *Biomaterials* **1993**, *14*, 648–656.

(171) Ramsden, D.; McKay, K. *Polymer Degradation and Stability* **1986**, *14*, 217–229.

(172) Andrady, A. L.; Barnes, P. W.; Bornman, J. F.; Gouin, T.; Madronich, S.; White, C.; Zepp, R. G.; Jansen, M. A. *Science of the Total Environment* **2022**, *851*, 158022.

(173) Molina, M.; Ivanov, A.; Trakhtenberg, S.; Molina, L. *Geophysical Research Letters* **2004**, *31*.

(174) Dubowski, Y.; Vieceli, J.; Tobias, D. J.; Gomez, A.; Lin, A.; Nizkorodov, S. A.; McIntire, T. M.; Finlayson-Pitts, B. J. *The Journal of Physical Chemistry A* **2004**, *108*, 10473–10485.

(175) Ye, T.; McArthur, E. A.; Borguet, E. *The Journal of Physical Chemistry B* **2005**, *109*, 9927–9938.

(176) D'Andrea, T. M.; Zhang, X.; Jochnowitz, E. B.; Lindeman, T.; Simpson, C.; David, D. E.; Curtiss, T. J.; Morris, J. R.; Ellison, G. B. *The Journal of Physical Chemistry B* **2008**, *112*, 535–544.

(177) Park, J.; Gomez, A. L.; Walser, M. L.; Lin, A.; Nizkorodov, S. A. *Physical Chemistry Chemical Physics* **2006**, *8*, 2506–2512.

(178) Attwood, A. L.; Edwards, J. L.; Rowlands, C. C.; Murphy, D. M. *The Journal of Physical Chemistry A* **2003**, *107*, 1779–1782.

(179) Poirier, G. E.; Herne, T. M.; Miller, C. C.; Tarlov, M. J. *Journal of the American Chemical Society* **1999**, *121*, 9703–9711.

(180) Zhang, Y.; Terrill, R. H.; Tanzer, T. A.; Bohn, P. W. *Journal of the American Chemical Society* **1998**, *120*, 2654–2655.

(181) Huang, J.; Hemminger, J. C. *Journal of the American Chemical Society* **1993**, *115*, 3342–3343.

(182) Hoeppener, S.; Maoz, R.; Cohen, S. R.; Chi, L.; Fuchs, H.; Sagiv, J. *Advanced Materials* **2002**, *14*, 1036–1041.

(183) Moise, T.; Rudich, Y. *Journal of Geophysical Research: Atmospheres* **2000**, *105*, 14667–14676.

(184) Norrod, K. L.; Rowlen, K. L. *Journal of the American Chemical Society* **1998**, *120*, 2656–2657.

(185) Finlayson-Pitts, B. J.; Pitts Jr, J. N., *Chemistry of the upper and lower atmosphere: theory, experiments, and applications*; Elsevier: 1999.

(186) Atkinson, R.; Arey, J. *Chemical Reviews* **2003**, *103*, 4605–4638.

(187) Katrib, Y.; Martin, S. T.; Hung, H.-M.; Rudich, Y.; Zhang, H.; Slowik, J. G.; Davidovits, P.; Jayne, J. T.; Worsnop, D. R. *The Journal of Physical Chemistry A* **2004**, *108*, 6686–6695.

(188) Vieceli, J.; Ma, O. L.; Tobias, D. J. *The Journal of Physical Chemistry A* **2004**, *108*, 5806–5814.

(189) Moise, T.; Rudich, Y. *The Journal of Physical Chemistry A* **2002**, *106*, 6469–6476.

(190) Usher, C. R.; Michel, A. E.; Grassian, V. H. *Chemical Reviews* **2003**, *103*, 4883–4940.

(191) Sagiv, J. *Journal of the American Chemical Society* **1980**, *102*, 92–98.

(192) Onclin, S.; Ravoo, B. J.; Reinhoudt, D. N. *Angewandte Chemie International Edition* **2005**, *44*, 6282–6304.

(193) Sánchez-López, L.; Chico, B.; García-Alonso, M. C.; Lozano, R. M. *Journal of Biomedical Materials Research Part A* **2024**.

(194) Wang, Y.; Lieberman, M. *Langmuir* **2003**, *19*, 1159–1167.

(195) Tamao, K.; Kakui, T.; Akita, M.; Iwahara, T.; Kanatani, R.; Yoshida, J.; Kumada, M. *Tetrahedron* **1983**, *39*, 983–990.

(196) Kern, W. *Journal of the Electrochemical Society* **1990**, *137*, 1887.

(197) Hook, D. A.; Olhausen, J. A.; Krim, J.; Dugger, M. T. *Journal of Microelectromechanical Systems* **2010**, *19*, 1292–1298.

(198) Brzoska, J.; Azouz, I. B.; Rondelez, F. *Langmuir* **1994**, *10*, 4367–4373.

(199) Adamkiewicz, M.; O'Hara, T.; O'Hagan, D.; Hähner, G. *Thin Solid Films* **2012**, *520*, 6719–6723.

(200) Booth, B. D.; Vilt, S. G.; McCabe, C.; Jennings, G. K. *Langmuir* **2009**, *25*, 9995–10001.

(201) Janssen, D.; De Palma, R.; Verlaak, S.; Heremans, P.; Dehaen, W. *Thin Solid Films* **2006**, *515*, 1433–1438.

(202) Schwartz, D. K. *Annual Review of Physical Chemistry* **2001**, *52*, 107–137.

(203) Carraro, C.; Yauw, O. W.; Sung, M. M.; Maboudian, R. *The Journal of Physical Chemistry B* **1998**, *102*, 4441–4445.

(204) Williams, D. B. G.; Lawton, M. *The Journal of Organic Chemistry* **2010**, *75*, 8351–8354.

(205) Assink, R. A.; Kay, B. D. *Annual Review of Materials Science* **1991**, *21*, 491–513.

(206) Brochier Salon, M.-C.; Belgacem, M. N. *Phosphorus, Sulfur, and Silicon and the Related Elements* **2011**, *186*, 240–254.

(207) Lecot, S.; Lavigne, A.; Yang, Z.; Géhin, T.; Botella, C.; Jousseaume, V.; Chevolot, Y.; Phaner-Goutorbe, M.; Yeromonahos, C. *The Journal of Physical Chemistry C* **2020**, *124*, 20125–20134.

(208) McElwee, J.; Helmy, R.; Fadeev, A. Y. *Journal of Colloid and Interface Science* **2005**, *285*, 551–556.

(209) Opila, R.; Legrange, J.; Markham, J.; Heyer, G.; Schroeder, C. *Journal of Adhesion Science and Technology* **1997**, *11*, 1–10.

(210) Wu, L.; Cai, L.; Liu, A.; Wang, W.; Yuan, Y.; Li, Z. *Applied Surface Science* **2015**, *349*, 683–694.

(211) Mizutani, W.; Ishida, T.; Tokumoto, H. *Applied Surface Science* **1998**, *130*, 792–796.

(212) Pujari, S. P.; Spruijt, E.; Cohen Stuart, M. A.; van Rijn, C. J.; Paulusse, J. M.; Zuilhof, H. *Langmuir* **2012**, *28*, 17690–17700.

(213) Effenberger, F.; Götz, G.; Bidlingmaier, B.; Wezstein, M. *Angewandte Chemie International Edition* **1998**, *37*, 2462–2464.

(214) Hoffmann, C.; Tovar, G. E. *Journal of Colloid and Interface Science* **2006**, *295*, 427–435.

(215) Moineau, J.; Granier, M.; Lanneau, G. F. *Langmuir* **2004**, *20*, 3202–3207.

(216) Meillan, M.; Buffeteau, T.; Le Bourdon, G.; Thomas, L.; Degueil, M.; Heuzé, K.; Bennetau, B.; Vellutini, L. *ChemistrySelect* **2017**, *2*, 11868–11874.

(217) Templeton, A. C.; Hostetler, M. J.; Warmoth, E. K.; Chen, S.; Hartshorn, C. M.; Krishnamurthy, V. M.; Forbes, M. D.; Murray, R. W. *Journal of the American Chemical Society* **1998**, *120*, 4845–4849.

(218) Iqbal, N.; Wolstenholme-Hogg, A.; Gompels, J. R.; Chechik, V. *Analytical Chemistry* **2025**.

(219) Karawdeniya, B. I.; Damry, A. M.; Murugappan, K.; Manjunath, S.; Bandara, Y. N. D.; Jackson, C. J.; Tricoli, A.; Neshev, D. *Chemical Reviews* **2022**, *122*, 14990–15030.

(220) Vashist, S. K.; Lam, E.; Hrapovic, S.; Male, K. B.; Luong, J. H. *Chemical Reviews* **2014**, *114*, 11083–11130.

(221) Ianni, J. C. In *Computational Fluid and Solid Mechanics 2003*; Elsevier: 2003, pp 1368–1372.

(222) Howard, J.; Chenier, J. *Canadian Journal of Chemistry* **1980**, *58*, 2808–2812.

(223) Maillard, B.; Ingold, K.; Scaiano, J. *Journal of the American Chemical Society* **1983**, *105*, 5095–5099.

(224) Carslaw, N. *Atmospheric Environment* **2007**, *41*, 1164–1179.

(225) Ewers, B. W.; Batteas, J. D. *The Journal of Physical Chemistry C* **2012**, *116*, 25165–25177.

(226) Scott, M. C.; Stevens, D. R.; Bochinski, J. R.; Clarke, L. I. *ACS Nano* **2008**, *2*, 2392–2400.

(227) Dhotel, A.; Chen, Z.; Sun, J.; Youssef, B.; Saiter, J.-M.; Schönhals, A.; Tan, L.; Delbreilh, L. *Soft Matter* **2015**, *11*, 719–731.

(228) Schreiber, F. *Progress in Surface Science* **2000**, *65*, 151–257.

(229) Kita, Y.; Matsugi, M., *Radical Initiators*; John Wiley & Sons, Ltd: 2001; Chapter 1.1, pp 1–10.

(230) Sigma-Aldrich Thermal Initiators: AIBN (Azobisisobutyronitrile), Accessed: 2025-02-11, n.d.

(231) Boros-Gyevi, E.; Tüd, F., et al. *European Polymer Journal* **1969**, *5*, 219–229.

(232) Lightfoot, P.; Kirwan, S.; Pilling, M. *The Journal of Physical Chemistry* **1988**, *92*, 4938–4946.

(233) Encina, M.; Lissi, E. *Journal of Photochemistry* **1978**, *8*, 131–143.

(234) Shemesh, D.; Lan, Z.; Gerber, R. B. *The Journal of Physical Chemistry A* **2013**, *117*, 11711–11724.

(235) Tadić, J.; Juranić, I.; Moortgat, G. K. *Journal of Photochemistry and Photobiology A: Chemistry* **2001**, *143*, 169–179.

(236) Yujing, M.; Mellouki, A. *Journal of Photochemistry and Photobiology A: Chemistry* **2000**, *134*, 31–36.

(237) Matsumi, Y.; Kawasaki, M. *Chemical Reviews* **2003**, *103*, 4767–4782.

(238) Dusciac, D.; de Villeneuve, C. H.; Allongue, P.; Ozanam, F.; Chazalviel, J.-N. *Surface Science* **2013**, *609*, 230–235.

(239) Schuchmann, H.-P.; Sonntag, C. *Tetrahedron* **1973**, *29*, 1811–1818.

(240) Eliason, T.; Gilman, J.; Vaida, V. *Atmospheric Environment* **2004**, *38*, 1367–1378.

(241) Mondal, K.; Chattopadhyay, A.; Bhattacharya, I.; Chatterjee, P.; Mandal, S.; Chakraborty, T. *ACS Earth and Space Chemistry* **2023**, *7*, 449–459.

(242) Ellis, S. R.; Pham, H. T.; in het Panhuis, M.; Trevitt, A. J.; Mitchell, T. W.; Blanksby, S. J. *Journal of the American Society for Mass Spectrometry* **2017**, *28*, 1345–1358.

(243) Hull, L.; Hisatsune, I.; Heicklen, J. *The Journal of Physical Chemistry* **1972**, *76*, 2659–2665.

(244) Khachatryan, L.; Fajgar, R.; Haas, Y.; Pola, J. *Journal of the Chemical Society, Perkin Transactions 2* **1996**, 1981–1984.

(245) Adachi, H.; Basco, N. *International Journal of Chemical Kinetics* **1982**, *14*, 1243–1251.

(246) Park, J.; Lee, L.; Byun, H.; Ham, S.; Lee, I.; Park, J.; Rhie, K.; Lee, Y.; Yeom, J.; Tsai, P., et al. *Journal of Cleaner Production* **2014**, *66*, 10–18.

(247) Aschmann, S. M.; Arey, J.; Atkinson, R. *The Journal of Physical Chemistry A* **2000**, *104*, 3998–4003.

(248) Johnston, H. S.; Heicklen, J. *Journal of the American Chemical Society* **1964**, *86*, 4249–4254.

(249) Schlosser, E.; Brauers, T.; Dorn, H.-P.; Fuchs, H.; Häseler, R.; Hofzumahaus, A.; Holland, F.; Wahner, A.; Kanaya, Y.; Kajii, Y., et al. *Atmospheric Chemistry and Physics* **2009**, *9*, 7923–7948.

(250) Dorn, H.-P.; Apodaca, R.; Ball, S. M.; Brauers, T.; Brown, S. S.; Crowley, J.; Dubé, W.; Fuchs, H.; Häseler, R.; Heitmann, U., et al. *Atmospheric Measurement Techniques* **2013**, *6*, 1111–1140.

(251) Cui, Y.; Duan, X.; Hu, J.; Lieber, C. M. *The Journal of Physical Chemistry B* **2000**, *104*, 5213–5216.

(252) Chen, X.; Wong, C. K.; Yuan, C. A.; Zhang, G. *Sensors and Actuators B: Chemical* **2013**, *177*, 178–195.

(253) Li, J.; Pud, S.; Petrychuk, M.; Offenhäusser, A.; Vitusevich, S. *Nano letters* **2014**, *14*, 3504–3509.

(254) Vardhan, V.; Biswas, S.; Ghosh, S.; Tsetseris, L.; Hellebust, S.; Echresh, A.; Georgiev, Y. M.; Holmes, J. D. *ACS Applied Materials & Interfaces* **2025**.

(255) Konstantinova, E.; Osminkina, L.; Sharov, K.; Kurepina, E.; Kashkarov, P.; Timoshenko, V. Y. *Journal of Experimental and Theoretical Physics* **2004**, *99*, 741–748.

(256) Singh, M.; Kaur, N.; Comini, E. *Journal of Materials Chemistry C* **2020**, *8*, 3938–3955.

(257) Cao, A.; Sudhölter, E. J.; De Smet, L. C. *Sensors* **2013**, *14*, 245–271.

(258) Li, D.; Song, S.; Fan, C. *Accounts of Chemical Research* **2010**, *43*, 631–641.

(259) Zhou, X.; Hu, J.; Li, C.; Ma, D.; Lee, C.; Lee, S. *Chemical Physics Letters* **2003**, *369*, 220–224.

(260) Wang, B.; Haick, H. *ACS Applied Materials & Interfaces* **2013**, *5*, 2289–2299.

(261) Riedel, F. The generation of reactive species downstream of an atmospheric pressure plasma jet, Unpublished, 2019.

(262) Schulz-von der Gathen, V.; Buck, V.; Gans, T.; Knake, N.; Niemi, K.; Reuter, S.; Schaper, L.; Winter, J. *Contributions to Plasma Physics* **2007**, *47*, 510–519.

(263) Schröter, S.; Wijaikhum, A.; Gibson, A. R.; West, A.; Davies, H. L.; Minesi, N.; Dedrick, J.; Wagenaars, E.; De Oliveira, N.; Nahon, L., et al. *Physical Chemistry Chemical Physics* **2018**, *20*, 24263–24286.

(264) Lietz, A. M.; Kushner, M. J. *Journal of Physics D: Applied Physics* **2016**, *49*, 425204.

(265) Murakami, T.; Niemi, K.; Gans, T.; O'Connell, D.; Graham, W. G. *Plasma Sources Science and Technology* **2014**, *23*, 025005.

(266) Mellouki, A.; Le Bras, G.; Sidebottom, H. *Chemical Reviews* **2003**, *103*, 5077–5096.

(267) McGillen, M. R.; Percival, C. J.; Shallcross, D. E.; Harvey, J. N. *Physical Chemistry Chemical Physics* **2007**, *9*, 4349–4356.

(268) Valiev, M.; Bylaska, E. J.; Govind, N.; Kowalski, K.; Straatsma, T. P.; Van Dam, H. J. J.; Wang, D.; Nieplocha, J.; Aprà, E.; Windus, T. L., et al. *Computer Physics Communications* **2010**, *181*, 1477–1489.

(269) Becke, A. D. *The Journal of Chemical Physics* **1993**, *98*, 5648–5652.

(270) Stephens, P. J.; Devlin, F. J.; Chabalowski, C. F.; Frisch, M. J. *The Journal of Physical Chemistry* **1994**, *98*, 11623–11627.

(271) Godbout, N.; Salahub, D. R.; Andzelm, J.; Wimmer, E. *Canadian Journal of Chemistry* **1992**, *70*, 560–571.

(272) Momma, K.; Izumi, F. *Applied Crystallography* **2011**, *44*, 1272–1276.

(273) Berndt, T.; Böge, O. *Physical Chemistry Chemical Physics* **2001**, *3*, 4946–4956.

(274) Caralp, F.; Forst, W.; Rayez, M.-T. *Physical Chemistry Chemical Physics* **2003**, *5*, 476–486.

(275) Lim, Y. B.; Ziemann, P. J. *Aerosol Science and Technology* **2009**, *43*, 604–619.

(276) Lloyd, A. C.; Darnall, K. R.; Winer, A. M.; Pitts Jr, J. N. *The Journal of Physical Chemistry* **1976**, *80*, 789–794.

(277) Atkinson, R.; Aschmann, S. M.; Winer, A. M.; Pitts Jr, J. N. *International Journal of Chemical Kinetics* **1982**, *14*, 507–516.